N°d'ordre NNT : **2025ISAL0008**

THESE de DOCTORAT DE L'INSA LYON, membre de l'Université de Lyon

Ecole Doctorale N° 34
Matériaux Lyon

Spécialité/ discipline de doctorat :
Matériaux

Soutenue publiquement le 24/01/2025, par :
Julien MOREAU

Sinter-based Additive Manufacturing of Mg-Zn Bio-degradable Metallic Materials for Orthopedic Implants

---

Devant le jury composé de :

SHABADI, Rajashekhara	Univ. De Lille	Rapporteur
BERNARD, Frédéric	Université bourgogne	Rapporteur
COFFIGNIEZ, Marion	INP de Grenoble	Examinatrice
BERTRAND, Ghislaine	INP de toulouse	Présidente
GREMILLARD, Laurent	INSA Lyon	Directeur de thèse
BOULNAT, Xavier	INSA Lyon	Encadrant

Thèse accessible à l'adresse : https://theses.insa-lyon.fr/publication/2025ISAL0008/these.pdf © [J. Moreau], [2025], INSA Lyon, tous droits réservés

Thèse accessible à l'adresse : https://theses.insa-lyon.fr/publication/2025ISAL0008/these.pdf © [J. Moreau], [2025], INSA Lyon, tous droits réservés

Département FEDORA – INSA Lyon - Ecoles Doctorales

SIGLE	ECOLE DOCTORALE	NOM ET COORDONNEES DU RESPONSABLE
ED 206 CHIMIE	**CHIMIE DE LYON** https://www.edchimie-lyon.fr Sec. : Renée EL MELHEM Bât. Blaise PASCAL, 3e étage secretariat@edchimie-lyon.fr	**M. Stéphane DANIELE** C2P2-CPE LYON-UMR 5265 Bâtiment F308, BP 2077 43 Boulevard du 11 novembre 1918 69616 Villeurbanne directeur@edchimie-lyon.fr
ED 341 E2M2	**ÉVOLUTION, ÉCOSYSTÈME, MICROBIOLOGIE, MODÉLISATION** http://e2m2.universite-lyon.fr Sec. : Bénédicte LANZA Bât. Atrium, UCB Lyon 1 Tél : 04.72.44.83.62 secretariat.e2m2@univ-lyon1.fr	**Mme Sandrine CHARLES** Université Claude Bernard Lyon 1 UFR Biosciences Bâtiment Mendel 43, boulevard du 11 Novembre 1918 69622 Villeurbanne CEDEX e2m2.codir@listes.univ-lyon1.fr
ED 205 EDISS	**INTERDISCIPLINAIRE SCIENCES-SANTÉ** http://ediss.universite-lyon.fr Sec. : Bénédicte LANZA Bât. Atrium, UCB Lyon 1 Tél : 04.72.44.83.62 secretariat.ediss@univ-lyon1.fr	**Mme Sylvie RICARD-BLUM** Laboratoire ICBMS - UMR 5246 CNRS - Université Lyon 1 Bâtiment Raulin - 2ème étage Nord 43 Boulevard du 11 novembre 1918 69622 Villeurbanne Cedex Tél : +33(0)4 72 44 82 32 sylvie.ricard-blum@univ-lyon1.fr
ED 34 EDML	**MATÉRIAUX DE LYON** http://ed34.universite-lyon.fr Sec. : Yann DE ORDENANA Tél : 04.72.18.62.44 yann.de-ordenana@ec-lyon.fr	**M. Stéphane BENAYOUN** Ecole Centrale de Lyon Laboratoire LTDS 36 avenue Guy de Collongue 69134 Ecully CEDEX Tél : 04.72.18.64.37 stephane.benayoun@ec-lyon.fr
ED 160 EEA	**ÉLECTRONIQUE, ÉLECTROTECHNIQUE, AUTOMATIQUE** https://edeea.universite-lyon.fr Sec. : Philomène TRECOURT Bâtiment Direction INSA Lyon Tél : 04.72.43.71.70 secretariat.edeea@insa-lyon.fr	**M. Philippe DELACHARTRE** INSA LYON Laboratoire CREATIS Bâtiment Blaise Pascal, 7 avenue Jean Capelle 69621 Villeurbanne CEDEX Tél : 04.72.43.88.63 philippe.delachartre@insa-lyon.fr
ED 512 INFOMATHS	**INFORMATIQUE ET MATHÉMATIQUES** http://edinfomaths.universite-lyon.fr Sec. : Renée EL MELHEM Bât. Blaise PASCAL, 3e étage Tél : 04.72.43.80.46 infomaths@univ-lyon1.fr	**M. Dragos IFTIMIE** Université Claude Bernard Lyon 1 Bâtiment Braconnier (ex-101) 21 Avenue Claude Bernard 69622 VILLEURBANNE Cedex Tél : 04.72.44.79.58 direction.infomaths@listes.univ-lyon1.fr
ED 162 MEGA	**MÉCANIQUE, ÉNERGÉTIQUE, GÉNIE CIVIL, ACOUSTIQUE** http://edmega.universite-lyon.fr Sec. : Philomène TRECOURT Tél : 04.72.43.71.70 Bâtiment Direction INSA Lyon mega@insa-lyon.fr	**M. Etienne PARIZET** INSA Lyon Laboratoire LVA Bâtiment St. Exupéry 25 bis av. Jean Capelle 69621 Villeurbanne CEDEX etienne.parizet@insa-lyon.fr
ED 483 ScSo	**ScSo**[1] https://edsciencessociales.universite-lyon.fr Sec. : Mélina FAVETON Tél : 04.78.69.77.79 melina.faveton@univ-lyon2.fr	**M. Bruno MILLY** (INSA : J.Y. TOUSSAINT) Univ. Lyon 2 Campus Berges du Rhône 18, quai Claude Bernard 69365 LYON CEDEX 07 Bureau BEL 319 bruno.milly@univ-lyon2.fr

[1] ScSo : Histoire, Géographie, Aménagement, Urbanisme, Archéologie, Science politique, Sociologie, Anthropologie

Thèse accessible à l'adresse : https://theses.insa-lyon.fr/publication/2025ISAL0008/these.pdf © [J. Moreau], [2025], INSA Lyon, tous droits réservés

Thèse accessible à l'adresse : https://theses.insa-lyon.fr/publication/2025ISAL0008/these.pdf © [J. Moreau], [2025], INSA Lyon, tous droits réservés

Acknowledgments

Je tiens tout d'abord à remercier tous mes encadrants de thèse, Xavier, Laurent, Benoît, Michel et Olivier, pour l'encadrement de mes travaux. Je leur suis très reconnaissant pour le temps et l'attention qu'ils m'ont accordés durant ces trois années, ainsi que pour toutes les compétences que j'ai pu acquérir auprès d'eux. Je remercie particulièrement Xavier, Benoît et Laurent, qui ont été présents au quotidien.

Je tiens également à remercier mon jury de thèse, Ghislaine Bertrand, Marion Coffigniez, Frédéric Bernard et Rajashekhara Shabadi, et plus particulièrement les deux rapporteurs, qui ont pris le temps de relire en profondeur mon travail.

Ce fut un plaisir de conduire cette thèse au sein du laboratoire MATEIS, et tout particulièrement dans l'équipe METAL. Une grande partie des travaux présentés dans ce manuscrit n'aurait pu être réalisée sans l'aide de nombreux collègues. Au-delà du travail, l'ambiance à METAL fait qu'il est toujours agréable de s'y rendre. Je remercie donc très chaleureusement tous mes collègues du laboratoire qui m'ont croisé de près ou de loin.

Je remercie tout particulièrement celles et ceux qui m'ont beaucoup aidé pour toutes les manipulations effectuées dans cette thèse : Bérangère, Florian, Jérôme, mais aussi Rodica, François et Mathias du LMI.

Ayant travaillé au sein de nombreuses équipes, je remercie aussi tous les collègues des équipes CORRIS, CERA et du LMI.

Je suis très heureux d'avoir pu effectuer cette thèse en même temps que de nombreuses personnes au sein de METAL. Merci à Sarah, Louis, Mathilde, Bassem, Jordan, Ian et Théo, qui étaient là depuis le début. Merci aussi aux personnes de CERA : Timothé, Arthur, Mathieu, Léonore et Hugo.

J'aimerais également remercier ceux qui m'ont le plus soutenu durant cette période de ma vie : les membres de mon bureau, Samuel, Maureen et Seb. Sans vous, l'aventure aurait été bien moins drôle. Merci encore pour tout ce que vous m'avez apporté.

Enfin, j'aimerais remercier mon frère, Théophile, qui m'a toujours aidé et soutenu, et qui rend la vie des gens autour de lui plus belle.

Je tiens aussi à remercier ma famille, qui m'a toujours soutenu, ainsi qu'Elina, qui m'a accompagné dans cette dernière ligne droite, qui a dû être difficile.

Bisous, je m'envole.

Thèse accessible à l'adresse : https://theses.insa-lyon.fr/publication/2025ISAL0008/these.pdf © [J. Moreau], [2025], INSA Lyon, tous droits réservés

Thèse accessible à l'adresse : https://theses.insa-lyon.fr/publication/2025ISAL0008/these.pdf © [J. Moreau], [2025], INSA Lyon, tous droits réservés

Thèse accessible à l'adresse : https://theses.insa-lyon.fr/publication/2025ISAL0008/these.pdf © [J. Moreau], [2025], INSA Lyon, tous droits réservés

Contents

Contents i

Résumé en francais 1

Introduction 7

1 Background of the manufacturing technique and the properties of Mg alloys for biomedical applications 11
- 1.1 Introduction . . . 12
- 1.2 Manufacturing processes of Magnesium . . . 12
  - 1.2.1 Main manufacturing processes . . . 12
  - 1.2.2 Resulting microstructures . . . 14
  - 1.2.3 Spark plasma sintering of Magnesium alloys . . . 15
- 1.3 Microstructure and mechanical Properties of Magnesium Alloys . . . 18
  - 1.3.1 Grain size . . . 18
  - 1.3.2 Solid solution and precipitates hardening . . . 19
  - 1.3.3 Mechanical properties for orthopedic implants . . . 20
- 1.4 Corrosion of Magnesium alloys . . . 21
  - 1.4.1 Activity and passivity of Magnesium alloys . . . 21
  - 1.4.2 Corrosion types of Magnesium alloy . . . 24
  - 1.4.3 Electrochemical measurements of Magnesium alloys corrosion properties . 27
  - 1.4.4 Microstructure tuning for improved corrosion resistance . . . 30
- 1.5 Magnesium alloys design for biodegradable implants . . . 33
  - 1.5.1 Influence of the alloying elements on the mechanical properties and the corrosion resistance . . . 33
  - 1.5.2 Mechanical properties and corrosion resistance depending of the Zn concentration . . . 34
  - 1.5.3 Addition of Zr . . . 36
  - 1.5.4 Aging treatment of MgZnZr alloys . . . 36
- 1.6 Conclusion . . . 37

2 Development of MgZnZr alloy prepared by Spark Plasma Sintering 39
- 2.1 Introduction . . . 39
- 2.2 Materials and methods . . . 40
  - 2.2.1 Powders . . . 40
  - 2.2.2 Densification via Spark Plasma Sintering . . . 40

Thèse accessible à l'adresse : https://theses.insa-lyon.fr/publication/2025ISAL0008/these.pdf © [J. Moreau], [2025], INSA Lyon, tous droits réservés

2.2.3 Microstructural characterization . . . 41
2.2.4 Microscopic observations . . . 42
2.2.5 Differential scanning calorimetry (DSC) . . . 43
2.2.6 Oxygen analysis . . . 43
2.2.7 Mechanical tests . . . 43
2.3 Preliminary sintering study . . . 44
2.3.1 Setup for the sintering cycle . . . 44
2.3.2 Influence of the oxide layer on the mechanical properties . . . 45
2.4 Thermodynamic-based ZK30 sintering cycle . . . 47
2.4.1 Evaluation of the liquid phase . . . 48
2.4.2 Development of the SPS cycle . . . 50
2.4.3 Thermodynamics of ZK30 . . . 51
2.5 Mechanical properties at higher sintering temperatures . . . 54
2.6 Observation of the microstructure . . . 57
2.7 Conclusion . . . 59

3 Study of the precipitation in ZK30 alloy to improve the corrosion resistance 61
3.1 Material and methods . . . 62
3.1.1 Manufacturing of the dense parts . . . 62
3.1.2 Solution treatment . . . 62
3.1.3 Isothermal aging . . . 62
3.1.4 Thermoelectric power (TEP) measurements . . . 62
3.1.5 X-ray diffraction . . . 63
3.1.6 Corrosion measurements . . . 63
3.1.7 Electrochemical measurements . . . 63
3.2 Precipitation in ZK30 alloy . . . 64
3.2.1 Solution treatment . . . 64
3.2.2 Hardness and TEP measurements . . . 65
3.2.3 Precipitation kinetics in ZK30 alloy using TEP . . . 65
3.3 Mass loss measurement of heat treated ZK30 alloy . . . 72
3.3.1 Mass loss test of pure Magnesium and ZK30 . . . 72
3.3.2 Influence of the precipitation state on the mass loss in different media . . . 76
3.4 Corrosion resistance after optimized sintering . . . 78
3.4.1 Mass loss test in saline solution . . . 78
3.4.2 Electrochemical measurement at initial state . . . 79
3.4.3 Electrochemical measurement during immersion and influence of the aging 84
3.5 Conclusion . . . 87

4 Pressure-free debinding/sintering of Magnesium alloy: application to 3D printed parts by direct-ink writing 89
4.1 Background of additive manufacturing of Magnesium . . . 90
4.1.1 Additive manufacturing via powder melting . . . 90
4.1.2 Additive manufacturing via powder sintering . . . 91
4.1.3 Liquid phase sintering (LPS) of Magnesium . . . 94
4.2 Sample manufacturing . . . 98
4.2.1 Ink formulation . . . 98

Thèse accessible à l'adresse : https://theses.insa-lyon.fr/publication/2025ISAL0008/these.pdf © [J. Moreau], [2025], INSA Lyon, tous droits réservés

4.2.2 Direct ink-writing . . . 99
4.2.3 Debinding and sintering . . . 99
4.3 Preliminary study and challenges of the sintering . . . 101
4.4 *In situ* tomography of the sintering of Magnesium alloys . . . 104
4.4.1 Material and method . . . 105
4.4.2 In situ observation of the sintering . . . 106
4.5 Sintering of Magnesium alloys in labyrinth crucible . . . 108
4.5.1 Initial samples . . . 109
4.5.2 Sintering setup . . . 111
4.5.3 Sintering tests . . . 112
4.5.4 Microstructure and hardness . . . 115
4.6 Conclusions . . . 120

General conclusion and perspectives **123**

Appendix A : Robocaster used in this study **127**

Appendix B : Setup used for tubular furnace sintering **129**

Bibliography **131**

Thèse accessible à l'adresse : https://theses.insa-lyon.fr/publication/2025ISAL0008/these.pdf © [J. Moreau], [2025], INSA Lyon, tous droits réservés

Thèse accessible à l'adresse : https://theses.insa-lyon.fr/publication/2025ISAL0008/these.pdf © [J. Moreau], [2025], INSA Lyon, tous droits réservés

Résumé en français

Cette partie est un résumé en français des travaux de thèse présentés dans ce manuscrit. Il présente les grands axes étudiés et les résultats associés. L'intégralité des résultats de ces travaux est détaillée dans le reste du manuscrit, rédigé en anglais.

Introduction

Dans le domaine de la chirurgie, les implants biomédicaux jouent un rôle crucial. Ils sont notamment utilisés en orthopédie [1], en cardiologie [2] et en neurologie [3], où ils permettent de réparer des os et des tissus. Actuellement, la demande en chirurgie orthopédique est en augmentation, avec l'un des taux de croissance annuels les plus élevés [4]. Cette hausse est principalement due à une population vieillissante et de plus en plus touchée par les fractures et l'arthrose, avec une augmentation prévue de 26% entre 2019 et 2034 en France [5].

Parmi les matériaux possibles pour les implants, les alliages métalliques se distinguent par leurs excellentes propriétés mécaniques (résistance mécanique, ductilité et résistance à la fatigue). Les alliages métalliques les plus couramment utilisés, comme les alliages de titane [6] et les alliages de cobalt [7], présentent deux problèmes majeurs.

Le premier est que ces implants sont trop rigides par rapport aux os. En effet, cette différence de rigidité entre un implant et le tissu osseux environnant entraîne le phénomène de "stress-shielding", ce qui peut limiter l'ostéointégration et entraîner une résorption des os [8]. Le second problème vient de la durabilité de ces implants, qui entraîne des complications à long terme. Des inflammations et une libération d'ions cytotoxiques peuvent survenir en raison de la corrosion et de la fatigue [9] [10]. Habituellement, les implants métalliques permanents sont retirés deux ou trois ans après la première opération [11].

Utiliser des implants biodégradables qui se dissolvent dans le corps après la guérison d'un os élimine le besoin de chirurgies de retrait, offrant des avantages significatifs pour les patients et les systèmes de santé en termes de coût [12]. Les implants métalliques temporaires présentent des avantages par rapport aux matériaux d'ostéosynthèse permanents, surtout pour les implants de petite taille. Ces implants soutiennent temporairement l'os pour assurer une stabilité mécanique et se dégradent progressivement, permettant au tissu osseux nouvellement formé de prendre en charge leur fonction.

La production d'implants biodégradables en alliages métalliques pose un défi complexe, combinant des exigences techniques et médicales. Les alliages à base de Mg émergent comme la prochaine génération d'alliages métalliques biodégradables offrant de bonnes propriétés d'ostéo intégration [13]. Comparés à d'autres alliages métalliques utilisés dans les implants orthopédiques, tels que le titane, l'acier inoxydable et les alliages de cobalt-chrome, les alliages de magnésium se

Thèse accessible à l'adresse : https://theses.insa-lyon.fr/publication/2025ISAL0008/these.pdf © [J. Moreau], [2025], INSA Lyon, tous droits réservés

distinguent par leur faible rigidité, similaire à celle de l'os humain, ce qui aide à prévenir l'effet de "stress-shielding" dans les structures osseuses [14].

Les biomatériaux à base de Mg et leurs alliages sont principalement utilisés comme implants temporaires, se dégradant complètement dans le corps et étant remplacés par du nouveau tissu osseux, éliminant ainsi le besoin de chirurgie de retrait pour les implants permanents après 10 à 15 ans. Cette propriété les rend très attractifs sur le marché des implants biodégradables dans les applications de réparation osseuse nécessitant un soutien temporaire. Cependant, dans l'environnement biologique, les alliages de Mg se dégradent rapidement, nécessitant un contrôle strict de leur vitesse de dissolution, qui correspond à la vitesse à laquelle l'implant subit une perte de masse dans le corps humain, pour correspondre au processus de guérison de l'os. Une dissolution rapide entraîne une perte de résistance mécanique de l'implant et peut avoir des effets toxiques sur les tissus environnants en raison des réactions secondaires et de l'accumulation de produits de corrosion. Ces facteurs ont des implications pour la santé, il est donc essentiel d'améliorer la résistance à la corrosion des alliages de Mg pour ces applications.

Pour que les alliages de Mg soient utilisés dans un cadre clinique sûr, le taux de dissolution doit être régulé jusqu'à la guérison de l'os. De nombreux travaux ont été consacrés à la recherche d'une solution au problème de la dissolution des implants, les techniques de modification de surface et de modification de la microstructure étant à l'avant-garde [16]. Une méthode potentielle pour contrôler le taux de dégradation est l'alliage à faible teneur, qui consiste à mélanger le Mg avec d'autres métaux nobles tels que le Zn [17] et le Ca [18]. Certains alliages commerciaux de magnésium existent, comme les vis Magnezix [19] et les endoprothèses DREAMS [20]. Magnezix a développé plusieurs broches et vis utilisant un alliage de Mg composé d'yttrium, de zirconium et d'éléments de terres rares non divulgués, mais l'alliage contient plus de 90% de Mg. Ces dispositifs existent en plusieurs tailles, bien que limitées, pour chaque gamme de produits. Bien que cela marque un début pour les implants biodégradables, des défis subsistent en raison de la réactivité et de la volatilité du magnésium.

Cependant, les dispositifs tels que les vis et les plaques ne conviennent pas à toutes les blessures ni à tous les patients. De plus, pour les vis commerciales en alliages de Mg, seules quelques tailles et formes sont disponibles. Pour satisfaire la diversité des implants et des patients, différentes techniques de mise en forme doivent être explorées. Des implants personnalisés pour chaque usage offriraient un meilleur ajustement à l'anatomie du patient, entraînant une amélioration des résultats pour le patient. Cela faciliterait la tâche du chirurgien, et réduirait également la durée de l'opération. Parmi les techniques permettant d'obtenir ce type de structure, la fabrication additive (FA) connaît une forte croissance, car elle donne également accès à la production d'implants spécifiques aux patients. La FA des alliages métalliques est déjà utilisée pour diverses applications biomédicales.

Cependant, les techniques de FA métallique suffisamment développées pour être utilisées pour la production d'implants reposent sur des équipements coûteux et techniques impliquant une consommation d'énergie élevée (laser, faisceau d'électrons). Des procédés alternatifs, plus simples et moins onéreux, seraient donc bienvenus pour augmenter l'accessibilité mondiale de ces types d'implants. En offrant la possibilité d'imprimer chaque classe de matériaux à température ambiante, le procédé de DIW semble prometteur pour répondre à ces exigences [28] [29]. Ce procédé consiste en une extrusion couche par couche d'une pâte, appelée encre, à travers une seringue montée sur un bras robotisé. Dans le cas d'une encre contenant des particules céramiques ou métalliques, une étape de déliantage est nécessaire pour retirer le liant qui fa-

Thèse accessible à l'adresse : https://theses.insa-lyon.fr/publication/2025ISAL0008/these.pdf © [J. Moreau], [2025], INSA Lyon, tous droits réservés

cilite le transport des particules à travers la buse. Ensuite, les propriétés finales des pièces sont atteintes après un traitement de frittage. Au-delà de l'aspect économique, ce procédé, basé sur une structure obtenue par frittage, peut également être un moyen d'améliorer l'ostéointégration en conservant un réseau microporeux par frittage partiel.

Le procédé de direct ink-writing (DIW) semble prometteur pour construire facilement ce type de structure, car les macropores peuvent être conçus lors du dépôt de l'encre, tandis que le réseau microporeux peut être obtenu par un frittage partiel. Cependant, ce procédé en est encore à ses débuts, ce qui signifie que des études sont encore nécessaires pour évaluer pleinement le potentiel et les limitations de cette technique.

Dans ce contexte, la présente étude se concentrera sur le développement d'un dispositif biodégradable imprimé en 3D pour implants orthopédiques, composé d'un alliage de Mg.

Le présent manuscrit est structuré comme suit :

Le premier chapitre passe en revue la littérature sur les alliages de Mg destinés aux implants orthopédiques. Il présente leurs propriétés actuelles ainsi que les motivations derrière le choix d'un alliage de Mg pour ce type d'applications.

Le deuxième chapitre se concentre sur le développement d'alliages de Mg en utilisant le SPS. La fabrication de pièces denses est essentielle pour évaluer et améliorer les propriétés de l'alliage en tant qu'implant. Ce chapitre examine notamment l'influence de la température de frittage sur la densité, la microstructure et les propriétés mécaniques.

Le troisième chapitre explore les propriétés de corrosion de l'alliage de Mg. Les alliages de Mg sont particulièrement sensibles à la corrosion, et la microstructure de l'alliage joue un rôle important sur la résistance à la corrosion. Afin de diminuer au plus la vitesse de dissolution des alliages de Mg, une étude approfondie de la précipitation dans l'alliage est également réalisée. Cette analyse vise à évaluer son impact et les avantages potentiels sur le contrôle du taux de dissolution.

Le quatrième chapitre introduit la littérature sur les techniques de fabrication additive appliquées aux alliages de Mg, en mettant l'accent sur les procédés basés sur le frittage et les défis associés au frittage sans pression. Ce chapitre présente ensuite l'impression par direct ink-writing de l'alliage, en détaillant l'optimisation des étapes d'impression et de déliantage. Le frittage des alliages de Mg est étudié dans différentes conditions de température, de temps et d'environnement. Enfin, une nanotomographie aux rayons X réalisée *in situ* permet d'approfondir la compréhension des mécanismes de frittage impliqués.

Enfin, le manuscrit se conclut par une synthèse générale qui rappelle les principaux résultats obtenus au cours de cette étude. Elle discute également des forces et des limitations du procédé, tout en proposant des perspectives pour les futures caractérisations et développements nécessaires. Ce dernier chapitre met en lumière les approches à explorer en profondeur pour aboutir à la fabrication de pièces métalliques biodégradables par DIW.

Chapitre 2 : Dévelopement d'un alliage de MgZnZr fritté par Spark Plasma Sintering (SPS)

Ce chapitre se concentre sur la fabrication de pièces denses de Mg par procédé SPS. Le cycle est développé petit à petit avec au début des tests sur du Mg pur. Suite au frittage, la dureté et la densité relative de tous les échantillons ont été mesurées. Ces mesures ont permis de déterminer

Thèse accessible à l'adresse : https://theses.insa-lyon.fr/publication/2025ISAL0008/these.pdf © [J. Moreau], [2025], INSA Lyon, tous droits réservés

des paramètres de température, de pression et d'atmosphère qui pourraient être adéquats pour des alliages de Mg. L'étude s'est donc ensuite concentrée sur la densification des alliages MgZnZr (ZK30). Par la même méthode de mesure de dureté et de densité relative, quelques cycles de frittage ont été identifiés comme intéressants. Cependant, suite à ces essais, des pièces frittées ont été soumises à des tests de traction, mettant en évidence un comportement fragile. Ce comportement, opposé à celui des alliages de Mg classiques, semble être causé par la couche d'oxyde résiduelle présente à la surface des particules de poudre. Pour éliminer cette couche d'oxyde, plusieurs options ont été envisagées mais celle privilégiée est de former une phase liquide à l'intérieur des particules de poudre pendant le frittage pour essayer de briser cette couche d'oxyde. Pour ce faire, une calorimétrie différentielle à balayage a été effectuée sur la poudre de ZK30 afin d'en déterminer les températures clés de transformation, dont le solidus. Cette analyse a permis de déterminer des nouvelles conditions de frittage à plus hautes températures. Avec ces nouvelles températures, les propriétés mécaniques sont améliorées. Les observations microscopiques montrent également que la couche d'oxyde semble plus diffuse qu'auparavant.

Chapitre 3 : Etude de la précipitation dans les alliages ZK30 pour optimiser la résistance à la corrosion

Ce chapitre est consacré à l'étude de la précipitation afin d'optimiser la résistance à la corrosion des alliages de ZK30. Pour ce faire, des pièces denses fabriquées par SPS sont préparées. Des températures adéquates de mise en solution du Zn dans le Mg ont été déterminées par analyse microscopique. Ensuite, deux températures de vieillissement (170 °C et 200 °C)se situant chacune dans un domaine du diagramme de phase MgZnZr différent ont été choisies. Des vieillissements à ces deux températures ont été effectués jusqu'à 44 h. A différents intervalles de temps, des mesures de dureté et de pouvoir thermoélectrique (PTE) ont permis de suivre l'évolution de la précipitation. Deux pics de dureté ont pu être observés et correspondent à l'apparition des précipités β_1' et β_2', identiques à ceux observés dans les alliages binaires de Mg-Zn. En se basant sur des études similaires de précipiation sur des binaires Mg-Zn, les mesures PTE ont permis de remonter à la teneur en Zn dans la solution solide, ainsi qu'à la fraction volumique des précipités.

Dans la suite de ce chapitre, une étude de la vitesse de dégradation de l'alliage ZK30 a été effectuée. Dans un premier temps, une simple étude de perte de masse en solution saline a été effectuée sur les pièces de ZK30 dense ayant subi différents traitements thermiques. Ce suivi de perte de masse permet en première approche d'identifier les traitements thermiques qui améliorent le plus la résistance à la corrosion. Suite à cette étude en solution saline, une autre série de mesures de perte de masse fut effectuée cette fois en milieu physiologique. A la différence de la solution saline, le milieu physiologique induit la formation de plus de produits de corrosion, augmentant ainsi la masse initiale de manière beaucoup plus importante. Une fois ces analyses préliminaires effectuées, des mesures de spectroscopie d'impédance électrochimique furent effectuées sur les alliages présentant la meilleure résistance à la corrosion en solution saline. Ces mesures permettent de remonter à un circuit électrique équivalent, qui reproduit le comportement électrochimique du système étudié. Les résistances associées à ce circuit équivalent permettent de remonter à la résistance de polarisation de l'alliage et à un courant de corrosion. Ensuite, une vitesse de dégradation est déterminée pour comparer le comportement de chaque alliage. Les mesures de perte de masse ainsi que les mesures électrochimiques indiquent que l'échantillon solubilisé, et ceux veillis à 170 °C pendant 4 h et 14 h semblent présenter la

Thèse accessible à l'adresse : https://theses.insa-lyon.fr/publication/2025ISAL0008/these.pdf © [J. Moreau], [2025], INSA Lyon, tous droits réservés

meilleure résistance à la corrosion. La présence de précipités de petites tailles et répartis de façon homogène après vieillissement à 170 °C pourrait améliorer la résistance à la corrosion, contrairement au vieillissement à 200 °C qui forme de trop gros précipités. Ces gros précipités accélèrent probablement la dissolution par couplages galvaniques importants.

Chapitre 4 : Fabrication 3D de pièce par DIW assistée par déliantage et frittage sans pression

Ce chapitre est dédié à la fabrication par DIW de pièces composées d'alliage de ZK30, ainsi que le déliantage et le frittage qui sont les étapes suivantes nécessaires. Une première partie est consacrée à l'état de l'art sur le frittage en phase liquide et les récents progrès dans le frittage du Mg sans pression. Ensuite, la formulation de l'encre et l'impression est abordée. Une pâte composée d'un polymère, d'un solvant et chargée en poudre de ZK30 est extrudée à travers une buse. Cette technique permet d'imprimer facilement et rapidement des pièces en 3D. Suite à l'impression, pour éliminer le liant restant dans la pièce, un déliantage doit être effectué. La température de déliantage adéquate est déterminée par analyse thermogravimétrique. Suite au déliantage, l'étape la plus difficile est le frittage. Afin de mieux comprendre les mécanismes impliqués dans le frittage, une nanotomographie à rayons X a été utilisée. L'observation au cours du temps des particules de poudres montrent plusieurs étapes observables et notamment la fuite du liquide une fois la couche d'oxyde brisée. Suite à ces observations, un creuset labyrinthe permettant de protéger les pièces de l'oxydation et de confiner les vapeurs de Mg a été fabriqué. Ce dispositif a été testé avec des pièces fabriquées en 3D et de la poudre compressée à froid et a permis d'identifier les paramètres de frittage optimaux pour obtenir des pièces denses en Magnésium. Des pièces imprimées, avec une densité relative après déliantage de 60%, ont été frittées avec une densité relative finale de 80%. Pour les pastilles compressées, de densité relative initiale de 70%, des hautes densités relatives (jusqu'à 98%) après frittage ont été obtenues. Le paramètre qui semble le plus influencer la densité finale est la densité relative initiale des pièces, mais l'apport en oxgène qui a lieu lors du déliantage des pièces imprimées peut aussi expliquer la différence de densité et de qualité du frittage.

Thèse accessible à l'adresse : https://theses.insa-lyon.fr/publication/2025ISAL0008/these.pdf © [J. Moreau], [2025], INSA Lyon, tous droits réservés

Thèse accessible à l'adresse : https://theses.insa-lyon.fr/publication/2025ISAL0008/these.pdf © [J. Moreau], [2025], INSA Lyon, tous droits réservés

General introduction

In the field of surgery, biomedical implants play a crucial role. They are notably used in orthopedics [1], cardiology [2], and neurology [3] where there is a need for bone and tissue repair. Currently, the demand for orthopedic surgery is growing, showing one of the highest annual growth rates [4]. This demand is explained by an aging population that is increasingly affected by fractures and osteoarthritis, with a predicted increase of 29% between 2019 and 2034 in France [5]. Among the possible materials used for implants, metallic alloys stand out for their excellent mechanical properties (mechanical strength, ductility, and fatigue resistance). The most commonly used metallic alloys, such as titanium alloys [6] and cobalt alloys [7] present two major problems. The first is that these implants are too stiff compared to bones. Indeed, this difference in stiffness between an implant and surrounding bone tissue leads to stress-shielding phenomenon, that may limit osseointegration and lead to the resorption of the bones [8]. The second issue comes from the durability of these implants, which leads to long-term complications. Inflammations and the release of cytotoxic ions can occur as a consequence of corrosion and fatigue [9] [10]. Usually, permanent metallic alloys orthopedic implants are removed after two or three years from the first operation [11].

Using biodegradable implants that dissolve in the body after a bone heals eliminates the need for removal surgeries, providing significant benefits for both patients and healthcare systems in terms of cost [12]. Temporary metallic alloys implants present advantages over permanent osteosynthesis materials, especially for smaller implants. These implants temporarily support the bone to ensure mechanical stability and gradually degrade, allowing newly formed bone tissue to take over their function.

The production of biodegradable metallic alloys implants, poses a complex challenge, combining both engineering and medical requirements. Magnesium (Mg) based alloys are emerging as the next generation of biodegradable metallic alloys with good osseointegration properties [13]. Compared to other metallic alloys used in orthopedic implants, such as titanium, stainless steel, and cobalt-chromium alloys, Mg alloys stand out for their rather low stiffness, close to that of human bone, which helps prevent the stress-shielding effect in bone structures [14].

Mg biomaterials and their alloys are primarily used as temporary implants, completely degrading in the body and being replaced by new bone tissue, eliminating the need for removal surgery required for permanent implants after 10–15 years. This property makes them highly attractive in the market for biodegradable implants in bone repair applications that require temporary support. However, in the biological environment, Mg alloys degrade quickly, necessitating strict control of the corrosion rate to match the bone's healing process. Rapid corrosion leads to loss of mechanical strength in the implant and can have toxic effects on surrounding tissues due to side reactions and accumulation of corrosion products. These factors have implications for patient health. Therefore, it is essential to enhance the corrosion resistance of Mg

Thèse accessible à l'adresse : https://theses.insa-lyon.fr/publication/2025ISAL0008/these.pdf © [J. Moreau], [2025], INSA Lyon, tous droits réservés

alloys for these applications. The advantages of Mg alloys and their biological characteristics are illustrated in Fig.1.

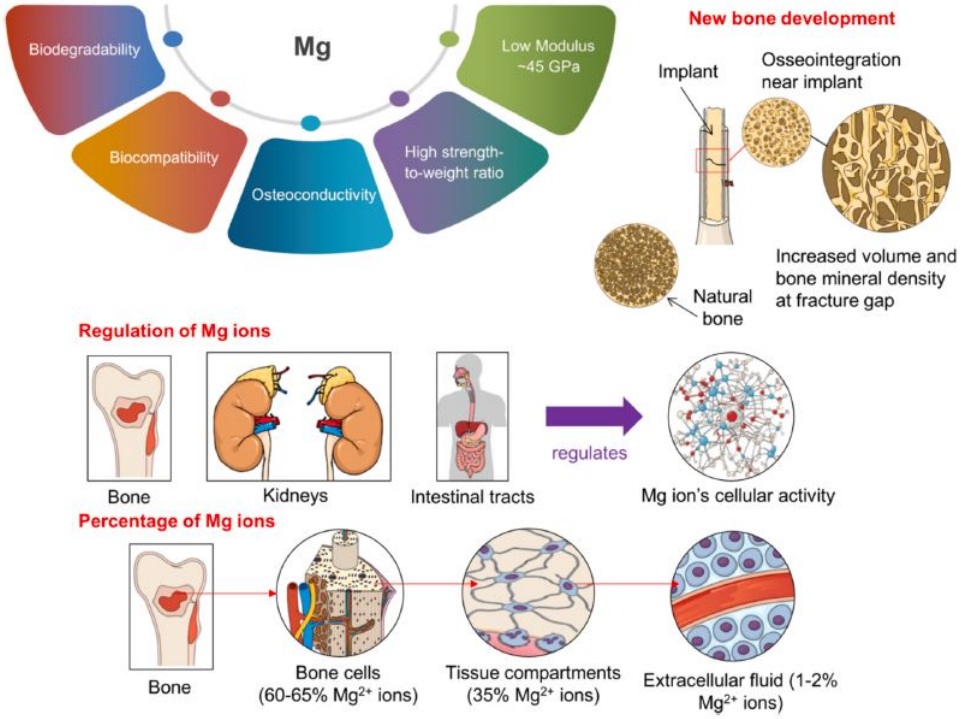


Figure 1: Characteristics and biological significance of Mg in orthopaedic implants, highlighting the presence of Mg in the body and the advantages of this material as an implant. Mg is naturally present in bones at different level and the concentration is naturally regulated by the organs, reproduced from [15]

.

For Mg alloys to be used in a safe clinical setting, the rate of deterioration must be regulated until the bone heals. A lot of work has gone into finding a solution to the deterioration problem, with surface modification and microstructural modification techniques taking the lead [16]. One potential way to control the degradation rate is by micro-alloying, which involves mixing Mg with other noble metals such as Zn [17] and Ca [18] for example. Some commercial Mg alloys exist, such as Magnezix screws [19] and DREAMS endoprostheses [20]. Magnezix developed several pins and screws using a Mg alloy composed of Yttrium, Zirconium and Rare earth elements which they did not disclose, but the alloy contain more than 90% of Mg. The design and application of the screws are shown in Fig.2. These devices are available in limited sizes, and while this marks a start for biodegradable implants, challenges remain due to Mg's reactivity and volatility.

However devices such as screws and plates are not appropriate for every injuries and every patient. Furthermore, for the commercial screws of Mg alloys, only a few different shapes and sizes exist. To satisfy the diversity of implants and patients, different shape forming techniques need to be explored. Implants personalized for every applications would offer a better fit of the patient anatomy, leading to improved patient outcomes. By making the surgeon's task easier, they would also reduce the operating time. Among the techniques that enable to achieve this

Thèse accessible à l'adresse : https://theses.insa-lyon.fr/publication/2025ISAL0008/these.pdf © [J. Moreau], [2025], INSA Lyon, tous droits réservés



Figure 2: a) Presentation of the Magnezix products, b) X-Ray imaging of the Hallux Valgus before the operation and c) X-Ray of the same Hallux Valgus after one year using a Magnezix screw with the outlines of the implant which has been transformed into bone still discernible

.

type of structure, additive manufacturing (AM) is particularly on the rise, as it also gives access to the production of patient-specific implants. AM of metallic alloys is already used for various biomedical applications as depicted in Fig.3

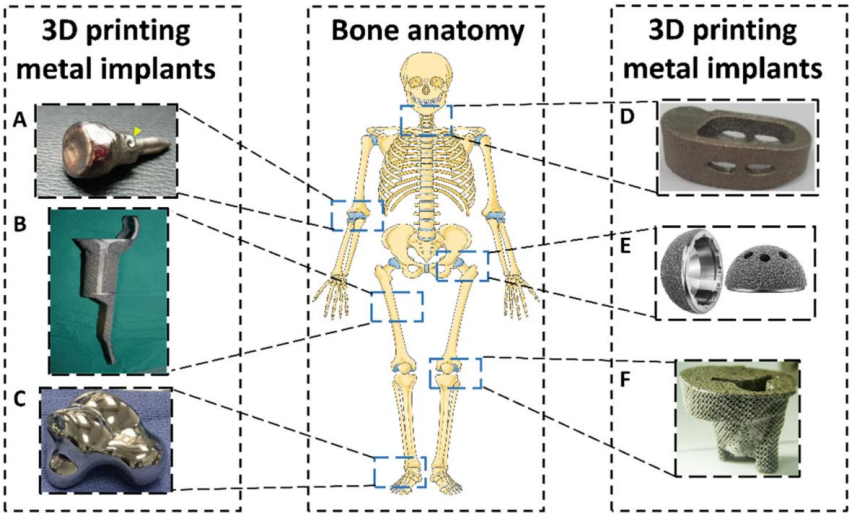


Figure 3: Clinical applications of metal 3D printing orthopedic implants a) Radial head prosthesis [21], b) Porous scaffolds in femoral defect [22], c) Total talus implant[23], d) Spine fusion device [24], e) Trabecular acetabular cup [25], f) Cones in total knee arthroplasty [26], reproduced from [27].

Currently, metallic AM techniques sufficiently developed to be used for implant production rely on expensive and technical equipments that involve large energy consumption (laser, electron beam). Alternative, simpler and cheaper processes would therefore be welcome to increase the worldwide accessibility of these types of implants. By offering the possibility to print each class of material at room temperature, the direct ink writing (DIW) process seems promising to reach these requirements [28] [29]. This process consists in a layer-wise extrusion of a paste, called ink,

Thèse accessible à l'adresse : https://theses.insa-lyon.fr/publication/2025ISAL0008/these.pdf © [J. Moreau], [2025], INSA Lyon, tous droits réservés

through a syringe mounted on a robotic arm. In the case of ink containing ceramic or metallic particles, a debinding step is necessary to remove the binder allowing the transport of particles through the nozzle. Then, the parts final properties are reached after a sintering treatment. Beyond the economic aspect, this process based on a structure obtained by sintering, can also be a way to enhance osseointegration by keeping a microporous network through partial sintering. Indeed, while vascularisation through macropores is actually needed for bone formation and long-term stability, as it ensures the supply of nutrients to the cells (and their oxygenation), numerous studies suggest that micropores (smaller than 100 μm) can also improve bone ingrowth [30] [31].

DIW process seems promising to easily build this type of structure as macropores can be designed during the ink deposition, while the microporous network might be obtained through a partial sintering. However, this process is still in its early stage of development meaning that studies are still needed to fully assess the potential and limitations of the technique.

In this context the present study will focus on the development of a 3D printed biodegradable device for orthopedic implants, composed of an Mg alloy. This work is also motivated by environmental considerations and the Mg alloy used will not be composed of Rare earth elements.

This raises a number of questions which it would be essential to be able to answer :

- Is it possible for an Mg alloy without rare earth elements to reach the requisite properties of an implant ?
- How far can the Mg alloy be optimized in both mechanical properties and corrosion resistance ?
- Is the DIW process compatible with the manufacturing of Mg alloys ?

To try to answer these questions the present work has been divided as follows :

The first chapter presents the literature of Mg alloys for orthopedic implants, their current properties and the motivations behind the choice of one Mg alloy

The second chapter focuses on the development of Mg alloys suing Spark Plasma Sintering (SPS). The manufacturing of dense parts is essential to assess and improve the properties of the alloy as an implant. The influence of sintering temperature on density, microstructure and mechanical properties is presented.

The third chapter follows the second chapter and focus on the corrosion properties of the alloy. Mg alloys are very sensitive to corrosion, and the corrosion resistance of the alloy is highly impacted by the microstructure. To better improve the corrosion properties of Mg alloys, a study of the precipitation in the alloy is performed to study the impact and the potential benefits on the degradation rate.

The fourth chapter introduces the literature of AM techniques for Mg alloys and more precisely the sinter based techniques with the challenges induced by the free pressure sintering of Mg alloys. Then, the DIW of the alloy is presented with the optimization of printing and debinding steps. the sintering of Mg alloys is presented under various temperature, time and setup conditions. An *in situ* X-ray nanotomography is also presented to better understand the sintering mechanisms involved in sintering of Mg.

Finally, this manuscript ends with a conclusion that recalls the main results obtained in this study, discusses the strengths and limitations of the process, and brings some perspectives on the further characterisations and possibilities needed for Mg alloys structure, as well as on the various approaches that should be explored in greater depth in order to achieve the manufacturing of degradable metallic parts by DIW.

Thèse accessible à l'adresse : https://theses.insa-lyon.fr/publication/2025ISAL0008/these.pdf © [J. Moreau], [2025], INSA Lyon, tous droits réservés

Chapter 1

Background of the manufacturing technique and the properties of Mg alloys for biomedical applications

Contents

1.1 Introduction 12

1.2 Manufacturing processes of Magnesium 12

1.2.1 Main manufacturing processes 12

1.2.2 Resulting microstructures 14

1.2.3 Spark plasma sintering of Magnesium alloys 15

1.3 Microstructure and mechanical Properties of Magnesium Alloys 18

1.3.1 Grain size 18

1.3.2 Solid solution and precipitates hardening 19

1.3.3 Mechanical properties for orthopedic implants 20

1.4 Corrosion of Magnesium alloys 21

1.4.1 Activity and passivity of Magnesium alloys 21

1.4.2 Corrosion types of Magnesium alloy 24

1.4.3 Electrochemical measurements of Magnesium alloys corrosion properties . . 27

1.4.4 Microstructure tuning for improved corrosion resistance 30

1.5 Magnesium alloys design for biodegradable implants 33

1.5.1 Influence of the alloying elements on the mechanical properties and the corrosion resistance 33

1.5.2 Mechanical properties and corrosion resistance depending of the Zn concentration 34

1.5.3 Addition of Zr 36

1.5.4 Aging treatment of MgZnZr alloys 36

1.6 Conclusion 37

Thèse accessible à l'adresse : https://theses.insa-lyon.fr/publication/2025ISAL0008/these.pdf © [J. Moreau], [2025], INSA Lyon, tous droits réservés

1.1 Introduction

Mg is one of the lightest metal with a density of $1.74\,g/cm^3$. Mg possesses a wide range of applications thanks to a large panel of properties. It provides an electromagnetic shielding which makes it suitable for extraterrestrial construction and thus, very interesting for aerospace applications [32]. Furthermore, Mg alloys possesses vibration, shock absorption and damping capacities [33]. All of these properties combined with his lightweight makes it a perfect material for the automotive industry which is mainly concerned about the flexibility and the weight reduction in the automotive parts [34].

Lastly, the most recent studies focus on the use of Mg alloys in the biomedical field. Mg possesses a very good biocompatibility with human bodies as well as mechanical properties close to bones [14].

Due to its versatility Mg offers multiples opportunities in different fields. The most common alloys in each field are represented in Fig. 1.1.

It is an essential element for the human body, and the Mg^{2+} ions produced from degradation enhance tissue regeneration and growth. The main challenge is to control the corrosion rate. Mg's high reactivity with air and volatility, making it a challenging material to use [35].

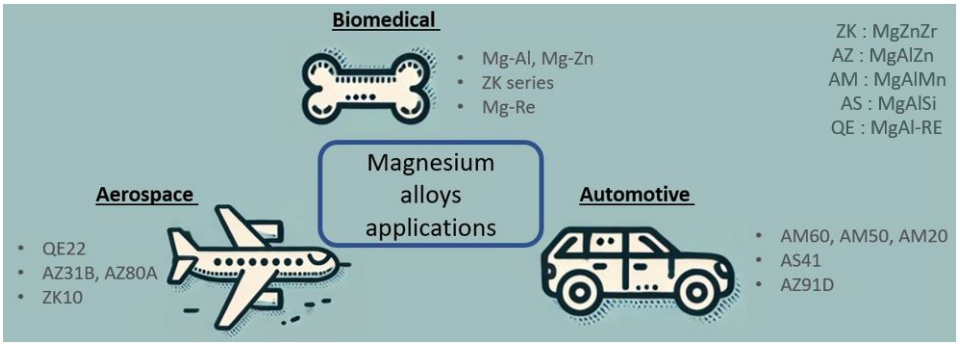


Figure 1.1: Summary of the applications of Mg alloys and the main alloys employed, highlighting the versatility of Mg alloys.

1.2 Manufacturing processes of Magnesium

1.2.1 Main manufacturing processes

The properties of Mg-based materials are highly influenced by the shaping method employed. In the industry, Mg is primarily shaped through rolling, casting, or extrusion and represents a few thousand tons per year in France and Europe [36]. Among its various uses it has recently emerged promising for orthopedic implants which are manufactured using different shaping techniques, as summarized in Fig.1.2.

Casting techniques offer several distinct advantages for Mg. The Mg exhibits good mold-filling characteristics suitable for die casting, enabling the production of complex and cost-effective structures. The low solidification temperature of Mg alloy results in short casting cycles. These short cycles, along with the work under protective atmosphere, greatly limit the contact of the

Thèse accessible à l'adresse : https://theses.insa-lyon.fr/publication/2025ISAL0008/these.pdf © [J. Moreau], [2025], INSA Lyon, tous droits réservés

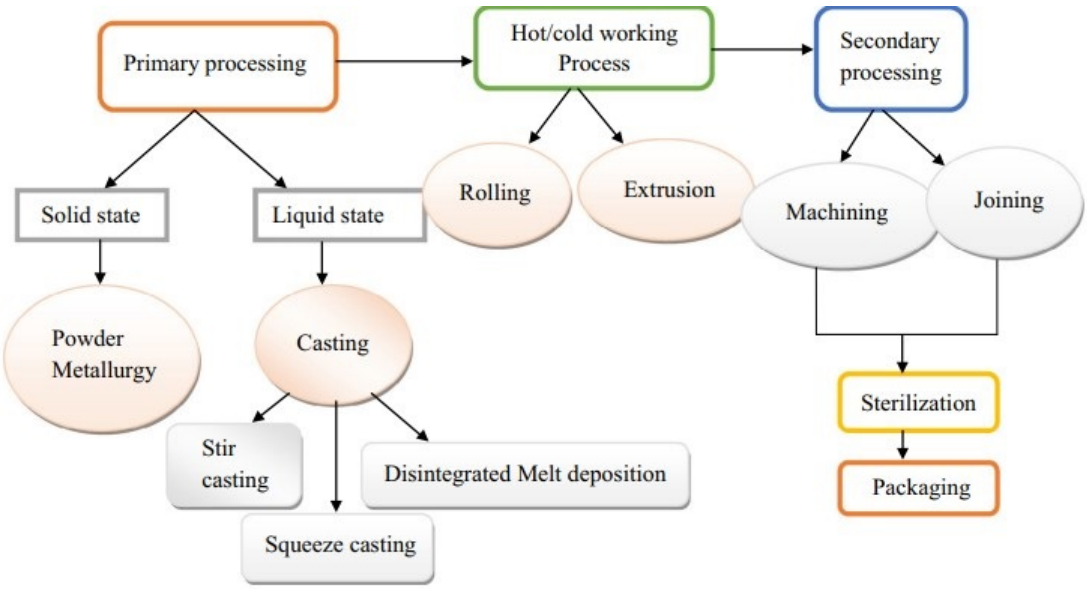


Figure 1.2: Summary diagram of shaping methods for Mg-based materials as orthopedic implants taken from [37]

melted metal with the air, reducing the formation of oxide. One of the drawbacks of some casting techniques is the possible presence of porosity due to the gas entrapped during the injection of molten metal, that can be resolved by modifying the parameters in some applications [38]. Other drawbacks include hot tearing, which can occur after the process, as studied on different alloys by Song *et al* [39]. Additionally, depending of the alloy, segregation can be observed, as studied in Mg alloys containing rare earth (RE) elements can be observed, as studied by Tong *et al* [40]. In 2016, casting represented 90% of Mg production [41].

The extrudability of Mg is relatively low compared to aluminum, resulting in low extrusion speeds and a limited range of available temperatures. This leads to low production rates and high production cost [42]. These challenges may necessitate extrusion at very high temperatures to press the material through the die, increasing the risk of surface cracking [43]. The alloying elements sometimes need to be adjusted to allow a proper extrusion. For example, the presence of Zn in Mg, which creates low melting temperature second phases, can make extrusion difficult, requiring a reduction in zinc concentration [44].

For the manufacture of Mg-based orthopedic implants, casting is the most widely used technique due to its cost-effectiveness and ease of implementation [45]. The castings are subjected to hot or cold working process to get the desired form such as plates, rods, wires, and tubes.

On the other hand, shaping through powder metallurgy, which involves compacting and sintering a powder of the desired composition, is very expensive and complex for Mg [46]. Powder metallurgy was neglected in the past due to the cost and the complexity of Mg sintering. Nevertheless, due to the diversity in applications and challenges that this technology can offer, the number of studies has recently increased significantly [47].

Thèse accessible à l'adresse : https://theses.insa-lyon.fr/publication/2025ISAL0008/these.pdf © [J. Moreau], [2025], INSA Lyon, tous droits réservés

1.2.2 Resulting microstructures

1.2.2.1 Die casting

Casting is mostly used in the automotive and aircraft industries. Indeed, in this field the main focus is on Mg-Al alloys to replace the aluminum parts and reduce overall weight. Recently, rare earth (RE) elements combined with aluminum have been explored to improve the mechanical properties of these alloys. In the casting process, the material is heated to a liquid state, which eliminates the oxide layer on the surface of the powder. Then, the liquid is solidified. For Mg-Al alloys the solidification begins with the nucleation of α-Mg dendrites. Depending on the cooling rate, eutectic solidification occurs with partially separated β-$Mg_{17}Al_{12}$ in the interdendritic and grain boundary regions, surrounded by eutectic α-Mg, enriched in aluminium [48]. The resulting microstructure is shown in Fig 1.3.

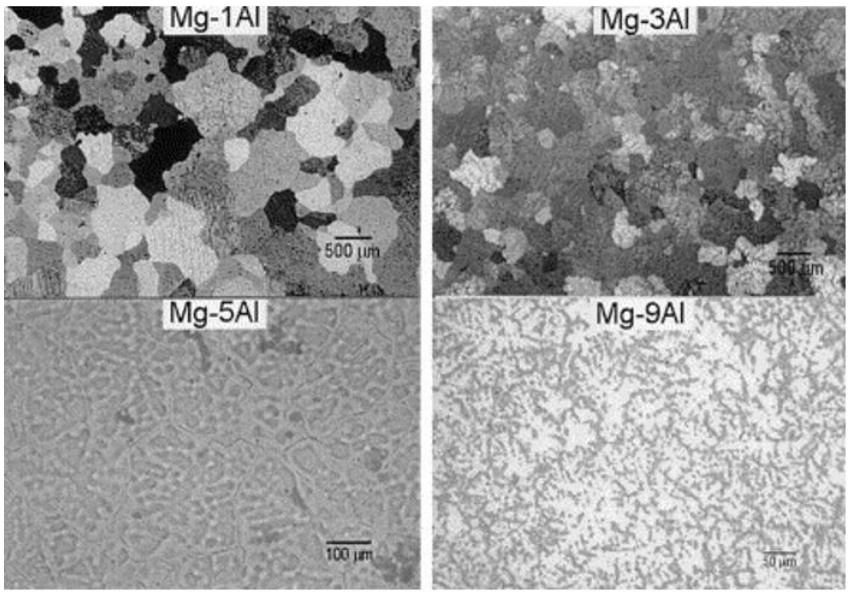


Figure 1.3: Micrographs of Mg-Al alloys with increasing aluminum content, with a visible transition from a globular dendritic structure to a fully developed dendritic structure with increasing aluminium content at a similar cooling speed, reproduced from [48]

Mg-Zn alloys, known for their biocompatibility, have recently gained attention and were initially developed with casting techniques. Similarly to Mg-Al the Mg-Zn alloys exhibit dendrites structures when the Zn content exceeds 1wt% [49]. However, the casting process results in alloys with large grain sizes, which can be detrimental to the mechanical properties and will be discussed later.

1.2.2.2 Extrusion

During extrusion, the microstructure undergoes significant changes compared to the cast ingot. These changes include dynamic recrystallization, static recrystallization (after exiting extrusion die), alignment of crystalline orientation, refinement of second phases and dynamic precipitation. These microstructural changes are illustrated in the Fig.1.4.

Thèse accessible à l'adresse : https://theses.insa-lyon.fr/publication/2025ISAL0008/these.pdf © [J. Moreau], [2025], INSA Lyon, tous droits réservés

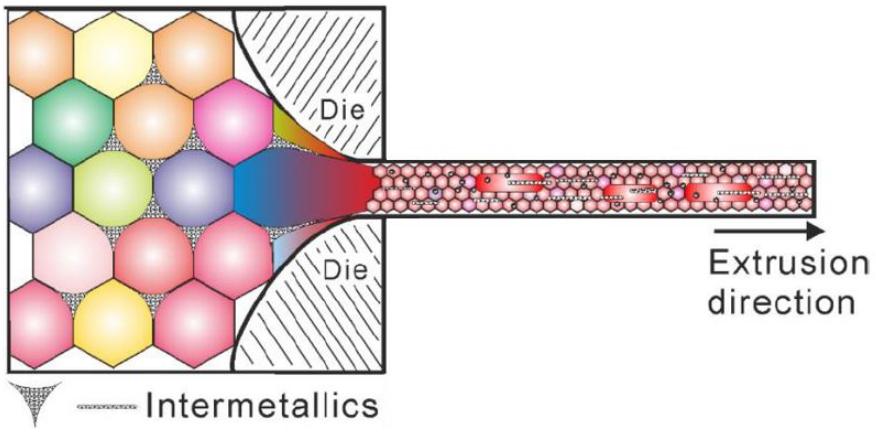


Figure 1.4: Schematic diagram showing microstructure evolution during extrusion, including deformation and recrystallization, refinement of intermetallic phases, reproduced from [42]

The main difference from casting is that the coarse grains are replaced by fine recrystallized grains during hot extrusion. Moreover, in certain alloys, solute atoms that are dissolved in the Mg matrix during the homogenization treatment can lead to dynamic precipitation. Additionally, eutectic phases that are normally present along grain boundaries become fragmented, making the refined second phase more uniformly distributed. These significant changes in microstructure greatly affect the mechanical properties and corrosion resistance, as shown in (Table.1.1).

Mechanical properties	Hot rolled sheet	Cast	Extruded
Compressive yield strength (MPa)	105 to 115	21	34 to 55
Tensile yield strength (MPa)	115 to 140	21	69 to 105
Ultimate tensile strength (MPa)	180 to 220	90	165 to 205
Hardness (HB)	45 to 47	30	35

Table 1.1: Mechanical properties of pure Mg depending on the manufacturing technique [50]

The manufacturing process greatly influences the resulting mechanical properties, primarily due to differences in grain size : large for casting and small for rolling and extrusion. After reviewing the usual manufacturing process for Mg alloys the next section will focus on the manufacturing of Mg alloys via powder metallurgy process.

1.2.3 Spark plasma sintering of Magnesium alloys

In Spark plasma sintering (SPS), metallic or non-metallic powders are introduced into a die in a controlled atmosphere. The powders are rapidly consolidated via applied pressure and the circulation of a pulse direct current (DC) which may result in a plasma discharge between the particles.

The die is connected to lower and upper electrodes that allow the input of external current. The circulation of the current induces a joule heating effect, followed by a diffusion-like effect that rapidly sinters the particle [51]. It has been observed that the discharge of the current can produce high temperatures, up to several thousand degrees. This phenomenon leads to

Thèse accessible à l'adresse : https://theses.insa-lyon.fr/publication/2025ISAL0008/these.pdf © [J. Moreau], [2025], INSA Lyon, tous droits réservés

evaporation and melting on the surface of powder particles, resulting of the formation of necks at the contact points between the particles.

During the first step of the spark discharge process, electrons are transferred between the contacting powder particles Fig. 1.5.a. This is because the powders act as miniaturized anodes and cathodes. Subsequently, ionization occurs, causing spark plasma discharging. A molten layer is formed, allowing for the discharge column to take place Fig. 1.5.b. After this, the formation of a spark impact pressure occurs, enabling a thermal diffusion layer and necking to form Fig. 1.5.c. For metal particles, the applied Joule heat directly warms up the powder particles in fast thermal cycles, constraining grain growth during densification. Thus, compared to cast Mg alloys, the SPS method can produce Mg-based alloys with finer grain sizes, which can improve their mechanical and electrochemical resistance [52]. Thus, compared to the conventional methods of sintering, fast densification of powders at low temperatures can be achieved by SPS. In addition, the consolidation process parameters can be optimized to minimize grain growth during the SPS process [53]

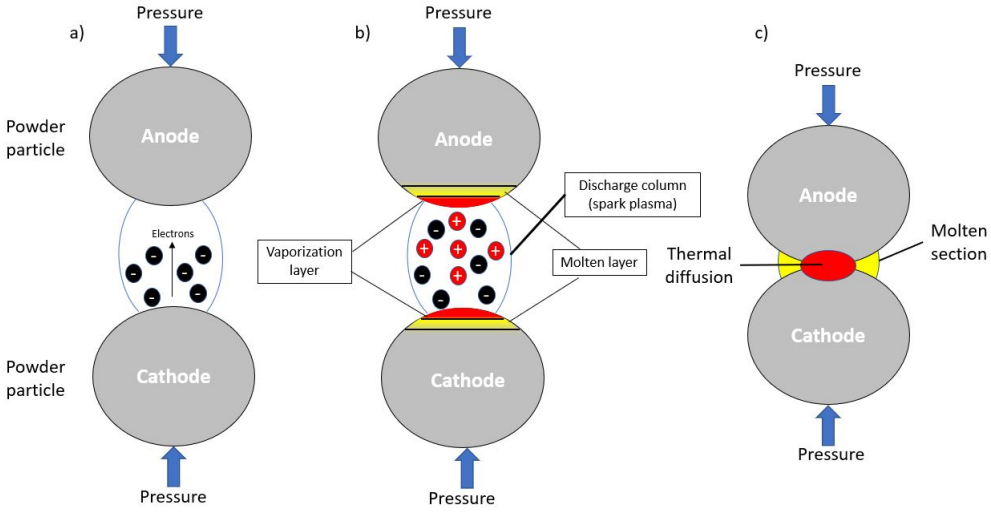


Figure 1.5: Scheme representing the different steps of SPS with a) the transfer of electrons between the particles b) Formation of a molten layer due to the ionization allowing the discharge column to take place c) The formation of the spark impact inducing the thermal diffusion

1.2.3.1 Density

Due to the nature of the SPS process, the properties obtained for a given Mg alloy are greatly influenced by the processing parameters. The main parameter influencing the properties of the material is the sintering temperature. However, some studies were also conducted on the influence of the powder size and the applied pressure. Chen *et al* [54] studied the impact of particle size on densification for pure Mg. Their results showed better densification for the smallest particles. Indeed, stronger driving forces induced by greater ratio of surface on volume, promote the particle migration and increase the contact area between particles. For larger particles, the densification process relies less on Joule heating and more on the application of high pressure. This high pressure enhances the initial density of the powder compact, increasing

Thèse accessible à l'adresse : https://theses.insa-lyon.fr/publication/2025ISAL0008/these.pdf © [J. Moreau], [2025], INSA Lyon, tous droits réservés

the number of contact points. However, this method is comparatively less effective. Ka ram kim *et al* [55], studied the influence of the applied pressure on the sintering of Mg-6Al. The results showed that the highest applied pressure, up to 130 MPa produced, the most dense materials with the highest tensile strength, similar to extruded Mg-6Al.

Finally, various studies have already determined the relationship between the sintering temperatures and density [56] [53] [57]. Similar to applied pressure, a higher sintering temperature results in higher density. The sintering temperature depends on the chemical composition but is frequently above 450 °C to achieve relative densities above 95% [52]. At this temperature, a spark discharge effect occurs. Once the particles are softened, necking and joule effect heating will occur, which increases the resulting density [58]. With higher temperatures, nearly complete densification takes place due to the interparticle diffusion. Once this densification occurs, the sintering temperature does not influence the density anymore as a maximum is reached, and using higher temperatures is not relevant [57].

Once the processes parameters are optimized, SPS can be applied to any Mg alloys and produce dense parts, for example on pure Mg [54] , on Mg-Al alloys [59] and on ZK alloys [60] with results showing more than 99% relative density.

1.2.3.2 Microstucture

Grain size Once the density is optimized, it is possible to adjust the grain size of the Mg alloys. The use of larger particles size leads to larger grain in the manufactured material [54]. The effect of temperature, studied by [61] [52], showed that an increase in temperature increases the grain size. The first phenomenon is that increasing the temperature induces a higher atomic diffusion between the connected particles, resulting in larger grain sizes, as observed in conventional sintering [62]. Secondly, depending on the initial state of the powder, at higher temperatures potential precipitates dissolve in the Mg matrix. This dissolution diminishes the potential Zener pinning effect that could lead to smaller grain [61]. To attain optimal mechanical properties, it is necessary to find a compromise between the density and the grain size, as the temperature has an opposite effect on these properties.

Precipitates The resulting microstructure depends on the alloys and the state of the starting powder but frequently consists of a α-Mg phase with the alloying elements dissolved in the matrix. Sometimes precipitates and intermettalics compounds can appear depending on the sintering cycle used. For example, in their AZ91 alloy Mondet *et al* [63] observed the formation of intergranular $Al_{12}Mg_{17}$ precipitates at low temperatures, at a fraction of 8%vol and a size around 200 nm, and the dissolution of these precipitates for temperatures above 350°C. Which is excepted given the precipitation sequence of MgAl alloy [64] :

$$Super\ saturated\ solid\ solution\ (SSSS) \longrightarrow \beta(\mathrm{Al_{12}Mg_{17}}) \tag{1.1}$$

1.2.3.3 Residual oxide layer

Due to the reactivity of Mg, a thin oxide layer naturally forms at the surface of the powder particles of Mg alloys [65]. This layer is also present in gas atomized powder [66]. This oxide layer remains during the SPS process and is very detrimental to the mechanical properties. It was observed in hot pressing of ZK60 alloy [60], visible in Fig.1.6. This remaining oxide layer in

Thèse accessible à l'adresse : https://theses.insa-lyon.fr/publication/2025ISAL0008/these.pdf © [J. Moreau], [2025], INSA Lyon, tous droits réservés

SPS is not well studied, but Muhammad *et al* [57] investigated the issue and according to their study increasing the temperature of the SPS process leads to the thinning of the layer and the enhancement of the tensile strength. This thinning could be caused by local high temperatures created in the contacting areas of the particles where Mg oxide films are ruptured by the spark plasma [67].

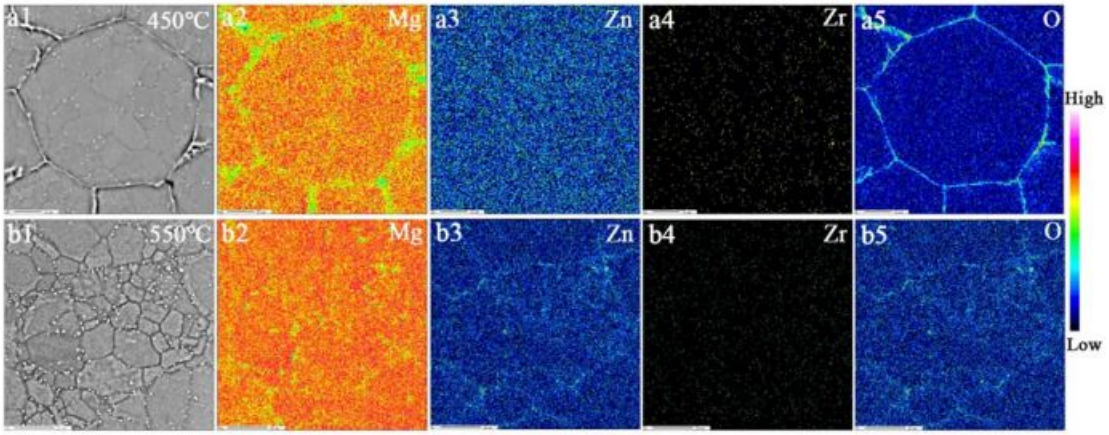


Figure 1.6: (1) SEM observation and (2-5) EDX maps of the Mg, Zn, Zr, Si and O distributions in the ZK60 alloy manufactured by hot pressing and sintered at a) 450°C and b) 550°C from [60]. The remaining oxide layer decreases with increasing temperature.

The manufacturing process used to shape the alloy impact the microstructure and mechanical properties of the alloy. However, it is possible to tune these mechanical properties by adjusting the microstructure after the manufacturing as detailed in the next section.

1.3 Microstructure and mechanical Properties of Magnesium Alloys

Mg has a hexagonal close-packed (HCP) crystallographic structure. According to the Von Mises criterion [68], the ductility of the material is possible when five independents slip systems are activated. This condition is not met in the HCP structure, thus, Mg deforms plastically by two mechanisms : slip and twinning. These deformation modes have an impact on the mechanical properties of the alloys and the various parameters that impact those properties will be detailed in this section.

1.3.1 Grain size

Grain boundary strengthening is crucial in Mg alloy, especially those manufactured by extrusion, as it produces fine grain sizes in the alloys. Analyzing the clear effect of grain size is difficult because it is often correlated with texture changes. However, studies have managed to develop an Hall-petch type relationships for Mg alloys [69] [70]. Zheng *et al* [71] highlighted the presence of two critical grain sizes d_{c1} and d_{c2} which are related to the alloy composition. When d is superior to a certain value called d_{c1}, and inferior to another value called d_{c2}, extension twinning and basal slips dominate plastic deformation. When d is superior to the value called d_{c2}, deformation is

Thèse accessible à l'adresse : https://theses.insa-lyon.fr/publication/2025ISAL0008/these.pdf © [J. Moreau], [2025], INSA Lyon, tous droits réservés

driven by grain boundary sliding, drastically increasing the ductility. Somekawa *et al* [70] found that for binary Mg alloys with Zn or Y, the strength in compression was related to the formation of $\{10\bar{1}2\}$ twins and followed the Hall-petch relation with no influence of the alloying elements (see Fig.1.7a). Caceres *et al* [69] studied Mg-Zn alloys with different concentrations and found a Hall-petch relationship for both tensile et compression tests. They studied different grain sizes in cast alloys after a solution treatment and also highlighted that the finer the grain the higher the yield strength, see Fig.1.7b.

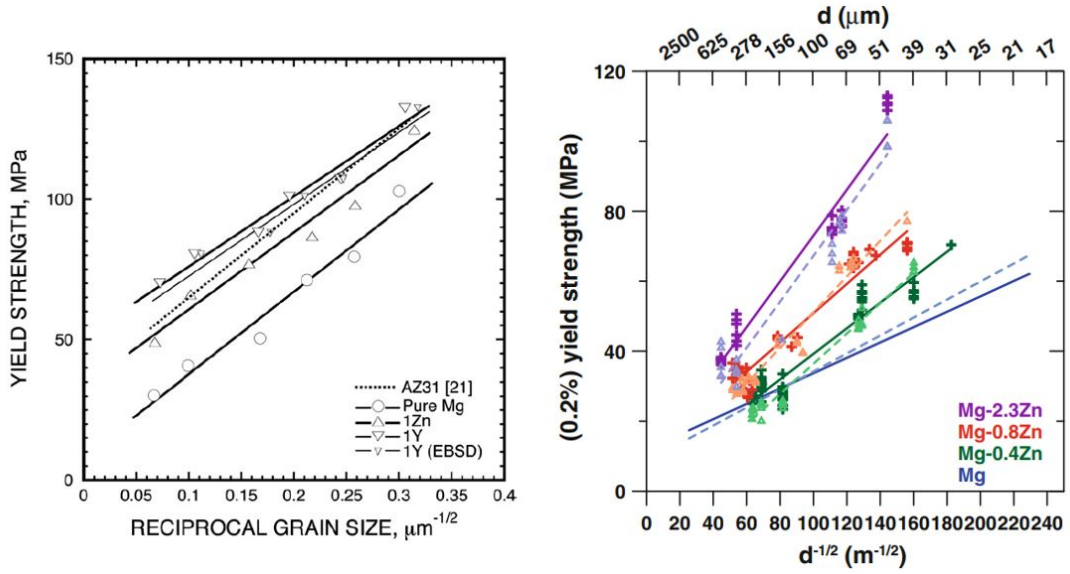


Figure 1.7: Ordinary Hall-Petch plot comparing the grain size vs the yield strength a) For binary MgZn and MgY alloys and b) For MgZn binary alloys with a variation of the Zn content, the crosses and solid lines denote tensile data and the triangles and dashed lines denote compression, reproduced from [70] [69]. The decrease of grain size induces an increase of the yield strength.

Grain refining is an effective strategy for improving the mechanical resistance of Mg [72]. However another important factor to consider is the chemical composition of the alloy. Optimized thermal treatments producing solution or precipitates hardening are also a viable strategies to improve the resistance of Mg alloy.

1.3.2 Solid solution and precipitates hardening

In Mg alloys, both the solid solution and the formation of precipitates improve the strength of the alloys. The usual thermal treatments that the alloys undergo after shaping by casting for example, are described below :

- Solid solution treatment in the α-Mg zone
- Water quenching to achieve a supersaturated solid solution of alloying elements in Mg
- Low-temperature aging treatment to achieve a fine distribution of precipitates in the matrix

The decomposition of the supersaturated solid solution leads to the formation of a series of metastable and equilibrium precipitates [73]. Mastering the precipitation sequence allows achieving the desired properties and depends on each alloy.

Thèse accessible à l'adresse : https://theses.insa-lyon.fr/publication/2025ISAL0008/these.pdf © [J. Moreau], [2025], INSA Lyon, tous droits réservés

1.3.2.1 Solid solution strengthening

Solid solution strengthening has been extensively studied by Akhtar *et al* [74], who showed how solid solution alloying strengthens the basal slip system. To summarize, basal dislocations find low-energy areas to reside between the solute atoms. The stress then rises high enough to push the dislocations past and pull them away from the pinning points represented by the solute atoms. Furthermore, depending on the composition of the alloy, solid solution strengthening can also reduce the influence of twinning as a function of strain. Hauser *et al* [75] showed that Li solid solution promoted prismatic slip, which makes it competitive with twinning. With more competition between the deformation types, twinning occurs less frequently, improving the ductility.

1.3.2.2 Precipitates hardening

Depending on the composition and the precipitation sequence of the alloys, precipitates hardening can be more effective than solid solution strengthening. However, the aging response of Mg is considered low compared to Al alloys for two main reasons. Firstly, there are few elements with significant high temperature solubility, making it challenging to achieve a high volume fraction of precipitates. Secondly, Nie [73]was the first to address the issue of precipitate shape and its influence on the mechanical properties of Mg alloys. Nie demonstrated that plate shaped precipitates Fig.1.8.a are the least effective in hardening. These precipitates are present in Mg-Al alloys Fig.1.8.c, which explains why hardening is reduced in these alloy systems. Similarly, the c-axis rod-shaped precipitates Fig.1.8.b were proven to have a poor hardening effect, and these types of precipitates are present in the Mg-Zn systems Fig.1.8.d.

Barnett *et al* [76] studied the Mg-Al system and observed that basal plates are particularly poor at hardening against basal slip due to the low fraction of precipitates that can be cut by a given basal plane. Plates on a prismatic place are the most effective for hardening, and these types of precipitates are commonly observed in Mg-RE alloys. These studies on precipitate shape explain why the precipitate hardening in the most commonly employed alloys (MgAl and MgZn) is not effective. They also suggest that the addition of RE could greatly enhance the resistance, as observed in the WE43[77] and WE54 alloys [78].

1.3.3 Mechanical properties for orthopedic implants

The critical mechanical properties for implants are Young's modulus, tensile strength, fatigue strength, and elongation at break. The mechanical properties of the material must be very close to those of bone, especially to avoid stress shielding resulting from the difference of material properties between bone and the implant [80]. The higher stiffness of the implant results in bone loss as a result of decreased physiologic loading of the bone [81]. This can cause chronic inflammations, accelerated implant loss, and reduced healing speed [82].

To avoid these modifications in the bone structure, new materials with mechanical properties closer to those of bone are being used (Table.1.2) [83].

Mg has mechanical properties closest to those of bone, making it an excellent candidate for orthopedic implant. Current permanent metallic implants like titanium and Co-Cr alloys have too high Young's modulus and high stiffness, often leading to complications [84]. Additionally, Mg implants are stronger than biopolymers and more ductile than bioceramics [85]. However, under high loads, the mechanical properties of Mg alloys are often insufficient.

Thèse accessible à l'adresse : https://theses.insa-lyon.fr/publication/2025ISAL0008/these.pdf © [J. Moreau], [2025], INSA Lyon, tous droits réservés

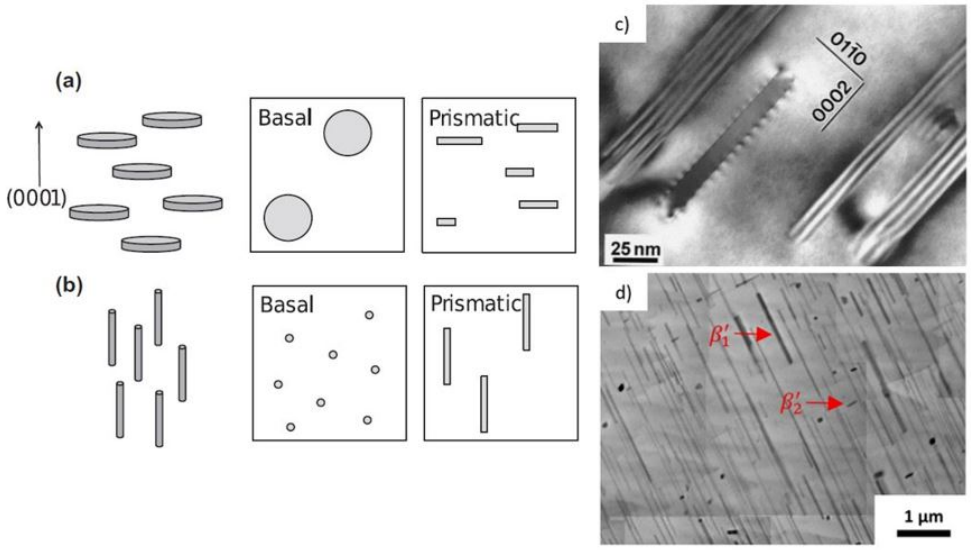


Figure 1.8: A schematic showing the (a) basal plates and (b) c-axis rod precipitate morphologies [76] c) TEM observation of the basal plate in MgAl alloys [73] d) TEM observation of the c-axis rod precipitates in MgZn alloys [79]

Materials / Alloys	**Density (g/cc)**	**Elastic modulus (GPa)**	**YS (MPa)**	**TS (MPa)**	**Elongation (%)**
Natural bone	1.7–2.0	3–20	60–90	80–150	1–6
Permanent implant materials					
SS-alloys	7.9–8.1	190–205	180–250	350–620	30–40
Ti-alloys	4.4–4.5	110–117	270–400	450–1000	8–15
Co-Cr alloys	8.3–9.2	210–230	290–410	530–950	8–40
Potential temporary implant materials					
Mg-based alloys	1.74–2.0	41–45	120–180	140–290	1–11
Zn-based alloys	7.14–7.3	90–100	115–205	160–390	3–15
Fe-based alloys	7.8–8.1	200–205	140–260	210–360	30–45
DL-PLA	–	1.9	–	27–41	3–10

Table 1.2: Comparison of the mechanical properties of various implant materials with bone [83]

1.4 Corrosion of Magnesium alloys

The mechanical properties of Mg alloys make them one of the best candidates for orthopaedic implants. However, the main issue when developing these implants is the corrosion rate, as Mg alloys are very sensitive to oxidation. In this section, we will present the various characteristics of corrosion of Mg alloys.

1.4.1 Activity and passivity of Magnesium alloys

Mg is very sensitive to oxidation as shown by the standard free Gibbs energy listed below :

$$\mathrm{Mg} + 2\mathrm{H_2O} = \mathrm{Mg(OH)_2} + \mathrm{H_2} \qquad \Delta \mathrm{G_0} = -833\,\mathrm{kJ/mol}$$

$$\mathrm{Mg} + 1/2\mathrm{O_2} = \mathrm{MgO} \qquad \Delta \mathrm{G_0} = -569\,\mathrm{kJ/mol}$$

Thèse accessible à l'adresse : https://theses.insa-lyon.fr/publication/2025ISAL0008/these.pdf © [J. Moreau], [2025], INSA Lyon, tous droits réservés

The value of standard Gibbs free energy suggests that Mg has a strong tendency to spontaneously transform into oxidized state. In an environment containing oxygen or water, the surface tends to oxidize rapidly, forming an oxide or hydroxide surface film [86]. The corrosion of Mg is a spontaneous process, making Mg thermodynamically unstable in most environments. When exposed to the atmosphere Mg tends to form a dense and stable passive layer a few nm thick [65]. The chemical composition of the formed passive layer depends on the medium to which Mg is exposed.

1.4.1.1 Corrosion mechanisms

Mg is a metal highly sensitive to oxidation, exhibiting strong reducing behavior with a standard potential of $-2.372\,\mathrm{V}$ vs Standard Hydrogen Electrode (SHE), one of the lowest among all metals [87].

Perrault *et al* [88] described the E-pH diagram of Mg in aqueous solution at 25 °C, see Fig.1.9. This diagram corresponds to the Mg-H_2O in the presence of H_2.

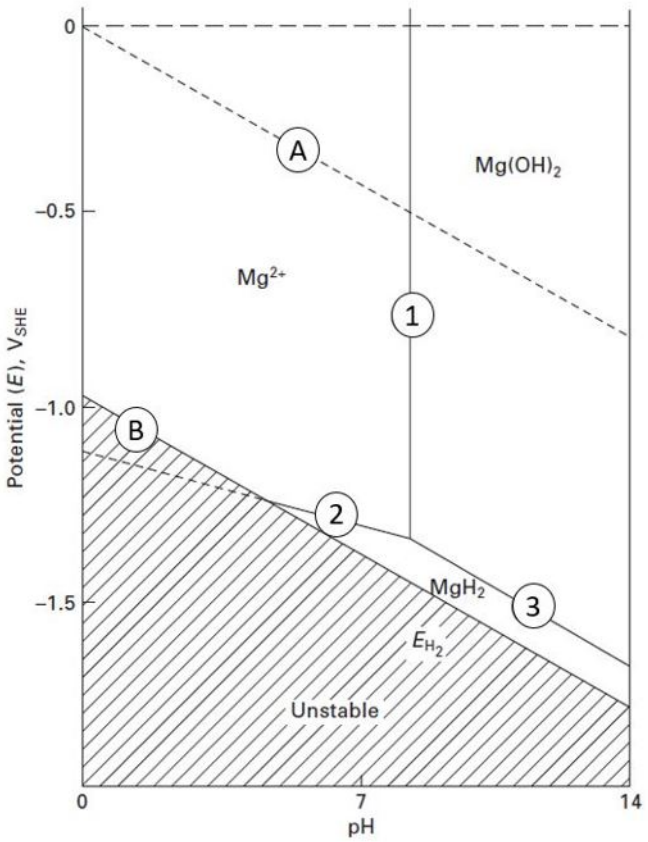


Figure 1.9: Stability domains of the Mg compounds in aqueous solutions with hydrogen overpotential of 1 V. With the reaction 1,2 and 3 corresponding to the one presented above and B the line below which hydrogen is evolved [88]

In this diagram the unstable and intermediate substances are excluded, such as H^-, MgOH, MgH. The diagram shows that under natural conditions, Mg is not stable in an aqueous envi-

Thèse accessible à l'adresse : https://theses.insa-lyon.fr/publication/2025ISAL0008/these.pdf © [J. Moreau], [2025], INSA Lyon, tous droits réservés

ronment. It predicts the thermodynamic stability of corrosion in Mg-water systems, excluding the kinetic processes.

The reactions involved are the following :

$$Mg^{2+} + 2OH^- \longrightarrow Mg(OH)_2(1)$$
$$Mg^{2+} + 2H^+ + 4e^- \longrightarrow MgH_2(2)$$
$$MgH_2 + 2OH^- \longrightarrow Mg(OH)_2 + 2H^+ + 4e^-(3)$$

The overall corrosion reaction for Mg in aqueous solution is :

$$Mg(s) + 2H_2O(l) \longrightarrow Mg(OH)_2(s) + H_2(g)$$

The global mechanism of the corrosion of Mg in an aqueous media are summarize on the Fig.1.10.

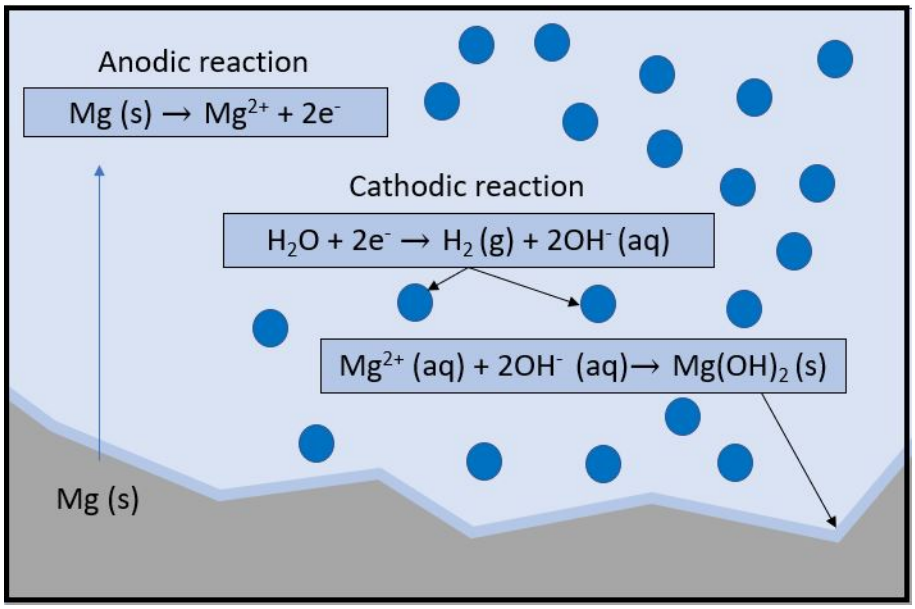


Figure 1.10: Schematic representation of the stages in the corrosion of pure Mg representing the main reactions involved in the process, with the formation of $Mg(OH)_2$ and H_2 gas

Ions from the metal surface in the solution will form an oxide layer on the metal's surface. When the surface is completely covered by oxide, it forms a passive layer composed of $Mg(OH)_2$ which limits the migration of ions at the metal/oxide interface. However, in various aqueous media this $Mg(OH)_2$ film does not offer significant corrosion protection. Moreover, the formed dihydrogen disturbs the hydroxide layer, thus preventing complete surface coverage and self-inhibition of corrosion [89].

1.4.1.2 Influence of the media

In a physiological environment, the presence of ions and proteins will modify the passive layer on the Mg surface. Specifically, in an environment containing chloride ions, the protective

Thèse accessible à l'adresse : https://theses.insa-lyon.fr/publication/2025ISAL0008/these.pdf © [J. Moreau], [2025], INSA Lyon, tous droits réservés

layer is even more compromised. The Cl^- ions reacts with the hydroxide layer, forming much more soluble $MgCl_2$, making the surface more reactive and hence accelerating Mg dissolution according to the following equation [90].

$$Mg^{2+} + 2Cl^- \longrightarrow MgCl_2$$
$$Mg(OH)_2 + 2Cl^- \longrightarrow MgCl_2 + 2OH^-$$

It has been shown [91] that in addition to the MgO and $Mg(OH)_2$ layers, the presence of calcium and phosphorus in a cell culture medium leads to the formation of Mg/calcium phosphates and carbonates. [91] The reactions are represented by the following equation:

$$2Mg^{2+} + CO_3^{2-} + 2OH^- + 3H_2O \rightleftharpoons Mg_2(OH)_2CO_3 3H_2O$$

The CO_3^{2-} comes from the reaction of CO_2 in the air with water [92]:

$$CO_2(aq) + H_2O \rightleftharpoons HCO_3^- + H_+$$
$$HCO_3^- \rightleftharpoons CO_3^{2-} + H_+$$

This new carbonate layer is thicker than the Mg hydroxide layer blocking the surface. It interferes with the anodic and cathodic reactions, thereby increasing corrosion resistance [93].

When evaluating a material's corrosion resistance, the environment plays a crucial role. Different materials behave differently depending on the environment they are immersed in. For Mg, an aqueous environment that stabilizes the protective passive film results in a low corrosion rate. An environment with a pH higher than 10.5 forms a stable $Mg(OH)_2$ film, while the presence of fluoride ions leads to the formation of insoluble MgF_2 and $MgSO_4$ forms in the presence of sulfuric acid [94]. Conversely, the presence of elements that can break the protective film, such as chlorides, greatly accelerates the corrosion rate. Song *et al* [94] studied the influence of chloride concentration on a MgAlZn alloy and showed that the corrosion rate depended on the chloride concentration in the environment. The influence of the media on the degradation and the corrosion product is summarized in Fig.1.11.

It is challenging to evaluate Mg's corrosion resistance as an implant because the environment in which it is immersed is very complex, as summarized in Figure 1.12. The physiological environment is composed of blood, proteins, and numerous ions such as $Na^+, K^+, Ca^{2+}, Mg^{2+}$, etc.

During degradation in the body, the released Mg ions are non-toxic and can even stimulate bone growth [37]. However, excessive degradation of pure Mg implants can generate a significant release of H_2 gas, which can lead to complications [97]. *In vivo* studies have shown that within a few days, the gas release can lead to the formation of gas pockets, which might cause complications as tumors [98]. The maximum concentration of H_2 should not be higher than the saturated concentration of hydrogen in water 0.08 mM [99]. Therefore, controlling the *in vivo* degradation rate is a crucial parameter.

1.4.2 Corrosion types of Magnesium alloy

The corrosion mechanisms of Mg and its alloys can be divided into two categories: uniform corrosion and localized corrosion. For localized corrosion, the most common modes are galvanic and pitting corrosion [100].

Thèse accessible à l'adresse : https://theses.insa-lyon.fr/publication/2025ISAL0008/these.pdf © [J. Moreau], [2025], INSA Lyon, tous droits réservés

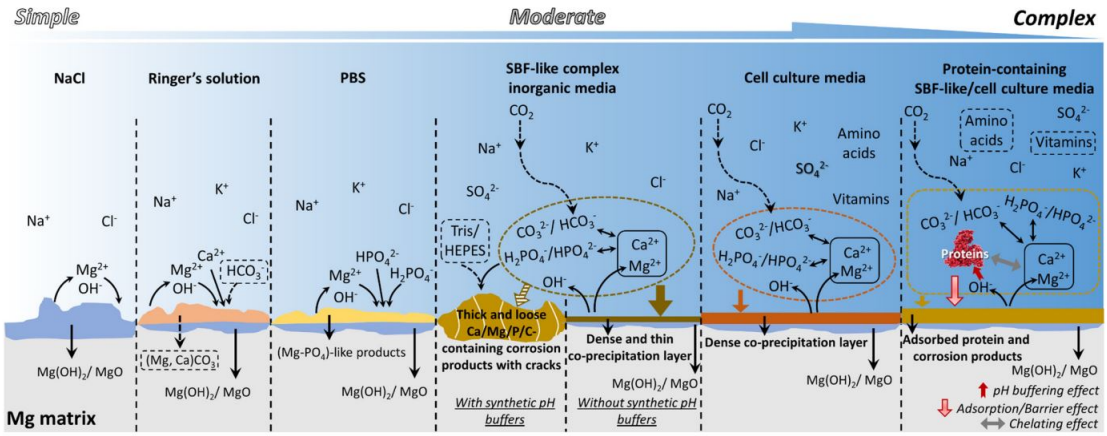


Figure 1.11: Schematic illustration of the corrosion behavior of Mg in the commonly used media. From simple media starting with only NaCl to complex ones with the presence of protein which are closer to the human body, reproduced from [95]

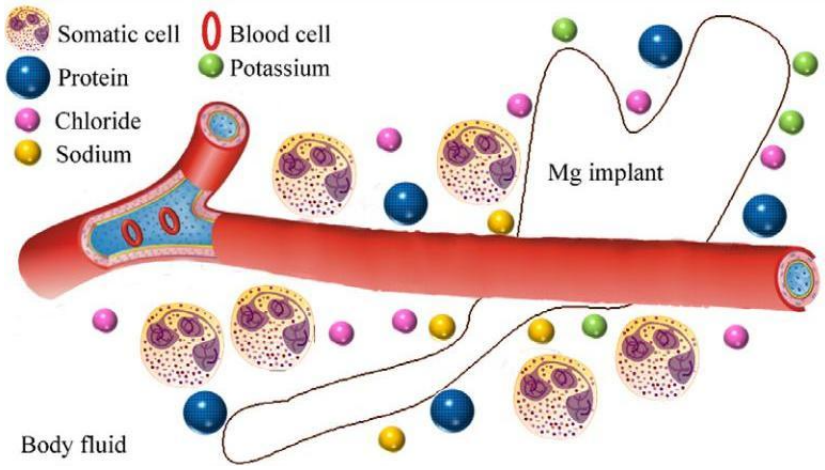


Figure 1.12: Representation of an implant in a physiological environment with the components influencing the corrosion behavior from [96]

Thèse accessible à l'adresse : https://theses.insa-lyon.fr/publication/2025ISAL0008/these.pdf © [J. Moreau], [2025], INSA Lyon, tous droits réservés

1.4.2.1 Passivation

Passivation results from the oxidation of the entire material surface, which is attacked at the same rate by the corrosive environment. For Mg, this indicates the formation of a passive layer. For example, this has been observed in the WE43 alloy (Mg-4Y-4Nd-0.4Zr) after T4 treatment and aging to peak hardness (T6) [101]. The passive layer consists of $Mg(OH)_2$ on the surface and MgO beneath.

1.4.2.2 Pitting Corrosion

Pitting corrosion or localized corrosion is dominant in single phases Mg alloys [94]. The protective film is unstable, and the pitting potential is lower than the free-corrosion potential in most Mg alloys, meaning pitting is preferred to uniform corrosion. The pitting corrosion in Mg alloys starts with the formation of irregular pits, which then spread laterally, and cover the whole surface. Once the pits form, they tend to connect, leading to particles falling out, as illustrated in Fig.1.13.

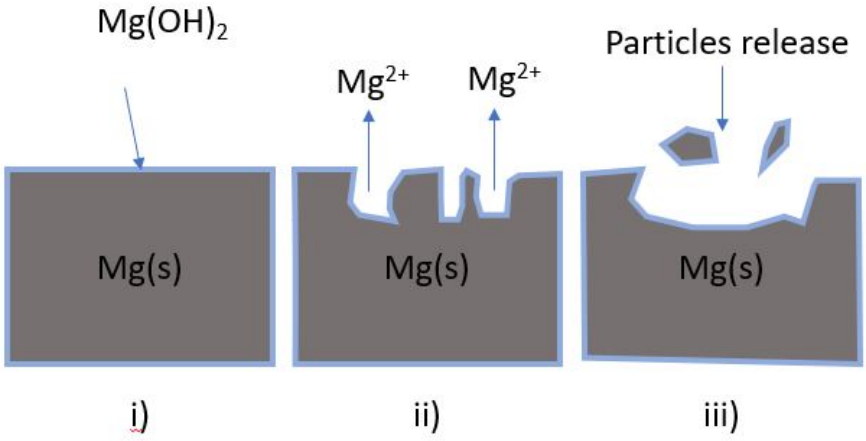


Figure 1.13: Schematic representation of the steps of the pitting corrosion i) initial state with the passive layer ii) Beginning of the corrosion with the pit formation iii) Release of particles due to the pitting formation

Pitting corrosion is a common mechanism in Mg alloys and results from the rapid oxidation of small localized zones due to the attack of anions that weaken the passive layer. Defects initiated in the passive layer will continue to grow and reach the α-Mg matrix. The chemical composition, grain size, morphology, and distribution of secondary phases strongly influence pitting corrosion. Oxidation within the pit can also be accelerated by galvanic corrosion [102]. Once pitting is initiated, the material is penetrated very quickly, which can lead to implant failure. Moreover, the presence of localized stress under mechanical loading condition such as fatigue at the pit level, have the potential to form cracks, which can accelerate degradation [103].

1.4.2.3 Galvanic Corrosion

When in contact with another metal or in presence of nobler precipitate, Mg, due to its strong reducing behavior, acts as an anode and oxidizes rapidly. Mg alloys are very susceptible to

Thèse accessible à l'adresse : https://theses.insa-lyon.fr/publication/2025ISAL0008/these.pdf © [J. Moreau], [2025], INSA Lyon, tous droits réservés

galvanic corrosion and the cathodes can be external or internal, such as secondary or impurity phases.

For example, galvanic corrosion can occurs when a Mg screw is attached to a titanium plate for bone repair, or even when the two systems are close. Blood vessels can act as a connection network, accelerating Mg corrosion [104].

Galvanic corrosion can occur at different levels, both macroscopic and microscopic. At the microscopic level, the potential difference between the α-Mg matrix and secondary or intermetallic phases leads to micro-galvanic corrosion. The matrix is preferentially oxidized compared to the intermetallic phases, involved in other corrosion modes such as pitting corrosion [105] and intergranular corrosion [106]. The potential difference can arise from variations in grain size, as seen in extruded Mg-Zn6wt%-Zr0.6wt% (ZK60) [107], where the middle layer composed of fine grains is preferentially corroded compare to the outer layer compose of larger grains.

Galvanic corrosion mainly occurs between the α-Mg matrix and the intermetallic phases. In AZ91 alloys, the corrosion potential of the second phases composed of Al_xMg_y is higher than the Mg matrix. This difference leads to galvanic corrosion between the Mg phase and the Al_xMg_y phase, with the Mg phase being preferentially oxidized, thereby accelerating pitting corrosion [108]. The mechanisms of microgalvanic corrosion are summarized in Fig.1.14.

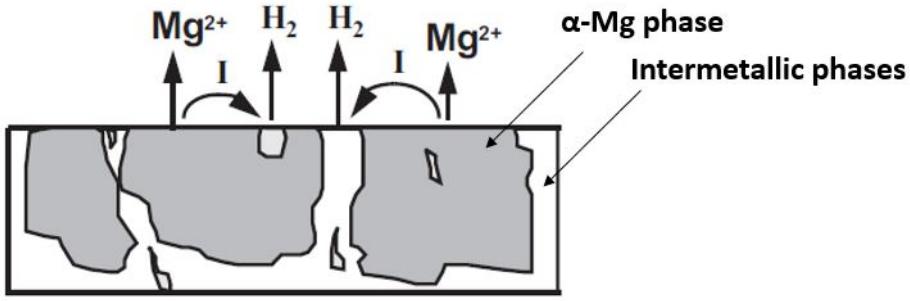


Figure 1.14: Schematic representation of the galvanic corrosion with the presence of intermetalics phases, reproduced from [87]

1.4.3 Electrochemical measurements of Magnesium alloys corrosion properties

The determination of the degradation rate of the Mg alloys is an important issue, and several methods are used to accurately evaluate the corrosion rate of these alloys. Mass loss, H_2 volume and pH measurements are commonly used but do not fully capture all the features of Mg alloys corrosion. To address this, electrochemical measurements techniques have been developed.

1.4.3.1 Potentiodynamic polarization (PDP)

This voltage control technique involves polarizing the working electrode over a range of potentials, and recording the current response to the generated electric field. This allows for the determination of the kinetics of the anodic and cathodic processes, indicating the passive behavior and helping to determine the corrosion current density. The measurement of the properties

Thèse accessible à l'adresse : https://theses.insa-lyon.fr/publication/2025ISAL0008/these.pdf © [J. Moreau], [2025], INSA Lyon, tous droits réservés

of the Mg alloys after the PDP relies on the Tafel-extrapolation. An alternative to this technique is the linear polarization resistance (LPR) measurement, which relies on the use of a very small range of potential. The instantaneous corrosion rate i_{corr} can be determined using the LPR technique during time [109]. The main advantage of this technique is the use of a small polarization, making it non-destructive technique [110]. The slope of a linear plot of current vs. potential when the current changes polarity (dE/dI), defined as the polarization resistance R_p, is inversely proportional to corrosion rate, as described by the stern-Geary equation [111]. A typical LPR curve of Mg alloys is shown Fig.1.15.a.

However, one drawback is that for Mg alloys, the calculations are difficult due to negative difference effect (NDE) [94], which opposes the expected behavior of an electrochemical system. For most metals, when the potential is increased, the anodic dissolution rate increases and the cathodic hydrogen-evolution rate decreases. However, on Mg, increasing the anodic polarization also increase the hydrogen evolution rate, as shown in Fig.1.15.b. The anomalous hydrogen-evolution induces an ohmic potential drop that dominate the shape of the PDP plot, making it difficult to identify the Tafel region [112], but also making it harder to identify the localized corrosion behavior. Various theories tried to explain this phenomenon [113], but so far, none have completely explained it, and it remains unresolved.

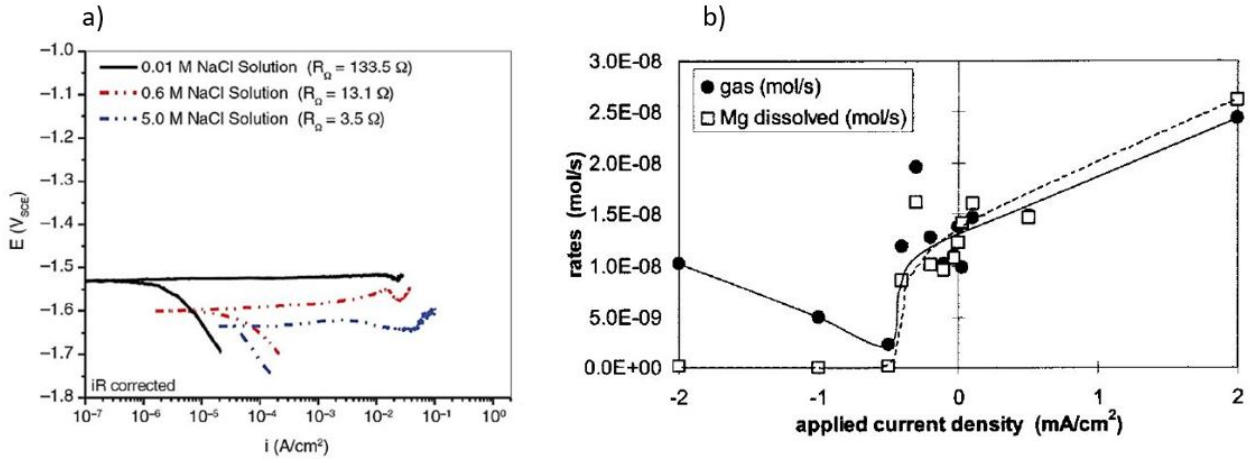


Figure 1.15: a) Linear polarization resistance curve showing the NDE in NaCl solution using pure Mg [94] b) Visualization of the increasing of the hydrogen release when increasing the anodic polarization [112]

1.4.3.2 Electrochemical impedance spectroscopy (EIS)

The EIS technique measures the complex impedance response of an electrode to a small amplitude sinusoidal potential perturbation at different frequencies. By fitting the results to an equivalent circuit, EIS provides the polarization resistance (R_p) and information about the capacitive and inductive response of the interface [114]. Furthermore, the non-destructive aspect of the technique allows continuous monitoring of the progress of corrosion on Mg alloys.

Generally the Nyquist plots of the EIS measurement consists of two loops [115] : a capacitive loop at high frequencies and an inductive loop at low frequencies. The capacitive loop at

Thèse accessible à l'adresse : https://theses.insa-lyon.fr/publication/2025ISAL0008/these.pdf © [J. Moreau], [2025], INSA Lyon, tous droits réservés

high frequencies is related to the charge transfer resistance as well as the effect of the ionic double layer capacitance of the electrode [110]. The inductive behavior is often associated with the occurrence of pitting corrosion caused by anodic dissolution of the Mg or linked to the relaxation of adsorbed intermediates [116]. A typical Nyquist plots of an EIS measurements is shown in Fig.1.16.a, displaying the imaginary component (Z") vs the real component (Z'), with Rt defined as the value corresponding to Z' when –Z"= 0, whilst RP is defined as the zero frequency impedance at –Z"=0.

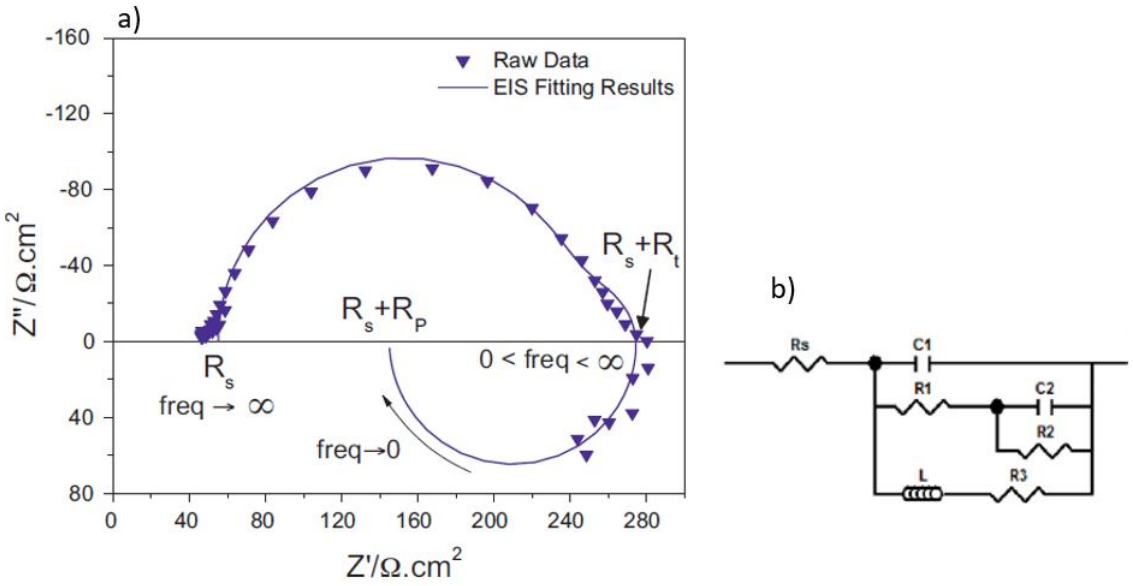


Figure 1.16: a) EIS measurement (scatter plot) and model fit (solid lines) of high purity Mg after 24 hrs of immersion at open circuit in quiescent 0.1 M NaCl displaying low frequency inductance, and b) Equivalent electrical circuits used to model the electrochemical impedance response, reproduced from [117]

From this Nyquist plot, it is possible to construct an equivalent electrical circuit, as shown in Fig.1.16.b. The impedance relationships of the circuit elements used in the equivalent circuit for EIS are shown (Table.1.3). To ensure the system is stationary, the direct integration of the Kramers-Kronig (K-K) transformations of the real and the imaginary components is used [118]. A good correlation and a low residual noise indicate the consistency of the impedance data.

Component	Impedance
Resistor	$Z_r = R \quad f \longrightarrow 0 \quad Z_R = R$
Capacitor	$Z_c = \frac{1}{2\pi fc} \quad f \longrightarrow 0 \quad Z_c = +\infty$
Inductor	$Z_L = 2\pi fL \quad f \longrightarrow 0 \quad Z_L \longrightarrow 0$

Table 1.3: Impedance relationships and low frequency asymptote for solid state circuit elements typically used in the equivalent circuit model of a corroding metal.

From the measurements, it is possible to extract R_p, the transfer charge resistance ($R_t \longrightarrow$

Thèse accessible à l'adresse : https://theses.insa-lyon.fr/publication/2025ISAL0008/these.pdf © [J. Moreau], [2025], INSA Lyon, tous droits réservés

$Z" = 0$) and the solution resistance (R_s, initial resistance at high frequencies). Combined with the values calculated for each component of the equivalent circuit, this allows for a comprehensive understanding of the corrosion behavior of the studied Mg alloy.

1.4.4 Microstructure tuning for improved corrosion resistance

1.4.4.1 Alloying elements

Impurities The rapid corrosion of early Mg alloys was mainly due to the presence of impurities such as iron, nickel, and copper, which significantly accelerated corrosion. Indeed, These impurities, in the form of segregated clusters within the Mg matrix, act as small cathodes, significantly accelerating the corrosion of the α-Mg matrix, which acts as the anode [119].

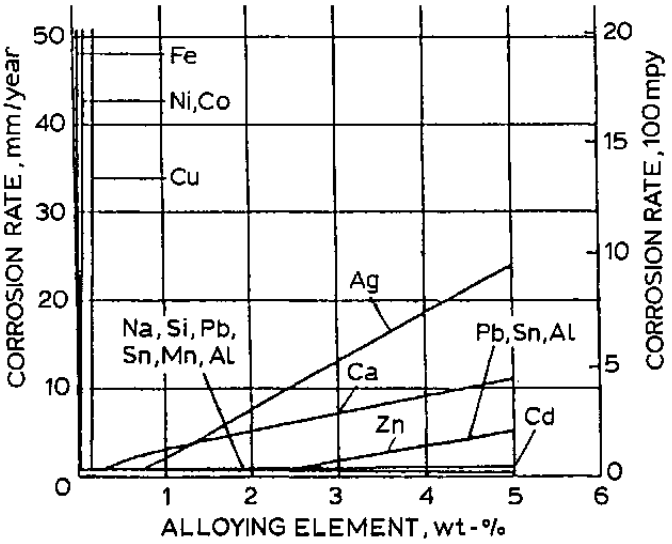


Figure 1.17: Influence of the alloying elements and impurities on the corrosion rate of Mg alloys [120]

Impurities play a crucial role in the corrosion rate beyond a certain tolerance value, beyond this concentration, the corrosion rate increases dramatically [121]. Moreover, the tolerance concentration limit varies depending on the solute studied [122]. This notion of tolerance limits impurities in Mg has been studied for multiple elements, as shown in Fig.1.17. Obtaining high purity Mg is a major concern, since, for example, around 170 ppm of Fe drastically increase the corrosion rate of the alloy [120].

Influence of the alloying elements The choice of the alloying elements in the design of the Mg alloy is very important as it defines the corrosion behavior. Esmaily *et al* [123] compiled more than 1000 studies on the corrosion of the Mg alloys and managed to give an overview of the effects of each element, as represented in Fig.1.18.

Each alloying element affects either the anodic reaction or the cathodic partial reaction. The extent of the impact on these reactions is symbolized by the position of the elements on the arrow. A large number of alloying elements enhance the cathodic kinetics, thereby increasing

Thèse accessible à l'adresse : https://theses.insa-lyon.fr/publication/2025ISAL0008/these.pdf © [J. Moreau], [2025], INSA Lyon, tous droits réservés

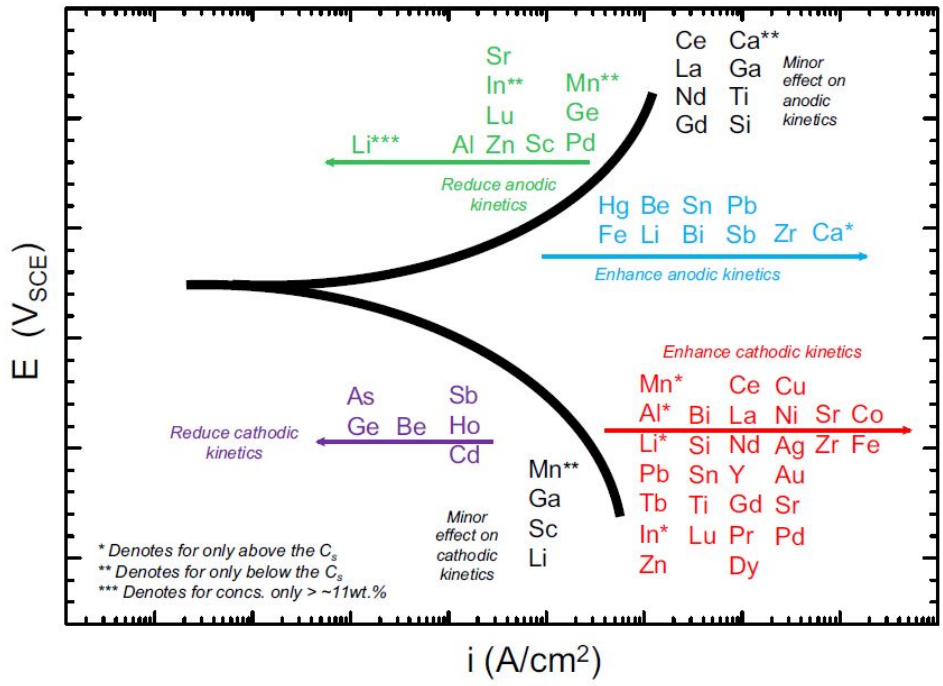


Figure 1.18: Influence of the alloying elements on the anodic and cathodic partial reactions. The extent of the impact is symbolized by the position on the arrow, reproduced from [123]

the corrosion rate. It is not shown in the graphic. It is also important to note that the effect of alloying elements depends on their concentration in the alloy, although this is not depicted in the graphic.

1.4.4.2 Heat Treatments of Alloys

Unlike pure Mg, alloys are not uniform in composition or microstructure. These differences result in electrochemical variations within the alloy and create galvanic couples. The corrosion reactions are similar to those presented earlier, but their activities may vary depending on the phases and grains. When the Mg phase is dominant, it acts as a micro-anode and will preferentially oxidize. Other constituents such as impurities, intermetallic particles, secondary phases, or even portions of the matrix with a higher solid solution concentration can act as micro-cathodes [94] [100].

Since the matrix is preferentially oxidized, elements in solution in the matrix have a strong influence on the degradation rate. In Mg-Al binary, the degradation rate decreases with an increase in the mass fraction of aluminum in solution [94].

Differences in concentration within the solid solution can lead to micro-galvanic corrosion, which will preferentially oxidize the grain center or grain boundaries depending on the alloying element [87].

In alloys, secondary phases can also appear. These intermetallic phases, more stable than the Mg matrix, often act as micro-cathodes and can accelerate the corrosion phenomenon. At

Thèse accessible à l'adresse : https://theses.insa-lyon.fr/publication/2025ISAL0008/these.pdf © [J. Moreau], [2025], INSA Lyon, tous droits réservés

their vicinity, these phases can also act as a corrosion barrier depending on their sizes and distributions within the material [108]. For instance, a well distributed β precipitate phase acts as a barrier, whereas a discontinuous distribution in small amounts accelerates degradation, as shown in Figure 1.19.

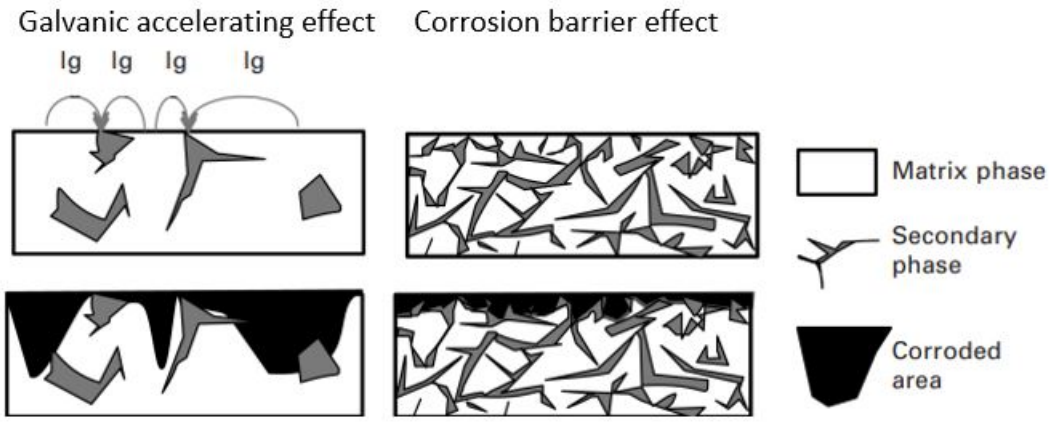


Figure 1.19: Influence of distribution of intermetallic phases on galvanic corrosion. With either an accelerating effect for large second phases or a slowing effect for fine and well distributed second phases [124]

Thus, the presence of secondary phases plays a dual role in the corrosion of Mg alloys. It is necessary to control the amount of second phases in the alloy to optimize the corrosion resistance.

1.4.4.3 Grain Size

Reducing the grain size increases the number of grain boundaries, optimizing the distribution of intermetallic phases and minimizing the size of phases that can accelerate corrosion. Thus, the reduction of the grain size might be able to reduce the corrosion rate. For example, the addition of strontium to the Mg-Al binary alloy has demonstrated a reduction in grain size as well as a modification of the oxide layer structure and the composition and electrochemical properties of the phases present [125]. These modifications enhance the corrosion resistance by creating a more uniform and protective passive layer on the alloy surface. However, it is difficult to assess the distinct effect of the composition and the grain size.

To achieve the best corrosion resistance it is necessary to find a compromise between the grain size and the size of the second phases. A representation of this compromised is shown in Fig. 1.20.

Thèse accessible à l'adresse : https://theses.insa-lyon.fr/publication/2025ISAL0008/these.pdf © [J. Moreau], [2025], INSA Lyon, tous droits réservés

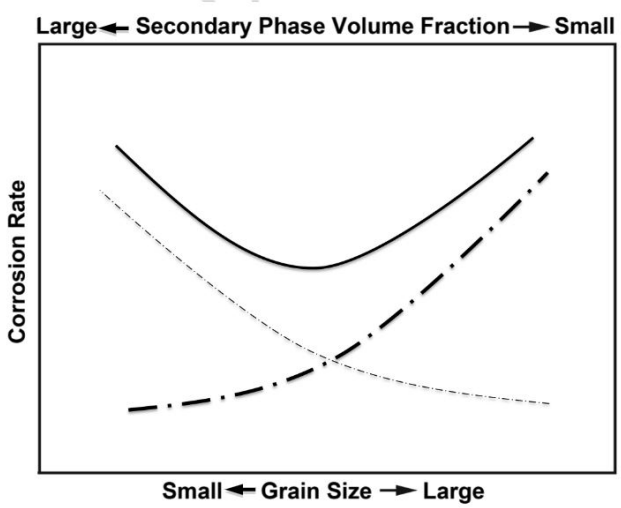


Figure 1.20: Schematic drawing showing how the corrosion rate decreases with decreasing secondary phase content (thin chain-dashed curve) and increases with grain size (thick chain-dashed curve) and the overall effect on the corrosion rate (indicated by solid curve), reproduced from [126]

1.5 Magnesium alloys design for biodegradable implants

1.5.1 Influence of the alloying elements on the mechanical properties and the corrosion resistance

Alloying elements significantly influences the final properties of the material. The elements used affect the alloy's microstructure, thus playing a predominant role in mechanical properties and corrosion resistance. Many alloying elements are studied, among which zinc [127] [128], strontium [129] [130], silver [131] [132], calcium [133] [134], and rare earths (RE) [135] [136] are prominent.

Mg-Zn Alloys Zinc is a material naturally present in the body, with 85% concentrated in muscles and bones [45]. Zinc has a maximum solubility of 6.2 wt% in Mg, allowing for solid solution and precipitation strengthening.

The presence of zinc also refines the grain size, improving corrosion resistance and mechanical properties. The MgZn second phase plays a crucial role in corrosion resistance by significantly influencing galvanic corrosion [49]. Corrosion tests on different Mg-Zn alloys identified Mg-3Zn as the most corrosion-resistant and having the best mechanical properties.

Mg-Ca Alloys Ca is a naturally occurring element in the body and a major component of bones. The microstructure of the Mg-Ca alloy consists of an α-Mg matrix and an intermetallic phase of $MgCa_2$. The fraction of this intermetallic phase increases with the calcium concentration in the alloy [137]. The addition of calcium has a grain-refining effect, and the alloy's hardness increases with calcium concentration due to the presence of $MgCa_2$ intermetallics. However,

Thèse accessible à l'adresse : https://theses.insa-lyon.fr/publication/2025ISAL0008/these.pdf © [J. Moreau], [2025], INSA Lyon, tous droits réservés

above 0.7 wt% calcium, galvanic corrosion between the matrix and intermetallic phases becomes significant, accelerating degradation [138]. Even though calcium is naturally present in the body, for Mg-2Ca and Mg-3Ca alloys, corrosion is too rapid and leads to a change in pH in *in vitro* tests, resulting in cell death [139] [134]. For concentrations around 1 wt% calcium, *in vivo* results with implantation of a rod in a rat's femur are more promising [139].

Mg-Sr Alloys Sr possesses chemical, metallurgical, and biological properties similar to Mg and Ca. Like Ca, it refines the grain size and strengthens mechanical properties [140]. Sr has very low solubility in Mg at 0.11 wt%. Above this concentration, secondary phases, notably $Mg_{17}Sr_2$, precipitate at grain boundaries. These secondary phases deteriorate mechanical properties and corrosion resistance. For an addition exceeding 2 wt%, degradation is faster, and the best *in vivo* resistance is observed for Mg-1Sr [141].

Mg-Ag Alloys Silver's advantage over other alloying elements lies in its antibacterial properties. Although Ag is considered toxic to humans, Bosetti *et al.* [142] demonstrated that it does not affect the material's biocompatibility. The presence of Ag increases the material's mechanical strength and ductility through grain refinement and the presence of precipitates [143]. However, the addition of Ag accelerates alloy degradation primarily due to galvanic corrosion between the Mg matrix and the MgAg intermetallic phase [144].

Mg-RE Alloys Rare earth (RE) atoms can substitute for Mg atoms in the crystal lattice. This can lead to solid solution strengthening, precipitation, and grain refinement. Some rare earths, such as yttrium [145], gadolinium [146], and dysprosium [147] have a very high solubility in Mg and are widely used to harden Mg alloys, significantly affecting corrosion resistance [90]).On one hand REs enhance corrosion resistance because impurities (Fe, Ni, Cu, ...) react with them to form intermetallic compounds, reducing their negative influence [148]. On the other hand, the composition of the passivation layer formed during corrosion is modified by the incorporation of RE atoms, increasing its stability and resistance to corrosive elements [149].

Following the previous paragraph describing the influence of each element, we decided to focus our study of one type of Mg alloy. Mg-Zn alloys were chosen due to their popularity and application as degradable biomaterials, thanks to their high specific strength and outstanding biocompatibility. In the next sections, the specific properties of Mg-Zn alloys and the effects of alloying elements will be discussed.

1.5.2 Mechanical properties and corrosion resistance depending of the Zn concentration

To design an alloy for biodegredable implants, it is important to combine the right mechanical properties and corrosion resistance, as presented before. Optimizing both properties often requires compromises as the optimal composition and microstructure may differ. The vast majority of the studies assessing the properties of Mg-Zn alloys manufactured their samples either by casting or extrusion. Due to the manufacturing techniques, different microstructures are obtained, as shown in Fig.(1.21.

These differences in microstructure lead to varying mechanical properties due to the intermettalic phases and the grain size. The mechanical properties of Mg-Zn alloys are summarized (Table.1.4).

Thèse accessible à l'adresse : https://theses.insa-lyon.fr/publication/2025ISAL0008/these.pdf © [J. Moreau], [2025], INSA Lyon, tous droits réservés

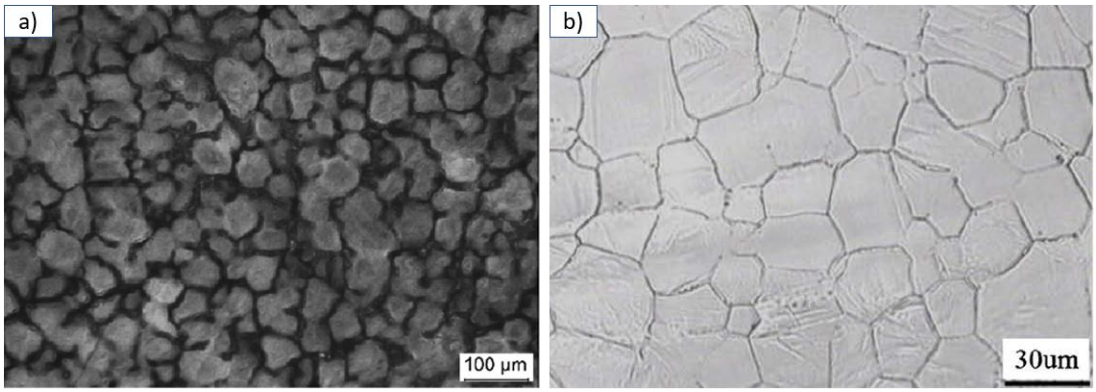


Figure 1.21: SEM images of a) Cast Mg-5Zn [49] and b) extruded Mg-6Zn [128]. Showing that extrusion produces finer grain and that casting promotes the formation of a denditric microstructure of intermettalics of MgZn at the grain boundaries

Alloy	Manufacturing process	yield strength (MPa)	Ultimate tensile strength (MPa)	Elongation (%)
Mg-6Zn [128]	Extrusion	169.5 ± 3.6	279.5 ± 2.3	18.8 ± 0.8
Mg-1Zn [49]	Casting	60.62	187.73	13.77
Mg-5Zn [49]	Casting	75.60	194.59	8.50
Mg-7n [49]	Casting	67.28	135.53	6.00
Mg-0.8Zn [70]	extruded	198	238	26.5
Mg-2.7Zn [70]	extruded	208	263	25.6
Mg-4.3Zn [70]	extruded	227	288	21.0

Table 1.4: Summary of the mechanical properties of the binary MgZn alloys with different Zn contents and different manufacturing processes

An overall effect is observed concerning the content of Zn in the alloy. With the increase of Zn content, the yield strength and the ultimate tensile strength tend to increase but the elongation to fracture decreases. This can be explained by the increase of intermetallic volume fraction with the increase of Zn content, which makes the alloys more brittle. Studies of binary MgZn alloys are still limited, and many inconsistencies are observed between each studies, a shown in (Table.1.4) and noted by Jiang *et al* [150] when analyzing MgZn alloy studies.

Regarding the corrosion properties, it is it is challenging to establish a clear trend about the effect of Zn content on the corrosion rate. This is due to several factors:

- Different corrosion medium used in various studies
- Impurities that significantly influence the corrosion rate
- Inconsistent control of the volume fraction of precipitates and intermettalics

However, Zhang *et al* [128] suggested that the Zn content should not exceed 4wt% to achieve the best combination of mechanical properties and corrosion resistance. When examining each studies individually rather than collectively, Mg-3wt% Zn appears to be a promising alloy for corrosion properties, as shown in Fig.1.22.

Thèse accessible à l'adresse : https://theses.insa-lyon.fr/publication/2025ISAL0008/these.pdf © [J. Moreau], [2025], INSA Lyon, tous droits réservés

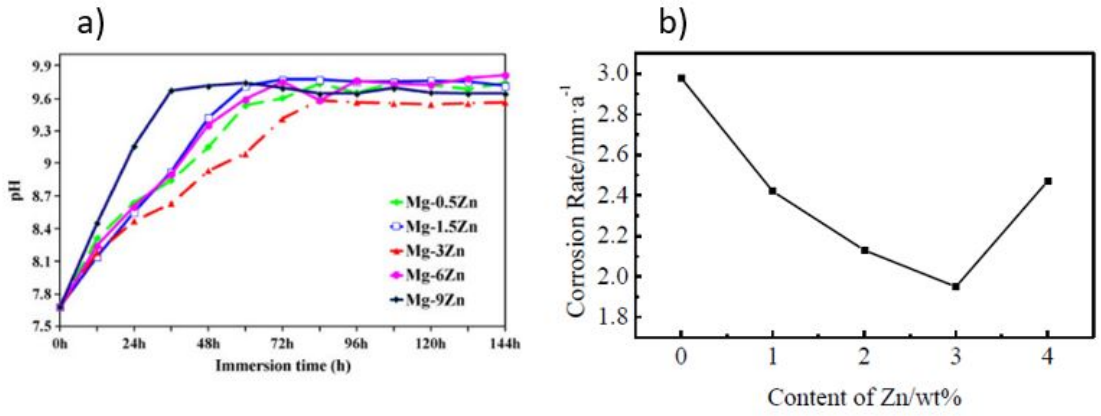


Figure 1.22: a) Evolution of the pH during an immersion test of MgZn binary alloys showing that the pH is less increasing with Mg3Zn [151] b) Corrosion rate of the MgZn alloys with the variation of the Zn content with a minimum for Mg3Zn [152].

Studies indicate that at 3 wt% Zn, the increase in pH is the lowest among the other concentration when manufactured by casting. Furthermore, below 4 wt%, the distribution of second phases is homogeneous [151]. Additionally, when Mg-Zn alloys are manufactured by powder metallurgy, the lowest corrosion rate is achieved by Mg-3wt% Zn [152].

1.5.3 Addition of Zr

Previously the Mg-3%wt Zn alloy was identified as promising for biomedical applications. To further improve the alloy for biomaterial applications, Zr was added to create the Mg-3wt%Zn-0.6wt%Zr (ZK30) alloy. Zr acts as a grain refiner, contributing to the strength of the alloy [153]. Zr has lattice parameters close to Mg, making it easy to form heterogeneous nucleation for Mg grains [154]. Additionally, using a low concentration of Zr (<0.48%) without forming Zr precipitates also improves corrosion resistance [155]. Finally, when studied for dental implants, Zr demonstrated sufficient biocompatibility and and osseointegration [156].

1.5.4 Aging treatment of MgZnZr alloys

The alloy of this study was previously selected as ZK30. To obtain the most suitable alloy for biodegredable implants, it is necessary to control the presence of second phases. The precipitation sequence of the ZK alloy is not well known, but studies suggest that it is close to the precipitation sequence of Mg-Zn alloys.

In an Mg-Zn alloy, precipitation begins with the formation of rod-shaped β_1', followed by coarse plate precipitates β_2', and reaches the β equilibrium phase after a long aging time (around 30h) [157]. Both β_1' rods and β_2' plates have been reported to have strong hardening effects on slip and twinning. The β_2' plates have been confirmed to display an hexagonal structure identical to the $MgZn_2$ phase. The structure of the β_1' rods is still debated, with reports suggesting it could be either hexagonal $MgZn_2$[158] or monoclinic Mg_4Zn_7 [159]. Recent observations in a cast Mg-3Zn alloy suggest it could consist of a mixture of both [160].

Thèse accessible à l'adresse : https://theses.insa-lyon.fr/publication/2025ISAL0008/these.pdf © [J. Moreau], [2025], INSA Lyon, tous droits réservés

Hadadzadeh *et al* [161] proposed an isopleth representation of the ZK60 alloy based on calculus from an unspecified database. During aging, they observed, similar to the MgZn alloy and in accordance with their calculations, the formation of $MgZn_2$. They also observed the formation of Zn_2Zr that creates drops of Mg concentration within the alloy. Lastly, Kang *et al*[62] studied the impact of aging treatments on the hardness of ZK60 alloy. They determined that the 170 °C was the most effective for increasing hardness, although, they did not study the microstucture changes responsible for this increase.

1.6 Conclusion

The manufacturing processes of Mg alloys significantly influence their final properties. Techniques such as casting and extrusion produce different microstructures, which affect the mechanical performance and corrosion behavior of the alloys. Casting typically results in large grain sizes, whereas extrusion leads to finer grains due to dynamic recrystallization. Spark Plasma Sintering has emerged as a promising method to produce Mg-based alloys with finer grain sizes and enhanced mechanical properties compared to traditional methods.

The mechanical properties of Mg alloys make them suitable candidates for orthopedic implants. These properties include Young's modulus, tensile strength, fatigue strength, and elongation at break. The ZK30 alloy, with the addition of zinc and zirconium, demonstrates promising mechanical strength and ductility. Zinc refines the grain size and strengthens the alloy through solid solution and precipitation hardening. Zirconium acts as a grain refiner and improves corrosion resistance without forming detrimental precipitates at low concentrations.

Corrosion resistance is a critical factor for biodegradable implants. The corrosion behavior of Mg alloys is influenced by the alloying elements, impurities, and the environment. The presence of impurities such as iron, nickel, and copper significantly accelerates corrosion by forming galvanic couples. Alloying elements like zinc and zirconium enhance the corrosion resistance by refining the grain size and modifying the passivation layer. However, the challenge lies in balancing the mechanical properties and corrosion resistance, as the optimal composition and microstructure for each may differ.

Aging treatment plays a crucial role in controlling the presence of second phases and optimizing the mechanical properties and corrosion resistance of the ZK30 alloy. The precipitation sequence in Mg-Zn alloys involves the formation of rod-shaped β'_1 and coarse plate β'_2 precipitates, which have strong hardening effects.

The ZK30 alloy, with its balanced mechanical properties and corrosion resistance, is a promising candidate for biodegradable implants. However, limited studies have investigated the impact of precipitates in Mg-Zn alloys on corrosion rates, with most focusing primarily on optimizing Zn content. A combined study of precipitation behavior and degradation rates could provide insights for designing materials suitable for orthopedic applications.

Optimizing manufacturing processes, controlling impurities, and implementing precise aging treatments are essential for developing Mg-based alloys with enhanced properties. A comprehensive study of this alloy would reveal its true potential as a degradable implant material.

Thèse accessible à l'adresse : https://theses.insa-lyon.fr/publication/2025ISAL0008/these.pdf © [J. Moreau], [2025], INSA Lyon, tous droits réservés

Thèse accessible à l'adresse : https://theses.insa-lyon.fr/publication/2025ISAL0008/these.pdf © [J. Moreau], [2025], INSA Lyon, tous droits réservés

Chapter 2

Development of MgZnZr alloy prepared by Spark Plasma Sintering

Contents

2.1 Introduction . . . 39
2.2 Materials and methods . . . 40
2.2.1 Powders . . . 40
2.2.2 Densification via Spark Plasma Sintering . . . 40
2.2.3 Microstructural characterization . . . 41
2.2.4 Microscopic observations . . . 42
2.2.5 Differential scanning calorimetry (DSC) . . . 43
2.2.6 Oxygen analysis . . . 43
2.2.7 Mechanical tests . . . 43
2.3 Preliminary sintering study . . . 44
2.3.1 Setup for the sintering cycle . . . 44
2.3.2 Influence of the oxide layer on the mechanical properties . . . 45
2.4 Thermodynamic-based ZK30 sintering cycle . . . 47
2.4.1 Evaluation of the liquid phase . . . 48
2.4.2 Development of the SPS cycle . . . 50
2.4.3 Thermodynamics of ZK30 . . . 51
2.5 Mechanical properties at higher sintering temperatures . . . 54
2.6 Observation of the microstructure . . . 57
2.7 Conclusion . . . 59

2.1 Introduction

The initial approach to evaluating the potential of the ZK30 alloy for biomedical applications involves obtaining dense samples. Spark Plasma Sintering (SPS) was selected as the manufacturing process. This chapter examines the sintering parameters, microstructure, and mechanical

Thèse accessible à l'adresse : https://theses.insa-lyon.fr/publication/2025ISAL0008/these.pdf © [J. Moreau], [2025], INSA Lyon, tous droits réservés

properties of the MgZnZr alloy, with the goal of optimizing density and hardness while minimizing the presence of harmful oxide layers. Subsequently, the mechanical properties will be assessed to establish the optimal sintering cycle.

2.2 Materials and methods

2.2.1 Powders

To develop a sintering method for Mg alloys, pure Mg (Mg) and the ZK30 alloy were selected for comparison. The pure Mg powder, atomized under argon, was supplied by SFM SA (Martigny, Switzerland), with its chemical composition provided in (Table 2.1). The second powder, ZK30 atomized under Argon, was provided by Université technique de Belfort-Montbélliard (UTBM) (Belfort, France) and its chemical composition is given in (Table 2.1).

Element	Al	Cu	Fe	Mn	Ni	Ca	Si	Zn	Zr	Mg
Mg powder (wt%)	0.01	<0.001	<0.001	0.012	<0.001	0.05	<0.001	0.093	-	99.87
ZK30 powder (wt%)	-	<0.1	<0.1	-	< 0.1	<0.1	-	3.5	0.6	95.9

Table 2.1: Chemical composition of the Mg powder and the ZK30 powder according to the suppliers

The as-received powders were characterized in terms of particle size distribution using a Laser granulometer Metasizer3000 (MALVERN, Vénissieux, France) in a dry environment, given in Fig.2.1 and in Table.2.2.

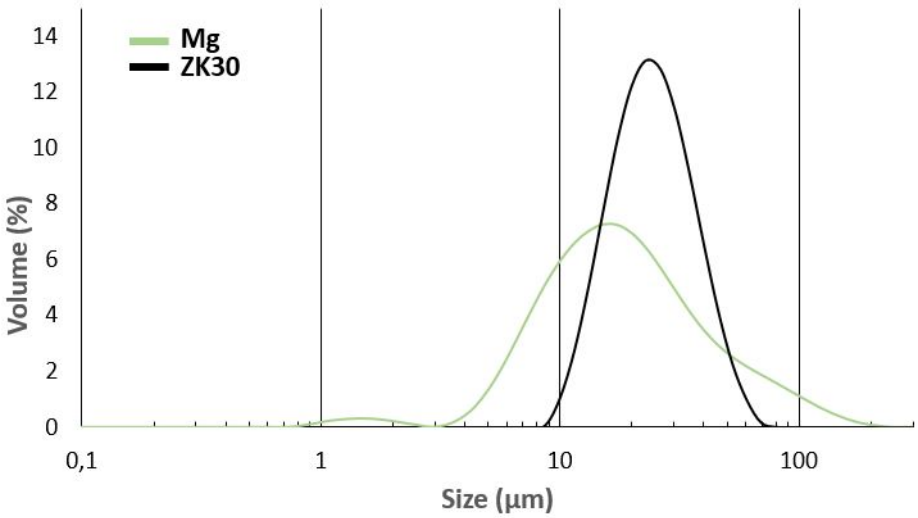


Figure 2.1: Size distribution of the Mg and ZK30 powders

The powders were kept in a glove box under Argon atmosphere to prevent oxidation.

2.2.2 Densification via Spark Plasma Sintering

A Spark Plasma Sintering (SPS) apparatus (FCT System HPD 25, Germany) was used for the densification process. Powders were loaded into a cylindrical carbon die with an internal

Thèse accessible à l'adresse : https://theses.insa-lyon.fr/publication/2025ISAL0008/these.pdf © [J. Moreau], [2025], INSA Lyon, tous droits réservés

-	D10	D50	D90
Pure Mg	7.6 µm	17.6 µm	52.5 µm
ZK 30	15.5 µm	25.6 µm	43.3 µm

Table 2.2: Particle size distribution of the Mg and ZK30 powders

diameter of 20 mm Fig. 2.3.b, with a graphite sheet inserted between the powder and the die to prevent any interaction between them. The samples were heated by passing a pulsed current through two graphite pistons also acting as electrodes, while the powder was maintained under uniaxial pressure by the electrodes. A load of 5 to 20 kN corresponding to pressure of 13 MPa to 63 MPa was applied using pistons. A low loading was used as a first approach to evaluate the potential sintering of Mg alloys without pressure. A vacuum step was then performed, then the gas used for the experiment is introduced into the apparatus. The temperature is monitored and automatically controlled by a thermocouple inserted into the die, see Fig.2.3.c. The load, pressure and piston displacement were all monitored and recorded during the sintering. After this procedure, discs with the same inner diameter as the graphite die are obtained. A typical cycle used during the study is shown in Fig.2.2.

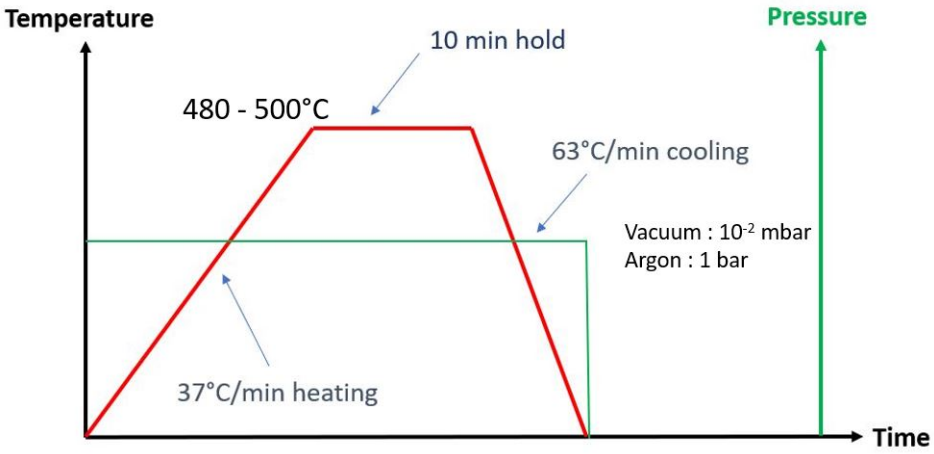


Figure 2.2: Cycle used during the study of the sintering with a vacuum step performed prior to the increases of pressure and temperature

2.2.3 Microstructural characterization

2.2.3.1 Density

The density of the samples was measured using the Archimedes method. The mass of each sample was recorded while immersed in ethanol and then dried at ambient temperature. Each measurement was repeated three times to ensure accuracy. The density is given by the formula :

$$\rho = \frac{m}{(m - m_{im})}\rho_{eth} \tag{2.1}$$

Thèse accessible à l'adresse : https://theses.insa-lyon.fr/publication/2025ISAL0008/these.pdf © [J. Moreau], [2025], INSA Lyon, tous droits réservés

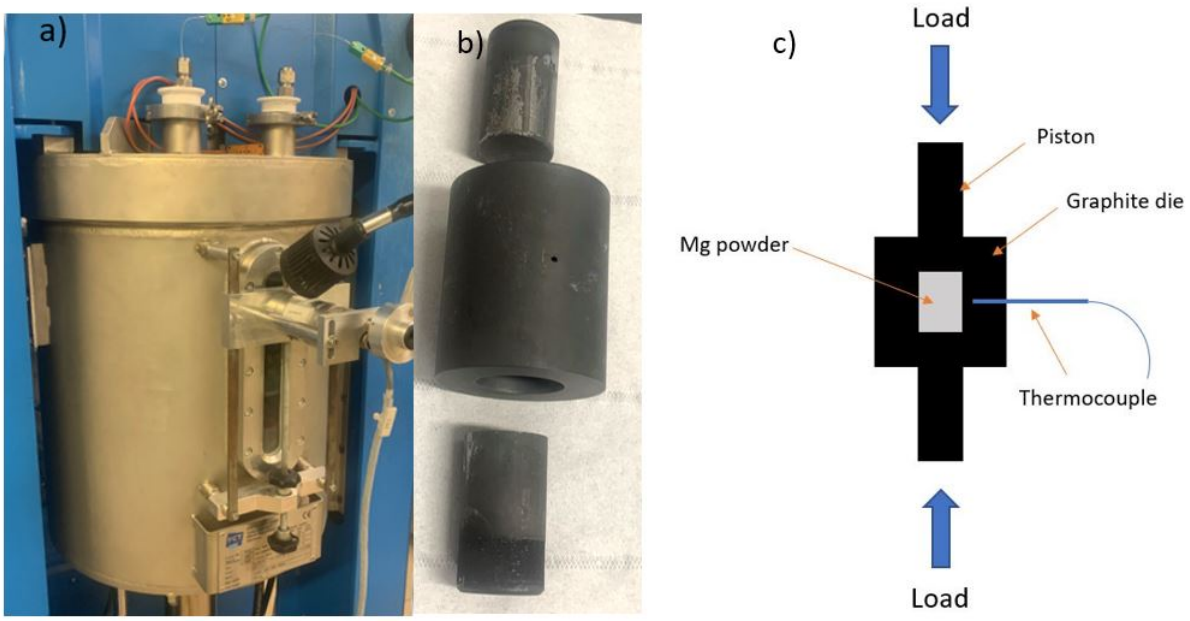


Figure 2.3: a) Chamber of the SPS seen from the outside, b) The pistons and graphite die used for the process c) Scheme of the setup

With m the mass of the sample, m_{im} the mass of the sample immersed in ethanol and ρ_{eth} the density of ethanol, calculated with the temperature in the room.

2.2.3.2 Polishing

The polishing procedure of the obtained samples was performed manually for optical microscopy to determine the porosity according to the following sequence :

- 2 min with 15 μm SiC paper
- 2 min with 8 μm SiC paper
- 2 min with 6 μm SiC paper

Ethanol was used during polishing to prevent the sample from corrosion.

For microstructure observation, the polishing was performed using Ilion II system polisher (Gatan, Pleasanton, USA) with the following sequence :

- 4 h, 6 keV, Angle 90°, 3 RPM
- 2 h, 2 keV, Angle 90°, 3 RPM
- 2 h, 1 keV, Angle 90°, 3 RPM

2.2.4 Microscopic observations

2.2.4.1 Optical micrography

The optical micrography was performed using an Hirox 3D microscope (Hirox, Limonest, France). The internal porosity was determined using Fiji software. After binarization and thresholding, porosity was analyzed with the "Analyze Particles" plugin.

Thèse accessible à l'adresse : https://theses.insa-lyon.fr/publication/2025ISAL0008/these.pdf © [J. Moreau], [2025], INSA Lyon, tous droits réservés

2.2.4.2 Electron microscopy

The microstucture was characterized using a Zeiss Supra 55V (Zeiss, Oberkochen, Germany) scanning electron microscopy (SEM) equipped with an energy dispersive X-ray spectrometer (EDS). SEM imaging was done in both secondary electrons (SE) and backscattered electron (BSE) mode. Electron backscattered diffraction (EBSD) and energy dispersive X-ray (EDX) maps were acquired using an Oxford Instrument camera (Oxford, Les Ulis, France). Most measurements were conducted with an accelerating voltage of 10 keV .

2.2.4.3 Tomography

Micro-computed tomography (μ-CT) was performed with a 1 μm voxel size using an EasyTom Nano tomography system (RX Solutions, Annecy, France). Internal porosity was quantified by X-Ray tomography scans analysis performed with Fiji software. After performing binarisation and setting the threshold, the porosity was determined using the analyze particles plugin. The closed porosity was determined by the plugin 3D counter object from [162] and the distance between the surface of the powder particles by the plugin local thickness developed by [163]. The plugin 3D counter object was applied on the remaining pores and the open pores were determined using the "exclude on edges" option to discriminate the pores connecting to the surface. The local thickness plugin was also applied to the remaining porosity after binarisation, the principle of the plugin is to insert the largest sphere possible inside the pores which gives an equivalent diameter and a pore size distribution. It is useful to determine the mean size of the open porosity in the different samples.

2.2.5 Differential scanning calorimetry (DSC)

Differential Scanning Calorimetry (DSC) measurements were performed using a DSC Sensys Evo (SETARAM) equipped with 3D sensor under Ar flow (10 mL/min, Air Liquide Alphagaz 2).

2.2.6 Oxygen analysis

The measurements of oxygen concentration in the samples were performed by internal gas analysis (IGA) in the laboratory of FILAB (Saint-Apollinaire, France).

2.2.7 Mechanical tests

2.2.7.1 Hardness measurements

The hardness measurements were performed on a Buehler machine with a load of 500 g with a holding time of 10s. The measurements were performed three times.

2.2.7.2 Tensile test

Tensile tests were conducted using an Electroforce 3200 test machine (Bose, Eden Prairie, MN) equipped with a 22 N load cell. Tests consisted in a preload of 0.2 N followed by a loading rate of 0.5 $\mathrm{N\,s^{-1}}$.

Thèse accessible à l'adresse : https://theses.insa-lyon.fr/publication/2025ISAL0008/these.pdf © [J. Moreau], [2025], INSA Lyon, tous droits réservés

2.2.7.3 Three point bending test

Three-points bending tests were conducted using an Electroforce 3200 test machine (Bose, Eden Prairie, MN) equipped with a 22 N load cell. Tests consisted in a preload of 0.2 N followed by a loading rate of $0.05\,\mathrm{N\,s^{-1}}$. The length between the two support points was fixed at 10 mm.

2.3 Preliminary sintering study

2.3.1 Setup for the sintering cycle

When optimizing the sintering cycle of Mg alloys the density is primary parameter to measure as discussed in Section 2.2.3.1. Key factors influencing sintering include temperature, loading, and atmosphere. A minimum temperature of 450 °C was selected, as sintering temperatures for Mg alloys typically exceed this value [52]. Two loading conditions were studied : a minimum of 5 kN corresponding to 13 MPa and a maximum of 20 N corresponding to 63 MPa. Three different atmospheres were tested : primary vacuum ($5\text{x}10^{-2}Pa$), Argon and pure Hydrogen. Hydrogen was tested for its potential to provide a reducing atmosphere, which might reduce the native oxide layer on the powder. A graphite die with a 20 mm inner diameter was chosen, aiming to produce disks with a 1 cm thickness corresponding to a powder mass of 5.7 g. The heating was determined to last approximately 10 min until reaching the final temperature, followed by a 10 min holding period, and then a 10 min cooling to room temperature. The melting point of Mg is 650 °C. To avoid evaporation of the powder, given the low vapor pressure of Mg, the temperature studied ranged from 480 °C to 550 °C. After removing the graphite sheet and performing manual polishing, the relative density (Archimedes method) and hardness of all samples were measured.

Initially, the cycle was tested on pure Mg and the resulting density and hardness are presented in Table.2.3.

Temperature (°C)	**Pressure (MPa)**	**Atmosphere**	**Relative density**	**Hardness (HV)**
500	13	Vacuum	0,94 ± 0,2	26 ± 5
500	13	Argon	0,90 ± 0,2	24 ± 5
500	13	H2	0,90 ± 0,2	19 ± 5
500	63	Vacuum	0,99 ± 0,1	42 ± 3
500	63	Argon	0,99 ± 0,1	40 ± 2
500	63	H2	0,99 ± 0,1	37 ± 2

Table 2.3: Density and hardness evolution depending the temperature, load and atmosphere used during the process

At a pressure of 63 MPa, using temperature above 500 °C resulted in the break of the graphite die in most trials. The table shows that for low pressure at 13 MPa the compaction was insufficient, leading to a resulting density of around 92% with low hardness around 23 HV. However, with higher loading, the resulting density was around 99%, and the hardness reached approximately 40 HV. The atmosphere did not significantly impact density or hardness within this range of parameters. After testing pure Mg the most favorable parameters identified were a high loading at 500 °C with an atmosphere of Argon or Vacuum because the use of H_2 was complex and did not lead better results in density and hardness. These conditions were subsequently tested on the ZK30 alloy, and the results are presented in (Table.2.4).

Thèse accessible à l'adresse : https://theses.insa-lyon.fr/publication/2025ISAL0008/these.pdf © [J. Moreau], [2025], INSA Lyon, tous droits réservés

Sample	Temperature (°C)	Pressure (MPa)	Atmosphere	Hardness	Relative Density
ZK30	480	63	Vacuum	57 ± 2	0,98 ± 0,1
ZK30	500	63	Vacuum	56 ± 2	0,98 ± 0,1
ZK30	480	13	Vacuum	53 ± 2	0,96 ± 0,1
ZK30	500	13	Vacuum	56 ± 2	0,98 ± 0,1
ZK30	500	13	Argon	50 ± 2	0,97 ± 0,1
ZK30	500	63	Argon	56 ± 2	0,98 ± 0,1
ZK30	500	13	H2	44 ± 5	0,96 ± 0,1
ZK30	500	63	H2	55 ± 2	0,98 ± 0,1

Table 2.4: Density and hardness evolution depending on temperature, load and atmosphere used during the process

For the alloy, at low pressure, the density is higher than that of pure Mg averaging 96% and reaching up to 98% under vacuum. Similar to pure Mg, the atmosphere does not influence the density and hardness under high loading conditions. The improved density compared to pure Mg for similar conditions can be attributed to two factors :

- The particles of ZK30 are smaller than those of pure Mg. These smaller particles generate stronger driving forces due to their greater surface energy, promoting particle migration and increasing the contact area between particles.

- The change in chemical composition with the addition of Zn enhances the transfer of electrons between the contacting particles, and the ionization step which causes the spark plasma discharge [58]

The microstructures of the sintered samples under Argon were observed for the pure Mg at 500 °C and 13 MPa. The remaining porosity in the sample was measured at 3.7 % for 500 °C and 13 MPa and 1.6% for 500 °C and 63 MPa, according to an analysis of the polished sample using optical microscopy. This measurements are coherent with the previous density measurement using Archimede relation. The observation reveals unsintered powder grains at low pressure, which explains the resulting low density, as shown in Fig.2.4. The insufficient loading does not provide enough force to overcome the oxide layer.

The ZK30 alloy samples sintered by SPS under Argon at 500 °C were observed under two loading conditions, as shown in Fig.2.5.

Even at low pressure, no isolated powder grains were visible, indicating that sintering is easier for the alloy due the powder size and the chemical composition. Increasing the pressure closes the remaining pores, resulting in nearly fully dense samples, with only 0.01% porosity visible in the optical micrograph for 63 MPa and 0.5% remaining porosity at 13MPa, similar to the archimede density measurement.

Based on the initial observations, the sintering cycle at 500 °C and 63 MPa, whether under Argon or vacuum, results in almost fully dense sample up to 98 % and hardness up to 60.1 HV.

2.3.2 Influence of the oxide layer on the mechanical properties

The nearly fully dense ZK30 pellets sintered at 500 °C and 63 MPa, were subjected to tensile testing, but the initial results revealed a brittle behavior. This brittleness is unusual for Mg

Thèse accessible à l'adresse : https://theses.insa-lyon.fr/publication/2025ISAL0008/these.pdf © [J. Moreau], [2025], INSA Lyon, tous droits réservés

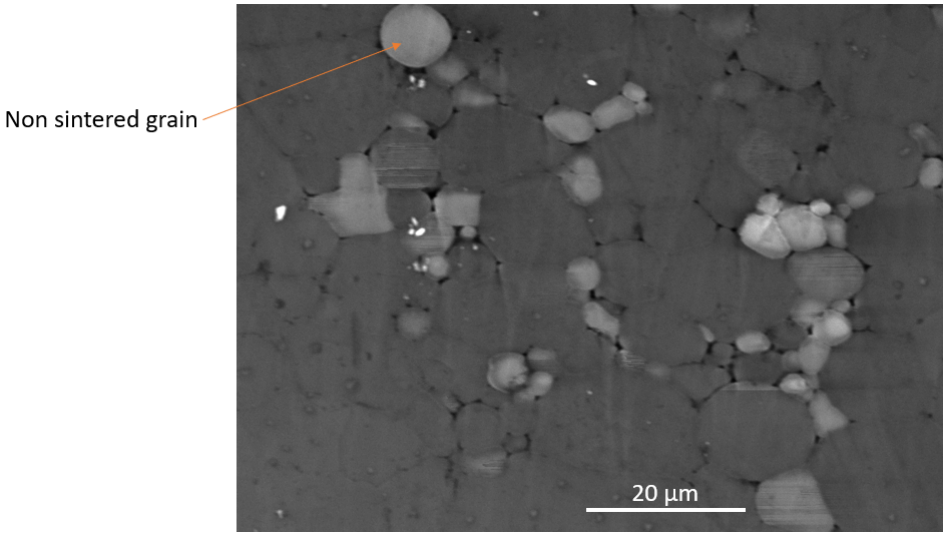


Figure 2.4: SEM observation in SE mode of pure Mg after a sintering at 500 °C and 13 MPa under Argon, showing the remaining porosity and the remaining non sintered powder particles.

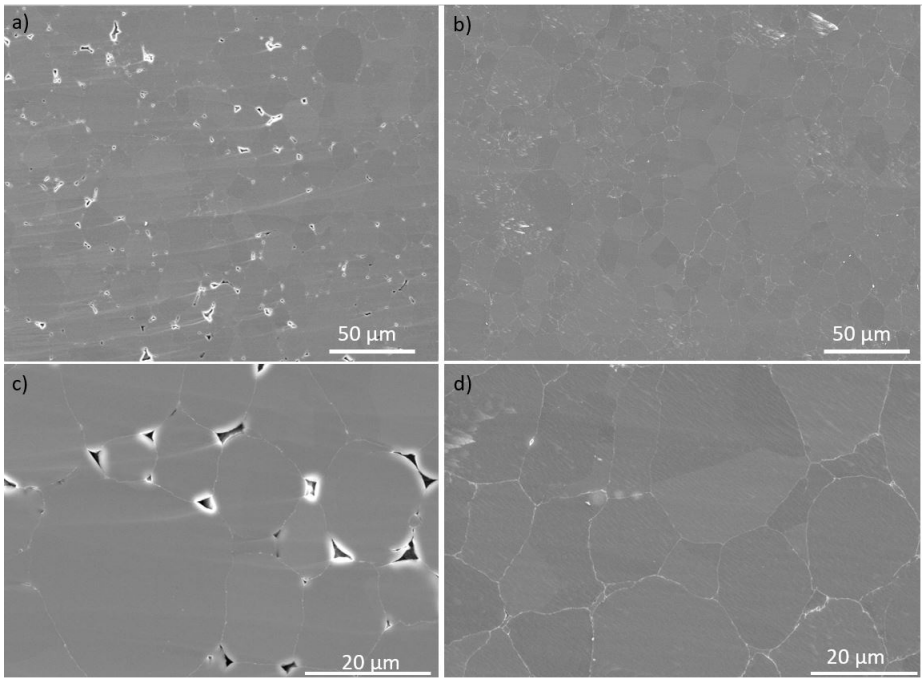


Figure 2.5: SEM observation in SE mode of ZK30 after a sintering at a)c) 500 °C and 13 MPa and b)d) 500 °C and 63 MPa under Argon, showing the closing of the pores due to the increased pressure.

alloys, which typically exhibit good ductility with elongation at fracture reaching up to 20%. However, the results obtained for the sintered ZK30 alloy contradict this, as it shows an elongation at fracture of only 0.03% as visible in Fig.2.6.a. Since the primary references for tensile

Thèse accessible à l'adresse : https://theses.insa-lyon.fr/publication/2025ISAL0008/these.pdf © [J. Moreau], [2025], INSA Lyon, tous droits réservés

testing of Mg alloys involve cast or extruded materials, this contrasting behavior could be attributed to the manufacturing technique. To explore this further, the surface fractures of the samples were examined, as illustrated in Fig.2.6.b.

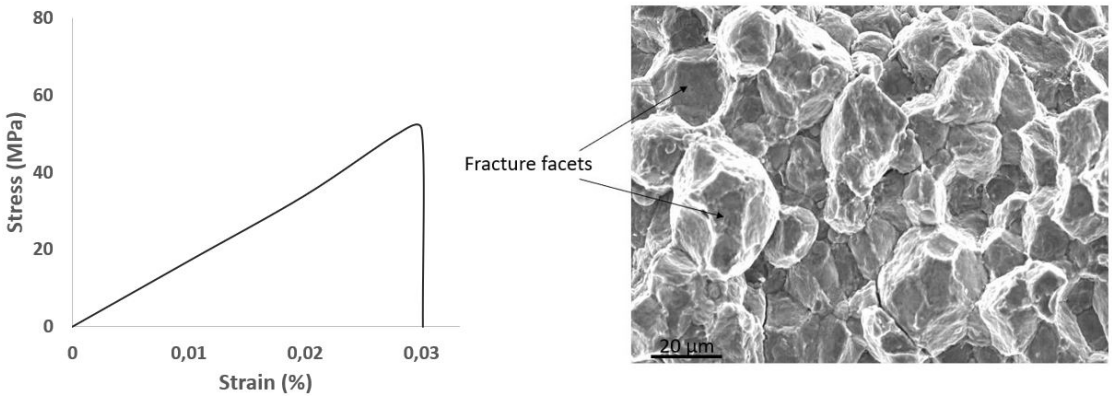


Figure 2.6: a) Tensile test of a sample of ZK30 alloy sintered at 500 °C and 63 MPa under Argon and b) Surface fracture of the same sample, showing the brittle behavior and intergranular fracture.

The observation of the fracture surface confirms the brittle behavior and reveals an intergranular fracture. Characterized by the absence of plastic deformation, brittle fractures caused by decohesion exhibit a flat appearance and lack any visible initiation zone or propagation direction. On a microscopic scale, these intergranular fractures expose juxtaposed polyhedra that correspond to the surfaces of the grains, defining the fracture facets, observed in Fig. 2.6.b.

As discussed and observed before in Section. 1.2.3.3, the native oxide layer surrounding the powder grains remain intact during the SPS process. This oxide layer is believed to be responsible for the grain decohesion, as it weakens the interfaces between the grains. Additionally, MgO typically exhibits brittle fracture behavior.

The EDX map shown in Fig. 2.7, reveals that the thin white layer visible in SEM images at the powder particles boundaries corresponds to the residual oxide layer. This layer has been shown to be highly detrimental to the mechanical properties [60], as some powder boundaries are weakened by the oxide film remaining on the powder surface, and then influenced fracture behavior. This could explain the brittle behavior observed in the manufactured ZK30 samples.

2.4 Thermodynamic-based ZK30 sintering cycle

To address the presence of the oxide layer, two potential solutions appeared promising. The first involves applying a higher pressure, up to 130 MPa, as demonstrated by Ma et al [60], where the mechanical pressure could break the surrounding oxide layer. The second approach involves taking advantage of the ZK30 ability to form a liquid phase. The presence of this liquid phase within the powder particles increases their volume, thereby exerting pressure on the oxide layer. This increase in internal pressure within the powder particles is believed to help break the oxide layer at powder boundaries. Since this study will focus on sintering Mg without applying pressure, and the SPS apparatus was not adapted to high pressure, it was decided instead to explore the effect of increasing the temperature. The increase of temperature is believed to be

Thèse accessible à l'adresse : https://theses.insa-lyon.fr/publication/2025ISAL0008/these.pdf © [J. Moreau], [2025], INSA Lyon, tous droits réservés

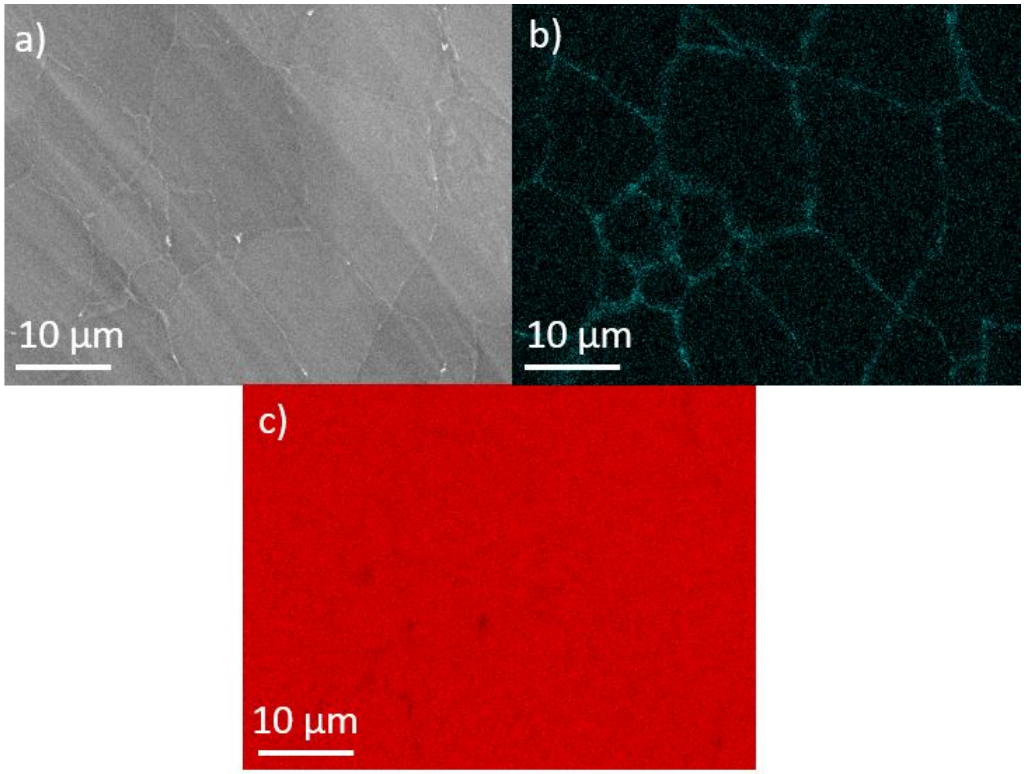


Figure 2.7: EDX maps of a ZK30 sample sintered at 500 °C and 63 MPa under Argon with a) SEM image in SE mode, b) Oxygen map and c) Mg map. The presence of oxygen surrounding the original powder grains is well visible.

able to disrupt the oxide layer, as visible in Fig.2.8.

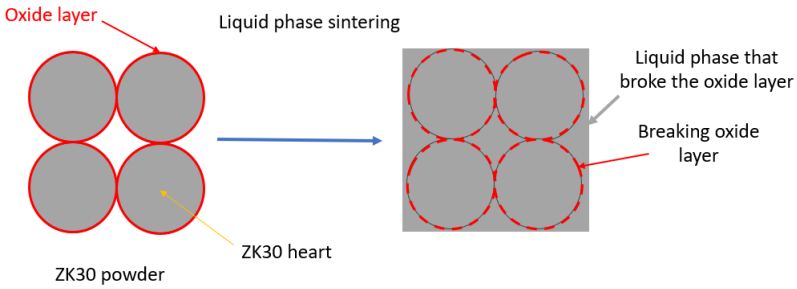


Figure 2.8: Schematic visualization of the mechanism of breaking the oxide layer during liquid phase sintering

2.4.1 Evaluation of the liquid phase

The ternary diagram of the Mg-Zn-Zr alloy is not well understood, so the first step was to accurately assess the presence of the liquid phase. To determine the liquid fraction during sintering, DSC analysis was performed on the raw powder. Given that Mg is highly reactive with platinum, which is part of the DSC apparatus, and to prevent evaporation, the powder

Thèse accessible à l'adresse : https://theses.insa-lyon.fr/publication/2025ISAL0008/these.pdf © [J. Moreau], [2025], INSA Lyon, tous droits réservés

was sealed in a tantalum crucible. The powder was loaded into the crucible under an argon atmosphere and sealed by welding, following a method similar to that used by [164]. An empty tantalum crucible filled with argon and sealed served as the reference. Three heating scans were conducted at 1, 5 and 10 °C/min up to 700 °C, the results are depicted in Fig.2.9.

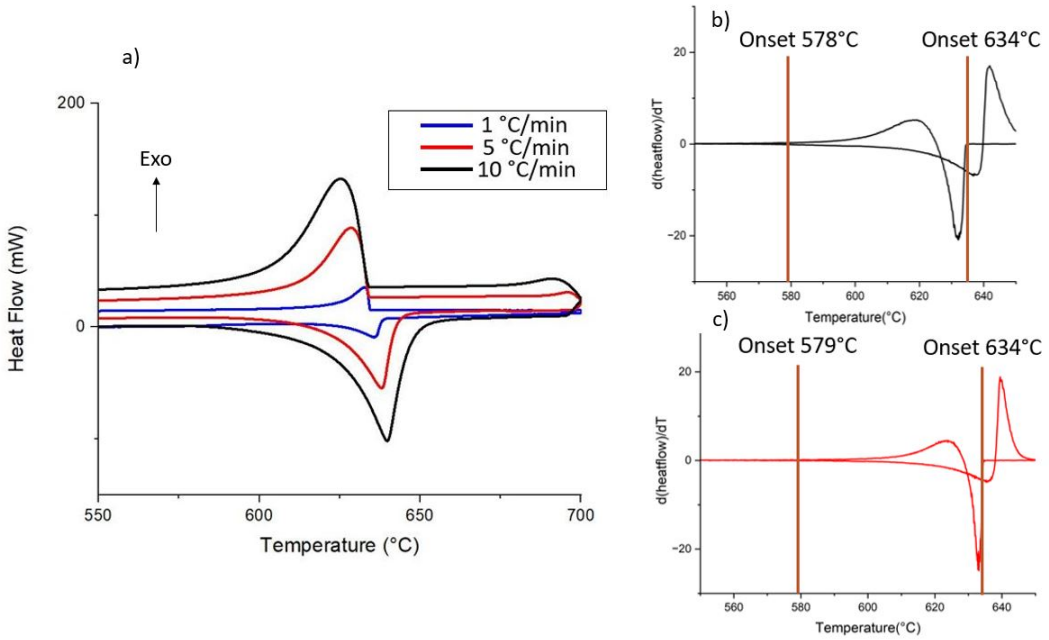


Figure 2.9: a)Results of the DSC under Argon with the a ramp of temperature at 1, 5 and 10 °C/min. b) Derivative of the heatflow indicating the solidus and liquidus of the alloy at 10 °C/min. c) Derivative of the heatflow indicating the solidus and liquidus of the alloy at 5 °C/min.

The results revealed a stable baseline, attributed to the use of a tantalum crucible, which did not react with the alloy. A solidus temperature of 578 °C and a liquidus temperature of 634 °C were determined using the onset during the heating for the solidus, and the top of the endothermic peak during the heating for the liquidus. The measures were taken from the derivative of the heatflow for more precision Fig.2.9.b.c. To evaluate these results a database from Arroyave *et al* [165] was used. Using this database the solidus is found at 556 °C and the liquidus at 632 °C. The liquidus value aligns with the one determined by DSC, but the solidus value is slightly lower. This discrepancy can be explained by the challenge of accurately determining the solidus point. Since the liquid fraction formed is minimal, the resulting signal is weak, making it difficult to precisely identify the onset. It can also come from the the rate used as it is not at equilibrium and it could shift the transformation towards higher temperature.

Furthermore, the signals from the 5 and 10 °C/min scans were integrated to evaluate the evolution of the liquid content with temperature. However, the signal from the 1 °C/min scan was too weak to perform proper integration. These results were compared to the liquid fraction calculated using the thermocalc database TTMg6 [166] and the database from Arroyave et al. [165] Fig. 2.10.

The DSC results appear to be in good agreement with the data from the databases, although

Thèse accessible à l'adresse : https://theses.insa-lyon.fr/publication/2025ISAL0008/these.pdf © [J. Moreau], [2025], INSA Lyon, tous droits réservés

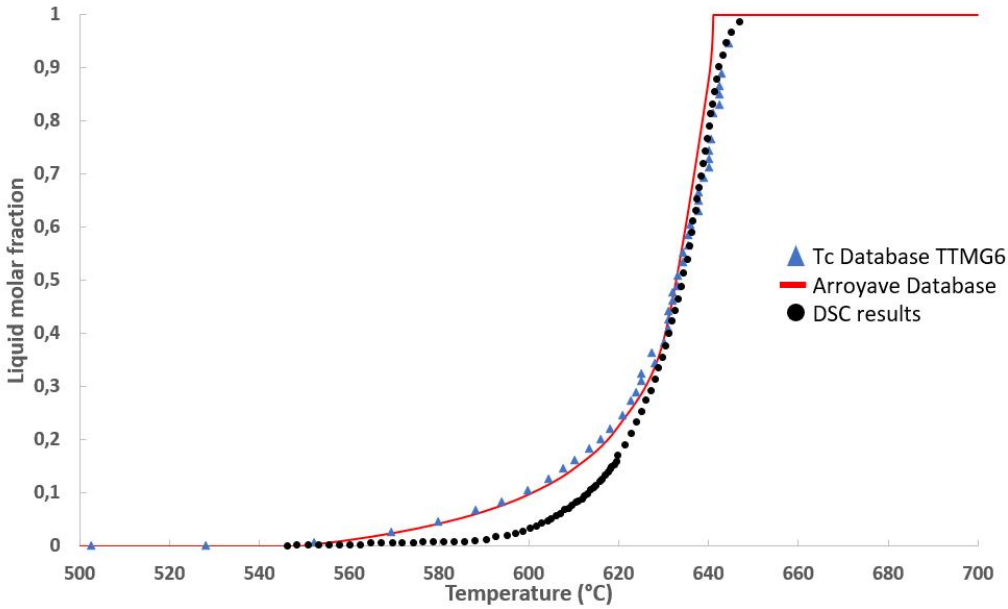


Figure 2.10: Comparison of the liquid fraction inside the alloy using Thermocalc database TTMg6 [166], database by Arroyave [165] and the DSC results obtained to determine the correct sintering temperature

there is a slight shift at the beginning, likely due to the heating rate's influence on the fraction of liquid formed.

2.4.2 Development of the SPS cycle

As previously mentioned, due to the increase of liquid content in the alloy and the resulting expansion of the material's volume, working with high pressure in the SPS using graphite die is challenging and led to frequent breakage of the dies. Consequently, the increase of temperature was performed at 13 MPa continuously for all cycles. The process started at 550 °C and was gradually increased until the liquid content became too high, causing the liquid phase to flow along the pistons, as visible in Fig.2.11.

The maximum temperature reached during sintering was 590 °C, corresponding to a liquid fraction of 9% using the Arroyave database and 1% based on the DSC calculations. However, the liquid fraction is probably higer than 1% because of the holding step during the sintering cycle. The density and hardness of the manufactured disk were measured, with the results shown in Table. 2.5. The liquid fraction indicated is calculated with the Arroyave database.

As observed in the table, the density increases above 500 °C and then reaches a plateau at 550 °C and above. However, the hardness seems to decreases with for the temperature of 590 °C. This decrease in hardness could be attributed to several factors. One possibility is a decrease in oxygen content, as the MgO phase is significantly harder than the Mg phase. A decrease in oxygen would lead to a lower MgO content and, consequently, maybe to a lower hardness. The oxygen content of the samples was measured by IGA, and plotted with the hardness and density in function of the temperature.

Thèse accessible à l'adresse : https://theses.insa-lyon.fr/publication/2025ISAL0008/these.pdf © [J. Moreau], [2025], INSA Lyon, tous droits réservés



Figure 2.11: Flowing of the liquid phase along the pistons due to the pressure and apparition of the liquid phase at 590 °C

Material	Temperature (°C)	Liquid fraction (%vol)	Pressure (MPa)	Atmosphere	Hardness (HV)	Relative density
ZK30	500	0	13	Argon	50 ± 2	0,97 ± 0,2
ZK30	550	0	13	Argon	57.0 ± 2	0,99 ± 0,1
ZK30	560	1,5	13	Argon	54.0 ± 3	0,99 ± 0,1
ZK30	570	4	13	Argon	54.0 ± 4	0,99 ± 0,1
ZK30	580	6,3	13	Argon	53 ± 4	0,99 ± 0,1
ZK30	590	9	13	Argon	50 ± 4	0,99 ± 0,1

Table 2.5: Hardness and equivalent density obtained for ZK30 alloy after increasing the sintering temperatures.

The difference in oxygen content however is not really significant, and does not fully explain the observed difference in hardness. It is possible that the increase in temperature and the presence of the liquid phase during sintering caused some MgO to be expelled, which might account for the slight decrease in oxygen content. The variation in hardness is likely more related to changes in microstructure, which will be examined in more detail later.

The samples were also observed in SEM and the resulting EDX maps are shown in Fig. 2.13.

As visible on the images, the oxygen layer at 550 °C Fig. 2.13.a is continuous along the powder particles boundaries. Conversely, at 580 °C Fig. 2.13.b the oxide layer appears more discontinuous, as if it has fractured in some areas. The increase of sintering temperature likely facilitated the breakdown of the oxide film along the powder boundaries, increasing the fraction of metal-to-metal bonding.

2.4.3 Thermodynamics of ZK30

The resulting mechanical properties of the sintered pellets were observed, but first, the thermodynamics of the alloys was studied. Hadadzaheh *et al* [161] studied the ZK60 alloy and proposed a Vertical section from Mg-0.6wt%Zr to pure Zn for ZK alloys (Fig. 2.14.a). According to the proposed vertical section, with the ZK30 alloy at 3%wt Zn, a domain where the $\alpha - Mg$ exists alone may be present. However, using the database from Arroyave *et al* [165] previously used to calculate the liquid phase content, the domain shifts to $\alpha - \mathrm{Mg} + \mathrm{Zn_2Zr}$ (Fig.2.14.b),

Thèse accessible à l'adresse : https://theses.insa-lyon.fr/publication/2025ISAL0008/these.pdf © [J. Moreau], [2025], INSA Lyon, tous droits réservés

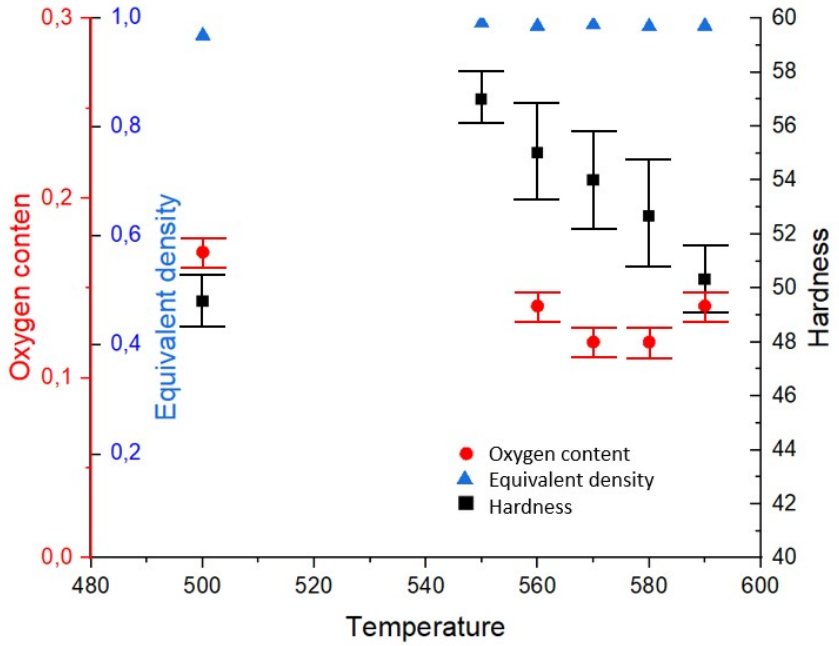


Figure 2.12: Plot of the Oxygen concentration (red circle), relative density (blue triangle) and hardness (black square) as a function of the sintering temperature, showing the decrease of the hardness with the sintering temperature.

despite the maximum solubility of Zr in Mg being 0.6 %wt [42]. All previously selected sintering temperatures fall within the same range, so the microstructure is expected to remain relatively constant due to the rapid sintering cycles, even if the apparition of the liquid phase migh modify the homogeneity.

During the SPS process the position of the piston is recorded over time, providing insights into the dimensional variation of the porous sample during sintering. The displacement of the piston was plotted against temperature and time for multiple samples, as shown in Fig.2.15.

The densification process begins at around 200 °C and continues as the temperatures rises. At approximately 580 °C, the movement of the piston suggests the formation of a liquid phase. Indeed, the displacement of the piston becomes significantly more pronounced at 580 °C and above, indication that the liquid may wet the powder particles and enhance densification and contact between them. Additionally, it is possible that a small fraction of the liquid phase flows through the space between the die and the piston. On Fig.2.15.c, the influence of pressure is visible. At high pressure the compaction takes place at the start of the cycle. The piston stops moving earlier than at low pressure meaning the maximum density is reached sooner. As the contact between the particles is more important the sintering happens faster. However, the compacted particles conserved the surrounding oxygen because the pressure is still too low.

Thèse accessible à l'adresse : https://theses.insa-lyon.fr/publication/2025ISAL0008/these.pdf © [J. Moreau], [2025], INSA Lyon, tous droits réservés

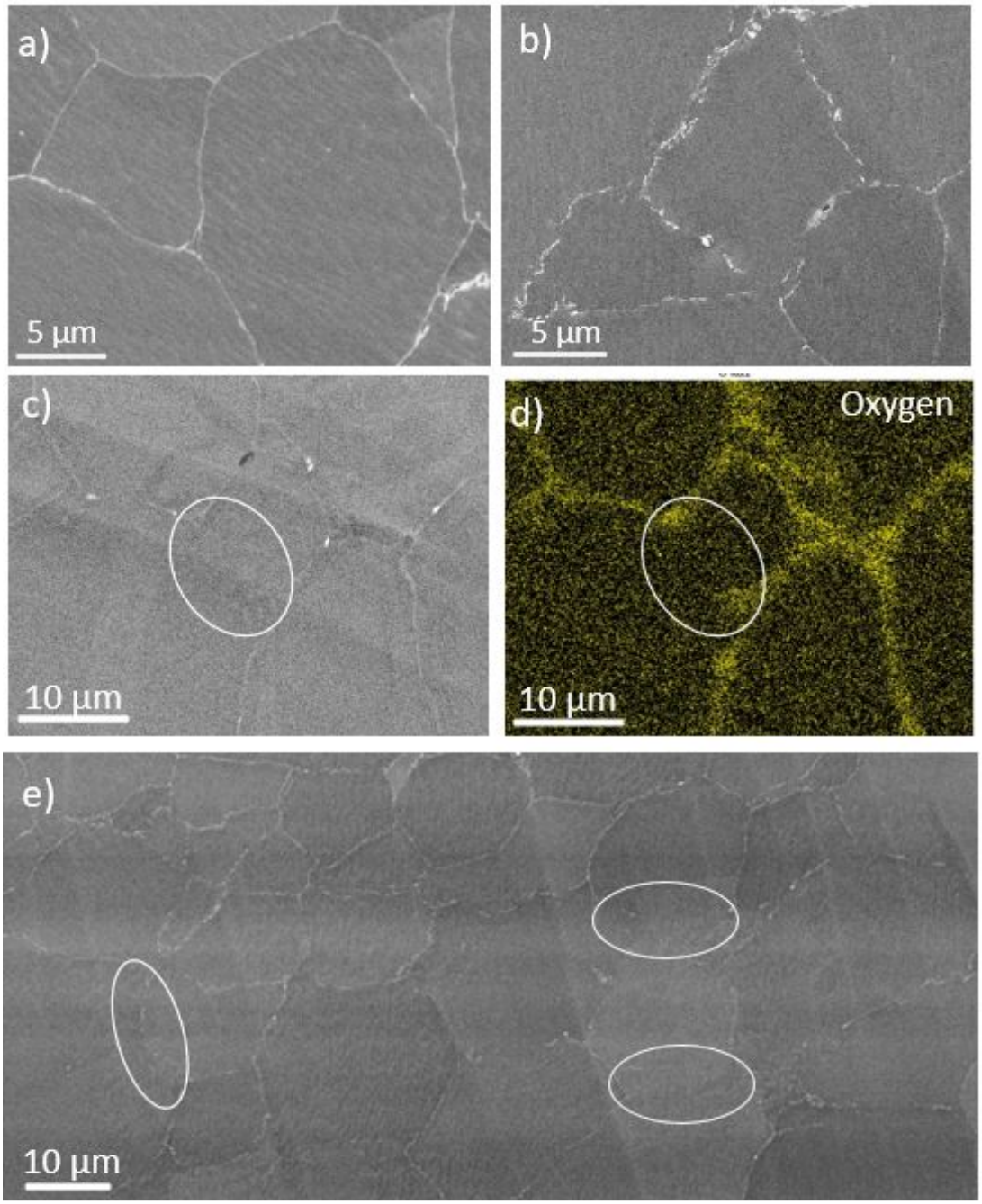


Figure 2.13: SEM images of the evolution of the oxide layer (white) depending on the sintering temperatures. With sinterings at a) 500 °C observed in SE mode and 580 °C with b)c) in SE mode showing the discontinuity in the oxide layer, d) the corresponding EDX map of oxygen, e) another image in SE mode of the same sample with white circles where the oxide layer looks to be more discontinuous

Thèse accessible à l'adresse : https://theses.insa-lyon.fr/publication/2025ISAL0008/these.pdf © [J. Moreau], [2025], INSA Lyon, tous droits réservés

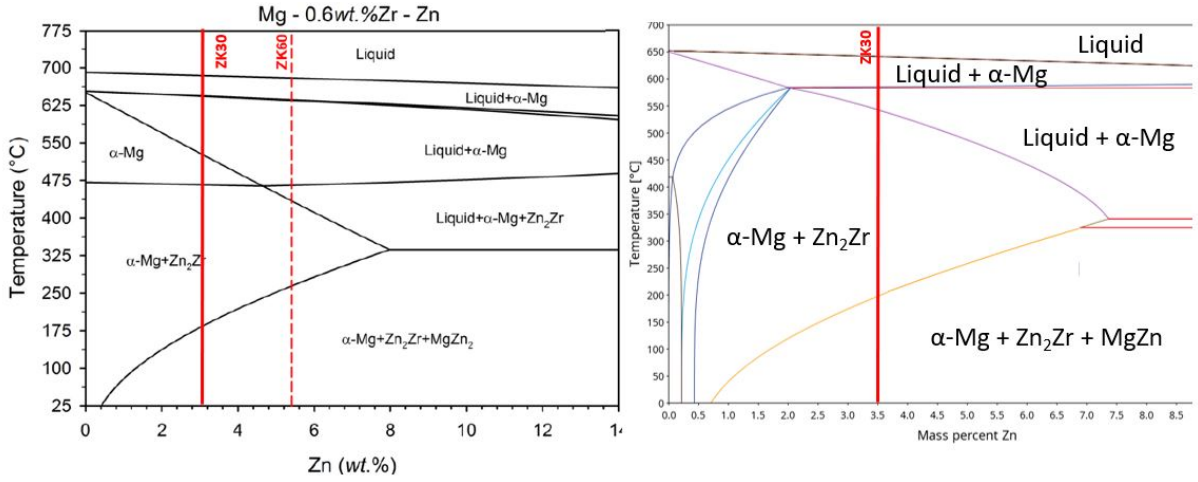


Figure 2.14: a) Comparison of the Vertical section from Mg-0.6wt%Zr to pure Zn determined by Hadadzaheh *et al* [161] and b) determined by the Arroyave database *et al* [165], exhibiting a different domain for the ZK30 alloy at 500 °C.

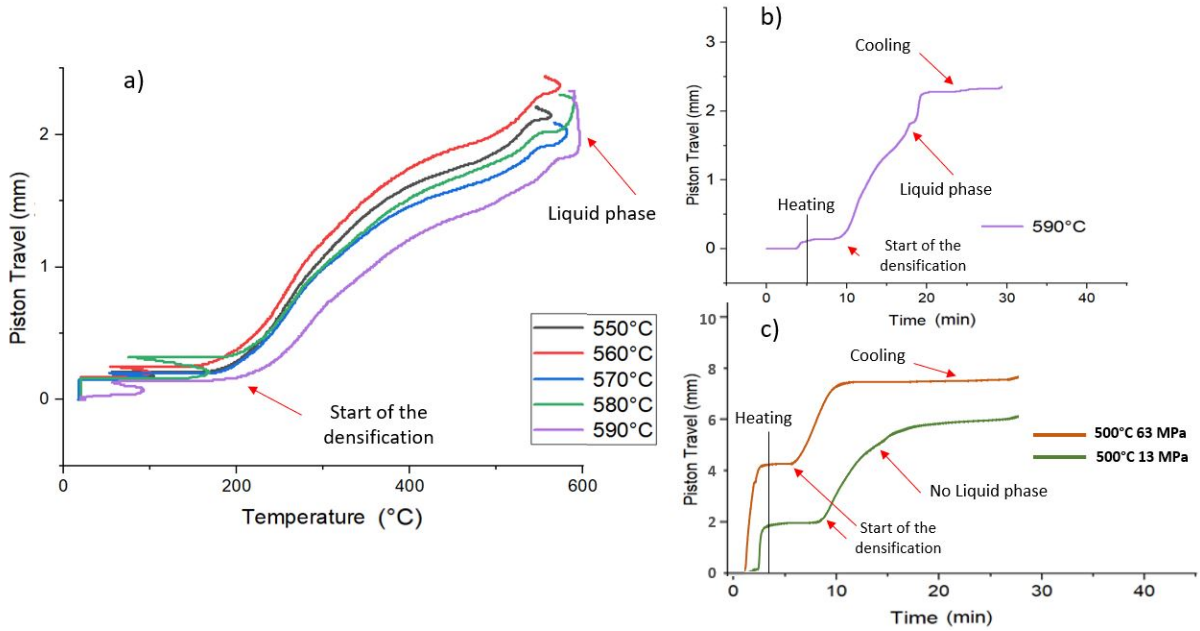


Figure 2.15: Displacement of the piston measured during the SPS process a) Influence of the temperature on the displacement b) Sintering steps visible in the plot of displacement vs time c) Influence of the pressure on the densification during the process.

2.5 Mechanical properties at higher sintering temperatures

Tensile tests from the literature show significant elongation at rupture, making Mg alloys promising for orthopedic implant applications. However, these alloys are predominantly produced through casting or extrusion. As observed before, in our case, using powder metallurgy and

Thèse accessible à l'adresse : https://theses.insa-lyon.fr/publication/2025ISAL0008/these.pdf © [J. Moreau], [2025], INSA Lyon, tous droits réservés

SPS, the specimens exhibited brittle behavior. Three-point bending tests were performed on the samples after modification of the sintering cycle. According to the isopleth diagram previously calculated, forming a liquid phase requires reaching 580 °C or higher, above the solidus temperature. Several ZK30 samples were prepared at different temperatures, ranging from 550 °C to 590 °C in the SPS process. These samples (two for each temperature) underwent three-point bending tests, and the results of these tests are illustrated in Fig.2.16.a. The cross-sectional area of each sample was measured using a caliper to enable the calculation of the quadratic moment corresponding to each sample. Calculations were performed at the point of rupture, considering the quadratic moment of the fracture surface. It was then possible to plot stress-train curves for each sample considering the following relations:

$$\sigma = \frac{FL}{4I} y \tag{2.2}$$

And

$$\epsilon = \frac{6Dy}{L^2} \tag{2.3}$$

With F the force applied on the sample, L the distance between support points, I the quadratic moment, y the distance to the neutral axis and D the deflection.

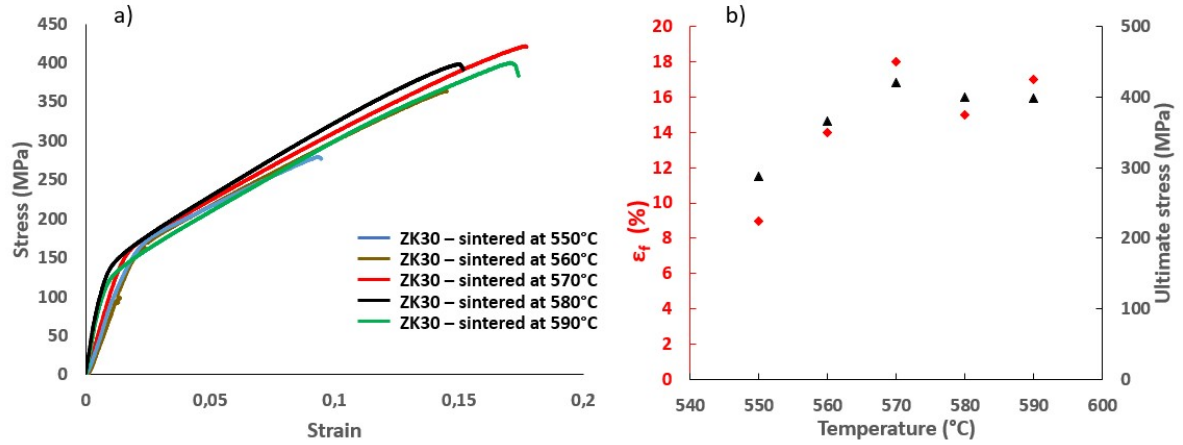


Figure 2.16: a) Stress-strain curves obtained in the three points bending test for the different sintering temperatures with b) their associated ultimate stress and elongation at break

At first, the increase of the sintering temperature increases drastically the ultimate stress and elongation at break compared to low temperatures. Then at 570 °C a maximum seems to be reached as the measurements remain stable as visible in Fig.2.16.b. These temperatures where the maximum is reached correspond to the temperature where a liquid phase is formed. Indeed, even at 570 °C which is lower than the supposed temperature of the solidus, drops of liquid can be observed on the matrix during the sintering. This liquid phase appears to break the oxide layer and improve the ductility of the material. SEM images of samples sintered at 570°C and 590°C show that at different locations, an oxide layer that seems to be porous and not continuous, as observed previously Fig.2.13.

Thèse accessible à l'adresse : https://theses.insa-lyon.fr/publication/2025ISAL0008/these.pdf © [J. Moreau], [2025], INSA Lyon, tous droits réservés

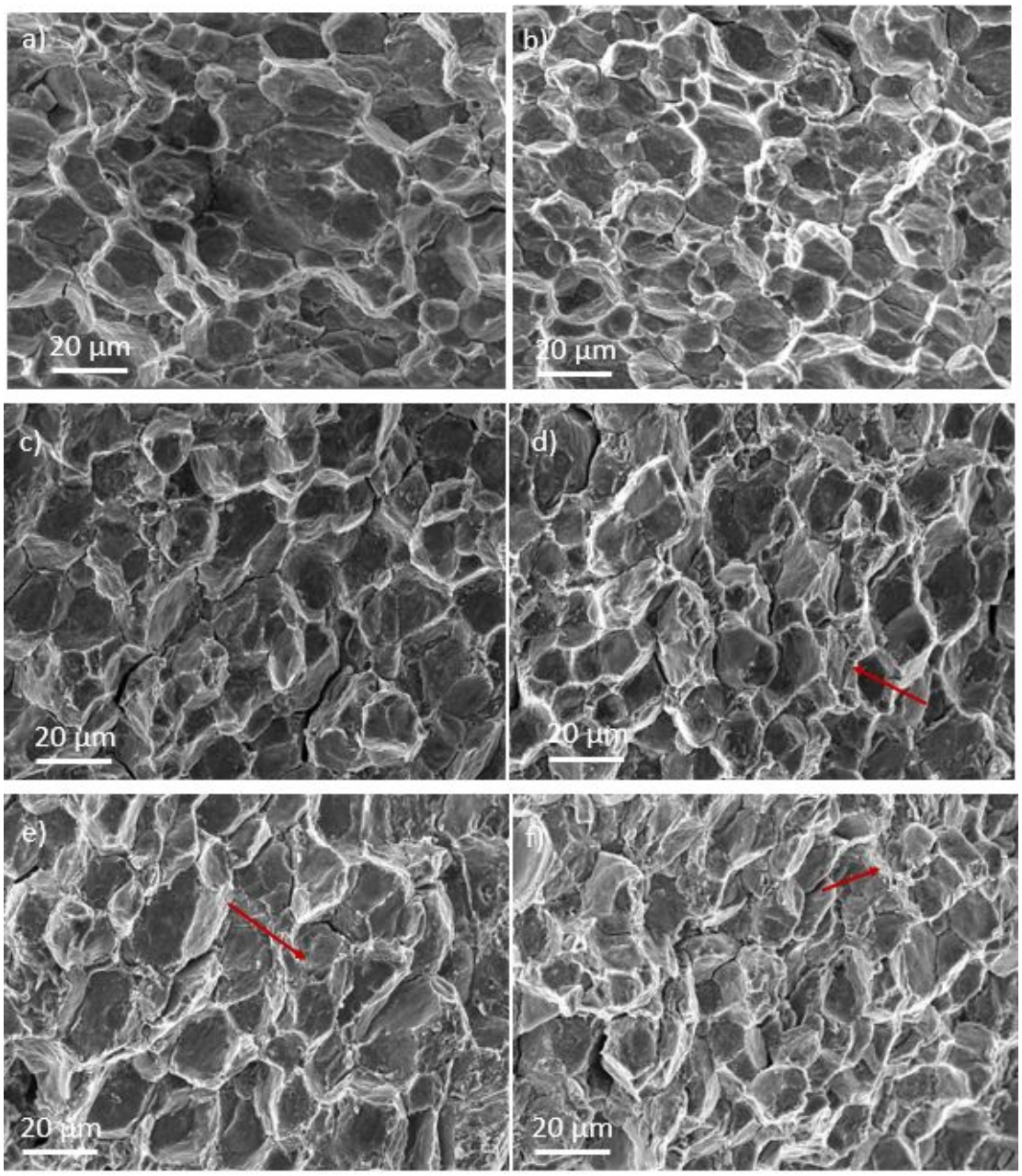


Figure 2.17: SEM image of the surface fracture of the sample sintered at a-b) 550 °C, c-d) 580 °C and e-f)590 °C after three point bending test. The images a)c)e) correspond to the side in compression and b)d)f) to the tensile side. The fracture remains mainly intergranular but with the increase in temperature some dimples (red arrows) may have appeared.

Furthermore, the fracture surface of the samples were observed and are visible in Fig.2.17.

The surface of the sample sintered at 500 °C exhibited a brittle behavior without any area of ductility observed. However, the sample sintered at 580 °C and 590 °C exhibit areas with a brittle behavior with an intergranular fracture but may also exhibit areas with a ductile behavior

Thèse accessible à l'adresse : https://theses.insa-lyon.fr/publication/2025ISAL0008/these.pdf © [J. Moreau], [2025], INSA Lyon, tous droits réservés

with the presence of dimples. However, it is difficult to conclude with the surface fracture as the ductile areas are rare and hard to observe. This may correspond to the improvement of the elongation observed before with the temperature and this areas more likely correspond to zones where the oxygen layer was disrupted.

The mechanical properties were improved through the increase in temperature in the next section the microstructure of the manufactured part will be observed to determine the structural state of the material after SPS.

2.6 Observation of the microstructure

Given the previous images, the microstructure appears homogeneous and primarily consists of the $\alpha - Mg$ phase. The microstructure is visible in the BSE image shown in Fig. 2.18.

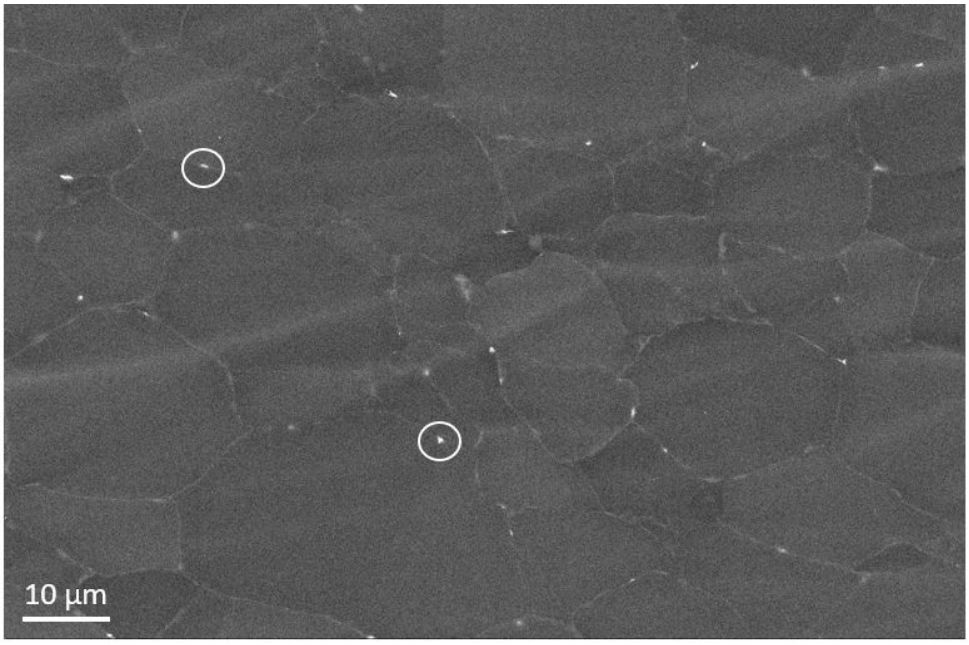


Figure 2.18: BSE image of the sintered ZK30 using SPS at 500 °C with the observation of small particles at powder particles boundaries

Small white particles can be seen at the powder particles boundaries, though they are too small to be identified with SEM and are likely intermetallics of MgZn. However, their fraction is under 0,5%, indicating that the primary phase composing the structure is $\alpha - Mg$.

The grain were analyzed using EBSD analysis, with the results shown in Fig.2.19.

The grains observed probably correspond to the original powder particles. The mean grain size is dependent on the SPS parameters, measured at 15.4 μm for 500 °C and 13 MPa, 6.7 μm for 500 °C and 63 MPa and 12.5 μm for 580 °C and 13 MPa. While increasing the temperature typically leads to larger grains, the short sintering time in this process limits significant grain growth. The presence of numerous oxides may also induce Zener pinning at grain boundaries, explaining the stable grain size with temperature.

As shown in Fig.2.20, the samples sintered at high temperature (580 °C) or high pressure

Thèse accessible à l'adresse : https://theses.insa-lyon.fr/publication/2025ISAL0008/these.pdf © [J. Moreau], [2025], INSA Lyon, tous droits réservés

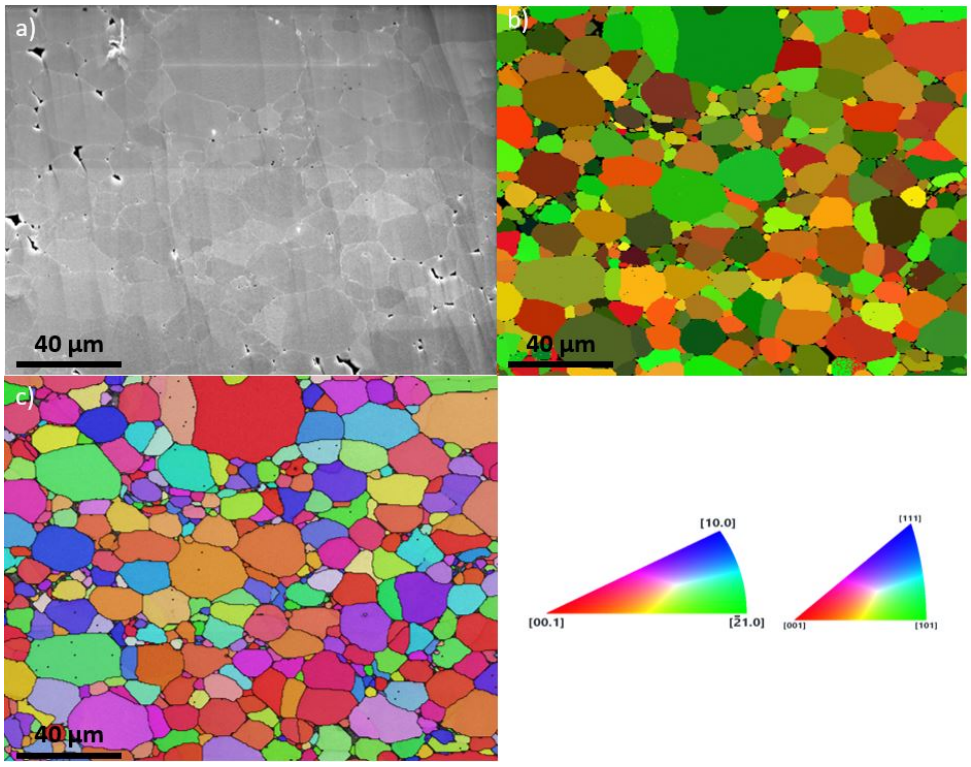


Figure 2.19: a) SEM image of the sintered ZK30 at 500 °C and 63 MPa alloy and EBSD maps corresponding to the area with b) all euler map and c) IPFZ map

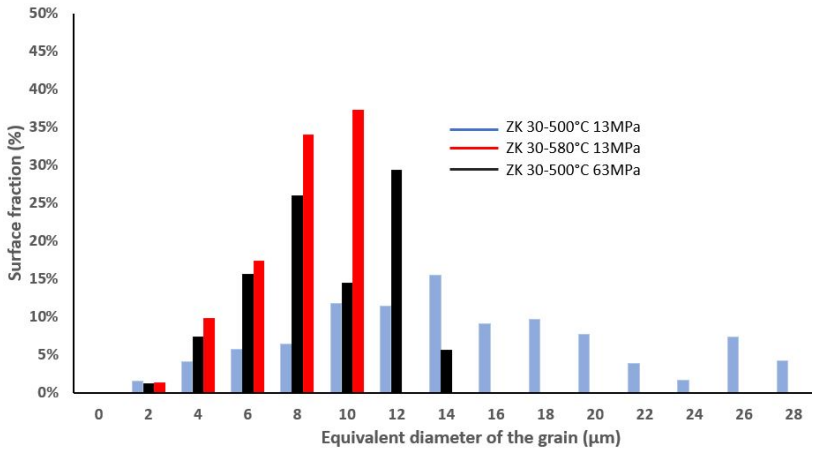


Figure 2.20: Evolution of the surface fraction of the grain with the corresponding equivalent diameter, with a bin size of 2 μm, depending on the sintering conditions

(63 MPa) exhibit a lower grain size and a distribution concentrated around 10 μm. It is likely resulting from the nucleation of new grains within the existing powder particles.The increased pressure during sintering also contributes to more plastic deformation, leading to enhanced dynamic recrystallization The low pressure and temperature of the other sample lead to a larger

Thèse accessible à l'adresse : https://theses.insa-lyon.fr/publication/2025ISAL0008/these.pdf © [J. Moreau], [2025], INSA Lyon, tous droits réservés

grain size and a broader distribution, as new grain didn't appear.

Another factor that can influence grain size is the dissolution of precipitates at higher temperatures, which reduces their Zener pinning effect and allows for greater grain growth. Additionally, part density should be carefully considered when fabricating Mg materials through SPS. Although hardness might be higher at lower temperatures, achieving high part density can have important effects on mechanical and corrosion performance. Therefore, achieving a balance between hardness and density is crucial during the fabrication of Mg materials using SPS.

2.7 Conclusion

To conclude this chapter, the study on the development of the ZK30 alloy through SPS has identified critical parameters that influence the density and hardness of the resulting samples. The analysis of the sintering cycles revealed that temperatures above 500 °C combined with high loadings (63 MPa), under vacuum or argon atmosphere produce nearly fully dense samples with hardness values close to reference standards. However, the microstructural observations highlighted the presence of a residual oxide layer at the grain boundaries, which is responsible for a brittle behavior that deviates from typical Mg alloys characteristics. By using a higher temperature, initial observations suggested that the oxide layer has weakened. The microstructure of the samples mainly consists of the α-Mg phase but some intermetallics have been observed at grain boundaries. The mechanical properties were greatly improved with increasing sintering temperatures and liquid phase fraction. The mechanical properties reached by the ZK30 alloy with SPS are promising and are similar to the one manufactured by casting.

The modification of the microstucture with thermal treatments can also enhance the mechanical properties post SPS process. This microstructural modification also impact the corrosion properties. Thus, it is necessary to control the microstructure to obtain the better compromise between mechanical and corrosion properties of the alloy. Therefore, in the next chapter, the study of the precipitation in the ZK30 alloy and their influence on the corrosion properties will be studied.

Thèse accessible à l'adresse : https://theses.insa-lyon.fr/publication/2025ISAL0008/these.pdf © [J. Moreau], [2025], INSA Lyon, tous droits réservés

Thèse accessible à l'adresse : https://theses.insa-lyon.fr/publication/2025ISAL0008/these.pdf © [J. Moreau], [2025], INSA Lyon, tous droits réservés

Chapter 3

Study of the precipitation in ZK30 alloy to improve the corrosion resistance

Contents

3.1 Material and methods 62
3.1.1 Manufacturing of the dense parts 62
3.1.2 Solution treatment 62
3.1.3 Isothermal aging 62
3.1.4 Thermoelectric power (TEP) measurements 62
3.1.5 X-ray diffraction 63
3.1.6 Corrosion measurements 63
3.1.7 Electrochemical measurements 63
3.2 Precipitation in ZK30 alloy 64
3.2.1 Solution treatment 64
3.2.2 Hardness and TEP measurements 65
3.2.3 Precipitation kinetics in ZK30 alloy using TEP 65
3.3 Mass loss measurement of heat treated ZK30 alloy 72
3.3.1 Mass loss test of pure Magnesium and ZK30 72
3.3.2 Influence of the precipitation state on the mass loss in different media . . . 76
3.4 Corrosion resistance after optimized sintering 78
3.4.1 Mass loss test in saline solution 78
3.4.2 Electrochemical measurement at initial state 79
3.4.3 Electrochemical measurement during immersion and influence of the aging . 84
3.5 Conclusion 87

The optimized sintering parameters were defined in the previous chapter, and the next step is to assess the corrosion properties of the alloy. The primary challenge for Mg alloys in orthopedic implant applications is their high corrosion rate. Therefore, this chapter will focus on trying to improve the corrosion resistance of the ZK30 alloy. After SPS sintering, the grain size is

Thèse accessible à l'adresse : https://theses.insa-lyon.fr/publication/2025ISAL0008/these.pdf © [J. Moreau], [2025], INSA Lyon, tous droits réservés

established, and it becomes possible to adjust the microstructure through thermal treatments to enhance corrosion resistance. This chapter will focus on identifying the precipitate sequence of the ZK30 alloy and analyzing their influence on the corrosion rate.

3.1 Material and methods

3.1.1 Manufacturing of the dense parts

The sample used in this study were manufactured by SPS as described in the previous chapter. The sintering temperature for the precipitation study was 580 °C and various sintering temperatures were used in the corrosion properties section and will be indicated when needed.

3.1.2 Solution treatment

The solution treatment was performed in vacuum sealed quartz tube. The samples were wrapped in a graphite sheet to prevent any reaction between the quartz and the Mg. They were then introduced in a semi-closed quartz tube, connected to a primary vacuum pump. Once the vacuum level reached 5×10^{-2} mbar, the tube was sealed using a blowtorch.

3.1.3 Isothermal aging

Isothermal aging was then performed at 150 °C and 200 °C using a silicon oil bath; all samples were quenched in water at ambient temperature after aging. The temperatures were chosen from two different domains in the isopleth previously calculated in Fig.2.14.

3.1.4 Thermoelectric power (TEP) measurements

Samples from all groups, both before and during the aging process were prepared for thermoelectric power (TEP) measurement with a gauge size of 75 mm × 5 mm × 1.5 mm. TEP measures the voltage (ΔV) generated by the Seebeck effect between two junctions of the studied material which are attached to a reference pure metal (here, pure Cu was used) [167], the setup is illustrated in Fig.3.1.

During the measurements a temperature gradient *(ΔT)* is established at the junctions. In the current study, the temperature of the blocks used were set to T and T+ΔT with $T = 15$ °C and $\Delta T = 10$ °C.

The relative TEP is defined as:

$$S = S^* - S^*_{\mathrm{Cu}} = \Delta V / \Delta T \tag{3.1}$$

Where S^* is the absolute TEP of the studied alloy and S^*_{Cu} is the TEP of pure Cu. The absolute TEP S^* of a Mg alloy is affected by the different structural defects present in the Mg matrix and can be expressed as :

$$S^* = S^*_{\mathrm{Mg}} + \Delta S_{SS} + \Delta S_d + \Delta S_{pp} \tag{3.2}$$

Where S^*_{Mg} is the TEP of pure Mg without defects. $\Delta S_{SS}, \Delta S_d, \Delta S_{pp}$ are TEP values induced by solid solution (ss), dislocations (d) and precipitates (pp), respectively.

Thèse accessible à l'adresse : https://theses.insa-lyon.fr/publication/2025ISAL0008/these.pdf © [J. Moreau], [2025], INSA Lyon, tous droits réservés

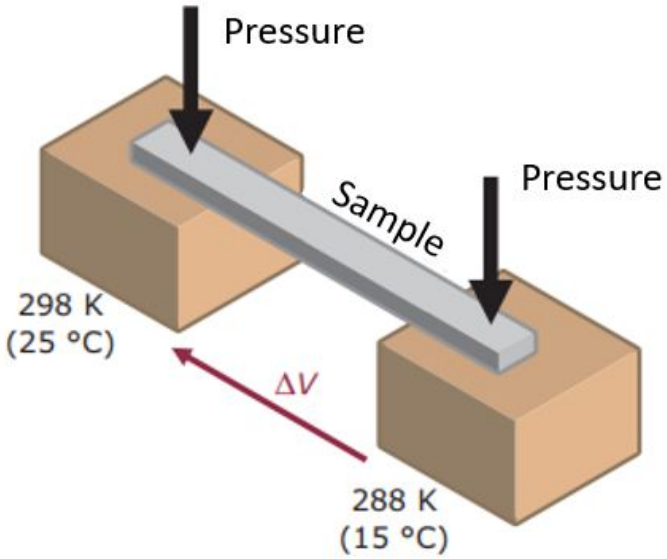


Figure 3.1: TEP setup used for the measurements [168]

3.1.5 X-ray diffraction

X-ray diffraction (XRD) analyses were conducted using an AXS Bruker D8 Advance diffractometer with Cu $k\alpha$ radiation (λ=0.154 06 nm) in Bragg–Brentano geometry. Locked coupled scans with 2θ from 20 deg to 80 deg, with each measurement lasting 28 min.

3.1.6 Corrosion measurements

3.1.6.1 Mass loss test

Aerated saline solution (0.9 % NaCl, pH: 7.4 (ISO 10271 [169]) was used as the electrolyte at 37 °C, NaOH was added to reach a pH close to 7. The electrolyte was prepared from NaCl (Carlo Erba Reagents, Val de Reuil, France) and deionized water (resistivity 18 MΩ cm). At each measurement time, the samples were dried and weighted.

3.1.7 Electrochemical measurements

The corrosion behavior of the ZK30 alloy was investigated through a sequence of electrochemical measurements. Electrochemical measurements were performed in a standard three-electrode cell using a potentiostat (Reference 600+, Gamry Instruments; Warminster, USA) with a graphite rod as the counter electrode and a Ag/AgCl reference electrode (RedRod, Radiometer Analytical-Hach; Loveland, Colorado, USA) (E = 0.209 V $vs.$ Standard Hydrogen Electrode (SHE)). The working electrode was the studied material. Before the electrochemical measurements, the disc surface was ground down to (8 μm) using abrasive papers. Aerated saline solution (0.9 % NaCl, pH: 7.4 (ISO 10271) was used as the electrolyte at 37 °C. In this setup the surface exposed is a disk with a diameter of 1 cm.

For smaller samples, another setup was tested and is very similar to the one used before but the samples were fixed on a small support with a surface exposed of a disk with a diameter of

Thèse accessible à l'adresse : https://theses.insa-lyon.fr/publication/2025ISAL0008/these.pdf © [J. Moreau], [2025], INSA Lyon, tous droits réservés

6 mm. The difference between the setups are shown in Fig.3.2.

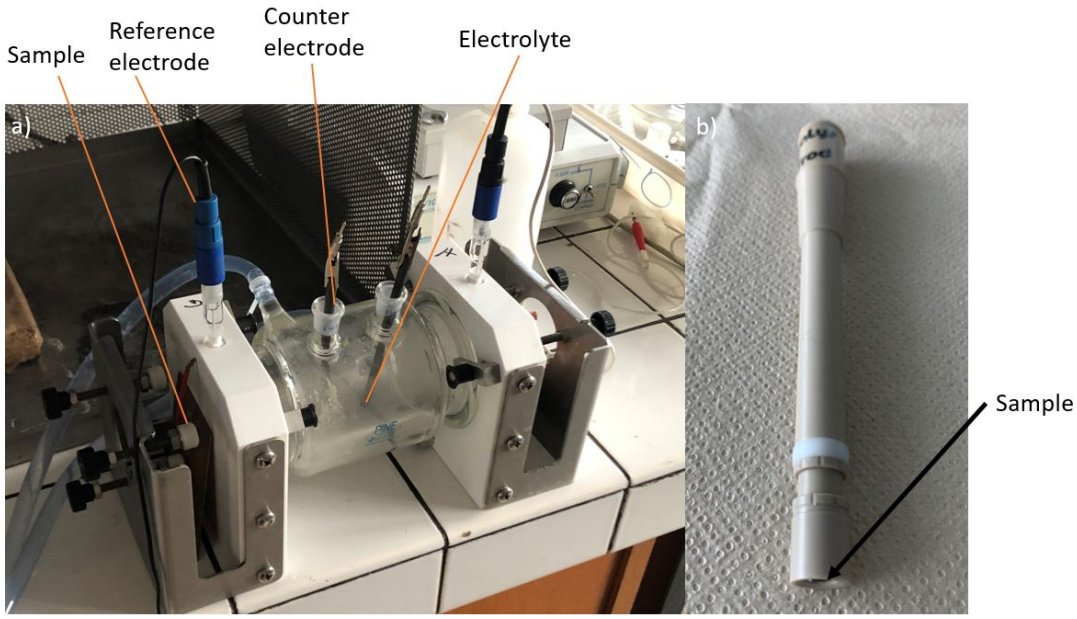


Figure 3.2: Corrosion setup with the three-electrode cell and the different sample holder. a) The sample is held by a copper plate and is in contact with the electrolyte and b) the sample is inserted into the holder, the holder is plugged to the potentiostat and is immersed into the electrolyte.

The sequence for the electrochemical measurements is the following :

- Firstly, the samples were let 2 h at open circuit potential (OCP) to reach equilibrium.
- Then Electrochemical impedance spectroscopy (EIS) measurements were conducted at OCP with an amplitude 0.03 V in the frequency range of 100 kHz to 5 mHz with 9 points per decade.
- Finally, Polarization curves were recorded at a scan rate of 10 mV/s from −2.5 V to +2.5 V *vs.* Ag/AgCl.

3.2 Precipitation in ZK30 alloy

3.2.1 Solution treatment

The temperature reached by SPS is localized in the α-Mg + Zn_2Zr zone (Fig.2.14). To ensure better homogenization and to prevent any contribution of microstructure parameters inherited from the SPS process, a homogenization treatment was carried out on the samples. Two different temperatures,were studied : 340 °C and 500 °C. The 340 °C treatment corresponds to the usual temperature to homogenize the MgZn alloys and to the α-Mg domain in the first isopleth in Fig.2.14.a. The 500 °C treatment corresponds to the α-Mg domain in the newly calculated isopleth in Fig.2.14. Both treatments were conducted for 24 h. A treatment at 340 °C and 24 h was already used for Mg-3Zn [79], but the addition of Zr could lead to the formation of unwanted intermetallics. The two temperatures were tested and the resulting microstructures

Thèse accessible à l'adresse : https://theses.insa-lyon.fr/publication/2025ISAL0008/these.pdf © [J. Moreau], [2025], INSA Lyon, tous droits réservés

were observed, as shown in Fig.3.3.

Several areas displayed intermetallic phases of MgZn and ZnZr, indicating that the temperature was not appropriate for the homogenization treatment. Conversely, the treatment at 500 °C did not show any intermetallics, as observed in Fig.3.4. This was expected given the isopleth calculated with the data from Arroyave *et al* [165].

3.2.2 Hardness and TEP measurements

The aging treatments were performed at two different temperatures : 170 °C and 200 °C. These two temperatures are part of the two different domains for precipitation and correspond to aging treatments for MgZn alloys [79]. The precipitation was followed by hardness and TEP measurements.

Fig.3.5 shows the TEP variations (ΔS) of the ZK30 alloy manufactured by SPS after a solid solution treatment and isothermally aged at 170 °C Fig.3.5.a and at 200 °C Fig.3.5.b.

At both temperatures, the TEP continuously decreases with the aging process, indicating that atoms in the solid solution are diffusing out of the matrix to form precipitates. Around 40 h, it is observed that the TEP stabilizes despite continued aging, indicating that the stable phase is formed, and there is no further diffusion of the solute atoms from the solid solution. The TEP variations are compared to the Vickers hardness evolution in Fig.3.5.c.d. The hardness evolution shows two different peaks for both temperatures. Furthermore, the peaks appear faster at 200 °C.

Three distinct stages during aging can be identified from this kinetics:

- Nucleation period (Stage I-II): In this stage, both the TEP variation and hardness increment are close to zero. This is because small coherent clusters act as solute elements, which do not significantly impact the TEP.
- Growth stage (Stage I-II): During this phase, the TEP decreases while the hardness increases. This corresponds to the precipitation of rod-shaped β_1' phase, which is known to be the dominant strengthening precipitate in Mg-Zn alloys [119].
- Coarsening stage (Stage III): At this point, both the TEP and hardness decrease, indicating the onset of over-aging in the alloy. However, during Stage III, the growth of another precipitate phase, β_2', also occurs. These two stages—coarsening of β_1' and growth of β_2' happen simultaneously, leading to a second hardness peak. The continued decline in TEP at 170 °C after the first hardness peak suggests that the matrix's solute content continues to decrease, meaning that the precipitation process is still ongoing. At 200 °C the TPE decreases continuously until a stable step that is not explained but could be attributed to the influence of Zr. Therefore, Stage III can be more accurately described as a "combined coarsening and precipitation stage."

3.2.3 Precipitation kinetics in ZK30 alloy using TEP

Monitoring TEP during aging enables the determination of precipitation kinetics. Since each alloying element contributes to the TEP value, the first step is to study Mg-Zn binary alloys to establish the contribution of Zn. After analyzing the binary alloys, the ZK30 alloy, which contains Zr, can be examined under the hypothesis that Zr will remain in solid solution during aging and, therefore, will not affect the TEP values.

Thèse accessible à l'adresse : https://theses.insa-lyon.fr/publication/2025ISAL0008/these.pdf © [J. Moreau], [2025], INSA Lyon, tous droits réservés

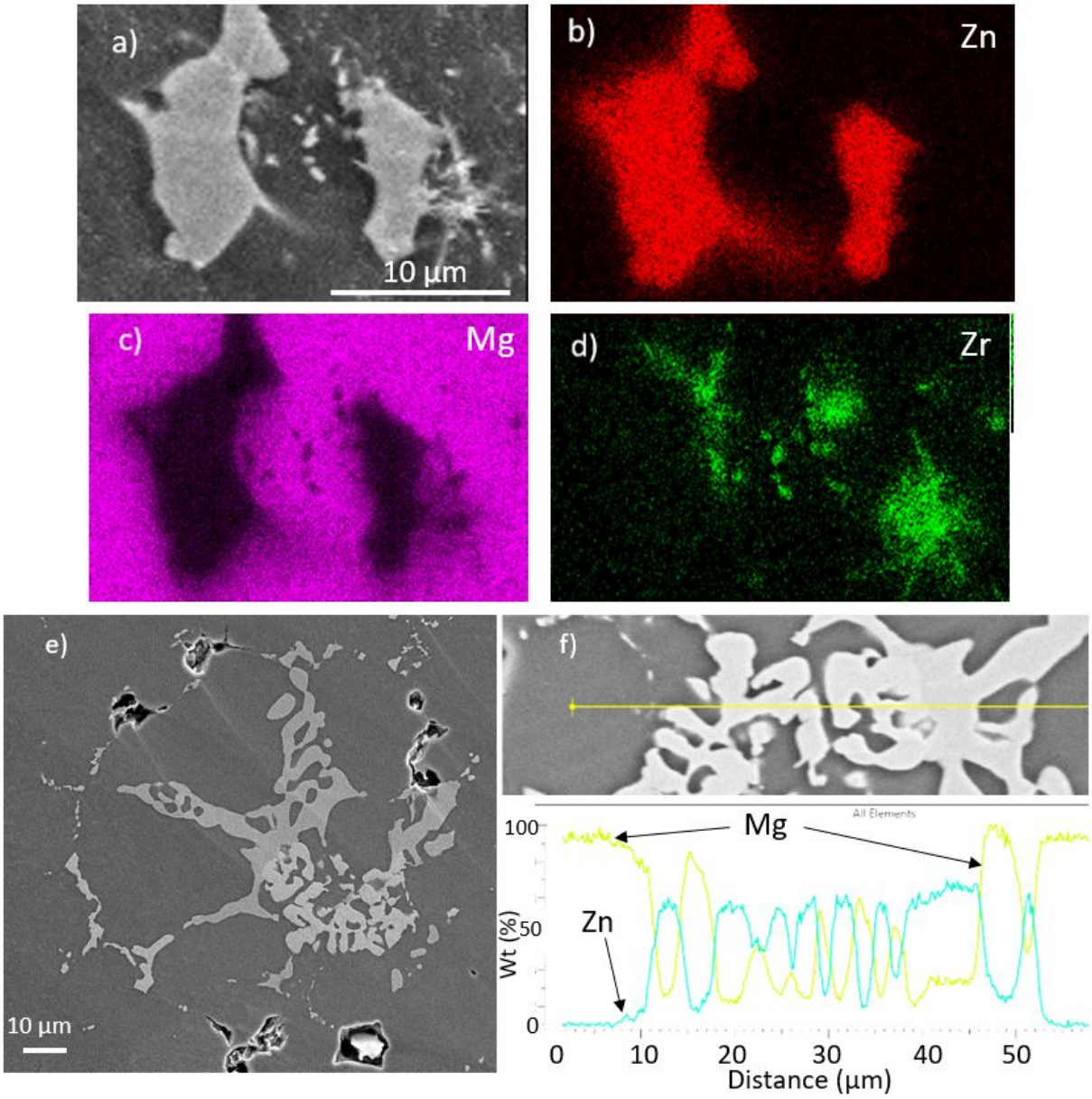


Figure 3.3: Observed intermetallics after a treatment at 340 °C for 24 h with a) SEM image of the intermetallics phase and the corresponding EDX containing b) Zn, c) Mg and d) Zr. e) SEM image and f) EDX line scan of an intermetallic of MgZn

Thèse accessible à l'adresse : https://theses.insa-lyon.fr/publication/2025ISAL0008/these.pdf © [J. Moreau], [2025], INSA Lyon, tous droits réservés

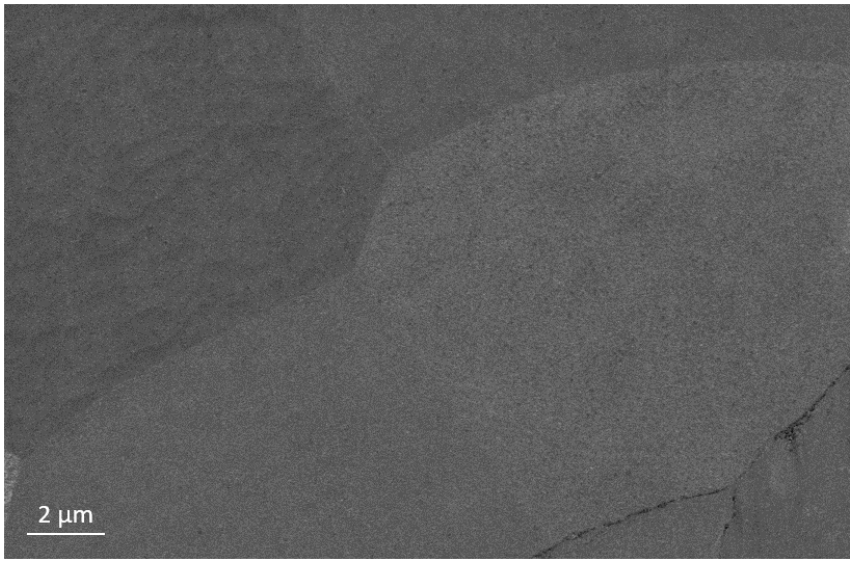


Figure 3.4: SEM observation of the surface of the sample after a solution treatment at 500 °C for 24 h, illustrating the absence of intermetalics at this resolution.

3.2.3.1 Binary alloys

When considering only a MgZn alloy, the contribution of solute element Zn (concentration $[Zn]_{at\%}$) on TEP of pure Mg ΔS_{ss} is given by the Gorter-Nordeihm law [170] :

$$\rho\Delta S_{ss} = (\rho_0 + \alpha_{Zn}\,[\mathrm{Zn}]_{\mathrm{SS}})\,\Delta S_{SS} = \alpha_{Zn}\Delta S_{Zn}\,[\mathrm{Zn}]_{\mathrm{SS}} \tag{3.3}$$

Furthermore, using Mathiessen's rule, which provides the electrical resistivity adapted to binary alloys, we obtain the following :

$$\rho = \rho_0 + \sum_i \rho_i\rho = \rho_{0,\mathrm{Mg}} + \alpha_{\mathrm{Zn}}[\mathrm{Zn}]_{\mathrm{SS}} \tag{3.4}$$

Where ρ_0 is the resistivity of pure Mg, α_{Zn} is the specific resistivity of Zn in Mg (expressed in $\mu\Omega.cm.wt\%^{-1}$and ΔS_{Zn} is the specific thermoelectric power of Zn in Mg (expressed in $\mu V.K^{-1}$.

As far as precipitates are concerned, small coherent or semi-coherent precipitates are likely to have an intrinsic effect, depending on their shape, size and volume fraction. While the influence of large incoherent precipitates is negligible [167] [171]. Dislocations may also have minor influence on the TEP. For example, in Fe alloys, the increased dislocation density was shown to result in a decrease of the TEP [172]. In the current study, the effect of dislocations is neglected and the precipitates are large enough that their effect on the TEP will be minimal [167] [173]. Assuming that only solute atom variations influence TEP (ΔS_d= ΔS_{pp} = 0), the Gorter–Nordheim law can be applied to estimate the solute variations [170] as follows :

$$\Delta S_{SS} = S - S_0 = \frac{\alpha_{Zn}\Delta S_{Zn}\,[\mathrm{Zn}]_{\mathrm{wt\%}}}{\rho_0 + \alpha_{Zn}\,[\mathrm{Zn}]_{\mathrm{wt\%}}} \tag{3.5}$$

Where S_0 is the relative TEP of pure Mg.

Thèse accessible à l'adresse : https://theses.insa-lyon.fr/publication/2025ISAL0008/these.pdf © [J. Moreau], [2025], INSA Lyon, tous droits réservés

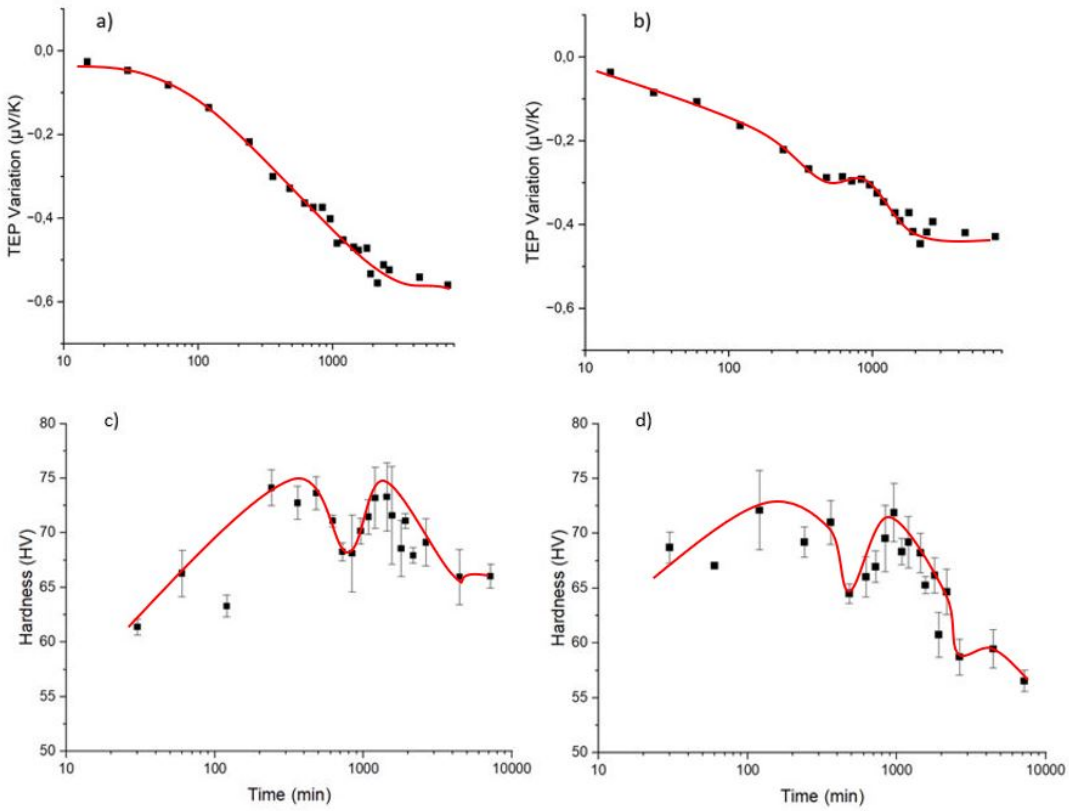


Figure 3.5: Evolution of TEP measured during aging at a) 170 °C and b) 200 °C and the corresponding hardness evolution for c) 170 °C and d)200 °C with the red lines showing the tendency

To determine the values of α_{Zn} and ΔS_{Zn}, TEP measurements of the binary MgZn from Yang *et al* [79] were exploited. The study focused on the TEP measurement for three binary alloys Mg-1,9Zn, Mg-2,8Zn and Mg-4,5Zn.

The influence Zr is visible in Fig.3.6 as the point of the ZK30 alloy is out of the ramp of the calibration for the MgZn alloy.

Using equation.3.4 and equation.3.5 with the results on MgZn alloys it is possible to plot the evolution of the resistivity and of the product $\rho\Delta S_{SS}$, as visible in Fig.3.7.

From Fig.3.7.a it is possible to determine the $\alpha_{Zn} = 0.38\,\mu\Omega\,\mathrm{cm\,wt\%^{-}1}$. Then, from Fig.3.7.b it is possible to obtain the product $\alpha_{Zn}\Delta S_{Zn} = 2.32\,(\mu\Omega\,\mathrm{cm\,wt\%^{-1}})(\mu\mathrm{V\,K^{-1}})$. Meaning $\Delta S_{Zn} = 6.11\,\mu\mathrm{V\,K^{-1}}$.

With the determination of the TEP parameters for Zn, it is possible to study the ZK30 alloy.

3.2.3.2 TEP of ZK30 alloy

The analysis of TEP for the ZK30 alloy is more complex because the Zr is also expected to be in solid solution. The study of the binary Mg-Zn system has already determined the influence of Zn on TEP variations. In this study, it is assumed that Zn is the only atom leaving the solid solution during aging. For the ZK30 alloy, the Gorter-Nordheim law can be adapted to account

Thèse accessible à l'adresse : https://theses.insa-lyon.fr/publication/2025ISAL0008/these.pdf © [J. Moreau], [2025], INSA Lyon, tous droits réservés

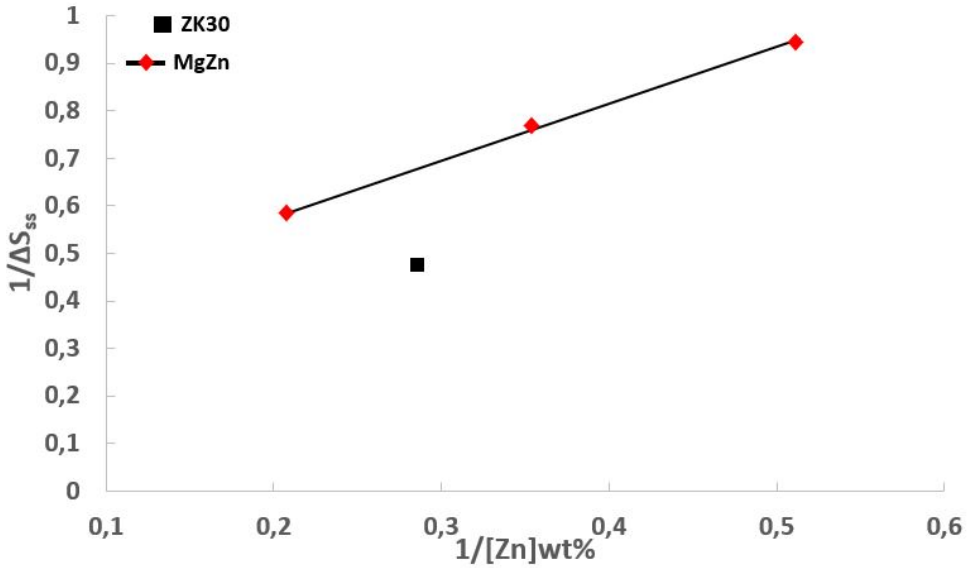


Figure 3.6: Plot of $1/[Zn]_{\%wt}$ vs $1/\Delta S_{ss}$ showing the linearity of the function and the ZK30 point which is out of the calibration due to the effect of Zr

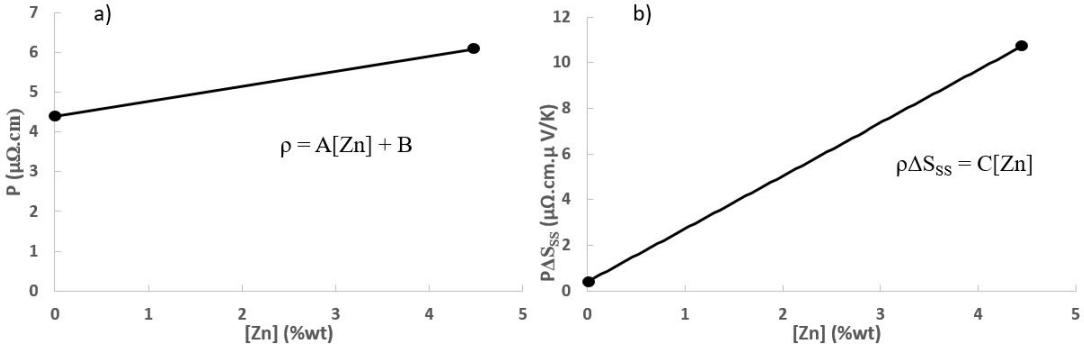


Figure 3.7: a) Plot of the resistivity of the alloy in function of the Zn concentration and b) the $\rho\Delta S_{ss}$ showing the linearity in both cases for the MgZn binary alloy

for the presence of Zr. When studying complex alloys, the contributions from each element are additive :

$$\rho \times \Delta S_{SS} = \sum_i \alpha_i \times \Delta S_i \times C_i \tag{3.6}$$

Thus, with the addition of Zr it becomes :

$$\rho\Delta S_{SS,t} = \alpha_{\mathrm{Zn}}\Delta S_{\mathrm{Zn}}\,[\mathrm{Zn}]_{SS,t} + \alpha_{\mathrm{Zr}}\Delta S_{\mathrm{Zr}}\,[\mathrm{Zr}]_{SS} \tag{3.7}$$

Assuming that Zr doesn't leave the solid solution the term $\alpha_{\mathrm{Zr}}\Delta S_{\mathrm{Zr}}\,[\mathrm{Zr}]_{SS}$ becomes a constant named K2.

Similarly when studying the resistivity it becomes :

Thèse accessible à l'adresse : https://theses.insa-lyon.fr/publication/2025ISAL0008/these.pdf © [J. Moreau], [2025], INSA Lyon, tous droits réservés

$$\rho = \rho_0 + \alpha_{\mathrm{Zn}} [\mathrm{Zn}]_{SS,t} + \alpha_{\mathrm{Zr}} [\mathrm{Zr}]_{SS} \tag{3.8}$$

Here, a constant K1 $= \alpha_{\mathrm{Zr}} [\mathrm{Zr}]_{SS}$ will take into account the influence of Zr.

With the assumption of a constant $[Zr]_{SS,t}$, plotting the resistivity of the ZK30 in function of the Zn concentration and the $\rho\Delta S_{SS,t}$, will allow the determination K1 and K2 with the variation compared to the MgZn alloy. The resistivity of the ZK30 alloy was measured with a conductivity measurement at $\rho = 6.2\,\mu\Omega\,\mathrm{cm}$. Influence of the Zr element is showed in Fig.3.8. Fig.3.8.a illustrates the resistivity difference between the ternary and the binary alloys, from this plot, we obtain K1 $= 0.5\,\mu\Omega\,\mathrm{cm}$. In Fig.3.8.b, the evolution of the $\rho\Delta S_{SS}$ is also plotted with the variation of Zn content. The strong negative influence of Zr is noticeable as the TEP values for ZK30 are considerably lower than the MgZn values. From this plot we obtain K2 $= -15.98\,\mu\Omega\,\mathrm{cm}$.

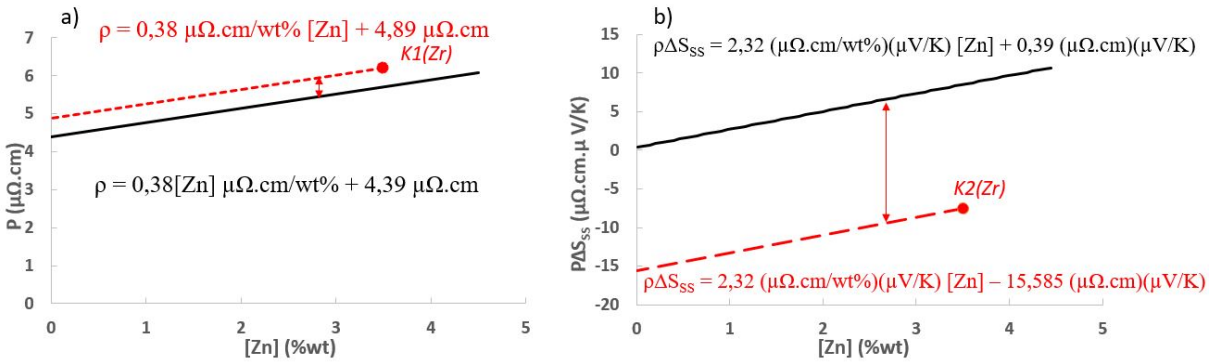


Figure 3.8: a) Comparison of the resistivity of MgZn alloy with the ZK30 to obtain the K1 shift between the two slopes and b) comparison of $\rho\Delta S_{ss}$ values to obtain the K2 shift

3.2.3.3 Determination of Zn solute through TEP

To determine the evolution of the Zn in the solid solution it is possible to write from the Gorter-Nordheim law :

$$[\mathrm{Mg}]_{\mathrm{SS},t} = \frac{\rho_0 \times \Delta S_{\mathrm{SS},t}}{\alpha_{\mathrm{Zn}}(\Delta S_{\mathrm{Zn}} - \Delta S_{\mathrm{SS},t})} \tag{3.9}$$

Eventually, when adapting the equation with the new K1 and K2 constants, for any time t, we obtain :

$$[\mathrm{Mg}]_{\mathrm{SS},t} = \frac{K_2 - \Delta S_{\mathrm{SS},t}(\rho_0 + K_1)}{\alpha_{\mathrm{Zn}}(\Delta S_{\mathrm{SS},t} - \Delta S_{\mathrm{Zn}})} \tag{3.10}$$

When using equation.3.10 we obtain the Zn content in solid solution evolution, depicted in Fig.3.9.a.b for both temperatures at 170 °C and 200 °C. It is visible that at 170 °C the Zn content in solid solution reaches a stable value lower than at 200 °C. The initial Zn concentration in solid solution is calculated at 3,6 wt%, which is slightly different from the expected value of 3,5 wt% corresponding to the Zn concentration in the ZK30 powder. However, it can be assumed

Thèse accessible à l'adresse : https://theses.insa-lyon.fr/publication/2025ISAL0008/these.pdf © [J. Moreau], [2025], INSA Lyon, tous droits réservés

that the Zn is completely in solid solution after the thermal treatment as observed before with SEM. Furthermore, the solute limit at 200 °C (2,7 - 2,8 wt%) is higher than the one found in Mg-Zn binary alloys (1,9-2,3 wt%) [79]. This effect could be attributed to the influence of the Zr element, which stabilizes Zn in the solid solution and lowers the solubility limit.

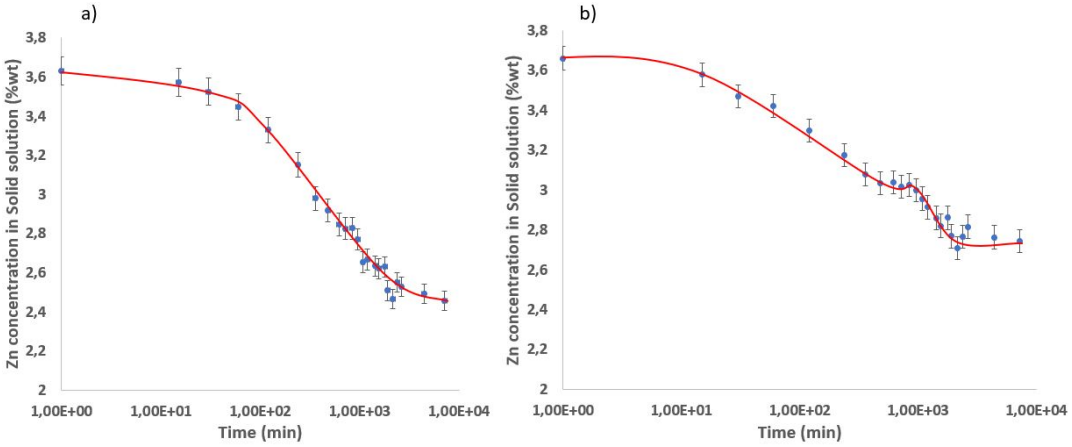


Figure 3.9: Estimated evolution of the Zn content from TEP in the solid solution for a) 170 °C and b)200 °C with the red line showing the tendency.

With the evolution of the Zn content in the solid solution it is possible to calculate the precipitate fraction evolution during the aging. The evolution of the precipitate fraction is defined by the following equation :

$$f_m(t) = \frac{[\mathrm{Zn}]_0 - [\mathrm{Zn}]_{\mathrm{SS},t}}{[\mathrm{Zn}]_p - [\mathrm{Zn}]_{\mathrm{SS},t}} \tag{3.11}$$

With $[Zn]_0$ being the total Zn content in the alloy, $[Zn]_{SS,t}$ the values obtained from the Zn content evolution and $[Zn]_p$ the Zn content in the precipitate. However, as observed before there are two types of precipitate with different Zn content. Furthermore, the exact composition of the precipitates is not well known. It will be assume that there is either only $\beta'1$ assumed to be composed of Mg_4Zn_7 $MgZn_2$ with $[\mathrm{Zn}]_\mathrm{p} = 0{,}825$, or only $\beta'2$ assumed to be $MgZn_2$ with $[Zn]_p = 0{,}843$ in this case. The results of the volume fraction of precipitate depending of the chemical composition are visible in Fig.3.10.

The precipitate fraction stabilizes around 1,3% at 170 °C and 0,9 % at 200 °C. For both temperatures, there is almost no difference between the two hypotheses: considering only $\beta'1$ or only $\beta'2$. These results were obtained considering the absence of Zr influence, however, as visible in the TPE evolution at 200 °C reaches a stable step during the ageing. This step may be attributed to the Zr that has an opposite effect on the TPE value and could explain the stability. Therefore, theses results could benefit from a more important study on the precipitation in the ZK30 alloy.

3.2.3.4 Observation of the precipitates

The precipitates that form during aging are typically only a few nanometers in size, making them difficult to observe with SEM [160]. XRD measurements also did not show any differences

Thèse accessible à l'adresse : https://theses.insa-lyon.fr/publication/2025ISAL0008/these.pdf © [J. Moreau], [2025], INSA Lyon, tous droits réservés

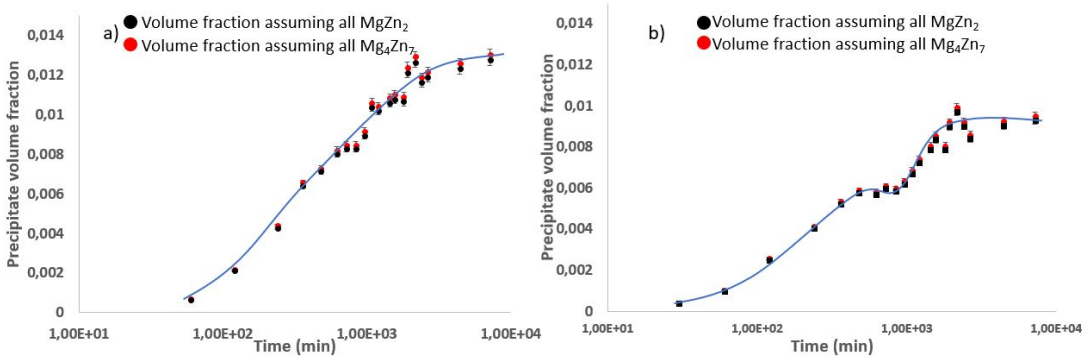


Figure 3.10: Estimated precipitate fraction from TEP evolution during aging at a)170 °C and b) 200 °C with the blue lines showing the tendency.

during aging at 170 °C and 200 °C. However, after prolonged aging, the precipitates grew, and it became possible to observe them after 44 hours of aging. An accelerating voltage of 1 kV was used to enable the observation, as shown in Fig.3.11.

As visible on the image, two types of precipitates appear. Rod-shape precipitates, identified as β_1' in the previous aging observation and disc-shape precipitates,which resemble the β_2' precipitates commonly observed in MgZn alloys. The rods are about 300-900 nm long with a thickness around 15-70 nm. The discs of β_2' have a diameter of 100-200 nm, although distinguishing them from rods oriented perpendicularly within the crystal can be challenging.

The kinetics of precipitation have been studied using various techniques, revealing the presence of two distinct precipitates. The evolution of their volume fraction during aging has been determined, and these findings provide valuable insights for modifying the alloy's microstructure to enhance its corrosion resistance. The impact of these precipitates on the corrosion properties of ZK30 will be analyzed in the following section of this chapter.

3.3 Mass loss measurement of heat treated ZK30 alloy

Various techniques were employed to evaluate the corrosion resistance and mechanisms, as well as to examine the influence of precipitation on the overall corrosion resistance. Firstly a simple mass loss test was performed on samples sintered at 500 °C and 63 MPa under Argon in different media. Then electrochemical measurements, allowing a more quantitative approach, were performed on samples sintered at 580 °C.

3.3.1 Mass loss test of pure Magnesium and ZK30

The influence of the alloying elements was studied first. Two samples, one made from pure Mg and the other from ZK30, were prepared using SPS at 500 °C at 63 MPa under Argon. Both samples were immersed in a 9 g/L NaCl solution at pH 7, and their masses were measured at each change of the immersion solution every 24 h. The solutions were continuously agitated, and the temperature was maintained at 37 °C to simulate physiological conditions. The mass ratio is defined by the ratio between the measured mass and the initial mass. The results are shown in Fig.3.12.

Thèse accessible à l'adresse : https://theses.insa-lyon.fr/publication/2025ISAL0008/these.pdf © [J. Moreau], [2025], INSA Lyon, tous droits réservés

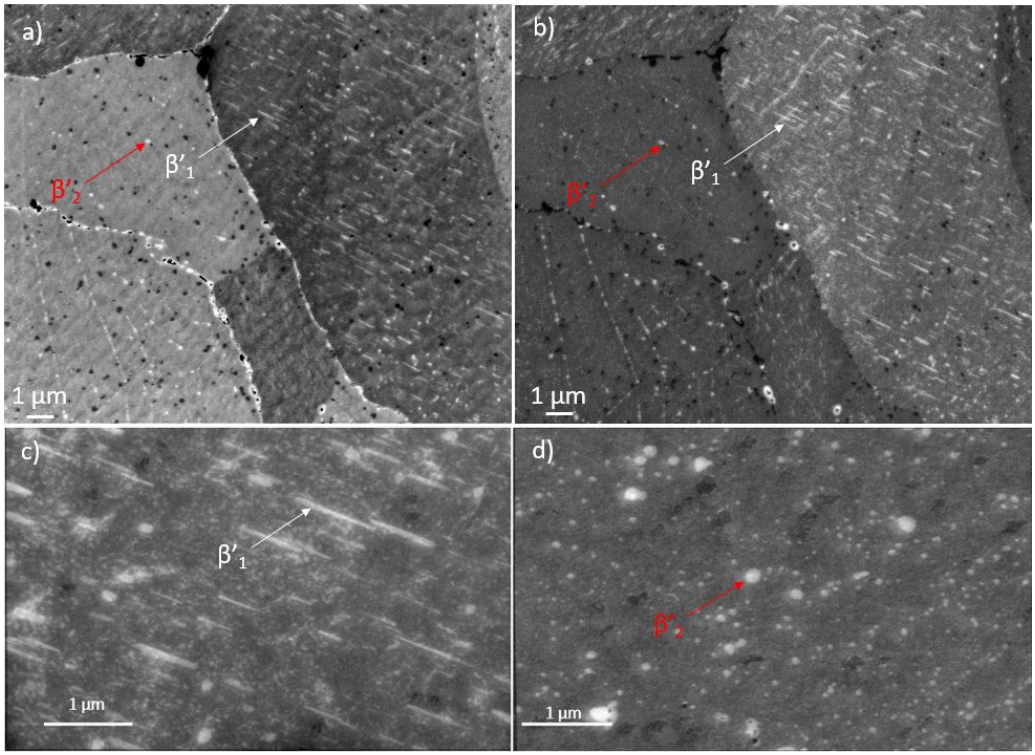


Figure 3.11: SEM observation at 1 kev of the precipitate after an aging of 44 h at 170 °C with different scale showing the rod shape precipitates assumed to be β_1' (white arrows) and the disc shape precipitate assumed to be β_2' (red arrows) with a) In lens b) BSE and c)d) SE mode.

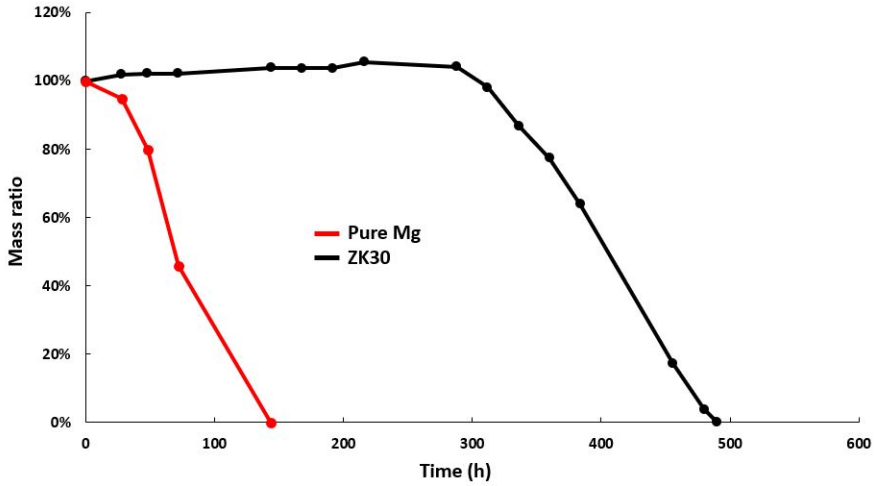


Figure 3.12: Mass lost test of pure Mg and ZK30 sintered at 500 °C in NaCl 9 g/L.

Thèse accessible à l'adresse : https://theses.insa-lyon.fr/publication/2025ISAL0008/these.pdf © [J. Moreau], [2025], INSA Lyon, tous droits réservés

The addition of Zn significantly increased the corrosion resistance of the alloy compared to pure Mg. Pure Mg forms an unstable passive layer that lasts only for a short time, leading to rapid degradation. In contrast, the ZK30 alloy forms a more stable passive layer, which is represented by the plateau, indicating the lifetime of the passive layer. Once this passive layer is broken, degradation occurs rapidly as for pure Mg.

The corrosion products forming on the surface of the ZK30 alloy were observed under an optical microscope, and the image is shown in Fig.3.13.

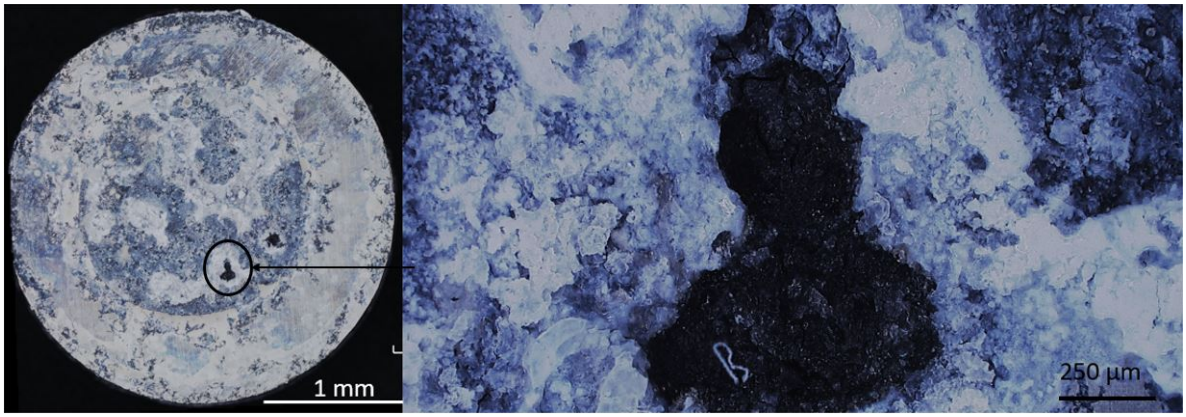


Figure 3.13: Optical images of corroded ZK30 alloy after a 196 h exposure to NaCl 9 g/L showing localized corrosion.

Localized corrosion is visible, with the formation of corrosion products once the passive film is unstable. The holes are induced by an inhomogeneous degradation due to the preferential attack of some grains. The depth of these holes was measured using a microscope, and the results are shown in Fig.3.14.

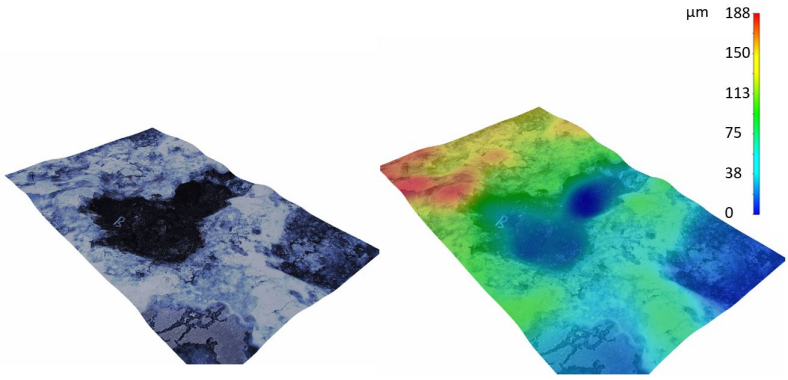
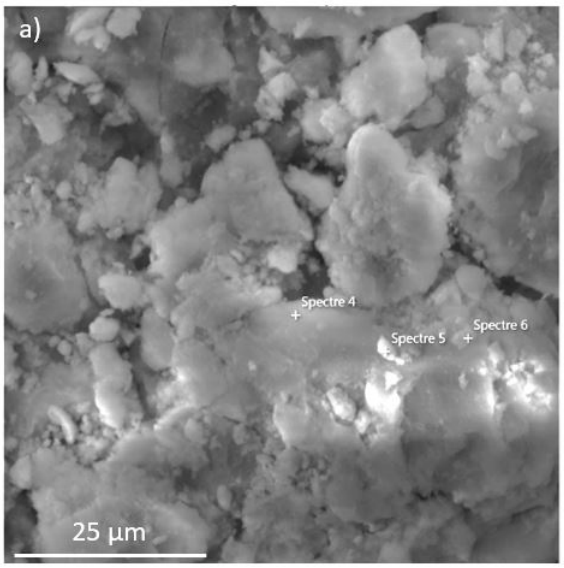


Figure 3.14: Optical observation and measurements of the localized corrosion in NaCl in ZK30

The hole is approximately 110 μm deep after 196 h of exposition to NaCl. The corrosion products at the surface were analyzed with EDX, as visible in Fig.3.15.

The composition of the products are more likely $Mg(OH)_2$ given the mass composition, as expected by the corrosion reaction.

Thèse accessible à l'adresse : https://theses.insa-lyon.fr/publication/2025ISAL0008/these.pdf © [J. Moreau], [2025], INSA Lyon, tous droits réservés



b)

Element	%wt
O	59.95
Mg	38.20
Cl	0.44
Zn	1.41

Figure 3.15: a) SEM observation of the corrosion products at the surface of the sample after immersion in NaCl and b) the EDX analysis result for the concentration of the different elements

Finally, the composition of the medium was analyzed at each replacement. ICP-MS was performed on the media and the concentration in Mg and Zn were measured. Each measurement was divided by the time interval between them to calculate the rate of species released into the solution. The evolution of the mass loss compared to the release of species was plotted and is shown in Fig.3.16. The measurements were conducted on two different samples prepared using SPS at 13 MPa and 500 °C under Argon and vacuum conditions.

The ICP results show a slight release of Mg and Zn at the beginning of the immersion. Then, the mass remains stable, but Mg and Zn are being released, indicating that mass stability is due to the formation of corrosion products. As the mass begins to decrease and the degradation accelerates, the concentration of the elements in the solution rises accordingly. Furthermore, the ratio between Zn and Mg remains stable throughout the entire degradation process, at around 3.4 wt%, which matches the concentration of the alloy. This suggests that there is no galvanic corrosion at the atomic scale and that the corrosion is global without preferential oxidation. Based on the ICP data, it is also possible to estimate the mass fraction of corrosion products formed during the degradation, as shown in Fig.3.17. The mass fraction in corrosion product is calculated by the difference between the sample's mass and the mass of Mg measured in solution by ICP.

The small initial mass increase of the sample corresponds to the formation of corrosion products. The fraction of corrosion products continues to increase until the passive layer is unstable. This chemical instability leads to the formation of corrosion product as the protective oxide of Mg are transformed in hydroxide of Mg which are not protective., the mass of the sample starts to decrease, while the mass of corrosion products increases significantly as more surface area becomes available for the reaction.

Thèse accessible à l'adresse : https://theses.insa-lyon.fr/publication/2025ISAL0008/these.pdf © [J. Moreau], [2025], INSA Lyon, tous droits réservés

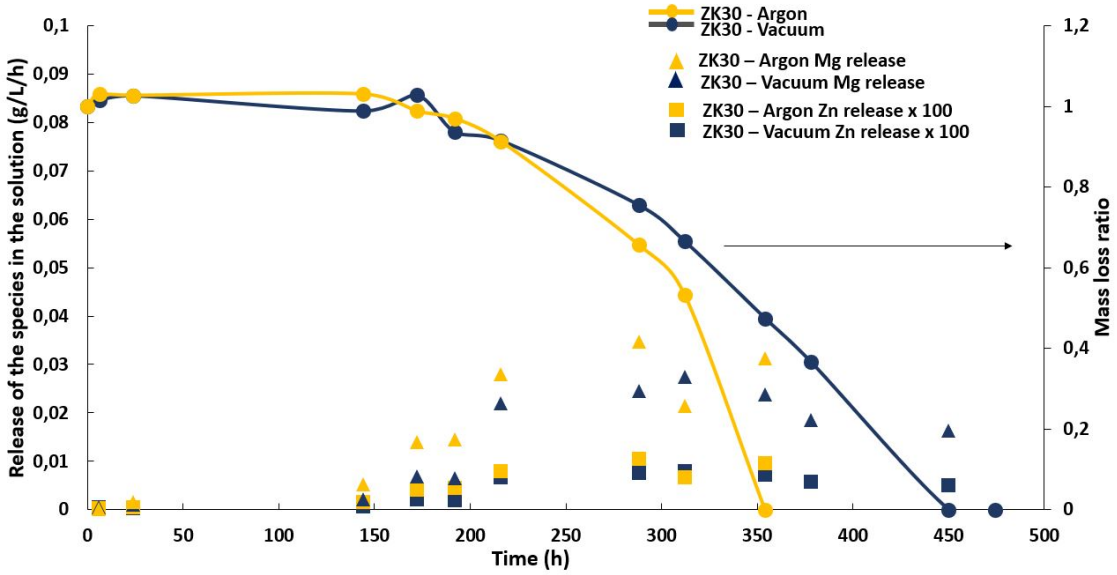


Figure 3.16: Evolution of the Zn and Mg ions in solution measured by ICP during the mass loss test for the two different samples sintered under vacuum and argon in SPS

3.3.2 Influence of the precipitation state on the mass loss in different media

3.3.2.1 Mass loss test in saline solution

The influence of microstructure on corrosion resistance was studied in both NaCl and physiological buffer solution (PBS). The formation of precipitates could potentially reduce the degradation of ZK30 or induce localized corrosion if they are not well distributed in the alloy. By forming a precipitate network with a lower corrosion potential, the passive layer should remain more stable and protect the material for a longer duration [90]. Samples were manufactured by SPS at 500 °C and 63 MPa under Ar pressure, and solutionnized at 500 °C for 24h. Subsequently, heat treatments at 170 °C and 200 °C were performed based on hardness measurements. To study different types of microstructures, several aging times were selected : 2 h, 8 h, 16 h and 44 h for 200 °C and 4 h, 14 h, 20 h and 44 h for 170 °C. These times correspond to the two peaks of hardness and the minimum in between, while 44h intended to be an over aged sample. All the samples were prepared with a similar size and mass (0.2 g) according to the ASTM recommendations, as described in the previous section.

The results from immersion in NaCl under the same conditions as before are shown in Fig.3.18.

Corrosion still occurs in two phases: first, the the plateau due to the presence of a passive layer that protects the material, followed by the layer conversion and a rapid mass loss. The results show a similar trend at 170 °C and 200 °C, where thermal treatment appears to delay the corrosion of the alloy up to a certain point. At 170 °C, the corrosion resistance is better for every aging duration of thermal treatment, with the best results at 4 h and 20 h. For 200 °C, the result is more debatable but it also shows an improvement in corrosion resistance at the two peaks of hardness at 2 h and 16 h. At 170 °C, the corrosion resistance is overall better than 200 °C, it could be explained by the fact that according to the study in Mg-Zn binary system [79], the size

Thèse accessible à l'adresse : https://theses.insa-lyon.fr/publication/2025ISAL0008/these.pdf © [J. Moreau], [2025], INSA Lyon, tous droits réservés

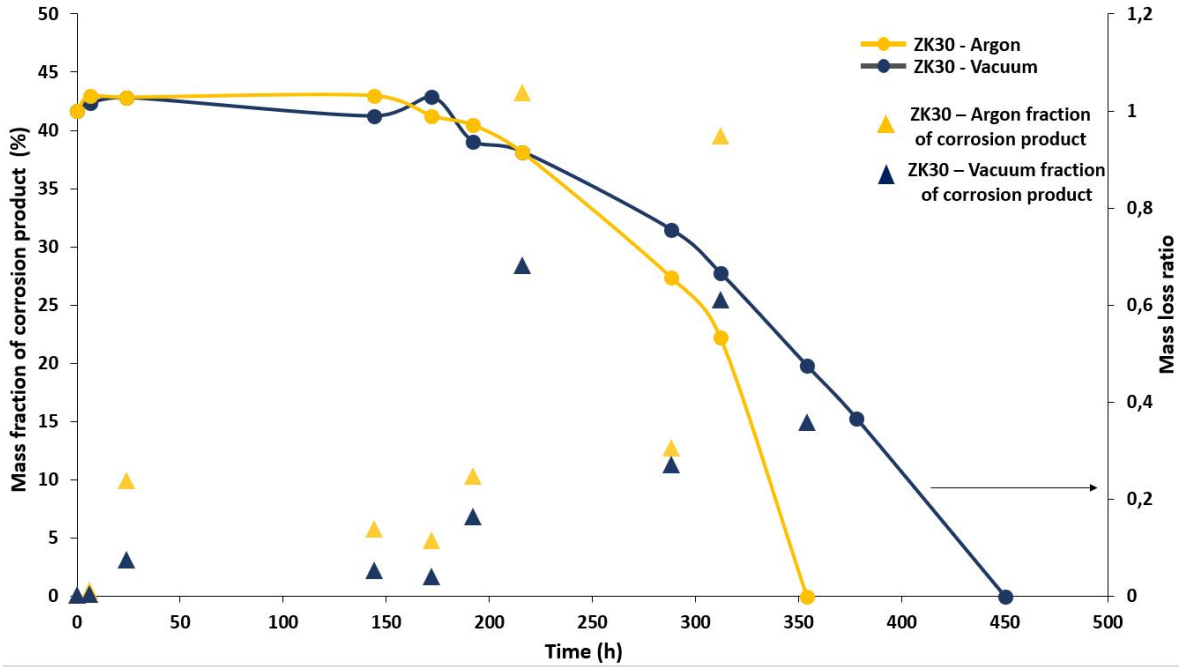


Figure 3.17: Evolution of the fraction of corrosion products composing the sample during the mass loss test

of precipitates at 170 °C is smaller and more evenly distributed, inducing less localized corrosion. Indeed, the overaged sample presenting larger precipitates degraded much faster than the other.

Furthermore, the mass loss data for the sample aged for 4 h at 170 °C shows a two-step degradation process. For most of the other samples, once the layer is destabilized, mass loss occurs rapidly until complete degradation. However, in this case, after an initial decrease in mass, the sample reaches a second, almost stable plateau. This could be due to the formation of a secondary barrier, possibly linked to the distribution of the precipitates. However, it is difficult to draw a conclusion, as this phenomenon may have occurred in other samples, but the time intervals between mass measurements were too long to capture it.

To summarize, based on the first observations, in solid solution, Zn seems to be too diluted in the sample and to not contribute to the film. With aging a local enrichment may have a positive effect on the stability of the film. With an overaged sample, due to larger precipitates, localised corrosion happens faster due to galvanic coupling.

3.3.2.2 Mass loss test in physical buffer solution (PBS)

Another immersion test was conducted in PBS, which better simulates the physiological environment due to the presence of multiple ions in addition to chloride. The results of the immersion test in PBS are shown in Fig.3.19. The presence of ions such as potassium promotes the formation of more corrosion products and phosphate complexes on the sample's surface, explaining the initial weight gain as the complexes remain adsorbed on the surface Fig.3.20.b. Furthermore, PBS also contains aggressive chloride but the mineral deposit at the surface provides more protection, allowing the sample to last much longer, with complete degradation occurring at 1300 h

Thèse accessible à l'adresse : https://theses.insa-lyon.fr/publication/2025ISAL0008/these.pdf © [J. Moreau], [2025], INSA Lyon, tous droits réservés

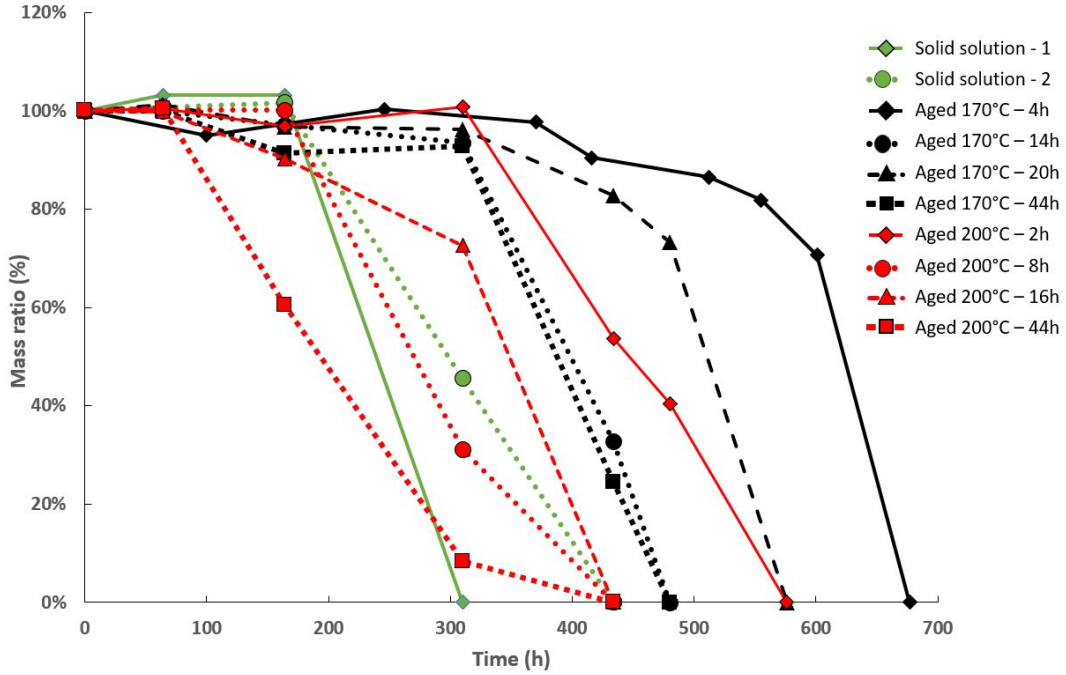


Figure 3.18: Mass loss measurement of the ZK30 alloy after different thermal treatment in NaCl 9 g/l until complete degradation with samples sintered at 500 °C in SPS

compared to 600 h in NaCl.

It was also observed that the mass of the immersed sample increased drastically compared to the initial mass indicating an important formation of corrosion product as visible with the comparison between NaCl and PBS samples in Fig.3.20. The corrosion in NaCl mainly consists of localized corrosion, with a thin layer of corrosion products at the surface which does not provide a high protection Fig.3.20.a. In PBS, localized corrosion occurs but thanks to the formation of a mineral deposit and corrosion products which are more protective against the medium, the geometry is retained Fig.3.20.c, contrarily, in NaCl pieces of the samples fall off.

The mass loss tests were the first observation of the degradation rate of ZK30 sample. However they do not accurately reflect the corrosion behavior. In the next section, the use of EIS measurements on sample sintered at 580 °C in SPS, which possess better mechanical properties as oberved before, will be used to monitor the corrosion behavior of ZK30 during immersion.

3.4 Corrosion resistance after optimized sintering

3.4.1 Mass loss test in saline solution

Due to the variations observed in the mechanical properties with different sintering temperatures, the experiment was repeated with the most promising heat treatments. The results are shown in Fig.3.21. This time, the samples were prepared using SPS at 580 °C and 13 MPa under Argon to observe whether the sintering temperature had an effect on corrosion resistance, while also aligning with the mechanical properties. Since all the samples underwent solution treatment, the only difference would be the oxide layer at the grain boundaries.

Thèse accessible à l'adresse : https://theses.insa-lyon.fr/publication/2025ISAL0008/these.pdf © [J. Moreau], [2025], INSA Lyon, tous droits réservés

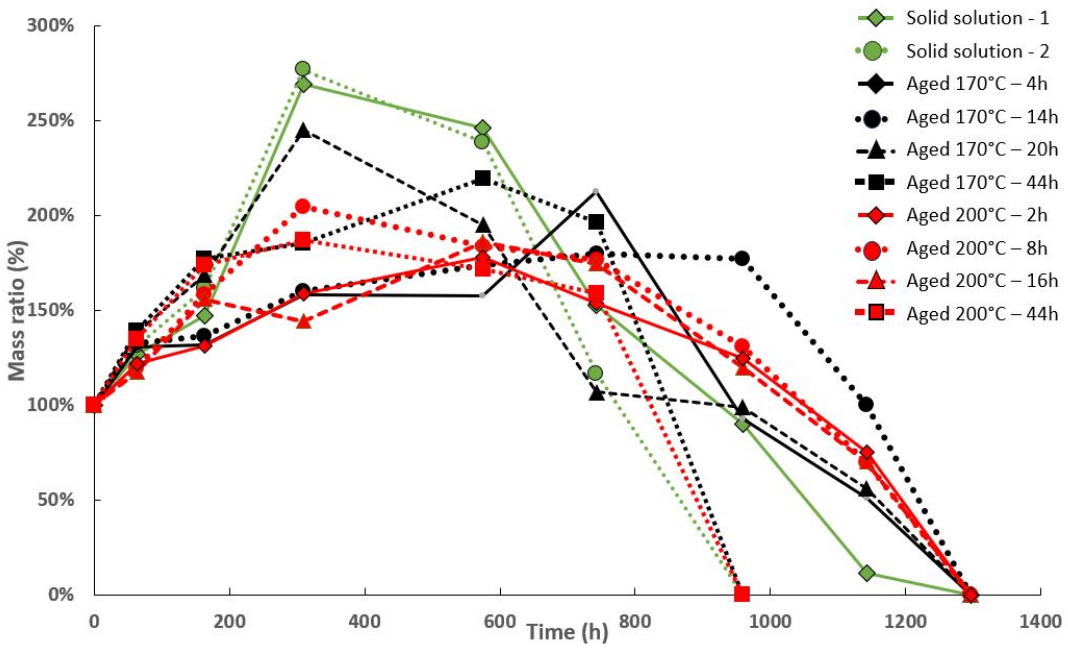


Figure 3.19: Mass loss measurement of the ZK30 alloy after different thermal treatment in PBS until complete degradation with samples sintered at 500 °C in SPS

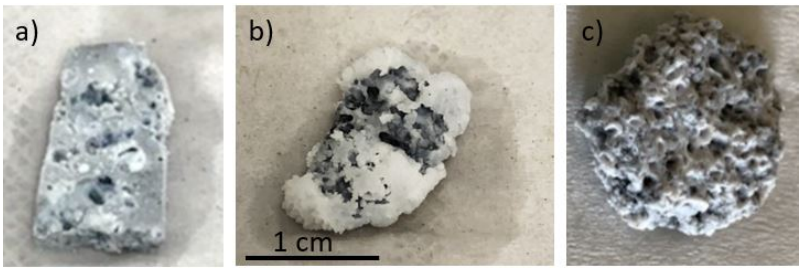


Figure 3.20: Picture of the sample immersed in a) NaCl and b) PBS after 100 h, showing the corrosion products, at the sample's surface, explaining the weight gain and c) Image of a sample immersed in PBS for 1000 h showing the localized corrosion

The degradation rate of the samples heat treated at 170 °C is still the slowest but this time the sample only solution treated showed the same degradation rate. This could be explained by either polluted samples in the previous experiments or by the fact that the oxide at grain boundaries in the sample in solid solution or the sample sintered at 500 °C was not stable and induced an accelerated corrosion at the grain boundaries.

3.4.2 Electrochemical measurement at initial state

The mass loss test provides information about the overall behavior of the material but does not reveal the evolution of the system and reactivity during the test. However, using electrochemical measurements, it is possible to obtain a better representation of the evolution of the system. The measurements were performed according to the protocol detailed in section 3.1.6. First, a

Thèse accessible à l'adresse : https://theses.insa-lyon.fr/publication/2025ISAL0008/these.pdf © [J. Moreau], [2025], INSA Lyon, tous droits réservés

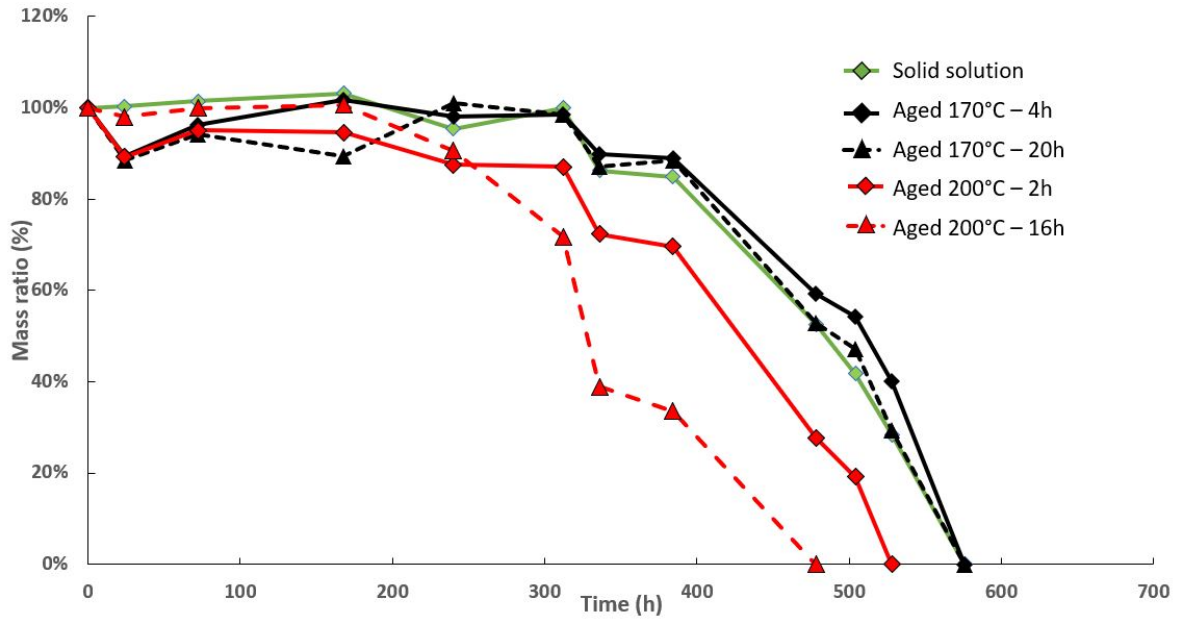


Figure 3.21: Mass loss measurement of the ZK30 alloy after different thermal treatments in NaCl 9 g/l until complete degradation with samples sintered at 580 °C in SPS

potentiodynamic polarization (PP) test was conducted on pure Mg and the ZK30 alloy after being manufactured by SPS. The results are shown in Fig.3.22.

PP allows the determination of the kinetics of both anodic and cathodic processes when the electrode potential is scanned above and below the corrosion potential E_{corr}. The Tafel regions are identified, and an extrapolation is performed. By analyzing the two PP branches, it is possible to determine the Tafel slopes, as shown in Fig.3.23. The Tafel slopes are determined by the following equation :

$$\eta = \pm A \cdot \log_{10}\left(\frac{i}{i_0}\right) \tag{3.12}$$

With η the overpotential, i the current density, i_0 the exchange current density and A the Tafel parameters for either the cathodic or anodic reactions.

When the rate-limiting step in the process becomes the charge transfer reaction, it allows the measurement of the cathodic and anodic branches, called Tafel lines. The measurements indicate a high dissolution current for relatively low anodic overpotential in both samples, which is characteristic of Mg. Both samples have the same E_{corr}, equal to -1.5 V vs Ag/AgCl.

This technique is useful at the beginning, but as corrosion progresses, the anodic slope becomes increasingly difficult to measure due to the rise in hydrogen release, this effect is called the negative different effect (NDE). The NDE is caused by the hydrogen release which induces a drop of the ohmic potential that will dominate the shape of the PDP curve, making it difficult to link the current measured and the real current of corrosion. Therefore, to better monitor the corrosion behavior during degradation, this method was coupled with EIS measurements. EIS provides a mean to determine the polarization resistance, Rp [114]. In our case we make the hypothesis, that even with a very thin native layer of oxide in our sample, there is no

Thèse accessible à l'adresse : https://theses.insa-lyon.fr/publication/2025ISAL0008/these.pdf © [J. Moreau], [2025], INSA Lyon, tous droits réservés

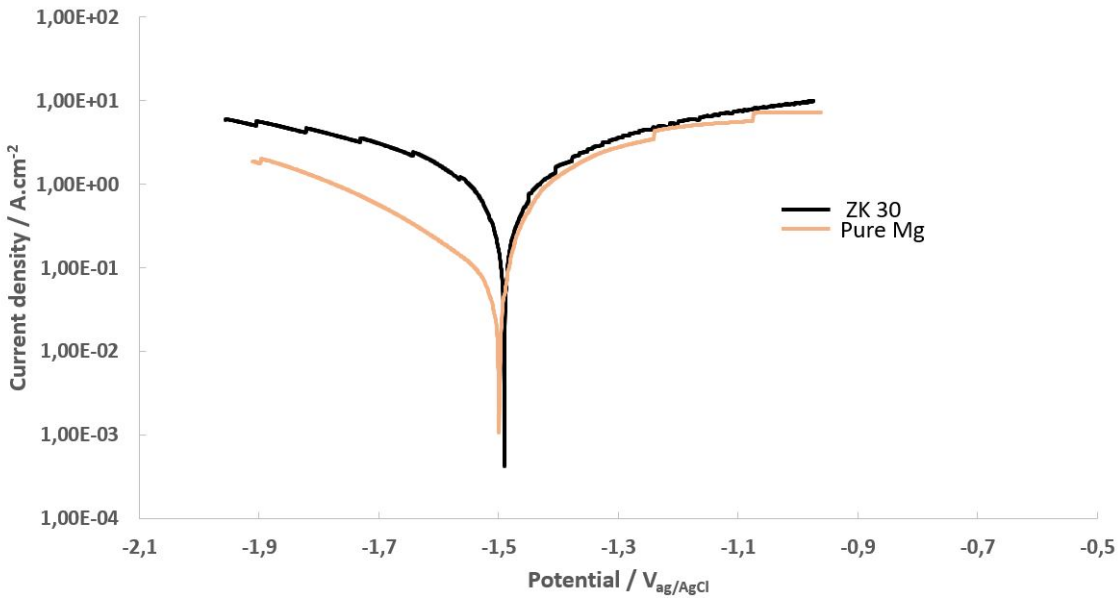


Figure 3.22: Polarization curves of the pure Mg and ZK30 alloy in NaCL solution 9 g/L

coverage effect in our measurement. Once this hypothesis is made, the corrosion rate of freely corroded metal is inversely proportional to polarization resistance according to the Stern-Geary relationship [111] :

$$j_{corr} = B/R_p \tag{3.13}$$

Where B is the Stern-Geary coefficient and function of the Tafel slopes :

$$B = \frac{\beta_a \beta_c}{2.3(\beta_a + \beta_c)} \tag{3.14}$$

With β_a and β_c being respectively the cathodic and anodic Tafel slopes and R_p the polarization resistance. Another assumption is that the Tafel' slopes will not vary during the measurement, even if the surface of the sample is modified.

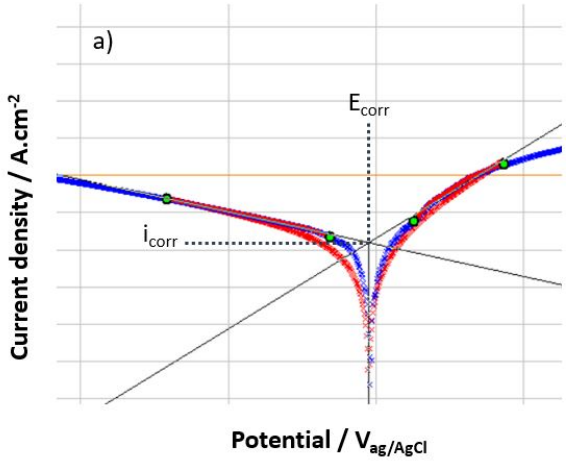
The form of the Stern-Geary equation is not strictly correct in the case of voltage dependant coverage effect which affects the value of B . However, j_{corr} still depends strongly on Rp and weakly on B. Usually, the charge transfer resistance R_t determined at intermediate frequencies is used instead of R_p. However, studies reported that the use of R_t often underestimated the corrosion rate [174].

Finally it is possible to calculate a corrosion rate in mm/y. Indeed, using the equivalent weight μ_{eq} :

$$\mu_{eq} = \frac{\mu}{n} \tag{3.15}$$

With μ the atomic weight and n the number of electrons transferred which is 2 in the Mg, with a modified form of the Faraday's law. It is possible to obtain a corrosion rate based on a penetration rate, given by the equation :

Thèse accessible à l'adresse : https://theses.insa-lyon.fr/publication/2025ISAL0008/these.pdf © [J. Moreau], [2025], INSA Lyon, tous droits réservés



b)

Parameter	ZK30	Mg	Unit
E_{corr}	-1504	-1491	mV
I_{corr}	125,4	808,7	μA
β_a	82,4	293	mV
β_c	230,4	343,4	mV
Corrosion rate	0.88	5,67	mm/y

Figure 3.23: a) Tafel extrapolation example on the ZK30 alloy with b) the corresponding parameters measured

$$v_p = \mu_{eq}\kappa_p \frac{i_{corr}}{\rho} \tag{3.16}$$

With ρ the metal density in (g/cm^3) and κ_p a constant equal to 3.2710×10^{-3} mm g/(μ cm y) to obtain a corrosion rate in mm/y.

Mg alloys usually exhibit in a Nyquist plot a capacitive loop at high frequencies and an inductive loop at low frequencies [115], as visible in Fig.3.24. The capacitive loop at high frequencies is related to the charge transfer resistance as well as the electronic double layer capacitance of the electrode [175]. The capacitive loop at medium frequencies is believed to account for the mass transport process [176]. A linear Kramer-Kronig validation test was performed on the real and imaginary components of the impedance and show good correlation and low residual noise ($< 1\%$) indicating that the data are consistent and causal [118] at medium and high frequencies. However, at low frequencies, some discrepancies were observed due to the sensitivity of the measurements.

The inductive behavior observed in Mg alloys is associated with the anodic dissolution of Mg and is linked to the relaxation of adsorbed intermediates, because the oxidation of Mg into Mg^{2+} has an intermediate step with the oxidation of Mg into Mg^{+} [116].

To determine the R_p, it is necessary to use an equivalent circuit to represent the impedance. Based on the obtained EIS spectra, the process can be modeled using an equivalent circuit. The chosen circuit commonly used for Mg alloys is shown in Fig.3.25.a [110]. In this circuit R_{er} represents the electrolyte resistance, R_2 is the charge transfer resistance and a constant phase element (CPE1) represents the non ideal capacitive behavior related to the electrochemical double layer [177]. An inductor (L) and a resistance R_3 have been included to represent the inductive response appearing at low frequencies [178].

The impedance of the CPE and the inductor are given respectively in Fig.3.25.b and Fig.3.25.c. Q represents the pseudo-capacitance of the pure capacitance and α is a correction compare to the ideal, when α is close to one it is close to the ideal and it exhibits the behavior of a blocking film. When α decrease and is close to 0.7 it indicates that the electrochemical double layer predom-

Thèse accessible à l'adresse : https://theses.insa-lyon.fr/publication/2025ISAL0008/these.pdf © [J. Moreau], [2025], INSA Lyon, tous droits réservés

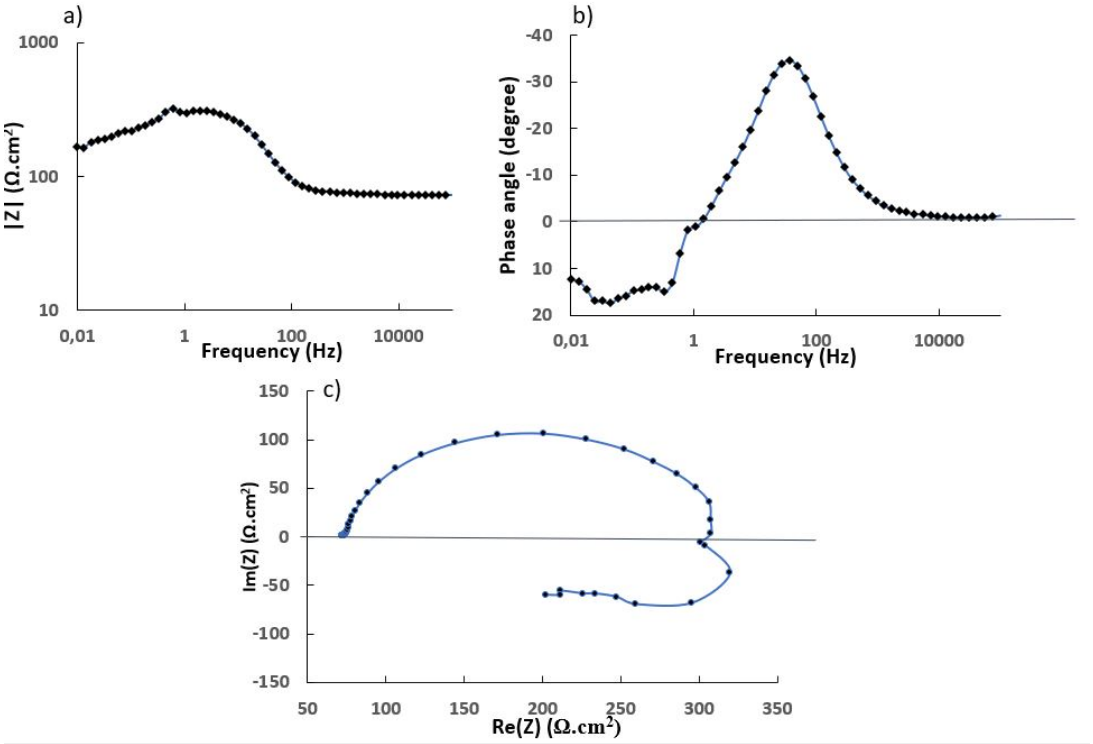


Figure 3.24: a)b) Bode diagrams measured for the ZK30 alloy at the initial state in NaCl and c) the Nyquist impedance plot corresponding

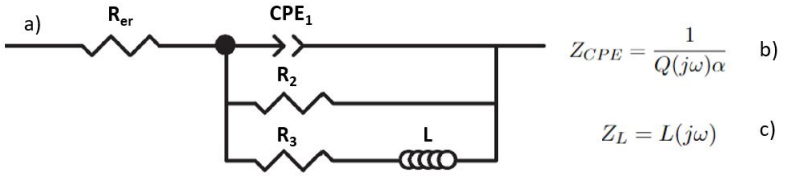
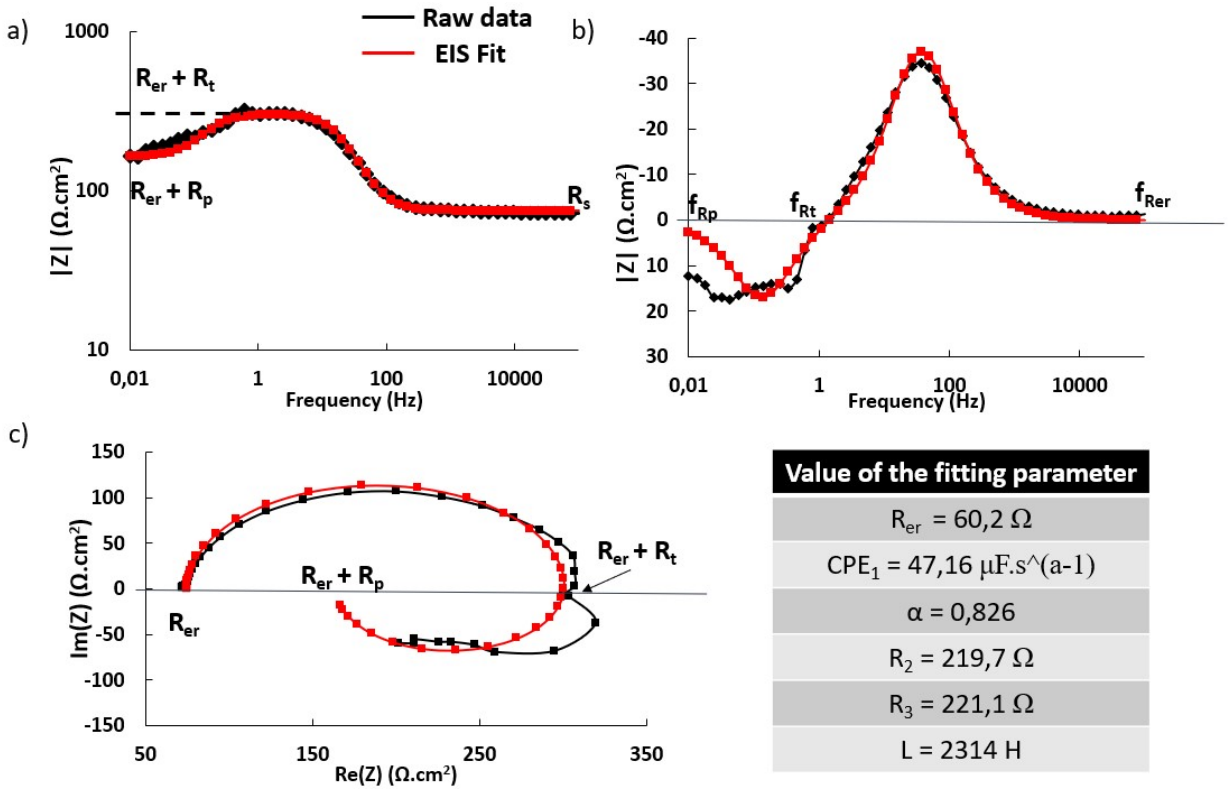


Figure 3.25: Equivalent circuit determine for the ZK30 alloy behavior in NaCl

inates in the corrosion behavior. The parameters of the equivalent electrical circuit were fitted to the experimental data with good correlation, with only slight deviations at low frequencies where measurements become more complicated, as shown in Fig.3.26.

At intermediate frequencies where Z"= 0, the difference between the impedance of the entire circuit and the electrolyte resistance is the charge transfer resistance R_t. The polarization resistance, R_p, for Mg, was defined as the difference in impedance between the electrolyte resistance (|Z| when f$\xrightarrow{\infty}$) and low frequency asymptote (|Z| when f$\longrightarrow$ 0). As frequency tends to zero, capacitive components tend to ∞ and inductive components tend to zero. This simplify the electrical circuit and allow to determine the polarization resistance as depicted in Fig.3.27.

Thèse accessible à l'adresse : https://theses.insa-lyon.fr/publication/2025ISAL0008/these.pdf © [J. Moreau], [2025], INSA Lyon, tous droits réservés



Value of the fitting parameter
R_{er} = 60,2 Ω
CPE_1 = 47,16 µF.s^(a-1)
α = 0,826
R_2 = 219,7 Ω
R_3 = 221,1 Ω
L = 2314 H

Figure 3.26: EIS measurements with the fitting of the equivalent circuit for a)b) the bode diagrams and c) the Nyquist impedance with d) the fitting parameters for the equivalent electrical circuit

3.4.3 Electrochemical measurement during immersion and influence of the aging

The next step was to monitor the corrosion behavior of the alloy over time. Measurements were conducted in a loop consisting of an OCV step to allow the alloy to reach equilibrium, followed by a quick LPR and an EIS measurement. Using the same setup as before, a ZK30 sample, sintered via SPS at 580 °C and solution-treated, then aged for 4 h at 170 °C was studied for 24 h. However, measurements over a longer period were challenging, as the rapid degradation of the sample caused the electrolyte to penetrate through the sample, and reach the copper plate. It resulted in a galvanic coupling between copper and Mg. The results of the EIS measurements and the corresponding polarization resistance R_p are depicted in Fig.3.28.

As visible in the results, R_p fluctuates a lot during the first 24 h. Initially, the sample in a solid solution state exhibits high resistance due to the natural oxide layer on its surface. This oxide layer does not protect the sample for long, and the R_p value drops once the layer breaks. Following this, a new layer, composed of corrosion products, forms and offers more stable protection, raising the R_p to a stable value. This changes are visible on the EIS with the variation of the semi-circle which is bigger when the R_p increases. These changes are similar between the solid solution sample and the one aged at 170 °C, confirming the mass loss test results where the duration for complete degradation was similar.

Thèse accessible à l'adresse : https://theses.insa-lyon.fr/publication/2025ISAL0008/these.pdf © [J. Moreau], [2025], INSA Lyon, tous droits réservés

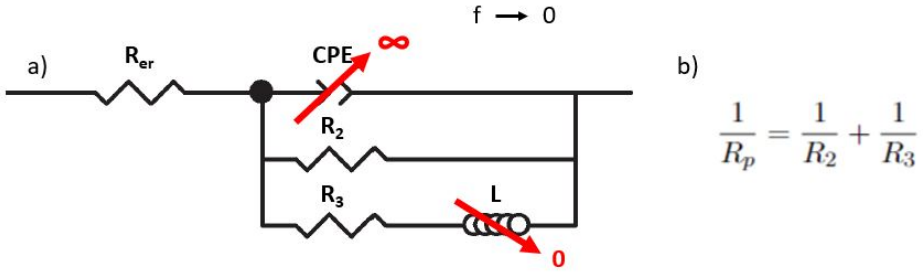


Figure 3.27: Equivalence of the circuit a low frequency allowing to determine b) the polarization resistance

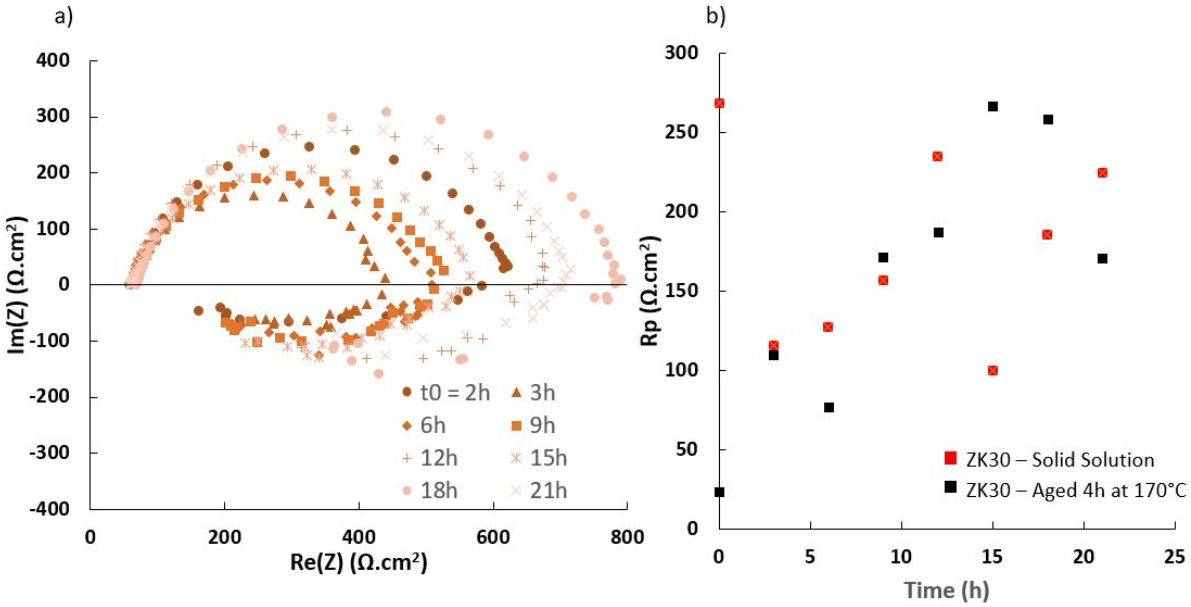


Figure 3.28: a) Nyquist impedance of the solutionnized ZK30 alloy and the evolution during time every 3 h for 24 h and b) the polarization resistance calculated based on the EIS measurements of the solutionnized sample and the sample aged at 170 °C for 4 h

The resistance values of the solid solution sample were compared to the one aged for 4 h at 170 °C. The main difference is at the beginning the resistance is really low for the aged sample. It indicates the absence of the native oxide layer during the measurement. The most plausible explanation is that the layer was not stable at all and broke during the OCP step before the EIS measurement. Then the variation are similar with an increase due to the formation of the corrosion products that protects the surface and the polarization resistance reaches a stable value (excluding one point at 15 h) almost equal to the resistance of the sample without aging.

During the first hours there is no significant difference between the two samples. To better evaluate the evolution of the corrosion resistance during the immersion a new setup described in (Section.3.1.6) was used. The measurement were the same but performed during the mass loss test in Fig.3.21. The objective was to try to correlate the mass loss tests with the EIS measurements. The measurements were complicated because the geometry of the samples changed

Thèse accessible à l'adresse : https://theses.insa-lyon.fr/publication/2025ISAL0008/these.pdf © [J. Moreau], [2025], INSA Lyon, tous droits réservés

during the immersion Fig.3.13.c, making the electric contact in the holder's probe difficult. However, some measurements were performed and are depicted in Fig.3.29.a. The corrosion rate associated with the resistance were also calculated and depicted in Fig.3.29.b.

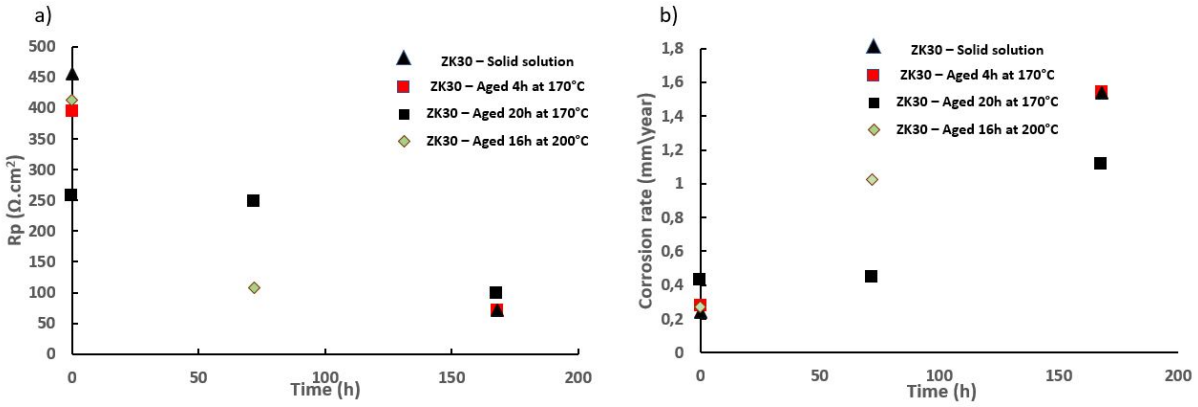


Figure 3.29: a) Polarization resistance calculated for the ZK30 alloy after various aging treatments and b) the corresponding corrosion rate of the same samples

The initial values does not really represent the global behavior as it depends of the initial oxide layer. However, after 72 h there is a clear difference between the sample aged at 200 °C and the others, as the corrosion rate reaches a high value earlier. After 168 h the values for the sample in solid solution and the ones aged at 170 °C are almost equal Fig.3.29 and it confirms the observation of the mass loss test were the duration for complete degradation were similar.

However, when plotting the resistance and the mass loss, it is visible that the resistance drops before the beginning of the mass loss Fig.3.30. This shows that the monitoring of the mass loss is not enough to explain the corrosion behavior as there is a competition between the mass loss due to the corrosion and the mass increase due to the corrosion products.

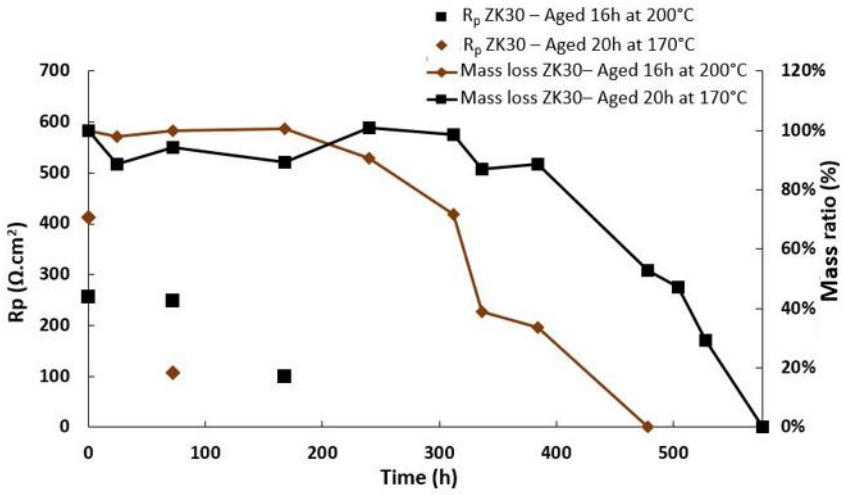


Figure 3.30: Plot of the mass loss and the corrosion rate vs time that shows that the corrosion resistance reaches a low value before the drop in mass

Thèse accessible à l'adresse : https://theses.insa-lyon.fr/publication/2025ISAL0008/these.pdf © [J. Moreau], [2025], INSA Lyon, tous droits réservés

The mass remains stable because the corrosion products increase which compensates the loss of Mg material. Thus, even if the mass remains stable, under a mechanical stress the structure will most likely collapse because it composed of a lot of corrosion products which was also observed in the ICP monitoring.

3.5 Conclusion

The precipitation sequence of the ZK30 alloy was studied based on previous observations made on Mg-Zn binary alloys. The use of hardness and TEP measurements provided an overview of the precipitation kinetics and the difference between the two aging temperatures of 170 °C and 200 °C.

The influence of microstructure on the corrosion rate was evaluated through the aging study. First, simple mass loss test measurements were performed to evaluate the degradation rate in different media and different microstructures. Then, EIS measurements were performed allowing to better monitor the corrosion behavior. The equivalent circuit model determined for the corrosion of ZK30 fit the data well, with minor discrepancies at low frequencies, and was used to determine the polarization resistance.

There was no clear evidence of a direct influence of precipitates on the corrosion rate; however, it was observed that aging at 200°C resulted in a microstructure that accelerated degradation compared to both the solutionized alloy and the alloy aged at 170°C. Additionally, during immersion, even when the mass remained stable, the material was primarily composed of corrosion products, and the polarization resistance reached low values before complete degradation occurred. This indicates that the mechanical properties of the alloy deteriorated significantly before the onset of mass loss, making it difficult to determine whether the alloy is suitable for orthopedic applications.

However, given this observation an optimal treatment for the alloy in terms of hardness and corrosion resistance would be a sample aged at a peak of hardness, either 4 h or 20 h at 170 °C

Thèse accessible à l'adresse : https://theses.insa-lyon.fr/publication/2025ISAL0008/these.pdf © [J. Moreau], [2025], INSA Lyon, tous droits réservés

Thèse accessible à l'adresse : https://theses.insa-lyon.fr/publication/2025ISAL0008/these.pdf © [J. Moreau], [2025], INSA Lyon, tous droits réservés

Chapter 4

Pressure-free debinding/sintering of Magnesium alloy: application to 3D printed parts by direct-ink writing

Contents

4.1 Background of additive manufacturing of Magnesium 90
4.1.1 Additive manufacturing via powder melting 90
4.1.2 Additive manufacturing via powder sintering 91
4.1.3 Liquid phase sintering (LPS) of Magnesium 94
4.2 Sample manufacturing 98
4.2.1 Ink formulation 98
4.2.2 Direct ink-writing 99
4.2.3 Debinding and sintering 99
4.3 Preliminary study and challenges of the sintering 101
4.4 *In situ* tomography of the sintering of Magnesium alloys 104
4.4.1 Material and method 105
4.4.2 In situ observation of the sintering 106
4.5 Sintering of Magnesium alloys in labyrinth crucible 108
4.5.1 Initial samples 109
4.5.2 Sintering setup 111
4.5.3 Sintering tests 112
4.5.4 Microstructure and hardness 115
4.6 Conclusions 120

Additive manufacturing (AM) has been under continuous development and offers new possibilities for implant design using various metallic alloys. Although challenging due to factors like the native oxide layer, low vapor pressure, and high reactivity of Mg, AM techniques for Mg alloys have been explored. This chapter aims to develop AM of Mg alloys using Direct Ink Writing (DIW), specifically avoiding mechanical pressure to mitigate oxide layer effects and achieve high-resolution implants with controlled porosity. Without mechanical pressure, it is possible

Thèse accessible à l'adresse : https://theses.insa-lyon.fr/publication/2025ISAL0008/these.pdf © [J. Moreau], [2025], INSA Lyon, tous droits réservés

to design complex geometries with macroporous architecture. This study initially focuses on developing the DIW process, including ink formulation, debinding, and sintering, followed by porosity and microstructure analysis to investigate the sintering mechanisms.

4.1 Background of additive manufacturing of Magnesium

Shaping orthopedic implants is primarily done through casting, which limits the accessible geometries and designs of the implants. Therefore, shaping through AM is a method that aligns with the needs of new orthopedic implants. AM of metals is widely spread and the main processes are shown in Fig.4.1. The AM of Mg allows for the production of complex and porous geometries that promote cell growth and can be tailored to individual patients. This approach introduces a new dimension to the manufacturing of orthopedic implants [179]. To date, a few studies have successfully shaped Mg alloys using power bed fusion (PBF) process for pure Mg[180] or with Mg-Zn-Zr alloy [181]; and also using extrusion based technique of Mg-Zn alloy[182].

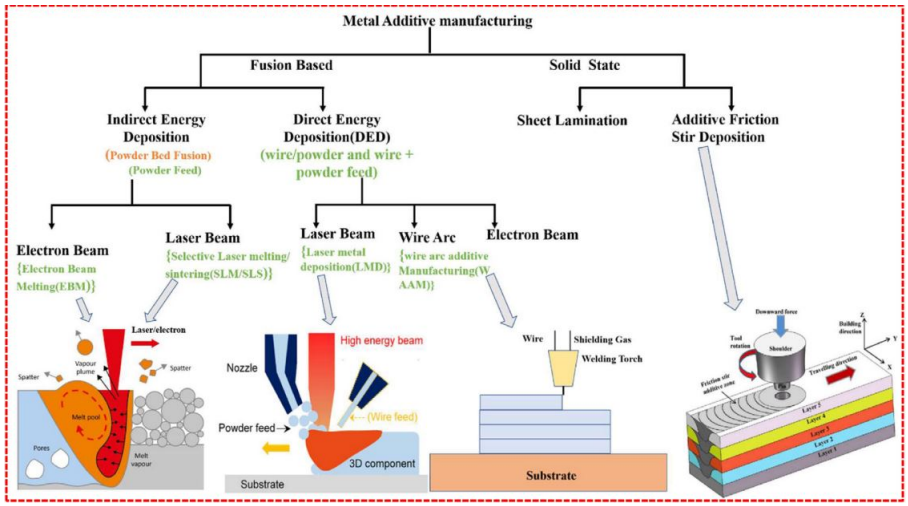


Figure 4.1: Summary of the main additive manufacturing techniques available for metals, taken from [183][184]

Among AM techniques for metals, the most established method for Mg alloys is laser beam powder bed fusion (LB-PBF). This technique relies on the fusion-solidification process, which effectively addresses the challenge posed by the oxide layer surrounding the powder grains. Consequently, the initial focus is placed on the melting processes.

4.1.1 Additive manufacturing via powder melting

Powder Bed-Fusion (PBF) technologies rely on a heat source to locally melt the powder spread on the building platform, constructing the structure layer by layer. After the current layer is consolidated, a new layer of powder is spread over the previous one by a roller, ready to be fused in turn [185]. The whole system must be maintained in an inert environment to prevent metal oxidation during the building process. This method allows for the creation of highly complex shapes, as the unmelted powder in the bed can act as support for the structure being built. However, unmelted powders can remain stuck on strut edges, leading to partial clogging of the

Thèse accessible à l'adresse : https://theses.insa-lyon.fr/publication/2025ISAL0008/these.pdf © [J. Moreau], [2025], INSA Lyon, tous droits réservés

drawn pores. This is an issue, in the case of material with a controlled macroporous architecture and it can limit the minimum achievable pore size. The process defects of the PBF technique are shown in Fig.4.2.

This process also raises safety considerations due to the fusion of Mg, which is flammable and explosive, for example in alloys such as WE43 (MgYREZr) [186].Furthermore, the fusion and evaporation can result in cracked parts with phase inhomogeneities [187]. Recently, Wang et al. [188] also successfully fabricated dense parts of a new Mg-Nd-Zn-Zr alloy by L-PBF.

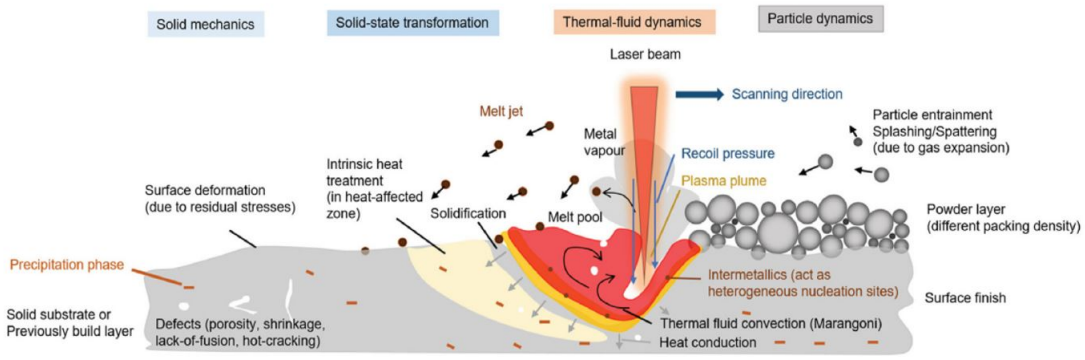


Figure 4.2: scheme of the PFB process higlighting the different defects and their origin during the printing, taken from [184]

Regarding ZK alloys, porosity is one of the major drawbacks of this AM processes, significantly affecting the mechanical properties of the as-built parts. Porosity of the built part is mainly influenced by the amount of energy put into the system, which is governed by parameters such as laser power (W), scanning speed (mm/s), hatching distance (mm), layer thickness (mm), and other parameters. In a study on ZK60 alloy, Wei *et al* [181] reported a relative density up to 94,5%. This low relative density, compared to conventional processes is due to the instability of the molten pool, disturbed by the recoil pressure imposed from vaporized metals. Furthermore, Zinc vaporized earlier than Mg leading to a change in the chemical composition by loosing up to 1%wt in Zinc. Even after optimizing the parameters, the resulting parts still exhibited porosity, as shown in Fig.4.3.

By optimizing the parameters, a density up to 97% can be achieved using the PBF process for ZK60 alloy [189]. However, the concentration of Zinc still decreases during the process.

In conclusion, while the PBF process effectively overcomes the challenge of the oxide layer by forming a molten pool, it has drawbacks, including managing metal vaporization and the need for extensive post-processing.

4.1.2 Additive manufacturing via powder sintering

AM techniques that use powder sintering present an alternative with the primary advantage of operating the shaping step in ambient atmospheric conditions. This approach also mitigates the issue of powder recyclability in the powder bed, which can become too rich in impurities due to the reactivity of Mg. It is true for the DIW but not for other technique such as Binder-Jetting which also uses a powder bed.

Sinter-based AM relies on pressureless sintering, as applying pressure would deform the

Thèse accessible à l'adresse : https://theses.insa-lyon.fr/publication/2025ISAL0008/these.pdf © [J. Moreau], [2025], INSA Lyon, tous droits réservés

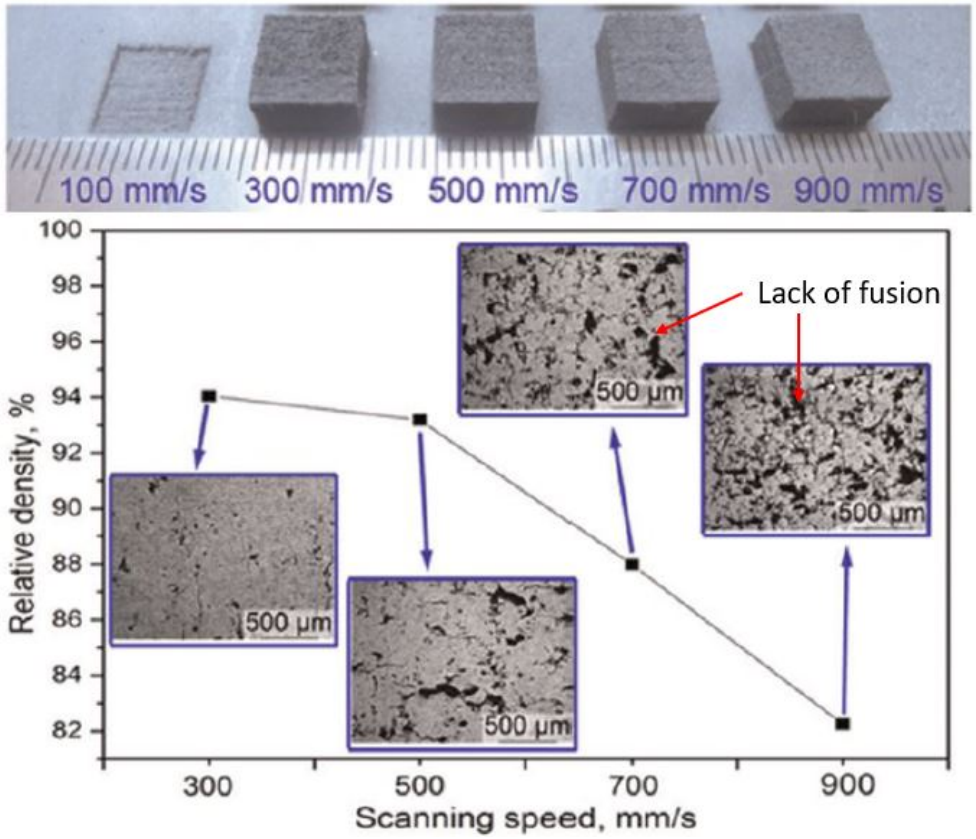


Figure 4.3: Example parts printed with L-PBF and the influence of the scanning speed of the resulting relative density, taken from [181]

printed parts. However, achieving high-quality sintering without pressure is challenging for Mg due to its native oxide layer. Historically, Wolf *et al* [190] were the first to achieve a density up to 98% from a green part uniaxially pressed with Mg-Ca alloys. It was achieved thanks to a labyrinth crucible (shown in Fig. 4.4).a and the high reactivity of calcium with oxygen, which helps capture ambient oxygen. Recently, they also worked on Mg-Gd produced with fused granular deposition and obtained near full density scaffolds (shown in Fig.4.4.b) [191]. However the mechanical properties of the scaffolds were still lacking compared to conventional manufacturing techniques, such as extrusion. Salehi *et al* [192] worked on ZK60 (Mg-6%wtZn-0.6%wtZr) and initially encountered challenges with sintering, as bubbles of liquid would surface due to the liquid fraction formed during sintering not wetting the powder particles, which then escaped through capillarity. Despite these efforts, no studies have yet explored direct ink writing (DIW) as a sinter based AM technique for Mg alloys. DIW involves the layer-by-layer deposition through a fine nozzle of a paste, containing the powder of interest dispersed in a binder. The resulting structure then undergoes thermal treatments to remove the binder and sinter the material. DIW was chosen for this study due to its ability to confine powder particles within the ink, potentially protecting Mg during printing and enabling multi-scale porosity, similar to what has been achieved with steel [193] and titanium [194].

The use of AM techniques based on sintering remains challenging, and the sintering of Mg

Thèse accessible à l'adresse : https://theses.insa-lyon.fr/publication/2025ISAL0008/these.pdf © [J. Moreau], [2025], INSA Lyon, tous droits réservés

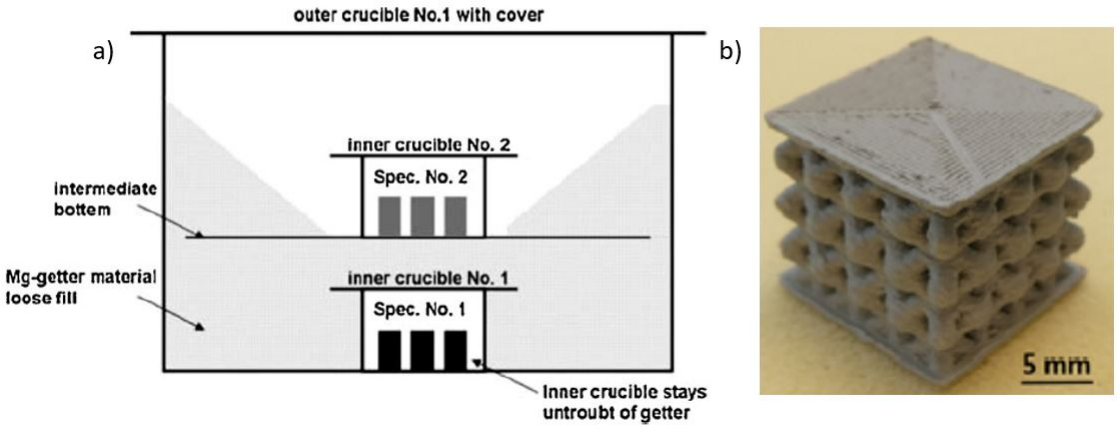


Figure 4.4: A) Scheme of the labyrinth crucible used for the sintering of Mg alloys, from [190] b) Printed parts of Mg-Gd produced with fused granular deposition, taken from [191]

will be discussed in greater details later.

4.1.2.1 Direct Ink Writing

DIW involves depositing layers sequentially through a nozzle in the form of ink. This ink can be either a filament or a solution composed of a binder, with or without particles.

Printing with filament, or fused deposition modeling (FDM) Fig.4.5.a, is the most popular currently due to its simplicity and accessibility to industries and individuals. In this process, the extrusion head is temperature-controlled to extrude a thermoplastic filament in a semi-molten state. As the material is deposited, the polymer solidifies, maintaining the desired shape. For metal printing, thermoplastic materials are heavily loaded with metal powder before being extruded into filaments. This technique allows for the printing of various types of metals such as steel [195], copper [196], or ceramics like titanium dioxide [197],...

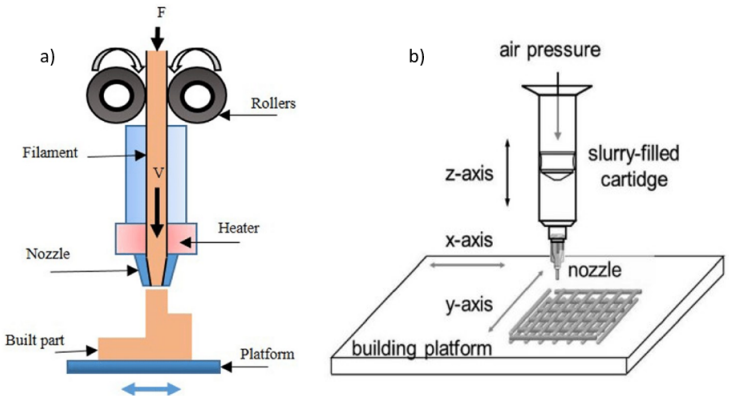


Figure 4.5: Representation of a) the fused deposition modeling (FDM) printing process and b) the DIW printing process [198][199]

Thèse accessible à l'adresse : https://theses.insa-lyon.fr/publication/2025ISAL0008/these.pdf © [J. Moreau], [2025], INSA Lyon, tous droits réservés

4.1.2.2 Direct ink-writing of Magnesium

It is also possible to work with a paste rather than a filament. This paste typically consists of a solvent and a polymer that serves as the binder, combined with a powder [200]. The ink is extruded through a nozzle using a piston to generate a continuous deposit in the form of a filament, as visible in Fig.4.5.b.

This technique called DIW, offers several advantages compared to previous methods, including the ability to operate at ambient temperature and pressure.

First, the ink formulated should be extrudable through a syringe at moderate pressure; ideally, the ink should exhibit shear-thinning behavior, meaning its viscosity decreases under shear, facilitating extrusion. Additionally, the ink must have sufficient viscosity to prevent it from flowing too easily within the syringe. To ensure the printed structure retains its shape, the ink should preferably exhibit thixotropic behavior, indicating that its viscosity returns to its original value after shear.

Finally, the ink must be robust enough to withstand layer superposition during printing. To achieve a printable ink, other parameters need to be taken into account (particle fraction, polymer fraction, printing temperature, etc.). With the consideration of these parameters, it is possible to obtain printing ranges based on these parameters.

The DIW of Mg alloys was only studied by Coffigniez *et al* [201], who developed an ink based on ethanol and ethyl cellulose suitable for the printing of Mg powders. They tried various binder compositions, as detailed in Table.4.1, and performed rheology measurements to demonstrate the printability of their formulation. The printed parts exhibited good geometric resolution and, printing was successfully with various nozzles sizes, as visible in Fig.4.6.

Mg powder content (vol%)	**Ethyl cellulose content in the binder (wt%)**		[201]
	9	**13**	**17**
0	EC9	EC13	EC17
50	EC9-Mg50	EC13-Mg50	EC17-Mg50
55	EC9-Mg55	EC13-Mg55	EC17-Mg55

Table 4.1: Example of ink compositions and their associated nomenclature

4.1.3 Liquid phase sintering (LPS) of Magnesium

Sintering relies on diffusion mechanisms, such as volume, surface, or grain boundary diffusion, which transport atoms to and through the points of contact between particles. Depending on the materials, the oxide layer formed on particles surface can either facilitate or hinder this diffusion [202]. For Mg, this layer, approximately 10 nm thick [65], prevents the diffusion in solid state as the self diffusivity of Mg is 10^{12} higher than the diffusion through the MgO layer at 650 °C [202]. Furthermore, MgO is a stable compound that does not decompose during the sintering and which also cannot dissolve in the Mg matrix due to the low solubility of oxygen in Mg. Mechanical pressure, often used to crack this layer in traditional sintering processes [203], is not an option for architectured macroporous structures processed by AM techniques. Instead, LPS could be a viable solution. LPS aims to create overpressure within the particles through the formation of a liquid phase, which can help crack the oxide layer. Additionally, the liquid phase offers a hundreds of times faster diffusion path than the solid phase [204].

Thèse accessible à l'adresse : https://theses.insa-lyon.fr/publication/2025ISAL0008/these.pdf © [J. Moreau], [2025], INSA Lyon, tous droits réservés

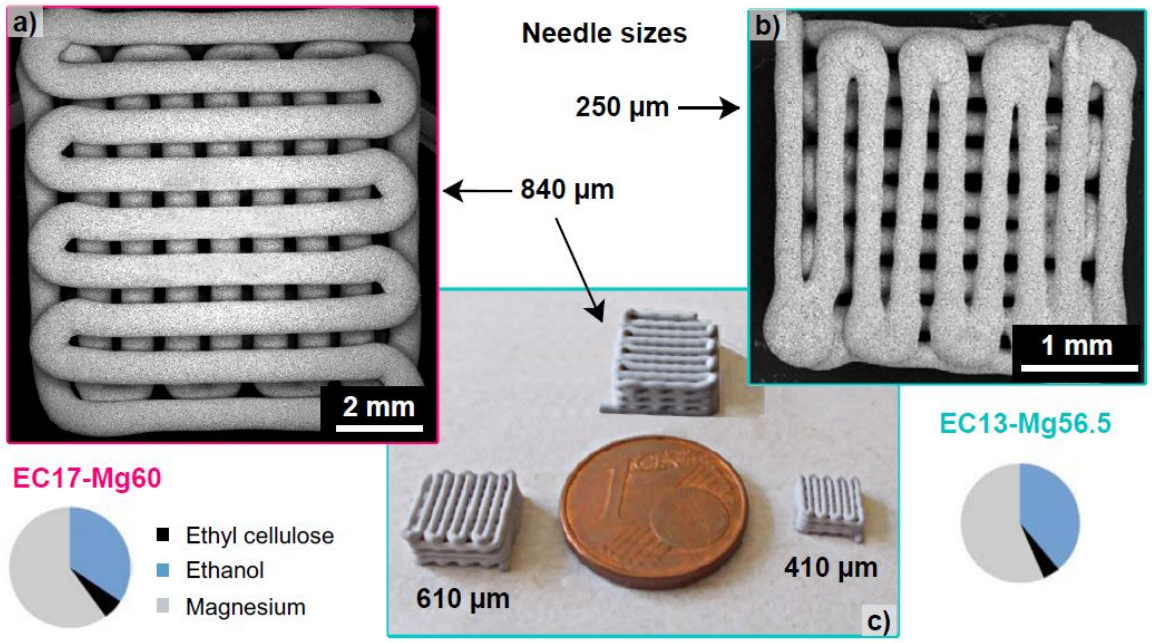


Figure 4.6: As printed scaffolds: SEM images (left and right) and picture (middle) of scaffold structures obtained with various inks and needle sizes, taken from [201]

Liquid phase sintering is separated in different steps that overlap each other, as detailed in Fig.4.7. Initially, mixed powders and pores between particles are present. As heating progresses, particles begin to sinter. When a melt forms, it spreads, causing the solid grains to rearrange. This is followed by densification and coarsening. Pore annihilation occurs as diffusion in the liquid phase accelerates grain shape changes, which facilitates pore removal. These steps are viable for a mix of powders and will be adapted for our alloy in the next section. Wolff *et al* successfully sintered uni-axially pressed Mg-1Ca using a 60 h sintering cycle at 600 °C, which formed an 8 wt% liquid fraction according to the phase diagram of MgCa. Following this success they developed Metal Injection Molding (MIM) technique for Mg alloys. MIM is based on the use of a binder loaded with metallic powder similarly to DIW. Then, the paste is pressured into a mold to obtain the desired shape. The accessible designs are limited but thanks to the pressure the relative density of the green part is higher than DIW. Their formulation was developed by analyzing the interactions of Mg with usual MIM binders composed of alkanes and alkenes [206]. Then, they successfully sintered Mg-Ca alloys with the MIM process [207] and managed to apply it to various alloys, especially Mg-Al alloys [208]. To perform the sintering, they employed a labyrinth crucible to purify the atmosphere from oxygen and subsequently produced parts using metal injection molding [209]. However, since their shaping process involved pre-application of mechanical pressure, it remains challenging to apply these methods directly to AM techniques due to the lower green density of AM parts as the feedstock of MIM are loaded with 64 % of Mg powder [209].

The green density plays an important in LPS process. For example, in system with an homogeneous density, with particle volume fraction fp < 70 vol.%, the powder particles maintain an almost spherical shape, except at their contact points with other particles. However, at higher

Thèse accessible à l'adresse : https://theses.insa-lyon.fr/publication/2025ISAL0008/these.pdf © [J. Moreau], [2025], INSA Lyon, tous droits réservés

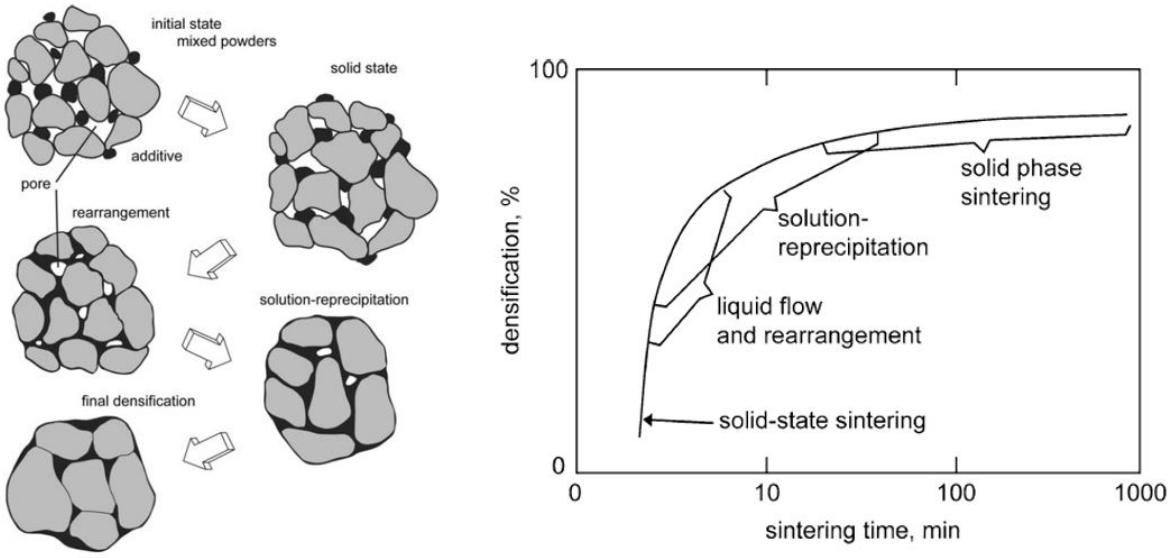


Figure 4.7: Schematic of the microstructure changes during LPS, starting with mixed powders and pores between the particles. During heating the particles sinter, but when a melt forms and spreads the solid grains rearrange. Subsequent densification is accompanied by grain coarsening [205]

.

solid-phase fractions, the powder particles faces flatten to eliminate pores, and the liquid forms pockets at the powder particles free surfaces [205]. The relationship between the distribution of dihedral angles and the wetting angle during liquid-phase sintering is crucial. A high dihedral angle means that more liquid is needed to fill the pores, and a high wetting angle will make it difficult to contain the liquid in the material. The coarsening of powder particles surrounded by the liquid, which occurs in the early stages of sintering, allows the particles to fill the pores, as observed by Kipphut *et al* [210]. This coarsening can be enhanced by the formation of liquid within the grains. Once the pores are closed, the liquid forms pocket at the grain boundary junction, as the density approaches its maximum. Initially, the oxide layer may act as a barrier and inhibit the swelling of the liquid, the pore filling of the liquid is delayed. For higher fractions of the solid phase, the grain faces flatten to eliminate pores and the liquid forms pockets at the grain boundary junctions. This means that for low particle volume fraction it is necessary to form more liquid fraction to fill the pores.

Salehi *et al* increased the proportion of liquid in Mg alloy particles in parts produced by AM, which led to the rupture of the oxide shell [211]. Despite this, they only achieved a maximum relative density 70%, with some loss of the geometric fidelity. Recently, they worked on binder jetting of AZ91 alloy [212] and observed unexpected leakage of liquid to the surface, visible in Fig.4.8.

This issue, not seen in earlier studies, highlights the complexity of the process. The green density before sintering is crucial, a long distance between powder particles makes it harder for the liquid to infiltrate the pores. Additionally, processes before the sintering can increase the thickness of the oxide layer, making it more difficult to break. The lack of a labyrinth crucible

Thèse accessible à l'adresse : https://theses.insa-lyon.fr/publication/2025ISAL0008/these.pdf © [J. Moreau], [2025], INSA Lyon, tous droits réservés



Figure 4.8: Images of the liquid bubbles that appear during sintering of AZ91 powder [212]

in Salehi *et al*'s study may have resulted in a less pure atmosphere, which could stabilize the oxide layer and requires a larger liquid fraction to break it. The increase of liquid fraction needs to be precisely controlled to avoid structural collapse [213]. To address this issue, the use of Ca nanoparticles [214] or Mg alloys containing Ca [190] have been proposed. Ca is more sensitive to oxidation and acts as a sintering aid by reacting with the MgO film and diffusing through the Mg particles, creating bonds between powder particles. However, deviations in chemical composition due to Ca nanoparticles have been observed, and the mechanical properties (yield strength, elongation at break) remain lower than those of samples produced by casting technology due to residual oxides introduced by the Ca.

The primary cause of leakage in liquid phase sintering is the wetting behavior between the liquid Mg phase and the solid MgO phase. The contact angle between the liquid phase and solid phase is crucial for liquid phase sintering. During sintering, the microstructure consists of grains and pores of varying sizes and shapes, each with different capillary conditions. A wetting liquid tends to move to the lowest energy configuration, preferentially flowing into smaller grains and pores, which promotes rearrangement and densification.

A low contact angle indicates good wetting, leading to the liquid spreading over the solid grains and enhancing capillary attraction, thus aiding densification. Conversely, a high contact angle signifies poor wetting, causing the liquid to retreat from the solid. This results in compact swelling and liquid exuding from the pores, as shown in Fig.4.9. Measurements of the contact angle between liquid Mg and solid MgO showed an angle of $\theta = 90°$ at 700 °C. It is a poor contact angle and it tends to decrease with the increase of the temperature, and is likely even less favorable at the lower temperatures typically used for sintering Mg alloys, around 600 °C. Furthermore, at 652 °C the viscosity of liquid Mg is measured at 12.36×10^{-3} Pa s, which is low meaning the liquid flows quickly.

Thèse accessible à l'adresse : https://theses.insa-lyon.fr/publication/2025ISAL0008/these.pdf © [J. Moreau], [2025], INSA Lyon, tous droits réservés

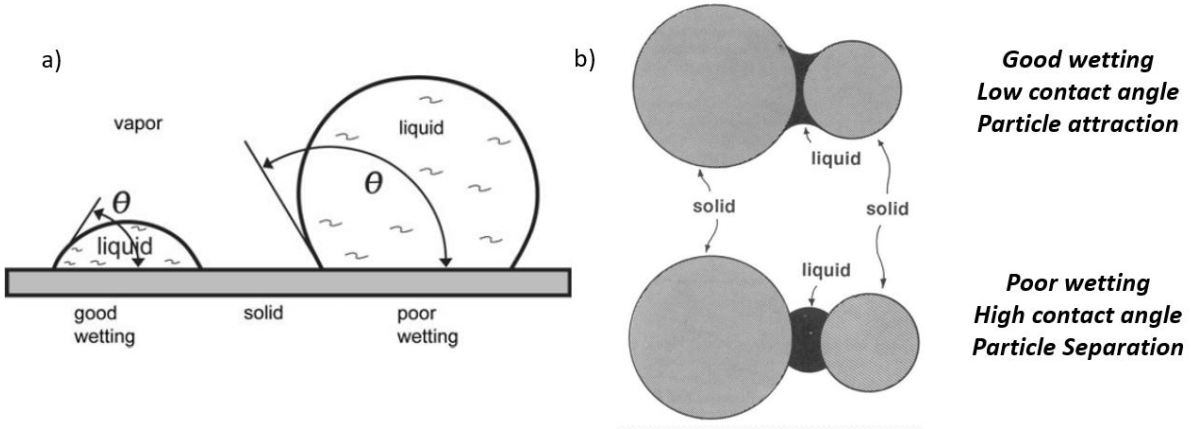


Figure 4.9: a) Representation of the contact angle between a liquid drop and a solid b) Influence of the contact angle on the attraction or separation of two particles [205]

4.2 Sample manufacturing

Samples of ZK30 alloy were printed with DIW in order to develop a debinding and sintering cycle effective for Mg alloys.

4.2.1 Ink formulation

Printing with the DIW technique relies on a paste formulation composed of a a mix of binder(s), solvent(s) and powder particles. Due to Mg's high sensitivity to water, the binder is based on ethanol. Ethyl-cellulose (EC) is added to ethanol to obtain a suitable rheology for printing. The development of the ink composition and the rheological measurements were performed by Coffigniez *et al*[201] and will not be discussed in this work.

Initially, the binding solution is prepared by mixing EC at 13 wt% with absolute ethanol using a dual asymmetric centrifugalmixer (SpeedMixer DAC 150.1 FVZ-K) for 10 min at 1500 rpm. The solution is stored at 4 °C for 24 h, and the mass is monitored to ensure that ethanol did not evaporate. The ZK30 powder is then added incrementally, with 5 min mixing periods at 1500 rpm each time to ensure homogeneity, until reaching a final volume fraction of 60 vol%. The ink is kept at 4 °C to prevent solvent evaporation. The corresponding weight fractions are provided in (Tab. 4.2).

	ZK30	Ethanol	EC
Ink	73 wt%	23,5 wt%	3,5 wt%
Ink	60 vol%	36.3 vol%	3.7 vol%
After drying	95,4 wt%		4,6 wt%
After drying	93 vol%		7 vol%

Table 4.2: Weight and volume fraction of the components in the ink and after drying

Thèse accessible à l'adresse : https://theses.insa-lyon.fr/publication/2025ISAL0008/these.pdf © [J. Moreau], [2025], INSA Lyon, tous droits réservés

4.2.2 Direct ink-writing

All samples presented in this study have been printed using a direct ink-writing apparatus called robocaster (3D Inks, LLC, Stillwater, OK, USA) controlled by the motion software Aerotech A3200 (Aerotech Inc., Pittsburgh, PA, USA). The printing was done on glass plates coated with a thin layer of grease to facilitate the removal of dried samples. Inks were extruded at 10 mm/s through plastic conical nozzles with an internal diameter of 840 µm. Images presenting the robocaster used in this study can be found in Appendix.4.6.

For all scaffolds, the rod spacing (distance between two rod centres) was fixed at 1.5 times the internal diameter of the nozzle. Similarly, the space between two layers along the building direction was fixed at 0.8 times the internal diameter of the nozzle, in order not to crush the filaments too much, while ensuring a slight interpenetration.

To ensure a stabilized flow during scaffold printing, a sacrificial length (few mm) of ink was extruded before printing each sample. For all samples, the temperature was maintained at 35 °C in the printing chamber to allow the evaporation of ethanol during printing and maintain the shape. The evaporation of ethanol change the rheological properties of the ink and allow to retain the shape once printed [201]. After the printing the parts are dried at ambient air for 24 h to evaporate the remaining ethanol. Small parts were printed with various shapes and will be named scaffolds in this chapter, to assess the feasibility of the sintering. Printed parts are visible in Fig.4.10.

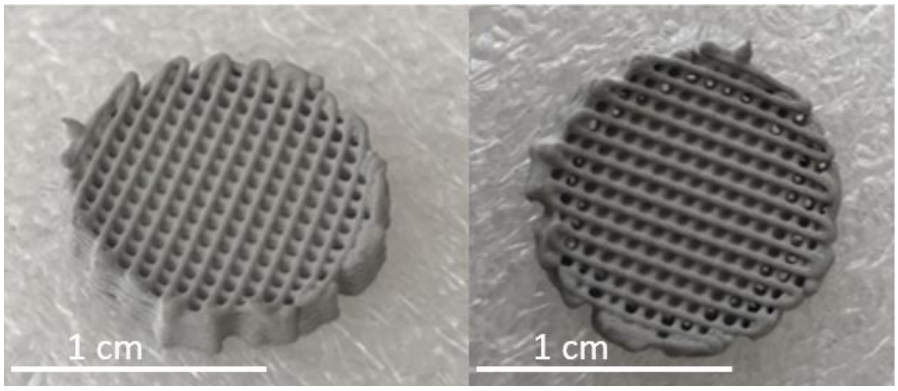


Figure 4.10: Images of the printed parts of ZK30 with a nozzle of 400 μm

4.2.3 Debinding and sintering

To determine the appropriate temperature for debinding the Mg structures, thermogravimetric analysis (TGA) was performed on a printed part after drying, therefore containing the binder and the powder. The TGA was conducted using a TGA Q50 analyser equipped with an EGA furnace (TA Instruments, New Castle, USA). Mass losses were measured during a heating cycle performed at 5 °C/min from room temperature to 500 °C under a flow of 150 mL/min Argon (after a purging step).

The degradation rate observed during TGA is consistent with that of the binder alone, as reported by [201], indicating that the presence of powder does not affect the degradation profile, as depicted in Fig.4.11. The initial mass at 101 % corresponds to water intake, while the total mass loss of 4.6% aligns with the ethyl cellulose (EC) content in the ink (Tab. 4.2).

Thèse accessible à l'adresse : https://theses.insa-lyon.fr/publication/2025ISAL0008/these.pdf © [J. Moreau], [2025], INSA Lyon, tous droits réservés

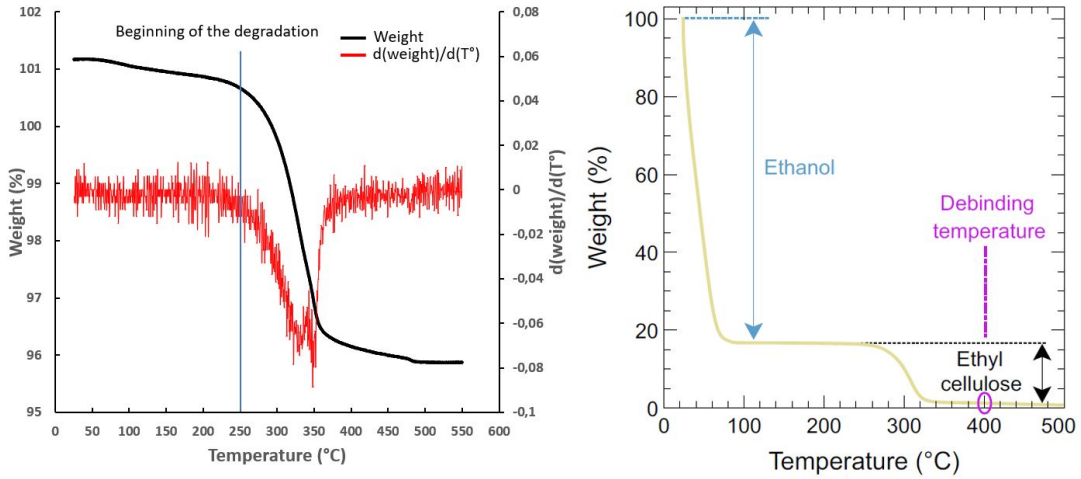


Figure 4.11: a) TGA results of the printed part at a 5 °C/min rate until 600 °C and the derivative of the mass in function of the temperature. The derivative highlights the beginning of the degradation at 250 °C, at 400 °C the degradation is completed. b) The TGA results of the ink without powder taken from [201]

With the same conditions, a TGA of the raw powder was performed to see if the debinding temperature showed a mass increase due to the oxidation. The TGA results are visible in Fig.4.12.

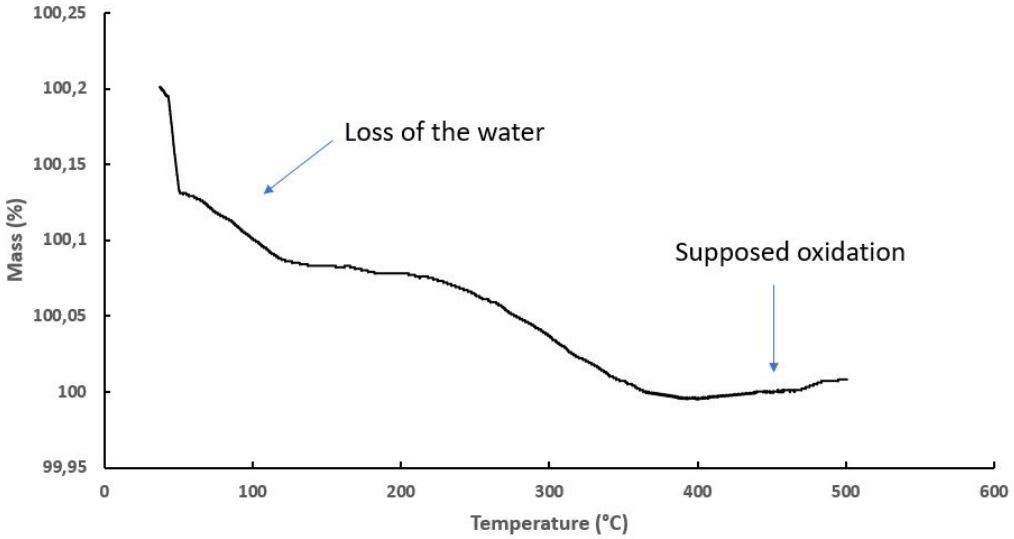


Figure 4.12: TGA results of the raw powder at 5 °C/min under Ar

Due to the possible reaction of the Mg with the platinum contained in the apparatus it is difficult to perform a slow ramp or a plateau. Thus, a ramp of 5 °C/min was applied with an immediate stop when the 500 °C are reached. As observed before the mass is higher than 100 % due to the water intake of the powder. There is a slight mass loss until 400 °C and then a slight

Thèse accessible à l'adresse : https://theses.insa-lyon.fr/publication/2025ISAL0008/these.pdf © [J. Moreau], [2025], INSA Lyon, tous droits réservés

increase of the mass around 450 °C. This increase might be attributed to oxidation. However, it is difficult to conclude because the mass increase of the oxidation may start earlier and be hidden in the mass loss. Nevertheless, oxidation doesn't seem to happen at 400 °C.

Based on these TGA results, a debinding temperature of 400 °C was selected because most of the debinding processes are nearly complete at this temperature, and higher temperatures could involve more oxidation. The debinding cycle chosen is a ramp of 3.5 °C/min to 400 °C followed by a 4 h step at 400 °C under a dynamic primary vacuum (5×10^{-2} mbar) to completely remove the binder.

After debinding, samples were characterized to confirm the success of the process. XRD patterns were acquired between 20 and 60° 2θ since this range includes the five main Mg diffraction peaks, with the same parameters as described in Section.3.1.5 XRD pattern of debinded samples presented on Fig 4.13.a shows the 5 same peaks as initial powder pattern, meaning that no crystallographic transformation occurs during the debinding process. Additionally, the SEM image of a dried sample shown on Fig. 4.13.b reveals the presence of ethyl cellulose around the contact points between particles. In comparison, the SEM image of the debinded sample Fig. 4.13.c confirms successful binder degradation, with no observable changes in particle morphology. These results indicate that the debinding step was successful, leaving only the sintering stage to achieve the final properties.

Following debinding, the next step is sintering. Due to the challenges associated with sintering, multiple conditions were tested, which will be discussed in the following sections.

4.3 Preliminary study and challenges of the sintering

The initial sintering conditions were based on the first experiments performed by Coffigniez *et al* [201], using a Naberthermn N 11/hr furnace enabling to work under various atmosphere conditions. Details of the setup and modifications are provided in Appendix.4.6. Vacuum conditions were deemed unsuitable for sintering due to the high volatility of Mg. Indeed, at 600 °C the vapour pressure of Mg has been reported to be comprised between 10^{-3} and 10^{-2} atm so between 1 and 10 mBar [215]. This means that a dynamic vacuum, even a primary vacuum, would lead to the continuous vaporization of the sample, as continuous pumping would prevent the sample from reaching equilibrium with its partial pressure. This issue was not encountered during the debinding stage, as the vapour pressure of Mg is comprised between 10^{-3} and 10^{-2} mBar at 400 °C , and the primary pump achieves vacuum levels around 0.05 mBar. Coffigniez *et al* initially found that sintering pure Mg in a quartz tube under static primary vacuum was problematic due to oxidation occurring between the quartz and Mg. Switching to a steel tube to prevent oxidation was also unsuccessful. The most successful approach involved using a quartz tube with the printed part enclosed in a 304L steel sheet surrounded by iron powder. This method confined Mg vapor close to the sample, which might have enhanced sintering, though the quartz still allowed some MgO phase to remain in the samples.

Based on these findings, a new experimental setup was developed in the same furnace. The static primary vacuum was replaced by a slight argon overpressure. The vacuum was switched to argon to try the same conditions as Wolff *et al* [190], also because it could help keeping the Mg vapor close to the sample compared to vacuum. The steel tube was substituted with a molybdenum tube, which is considered inert to Mg vapor. The setup now included a graphite sheet and Mg powder instead of the steel sheet and iron powder. The graphite sheet could

Thèse accessible à l'adresse : https://theses.insa-lyon.fr/publication/2025ISAL0008/these.pdf © [J. Moreau], [2025], INSA Lyon, tous droits réservés

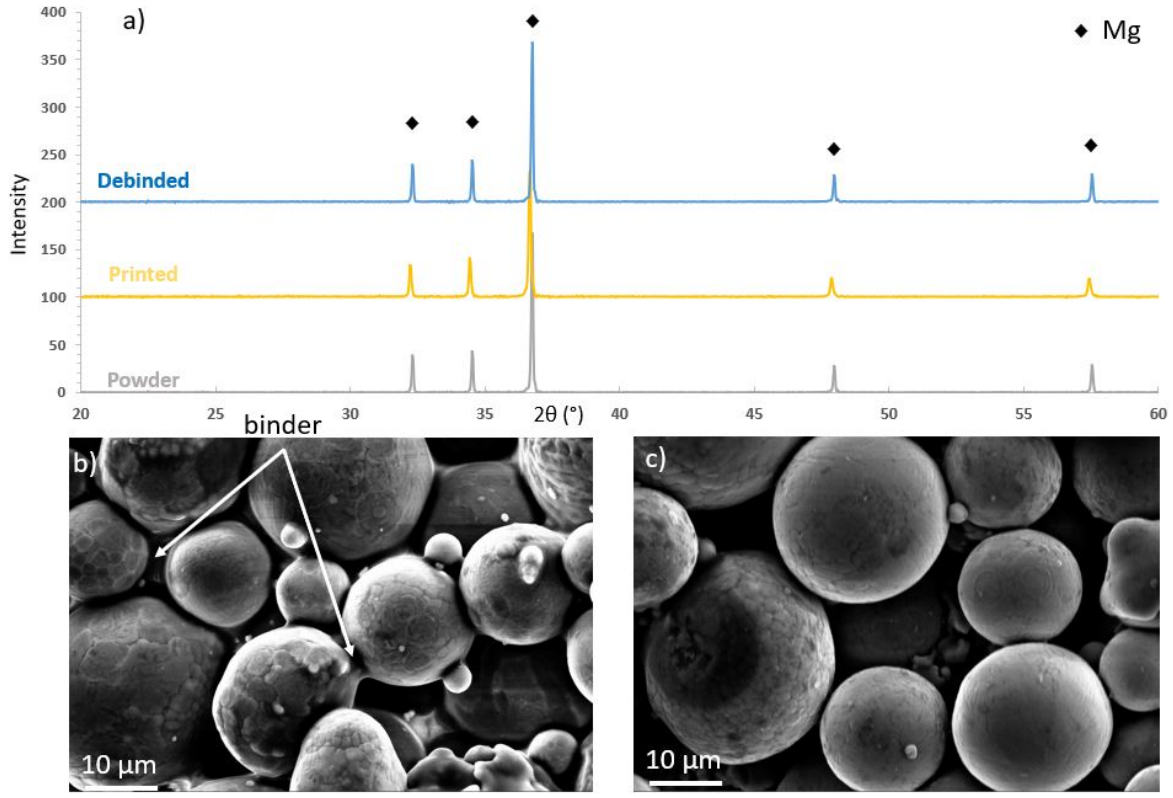


Figure 4.13: Characterization of the debinding step: (a) XRD pattern of both as-received powder and debinded sample showing only Mg peaks; (b) SEM image in SE of a dried sample highlighting the presence of ethyl cellulose around the points of contact between particles; (c) SEM image of a debinded sample highlighting the success of the debinding step.

provide a reductive environment and weaken the oxide layer, carbon also remain inert with Mg for temperature up to 650 °C [216]. While the Mg powder aimed to increase the vapor of Mg and protect the green parts from oxidation by reacting with surface oxygen. The setup is represented in Fig.4.14.a. It is important to note that in this cycle, debinding was performed prior to sintering, within the same heat cycle, similar to the approach used by Wolff *et al* [190]. Thus, in every sintering cycle, a debinding step of 4 h at 400 °C is included.

The goal was to sinter the ZK30 alloy through super-solidus sintering, which involves forming a liquid phase to break through the oxide layer. The liquid phase must be sufficient to break the oxide layer while low enough to maintain the shape of the printed object. According to the DSC results and liquid fraction calculus in Section2.4.1, trials were conducted at temperature above 580 °C, which is believed to be the solidus temperature. The heating ramp was set to 10 °C/min to align with DSC experiments. Controlling the liquid fraction is crucial, as the right amount enhances sintering [217]. However, the optimal liquid phase content needed to effectively perform liquid phase sintering and break the oxide layer remains uncertain.. According to German [213], the content can vary to 5% up to 65% depending of the alloying elements. However, successful sintering of Mg-1Ca was performed at 8 wt% by Wolff *et al* [190], which could indicate that the appropriate liquid fraction for the ZK30 alloy is close to this value.

Thèse accessible à l'adresse : https://theses.insa-lyon.fr/publication/2025ISAL0008/these.pdf © [J. Moreau], [2025], INSA Lyon, tous droits réservés

Various temperatures and sintering durations were tested, ranging from 580 °C to 630 °C, and from 10 h up to 60 h. Most samples, due to their aspect, seemed to exhibit insufficient sintering, with visible liquid bubbles on the surface, as shown in Fig.4.14.b.c.

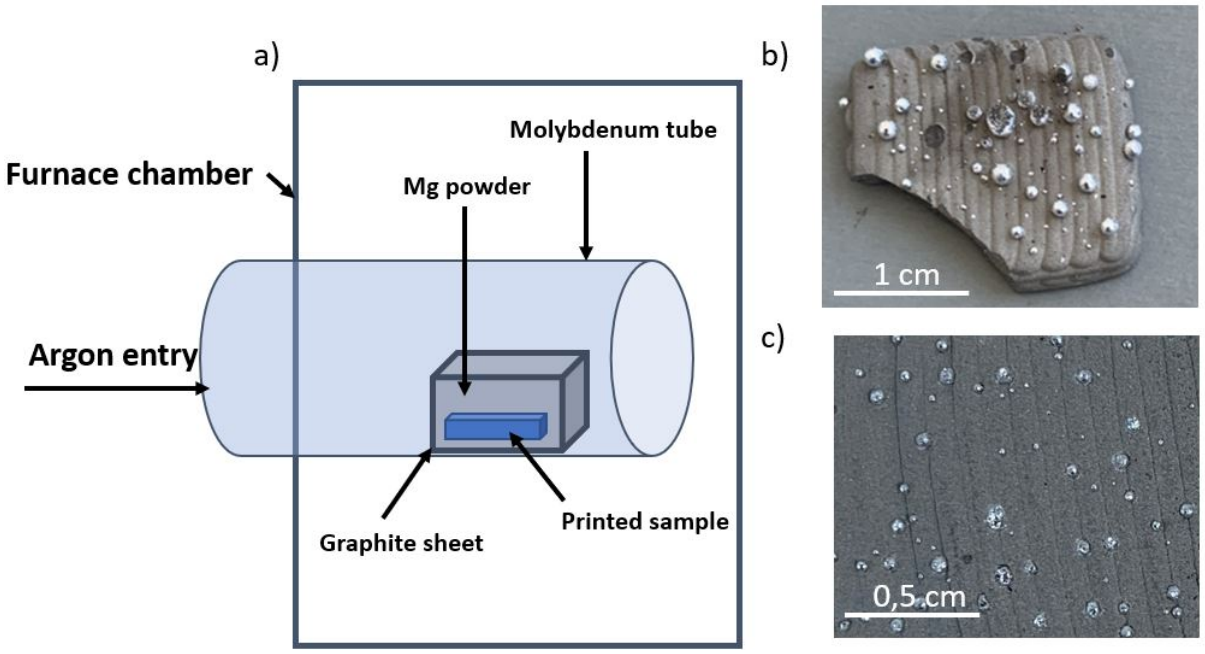


Figure 4.14: Representation of the setup used for the sintering experiments and images of the formation of bubble at the surface after sintering for scaffold sintered at b) 630 °C for 10h and c) 600 °C for 20h

The microstructures of the scaffolds were systemically observed to identify possible sintering issue. The microscopic observations confirmed that sintering of the parts did not occur. Microstructures mainly consisting of non-sintered powder grains, with some areas indicating the presence of liquid. Due to the brittleness of the samples caused by the lack of sintering, observations were challenging. The samples were delicately manually polished and observed as visible in Fig.4.15.

The observations revealed that while some sinter necks between particles were present, they were very sparse. Images showed that some powder grains appeared empty, with only an oxide shell remaining. This indicates that the lack of effective sintering is due to inadequate wetting between the liquid phase and the MgO layer. Although some of the oxide layers were broken, enabling the formation of necks, others allowed the liquid to flow either to the surface or to the bottom of the part. Due to gravity, the liquid phase predominantly accumulated at the bottom of the scaffold, as shown in Figure 4.16, thereby preventing effective (LPS).

After multiple trials with varying parameters, a cycle of 60 h at 600 °C resulted in a part that appeared sintered and could be handled with sufficient mechanical strength. The part was observed in SEM after ionic polishing, the results are shown in Fig.4.17. The EDX analysis of the surface did not indicate a higher concentration of oxygen in the network, which could be due to material reaction with air despite precautions to protect it.

The SEM images reveal a network forming around the original powder grains. The liquid

Thèse accessible à l'adresse : https://theses.insa-lyon.fr/publication/2025ISAL0008/these.pdf © [J. Moreau], [2025], INSA Lyon, tous droits réservés

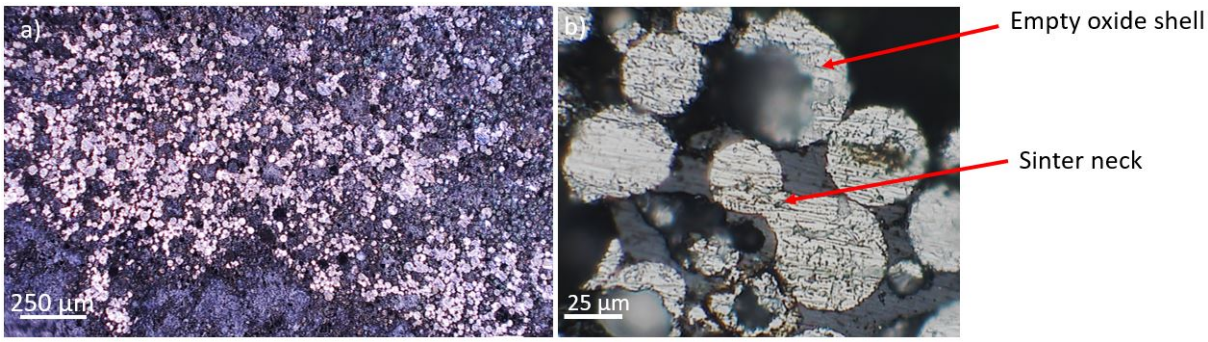


Figure 4.15: Optical micrography of a scaffold sintered at 600 °C for 18 h, and b) observation of a sintering neck that formed during sintering

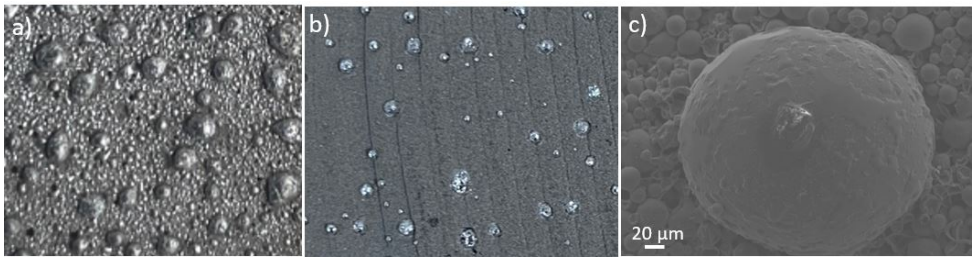


Figure 4.16: Images of the liquid at the surface of the scaffold after sintering at the a) bottom and b) the top. Showing that due to gravity the liquid tended to flow to the bottom and c) SEM image of the liquid at the surface

phase was able to break through the oxide layer on each grain and fill the interstitial spaces, creating a weak network of MgO. This network resulted in significant porosity, as the empty grains contribute to the material's overall porosity. This network, was observed in other material as the last step of liquid phase sintering [205]. The density of the printed part, considering the solid loading in the ink, is around 60%. This suggests a high dihedral angle of the liquid at triple grain junctions, as particles are relatively far apart from each other. For dihedral angles above 60°, the liquid tends to form isolated pockets at the triple points between grains [218] [219]. Furthermore, the distribution of the powder particles in the debinded scaffold is more likely heterogeneous, creating a lot a preferential path for the liquid to flow outside. Consequently, the sintering setup appears to be a dead end. Lowering the temperature to 590 °C with a 60 h sintering time led to non sintered parts. The liquid fraction needed to break the oxide layer is too high, causing excessive liquid formation that prevents proper liquid phase sintering and leaves the powder particles empty, connected only by an oxide network.

4.4 *In situ* tomography of the sintering of Magnesium alloys

Following the issues encountered during sintering, *in situ* sintering tomography was conducted to gain a deeper understanding of the parameters influencing Mg sintering.

Thèse accessible à l'adresse : https://theses.insa-lyon.fr/publication/2025ISAL0008/these.pdf © [J. Moreau], [2025], INSA Lyon, tous droits réservés

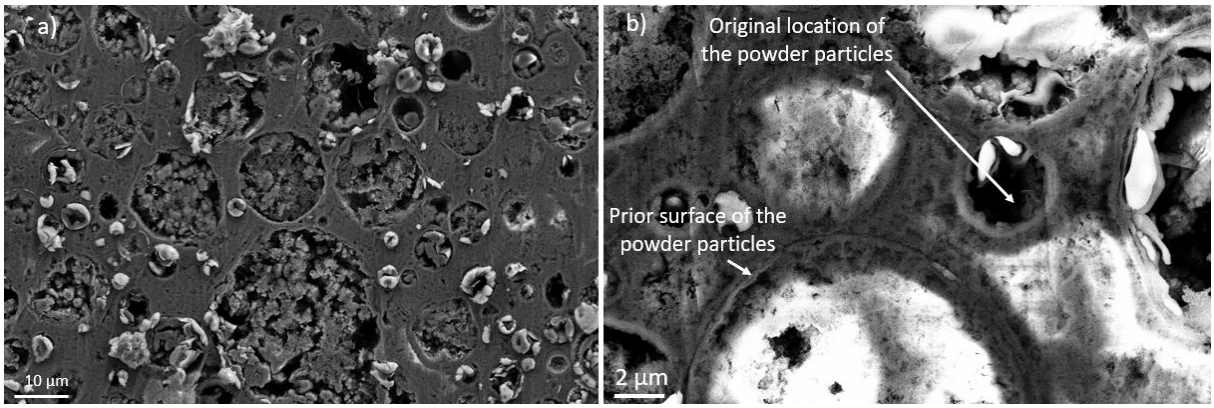


Figure 4.17: SEM observation in SE mode of the scaffold sintered at 600 °C for 60h, showing the oxide network connecting the empty former powder particles

4.4.1 Material and method

4.4.1.1 X-ray nanotomography

X-ray nano-CT experiments were carried out at the ID16B nanoanalysis beamline of the European Synchrotron Radiation Facilities (ESRF, Grenoble, France). This beamline is equipped with a set of Kirkpatrick-Baez (KB) mirror systems. These mirrors focus the incoming parallel X-ray beam onto a small beam size of $50 \times 50\,\mathrm{nm}^2$, which acts as a secondary source. Imaging was carried out at a resolution of 100 nm, providing a field of view of $204 \times 204 \times 204\,\mu\mathrm{m}^3$. 2D phase contrast images of the specimen were recorded during the sample rotation using a CMOS camera. The 3D X-ray nano-imaging was performed *in situ* during the heat treatments. A dedicated furnace can be mounted and removed on the sample to apply a heat treatment at 600 °C without moving the sample, see Fig.4.18. The details of the beam line are reported by G.Martinez-Criado et *al.* [220].

The sample was mounted on a rotating platform to allow imaging during the heat treatment. The furnace was preheated at 600 °C and lowered onto the sample. The imaging time was around 1 min 30 s and each measure was separated by 2 min. The heating was performed for 1 h leading to 20 volumes scans over time.

4.4.1.2 Sample preparation

To conduct the experiment under an argon atmosphere, the ZK30 powder needed to be encapsulated in a quartz tube and mounted on a support. The preparation involved the following steps:

- Encapsulation : Quartz tubes with an internal diameter of 1.5 mm were used. These tubes were filled with ZK30 powder to a height of 2 mm. The powder was manually compacted using a thin rod.
- Rod Selection: Typically, a ceramic rod is used to support the powder. However, because Mg could react with the oxygen present in the ceramic, a graphite rod was chosen instead. This rod was inserted into the quartz tube to support the powder.
- Mounting: The quartz tube was then attached to a support as straightly as possible using

Thèse accessible à l'adresse : https://theses.insa-lyon.fr/publication/2025ISAL0008/these.pdf © [J. Moreau], [2025], INSA Lyon, tous droits réservés

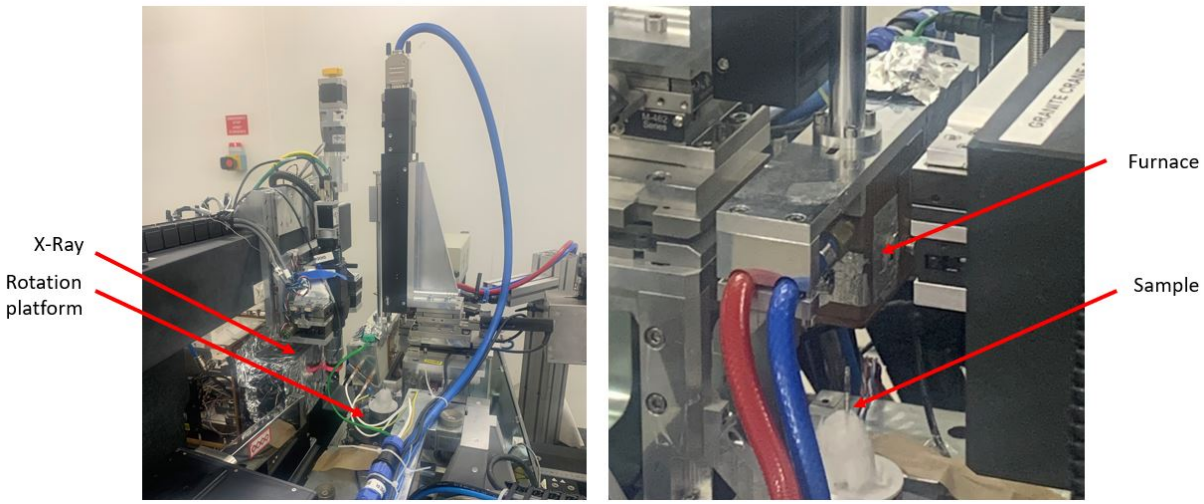


Figure 4.18: Image of the nano-tomography setup at ESRF, with the removable furnace and the quartz tube containing the powder

a ceramic glue. After the adhesive dried, the entire assembly was placed inside a glove box filled with argon.

- Within the glove box, the tube was sealed by filling the bottom of the support with ceramic glue. This step ensured that the argon atmosphere was maintained within the tube, preventing any exposure to oxygen.

This preparation method was crucial to maintaining an inert environment for the Mg powder during the X-ray nano-CT imaging and subsequent sintering experiments.

4.4.2 In situ observation of the sintering

The sintering was observed *in situ*, starting with the initial image taken at t=0. The zone acquired was localized in the middle of the quartz tube. The apparent density and equivalent diameter of the pores were measured Fig.4.19.b.

The packing density is slightly higher than the packing density of the scaffold. The local thickness ImageJ plugin was used to assess the mean distance between the particles. This plugin tries to fit the biggest possible circle in 2D ans sphere in 3D, inside the residual porosity. It gives an idea of the pore equivalent diameter and the average distance between the particles' surfaces. The average distance calculated between the particles is around $2{,}39 \pm 0.1\,\mu$m, meaning the particles were relatively close to each other. Before analyzing the sintering it is necessary to precise that even under argon the quartz tube contains oxygen that can react with the Mg powder, however it was not possible to replace it. After heating, one slice perpendicular to tube axis was analyzed, revealing that the particles showed minimal movement in that dimension, making them easy to track. Several distinct steps were observed during the heating process. At the beginning, what appeared to be the oxide layer also grew in different directions, causing distortion of the particles Fig.4.20a.b. As heating continued, some of the larger particles burst, leaving behind only the oxide shell, while the liquid phase descended due to gravity Fig.4.20.c. Then, the particles were either linked, probably through the oxide, or they burst Fig.4.20.d. Finally, when the densification seemed to reach its final step, more and more particles continued

Thèse accessible à l'adresse : https://theses.insa-lyon.fr/publication/2025ISAL0008/these.pdf © [J. Moreau], [2025], INSA Lyon, tous droits réservés

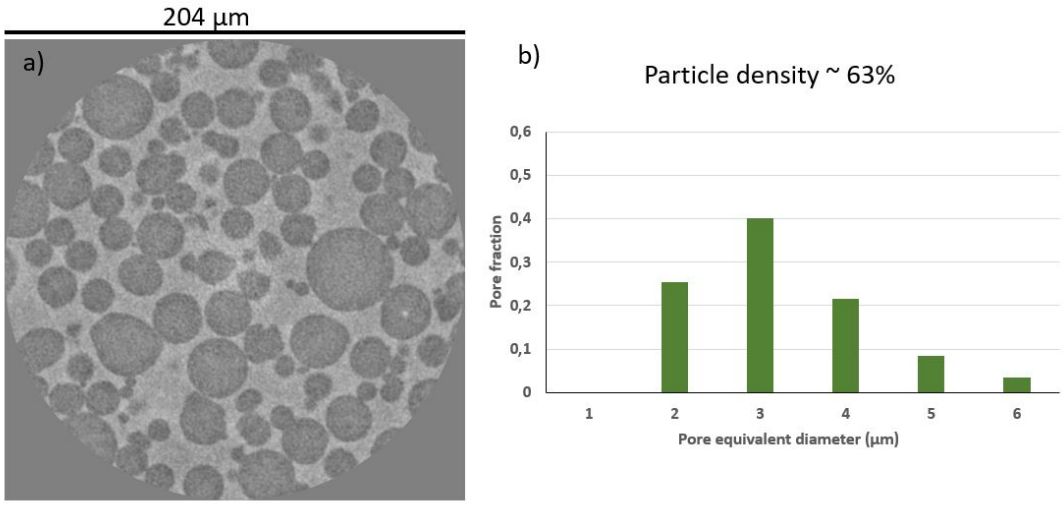


Figure 4.19: a)Tomography slice of the initial state and b) the pore equivalent diameter calculated with the local thickness plugin, measured for this state with a bin size of 1 μm

to burst, creating a network of oxide shells Fig.4.20.e.f, similar to the one observed before in Fig.4.17.

The volume analysis further highlighted the network formation during sintering. A volume of $50 \times 70 \times 20\,\mu m^3$ was isolated. The observations made in 2D were confirmed and expanded upon in 3D. The formation of the oxide shell network became much more apparent, as shown in Fig.4.21. The swelling of the liquid phase leaves behind oxide shells that connect through oxide growth between the powder grains, similar to those seen in Fig.4.17, as depicted in Fig.4.21.e.f.

A single particle was also isolated during the heating process. The sintering steps observed on the volume before are more visible. The sequence of events observed was consistent with the broader observations:

- Oxide growth and bond formation: Initially, the oxide layer around the particle began to grow and establish bonds (blue arrows) with neighboring particles, causing the particle to distort. Fig.4.22.b-d (blue arrows).
- Formation of bonds and densification: As the process continued, more bonds were formed, and it appeared that the final densification stage was approaching Fig.4.22.e.
- Breakage and liquid loss: Eventually the oxide layer broke, and the liquid inside the particle began to escape from the volume Fig.4.22.f.
- Final stages: The liquid continued to flow out, leaving only the oxide shell behind, forming an oxide network Fig.4.22g.h (red arrow).

Several conclusions can be drawn from these experiments. Firstly, conversely to the experimental sintering of the previous section, the different steps occurred much faster. After 1 h of heating a significant fraction of the particles were observed to be empty, which was observed after 60 h previously. This discrepancy could be attributed to the amount of Mg powder used or the confinement within the tube. A very small amount of Mg was introduced into the tube, which could explain the faster mechanisms. Furthermore, the available space in the tube is quite limited and the vapor couldn't leave the surrounding of the powder, which could have

Thèse accessible à l'adresse : https://theses.insa-lyon.fr/publication/2025ISAL0008/these.pdf © [J. Moreau], [2025], INSA Lyon, tous droits réservés

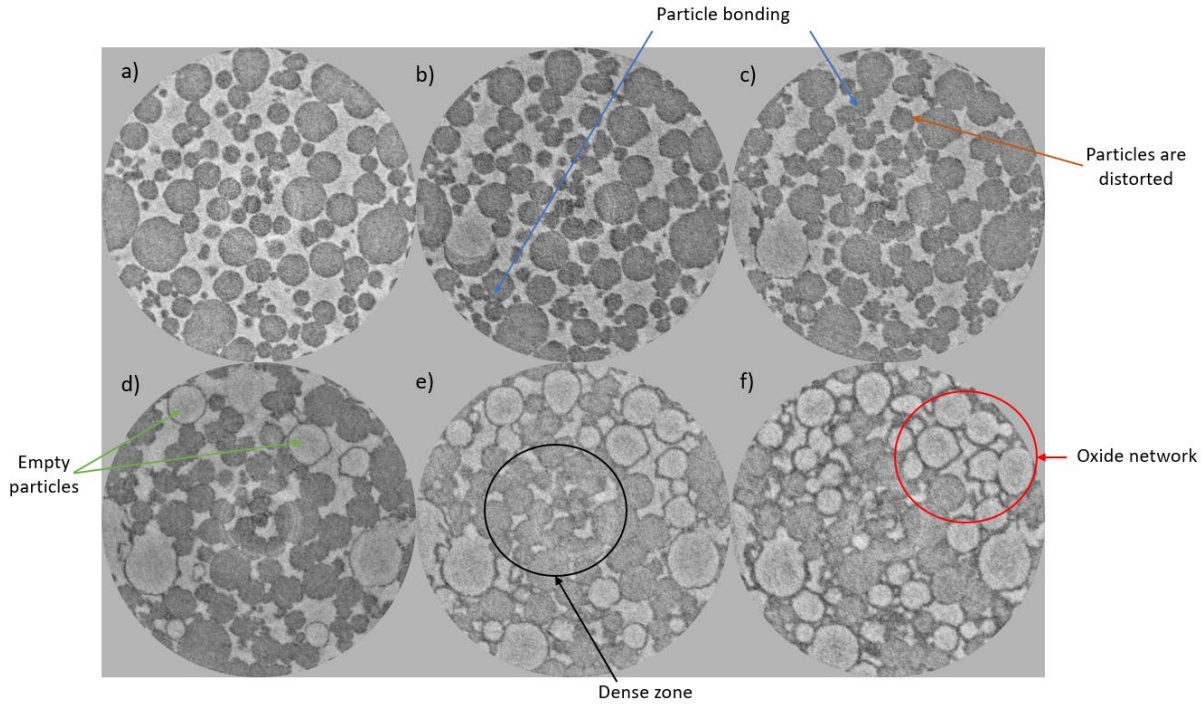


Figure 4.20: Observation of the same slice in the volume after tomography at different times a) 7 min b) 9.5 min c) 13 min d) 20 min e) 45 min and f) 60 min

accelerated the sintering. Lastly, the quartz tube is a large source of oxygen compared to Mo tubes, which could accelerate the oxide growth during sintering.

The conditions used in this experiment did not result in a fully dense part. The apparent density, measured from the acquired volume data, did not exceed 70% over time, as shown in Fig.4.23.

This outcome suggests that the balance between bonding and the flow of the liquid phase is not optimal. The bonding process is too slow, while the particles burst too quickly, preventing the formation of a dense structure. A potential solution could involve decreasing the sintering temperature to reduce the rate of particle expansion and subsequent liquid flow. However, it was previously observed that temperatures below 600 °C did not yield favorable results.

Another approach is to reduce the oxygen content in the sintering atmosphere, which has not yet been explored. Addressing this parameter could potentially enhance the sintering process by minimizing oxidation and improving the densification of the material. In the next section, a new setup designed to lower the oxygen content and better confine the samples will be investigated to address these issues and improve the sintering outcomes.

4.5 Sintering of Magnesium alloys in labyrinth crucible

Following the insights gained from the tomography observations and the initial sintering tests conducted in the molybdenum tube, several strategies were considered to enhance the sintering process. It was decided to use a labyrinth crucible combined with a different furnace setup to

Thèse accessible à l'adresse : https://theses.insa-lyon.fr/publication/2025ISAL0008/these.pdf © [J. Moreau], [2025], INSA Lyon, tous droits réservés

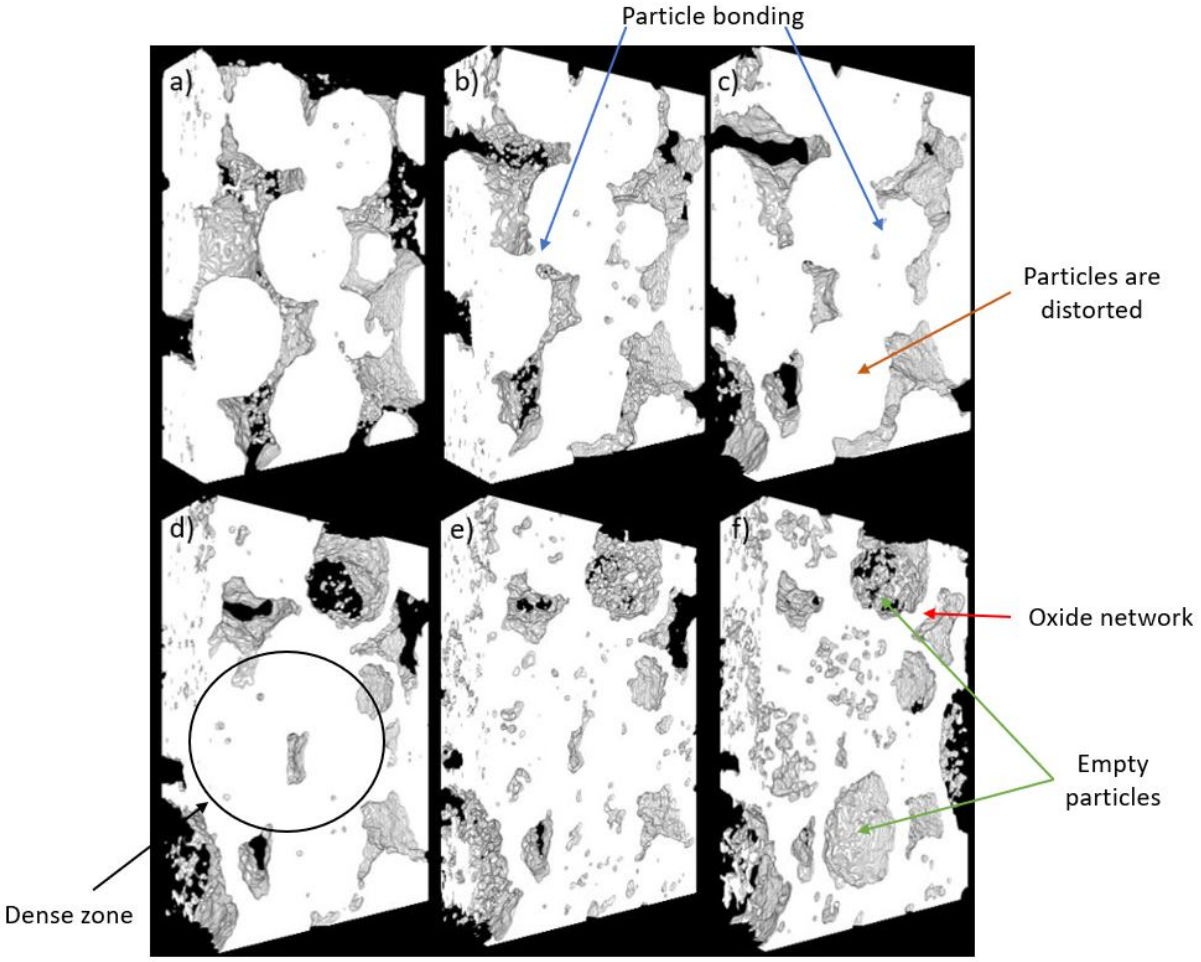


Figure 4.21: Observation, of a volume during the heating at different times, a) 7 min b) 13 min c) 20 min d) 40 min e) 45 min and f) 60 min

more effectively purify the atmosphere and reduce the oxygen content.

The labyrinth crucible was selected for its ability to provide a more controlled environment and minimize oxygen exposure during sintering. Its design includes multiple passages that help trap and neutralize oxygen, thereby creating a more favorable atmosphere for the sintering of Mg alloys. This approach aims to mitigate oxidation and enhance the LPS, leading to better densification of the printed Mg parts. The effectiveness of this setup will be evaluated in the subsequent experiments.

4.5.1 Initial samples

To identify more precisely the issue with the sintering and assess the impact of the DIW, die-pressed samples were prepared. This approach aimed to eliminate the debinding step and its associated interactions with the binder, which are believed to introduce additional oxygen into the samples, as indicated in Table 4.3). For the scaffold, the debinding remained the same at 400 °C for 4 h. However, in this experiment, debinding was performed prior to sintering, rather

Thèse accessible à l'adresse : https://theses.insa-lyon.fr/publication/2025ISAL0008/these.pdf © [J. Moreau], [2025], INSA Lyon, tous droits réservés

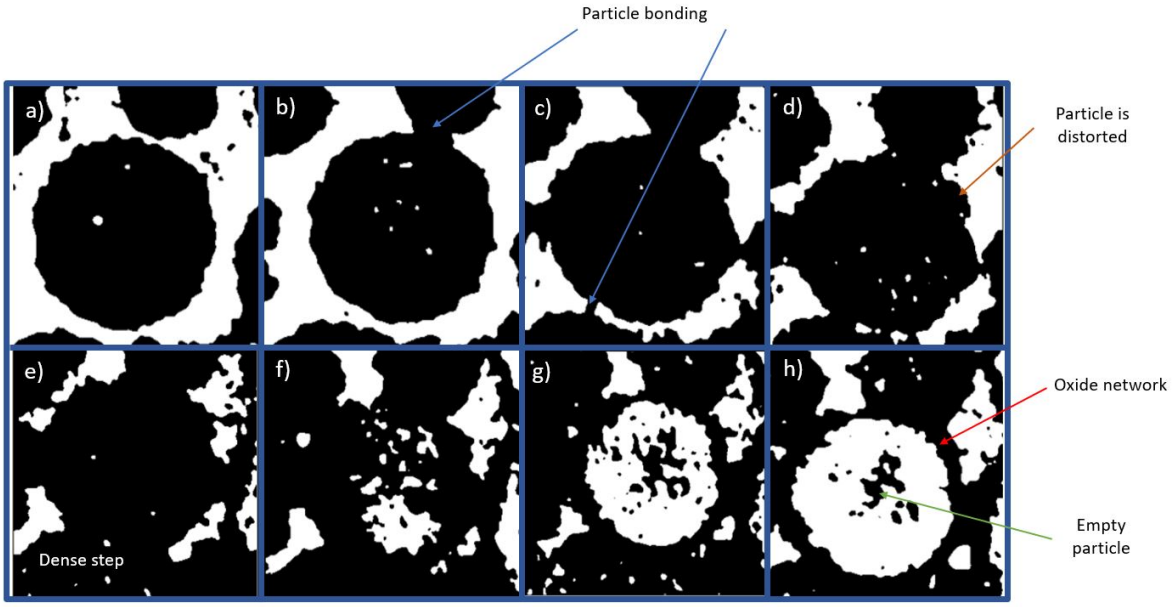


Figure 4.22: a-h) Observation of a particle after binarisation from ImageJ during the heating at regular interval from t = 0 to t = 25 min, with the void in white and the material in black.

than simultaneously. This change may facilitate the sintering by removing the degraded species from the binder from the atmosphere. The oxygen concentration was measured with the protocol detailed in section.2.2.6.

Sample	Oxygen concentration (wt%)
Powder of ZK30	0.17 ± 0.01%
Debinded scaffold	0.68 ± 0.12%

Table 4.3: Evolution of the oxygen concentration during the printing process and comparison with the die-pressed pellet

The printing and debinding steps brought a lot of oxygen into the powder due to the reaction with the binder at ambient temperature and at 400 °C, leading to a oxygen concentration four times more important than the original powder. The die-pressed pellet and the debinded scaffold were observed under μCT-tomography with a resolution of 1 μm, as visible in Fig.4.24.

Die-pressing of the powder resulted in a relative density of 70%, as evidenced by tomography scans. This high density is attributed to the deformation of the powder grains under pressure, which is not visible on the tomography scan. Conversely, the debinded scaffold achieved only 60% relative density due to the DIW process, as expected given the solid loading of 60 vol% in the ink. The relative density of the as-printed filament was also 60%, indicating that the debinding process did not modify the relative density. Analysis of interconnected pore thickness reveals an average distance of approximately $3-4\,\mu$m between the powder particles surfaces in the pellet, with a narrower distribution around this value compared to the less homogeneous distribution in the debinded scaffold resulting from printing. In the debinded scaffold, the average distance between powder particles is approximately $6-7\,\mu$m, with a maximum of $9\,\mu$m, a significant

Thèse accessible à l'adresse : https://theses.insa-lyon.fr/publication/2025ISAL0008/these.pdf © [J. Moreau], [2025], INSA Lyon, tous droits réservés

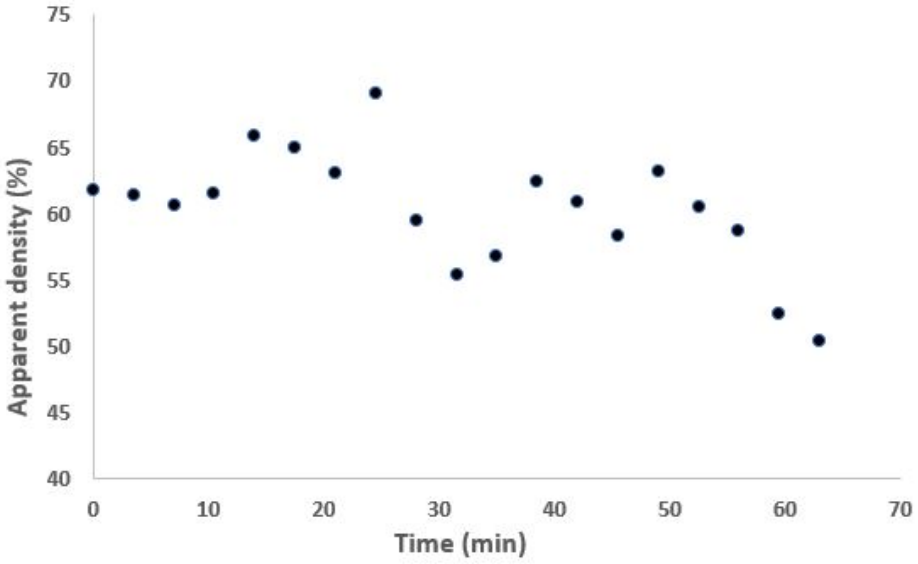


Figure 4.23: Evolution of the apparent density inside the studied volume during the heating with a maximum observed at 25 min

spacing considering the powder's D50 value of 25.6 μm. The observation of the pore distribution indicates that the densification of the printed parts is more difficult due to the larger space between powder particles. It would have been interesting to manufacture pellets with the same density as the printed part, but without the binder at 60% realtive density they didn't retain their shape.

4.5.2 Sintering setup

The sintering process was carried out in a hot wall furnace (XRetort, Xerion). Identically to the first study, multiple temperatures between 580 °C and 630 °C and duration between 10 h and 60 h were tested. This furnace allow to work under a continuous flow of argon to minimize the oxygen content. Before beginning the sintering cycle, two primary vacuum steps were performed to clean the furnace. The complete cycle was performed under Argon (purity > 99,999 %) with a first ramp of 2 h until the final temperature followed by a 10 to 60 h dwell at this temperature. The cooling rate was not controlled but was measured at about 100 °C/h. The flow of Argon was maintained at 7 L/min during the whole process. The cycle is depicted in Fig.4.25.

A labyrinth like crucible inspired by Wolff *et al* [190] was designed, as visible in Fig.4.26. It consists of a large outer molybdenum crucible, in which are introduced two small steel (316L) crucibles containing the sample. A steel cover is put on top of the steel crucibles but allow the atmosphere to pass below. Protective powder of Mg is introduced around the steel cover and then the molybdenum cover is put at the end. Protective powder was employed to purify the atmosphere and the labyrinth shape allowed a circulation of the atmosphere through the powder.

Thèse accessible à l'adresse : https://theses.insa-lyon.fr/publication/2025ISAL0008/these.pdf © [J. Moreau], [2025], INSA Lyon, tous droits réservés

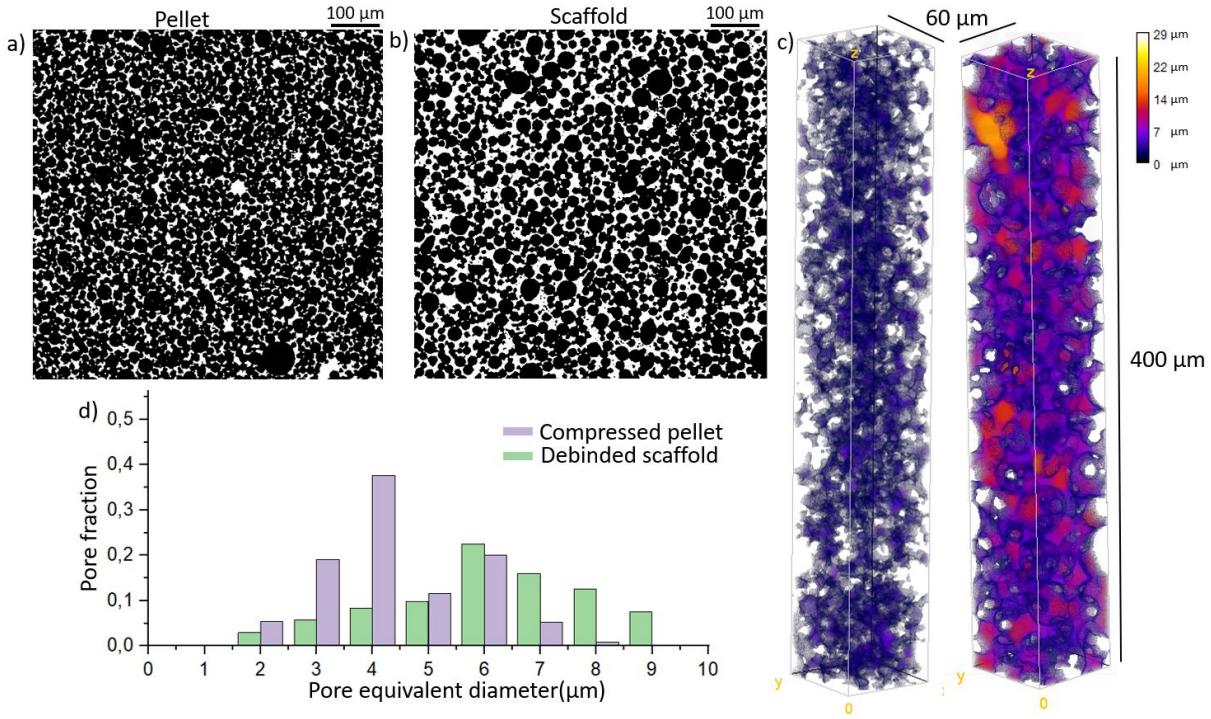


Figure 4.24: a)b) Remaining porosity in the pellet and the debinded scaffold. c) μ-CT scan with a local thickness calculation on the pore calculated on a $60\times60\times400\,\mu$m volume for the pellet and the debinded scaffold. d) Pore distribution according to the local thickness calculation showing the average size of the pore.

4.5.3 Sintering tests

The initial tests were carried out with various parameters, see (Table.4.4). The results were similar to previous experiments, with an absence of sintering with some areas showing the presence of a liquid phase.

Sample	Temperature (°C)	Duration (h)
Debinded scaffold	580	30, 40, 60
Debinded scaffold	600	10, 20, 30, 60
Debinded scaffold	620	10, 20
Debinded scaffold	630	10

Table 4.4: Summary of the tested parameters for the sintering in the labyrinth crucible

However, these results were somewhat encouraging, as the regions where liquid appeared and remained within the sample were more frequent compared to earlier tests. This suggests that the sintering process was better. One identified issue was the lack of confinement of Mg vapor near the sample. The steel crucible used in the setup was 5 cm in height, while the parts were less than 1 cm thick. This configuration allowed the vapor to stay within the crucible but at a considerable distance from the sample, reducing its effectiveness in promoting sintering.

To address this, the setup was modified to operate on a smaller scale, improving vapor

Thèse accessible à l'adresse : https://theses.insa-lyon.fr/publication/2025ISAL0008/these.pdf © [J. Moreau], [2025], INSA Lyon, tous droits réservés

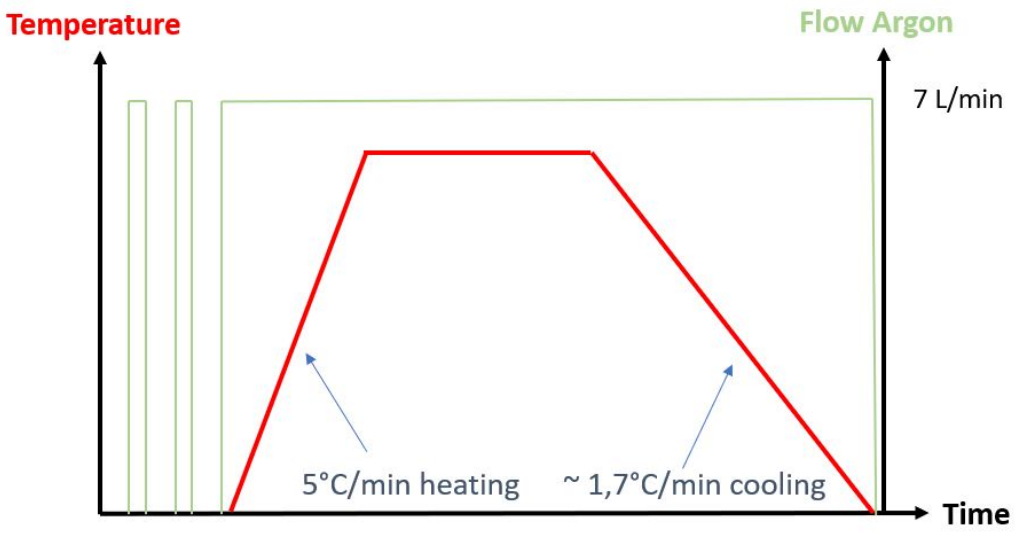


Figure 4.25: Sintering cycle used with the temperature and the evolution of the Argon with two vacuum steps prior to the increase of temperature

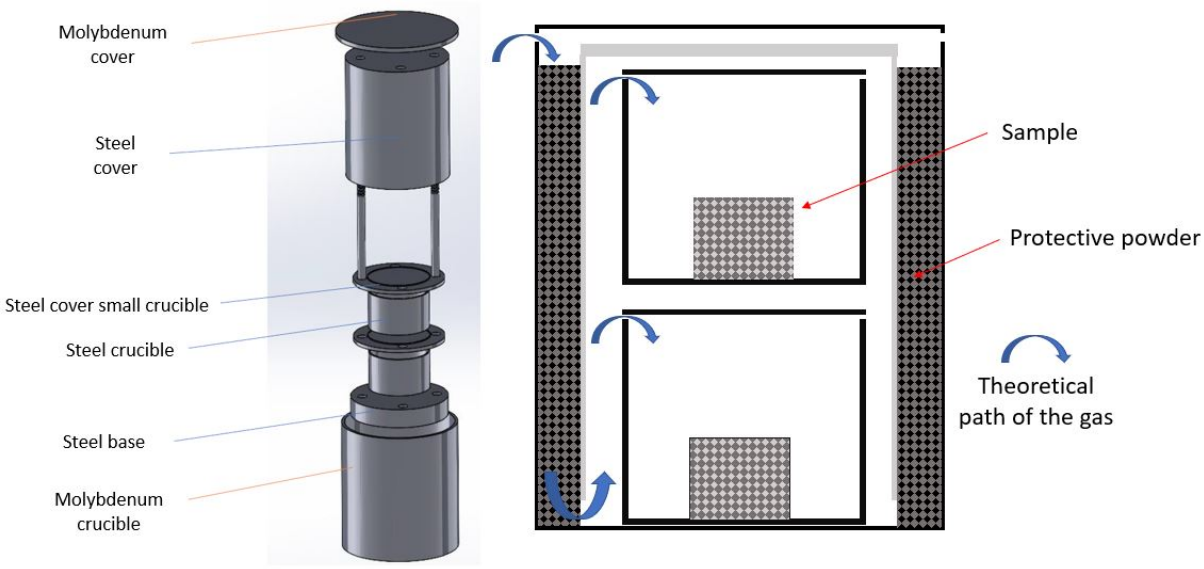


Figure 4.26: Scheme of the designed crucible for sintering in a protective atmosphere. With the path of the gas through the powder visible

confinement. The steel crucible was retained as the base, but a graphite part was added around the sample to keep the Mg vapor closely confined. Additionally, a graphite sheet was also added to protect the crucible from the Mg powder. These modifications aimed to create a more controlled and effective sintering environment. The new setup is visible in Fig.4.27.

Using this setup for the first time the scaffold was sintered in a cycle of 600 °C and 10 h. Areas successfully sintered were visible but it was still incomplete Fig.4.28.a. The duration was increased to 20 h with success obtaining a fully sintering scaffold, as visible in Fig.4.28.b. As

Thèse accessible à l'adresse : https://theses.insa-lyon.fr/publication/2025ISAL0008/these.pdf © [J. Moreau], [2025], INSA Lyon, tous droits réservés

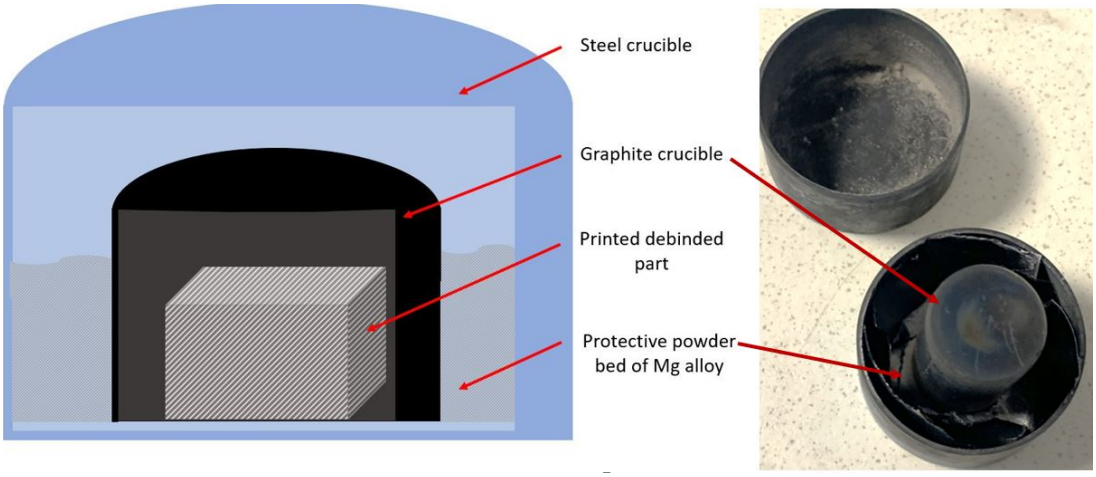


Figure 4.27: Scheme and image of the improved crucible and it's components, with a protective bed composed of ZK30 powder

visible on the image, the sintering is more advanced for 20 h. There were fewer bubbles on the surface, indicating that the liquid phase remained within the part rather than escaping, which is a positive sign of successful sintering. For the die-pressed pellet, a cycle of 10 h at 600 °C was sufficient to achieve successful sintering.

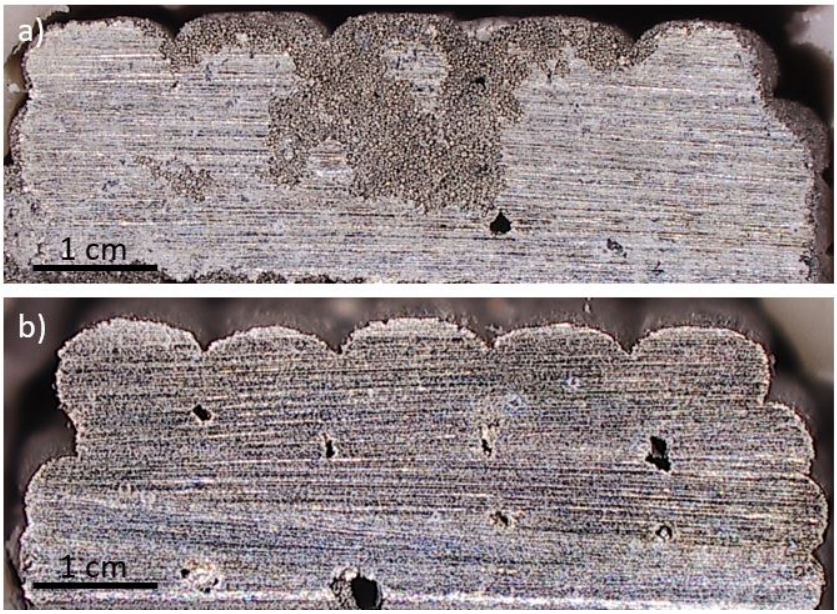


Figure 4.28: Optical micrograph of the two sintered scaffolds at a) 600 °C for 10 h and b) at 600 °C for 20 h, with an improvement visible at the middle of the scaffold when increasing the sintering duration as the upper middle zone is not sintered for a 10 h sintering.

Thèse accessible à l'adresse : https://theses.insa-lyon.fr/publication/2025ISAL0008/these.pdf © [J. Moreau], [2025], INSA Lyon, tous droits réservés

4.5.4 Microstructure and hardness

Following the first success of sintering, the samples were prepared using ionic polishing and were examined using SEM analysis, depicted in Fig. 4.29. For the pellet, the structure appears nearly fully dense, with the former powder particles surrounded by a thin layer of MgO, as observed in the image. For the scaffold, the structure resembles more an interdigitate network of powder grains connected by sintering necks. The hardness of the samples was measured and compared to the hardness of the as-cast alloy [221] (Table. 4.5).

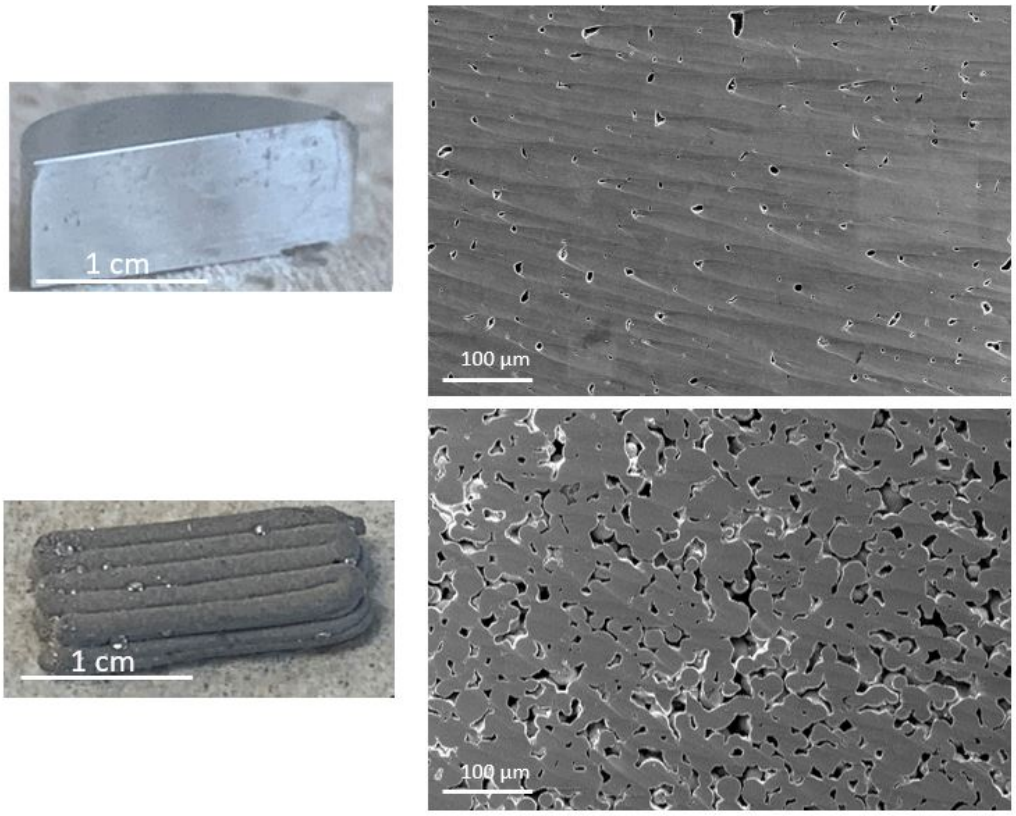


Figure 4.29: Pictures of the pellet and scaffold after the sintering and the corresponding observation of the microstructure, highlighting the differences in relative density after sintering

Sample	As-cast ZK60	SPS sample	Annealed SPS sample	Pellet	Scaffold
Hardness (HV)	70	54 ± 3	70,2 ± 3,4	64.7 ± 2.1	51 ± 2.1

Table 4.5: Hardness comparison between the ZK30 alloy using different processes. As-cast alloy of ZK60 is from [221].

The hardness of the pellet closely resembles that of the as-cast alloy, with a slight variation possibly attributed to differences in density or microstructure. Furthermore, the hardness of the pellet is higher than the sample after SPS at 580 °C but lower than the one after annealing. The slow cooling during sintering may induce annealing or precipitation of MgZn precipitates [79], but not completely as the hardness is lower than annealed sample. In contrast, the scaffold

Thèse accessible à l'adresse : https://theses.insa-lyon.fr/publication/2025ISAL0008/these.pdf © [J. Moreau], [2025], INSA Lyon, tous droits réservés

exhibits lower hardness due to reduced density and thin sintering necks, resulting in less particle contacts.

4.5.4.1 Porosity

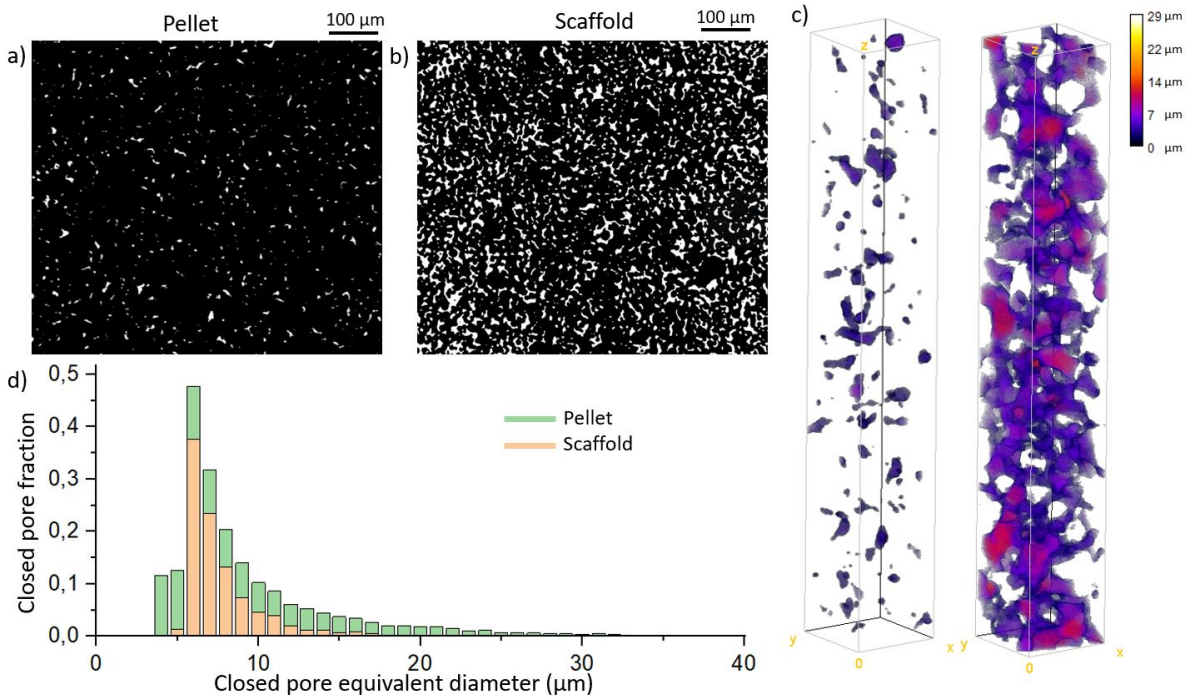


Figure 4.30: a)b) Remaining porosity in the sintered pellet and scaffold. c) μ-CT scan with a local thickness calculation on the pore calculated on a $60\times60\times400\,\mu m^3$ volume for the sintered pellet and scaffold. d) Pore distribution according to the local thickness calculation showing the average size of the pore.

After sintering the two distinct parts, the remaining porosity was quantified using X-ray tomography with a resolution of $1\,\mu$m, with results depicted in Fig. 4.30. The density of the debinded scaffold reached 80%. Analysis from tomography reveals that the pores mainly consist of an open interconnected porosity, with a closed pore fraction of only 0.05%. In contrast, the pellets achieve a density of 98.5%, primarily due to superior initial apparent density. Additionally, the closed porosity fraction is higher reaching 84% of the total porosity, with only small pores remaining, mostly around $6-7\,\mu$m equivalent diameter. In comparison, the sintered scaffold exhibits a broader distribution of pore sizes, with pores reaching up to $30\,\mu$m equivalent diameter, indicating that the initial porosity expanded during sintering.

4.5.4.2 Sintering mechanisms

Two distinct sintering progresses are observed, resulting in varying densities of 98,5% for the pellet and only 80% for the scaffold. We will investigate the causes of this variations between the two parts.

The distribution of pores plays a crucial role in these differences, as observed in various

Thèse accessible à l'adresse : https://theses.insa-lyon.fr/publication/2025ISAL0008/these.pdf © [J. Moreau], [2025], INSA Lyon, tous droits réservés

mechanisms during liquid-phase sintering, leading to variations in size, shape, and distribution of phases [205]. Liden *et al* [222] emphasized the impact of a homogeneous green structure on the sintering. Inhomogeneous pore distributions can create preferential paths for liquid filling, resulting in bubble formation at the surface, as observed in our study in the scaffold at higher liquid fractions.

In the die-pressed pellet, the majority of pores exhibit an equivalent diameter of $3 - 4\,\mu$m, indicating effective powder stacking facilitated by the applied pressure. Conversely, in the debinded scaffold, pores are evenly distributed from 2 to $9\,\mu$m, with a slight majority at $6\,\mu$m, the inhomogeneity in the paste reflects on the porosity with a non optimal stacking.

To further investigate this observation, the crystallographic grains were observed using EBSD as shown in Fig. 4.31).

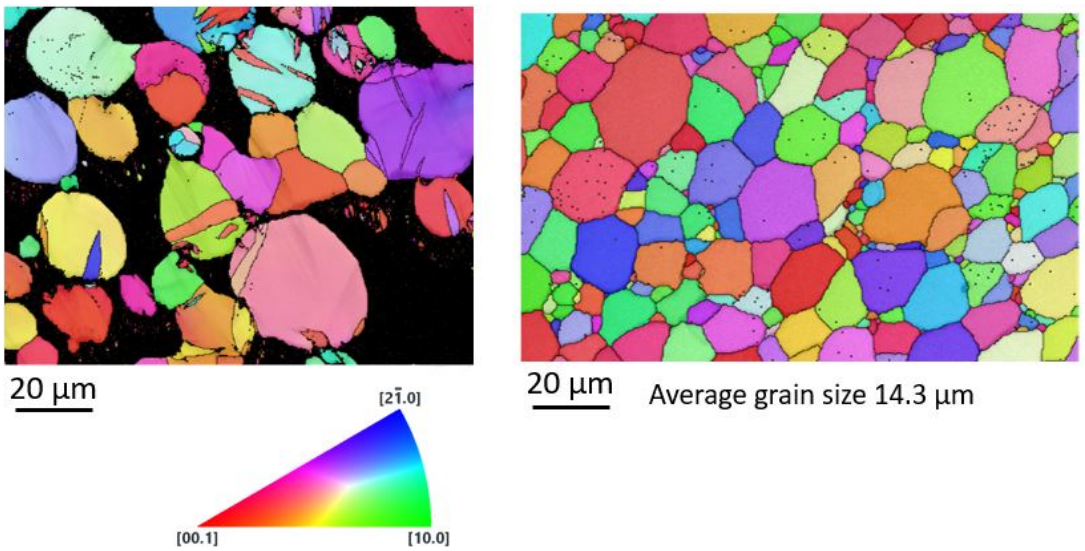


Figure 4.31: EBSD maps of the a)scaffold and the b) pellet with an IPFZ map showing the differences of the grains between the two processes.

As observed on the EBSD maps Fig. 4.31, for the scaffold, the crystallographic grains mainly consist of one powder particle, with some grains that look to have nucleated at the sintering necks. For the pellet, similarly, the powder particles mainly contain one crystallographic grain. Furthermore, small grains seem to have nucleated at the grain boundary junction. They could correspond to the formation of pocket of liquid to eliminate the pores.

This two different observations may show the impact of the initial green density on the sintering. For a low green density like the scaffold, the powder particles maintain an almost spherical shape, except at their contact points with other particles. However, at higher solid-phase fractions, the powder particles faces flatten to eliminate pores, and the liquid forms pockets at the powder particles free surfaces.

Another possible explanation for the differences observe between the two structures is the use of mechanical pressure prior to sintering in the die-pressed pellet. The powder particles within the pellet were observed prior to sintering, as depicted in Fig.4.32. It shows that some powder particles are already pressed into each other. Furthermore, a cracked layer is visible at the surface, which is probably the oxide layer who broke due to the pressure. This breaking may

Thèse accessible à l'adresse : https://theses.insa-lyon.fr/publication/2025ISAL0008/these.pdf © [J. Moreau], [2025], INSA Lyon, tous droits réservés

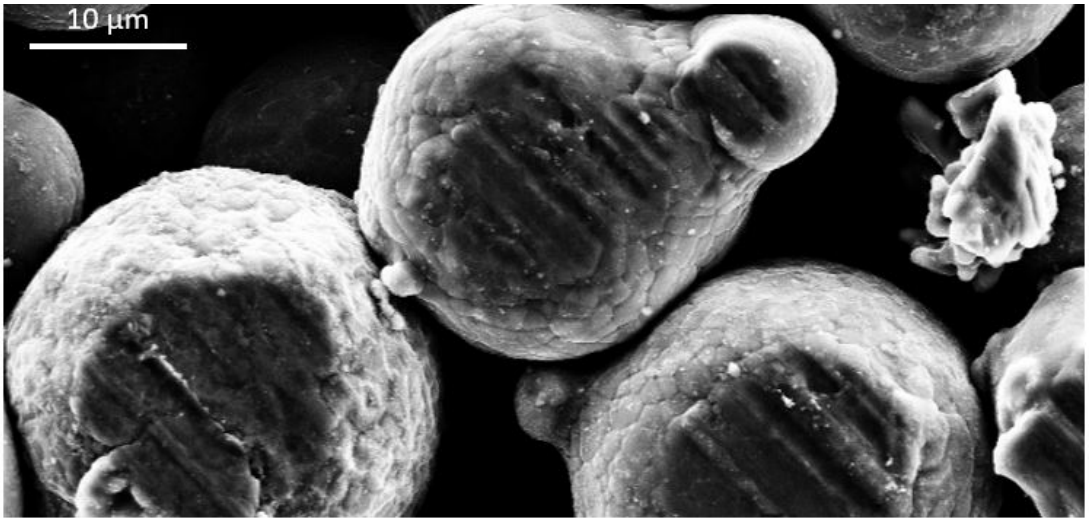


Figure 4.32: SEM observation in SE mode of the powder particles at the surface of the sample after the compression, showing the cracks that appeared on the oxide layer at the surface of the grain

have facilitated the diffusion of atoms that enable densification by causing shrinkage.

In the sintered scaffold, pores are larger and more heterogeneous. Coarsening occurs, and as observed by salehi *et al* [211], the Mg powder bursts due to sintering in the super solidus domain. This burst releases liquid and the capillarity force draws the liquid toward other burst grain of powder.

The oxide film gets transported along with the liquid phase, and accumulates along the powder particles free surfaces, as visible on the EDX analysis of the scaffold Fig.(4.33). In contrast, the oxide layer remained intact during the sintering of the pellet, resulting in a structure resembling that of a sample manufactured by SPS. This suggests that densification in the pellet occurred primarily through grain coarsening in the solid phase and not by the breaking of the oxide layer. In contrast, in the sintering necks of the scaffold, the native oxide layer is not visible at the bonding of the grains. This indicates that the liquid likely penetrated the barrier and wet the other powder particles, facilitating the formation of the necks. This is shown on the whole structure in Fig.4.34.

Furthermore, a columnar like structure similar to the one observed in the sintering of Ti64 [223] is visible on the SEM image of the sintered scaffold 4.35. This columnar structure corresponds to the growth of the oxide layer under sintering temperature.

This structure corresponds to the growth observed in the *in situ* tomography. The oxide layer begins to grow and eventually reaches another oxide layer undergoing the same process. Once the layers join, oxygen migrates probably because of the difference in surface energy to the sides of the grains. This migration facilitates the formation of a neck between the particles. In the image, the neck is in the process of forming, and the oxide has started to migrate to the sides. However, the Mg material did not have sufficient time or energy to diffuse through the free space between the two particles.

Thèse accessible à l'adresse : https://theses.insa-lyon.fr/publication/2025ISAL0008/these.pdf © [J. Moreau], [2025], INSA Lyon, tous droits réservés

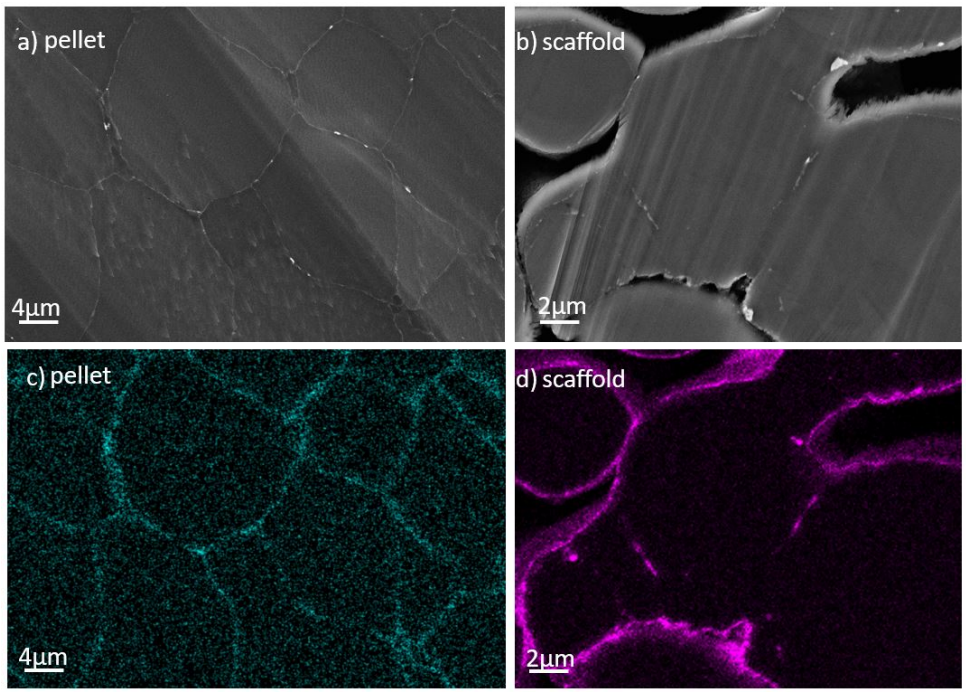


Figure 4.33: a-b) Observation of the pellet and the sintered scaffold with SEM and c-d) the corresponding oxygen distribution using EDX. For the scaffold, oxygen is located around the powder particles but not in the sintering necks, for the pellet, oxygen is evenly distributed around the powder particles, showing the main difference between the two sintering mechanisms

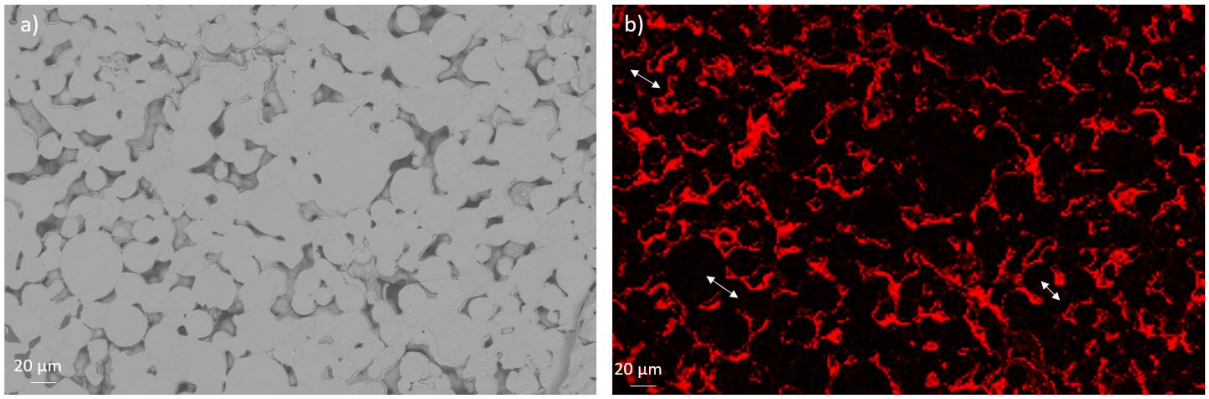


Figure 4.34: a) BSE observations of the structure in the sintered scaffold, along with b) EDX maps showing the distribution of oxygen. White arrows indicate sintering necks without oxygen.

4.5.4.3 Oxygen pollution

Another concern is the pollution that appears during the debinding. During the thermal decomposition of the binder the Mg tends to react with oxygen, forming a thicker oxide layer around the grain. The analysis of oxygen concentration conducted on the various samples throughout the process highlight a significant difference between them (Table. 4.6). The measurement were

Thèse accessible à l'adresse : https://theses.insa-lyon.fr/publication/2025ISAL0008/these.pdf © [J. Moreau], [2025], INSA Lyon, tous droits réservés

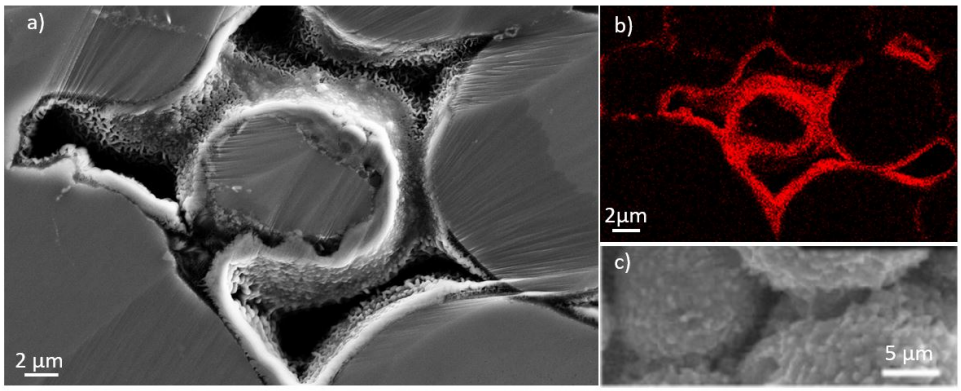


Figure 4.35: SEM and EDX observations of the columnar structure observed in the sintered scaffold that looks like an oxide growth with b) the EDX map of oxygen. c) *in situ* SEM image of the columnar structure of oxygen visible in Ti64, taken from [223]

performed according to section.2.2.6.

Sample	Oxygen concentration (wt%)
Powder of ZK30 (as-atomised)	0.17 ± 0.01%
Sintered pellet	0.11 ± 0.01%
Debinded scaffold	0.68 ± 0.12%
Sintered scaffold	0.52 ± 0.01%

Table 4.6: Evolution of the oxygen concentration during the printing process and comparison with the die-pressured pellet

The oxygen concentration in the debinded scaffold is four times more important than in the raw powder, confirming the significant impact of the interaction between the binder and the powder. This thick oxide layer hinders the sintering of the powder particles. It explains why only 10 h were required to sinter the pellet and 20 h were needed to sinter the scaffold. Furthermore, the sintered pellet contains a lower oxygen content compared to the raw powder. This difference may be attributed to the distinct specific surface areas of powder and dense parts, as powders are more susceptible to atmospheric water, potentially influencing measurements. Lastly, the debinding process significantly contaminates the powder particles with oxygen, likely due to interactions between the powder and binder during the debinding at 400°C in the furnace. Further investigation into the interaction with the ethyl-cellulose binder and the powder are needed to reduce the oxygen concentration, as it leads to significant differences in density.

4.6 Conclusions

In this study an additive manufacturing process followed by a pressure-less sintering without additive was developed. Detailed analysis of the sintering from die-pressured pellet and scaffold printed with DIW were investigated. The following conclusions can be drawn from this study :

- The confinement of the printed parts in the labyrinth-like crucible is effective for the sintering of Mg, with a high efficiency with a pressure applied in advance. The crucible

Thèse accessible à l'adresse : https://theses.insa-lyon.fr/publication/2025ISAL0008/these.pdf © [J. Moreau], [2025], INSA Lyon, tous droits réservés

helped to retain the vapor of Mg close to the material and probably improved the wetting between the liquid and solid phases of the alloy.

- The DIW process proves to be possible for AM of Mg, however, the achieved density is currently insufficient for implant applications. This limitation can compromise mechanical properties due to inadequate particle cohesion, evidenced by lower hardness and visible intergranular fractures post-hardness testing.One possible solution is to increase the density of printed parts by raising the solid loading. This can be achieved by adjusting the binder composition to allow for a higher concentration of powder in the ink while maintaining its printability.
- Two different sintering mechanisms can be observed depending of the initial grain arrangement, one involves the formation of a liquid phase that disrupts the oxide layer, while the other relies on solid-state sintering. The oxygen concentration, influenced by the sample's manufacturing method, likely contributes significantly to these observed differences.

The sintering process for a high particle fraction with low oxygen is depicted in Fig.4.36.a. The oxide growth allow to bring the powder grains closer together. Once they are sufficiently close, the grain boundaries tend to flatten, resulting in dense parts, though the oxygen layer remains around the grains. The role and presence of the liquid phase is not yet well understood. For lower particle fractions and higher oxygen content, the sintering steps are shown in Fig.4.36.b. The initial stage is similar, with oxide growth. A liquid phase begins to form, likely at the boundary between the Mg and MgO phases. This liquid may lead to two possible outcomes. Once the powder particles come closer and increase the contact area, it is hypothesized that the oxide layer becomes trapped around the liquid. In one scenario, the oxide migrates toward the grain boundary, which is not surrounded by liquid, via capillary action. As a result, oxygen-free sinter necks may form upon cooling. However, if the liquid fraction is too high or the sintering duration too long, the oxide layer retaining the liquid may break. Due to the low viscosity of the liquid and the high contact angle between liquid Mg and solid MgO, the liquid is not retained and flows out of the structure by capillarity. This leads to empty oxide shells forming within the structure, resulting in high porosity.

Thèse accessible à l'adresse : https://theses.insa-lyon.fr/publication/2025ISAL0008/these.pdf © [J. Moreau], [2025], INSA Lyon, tous droits réservés

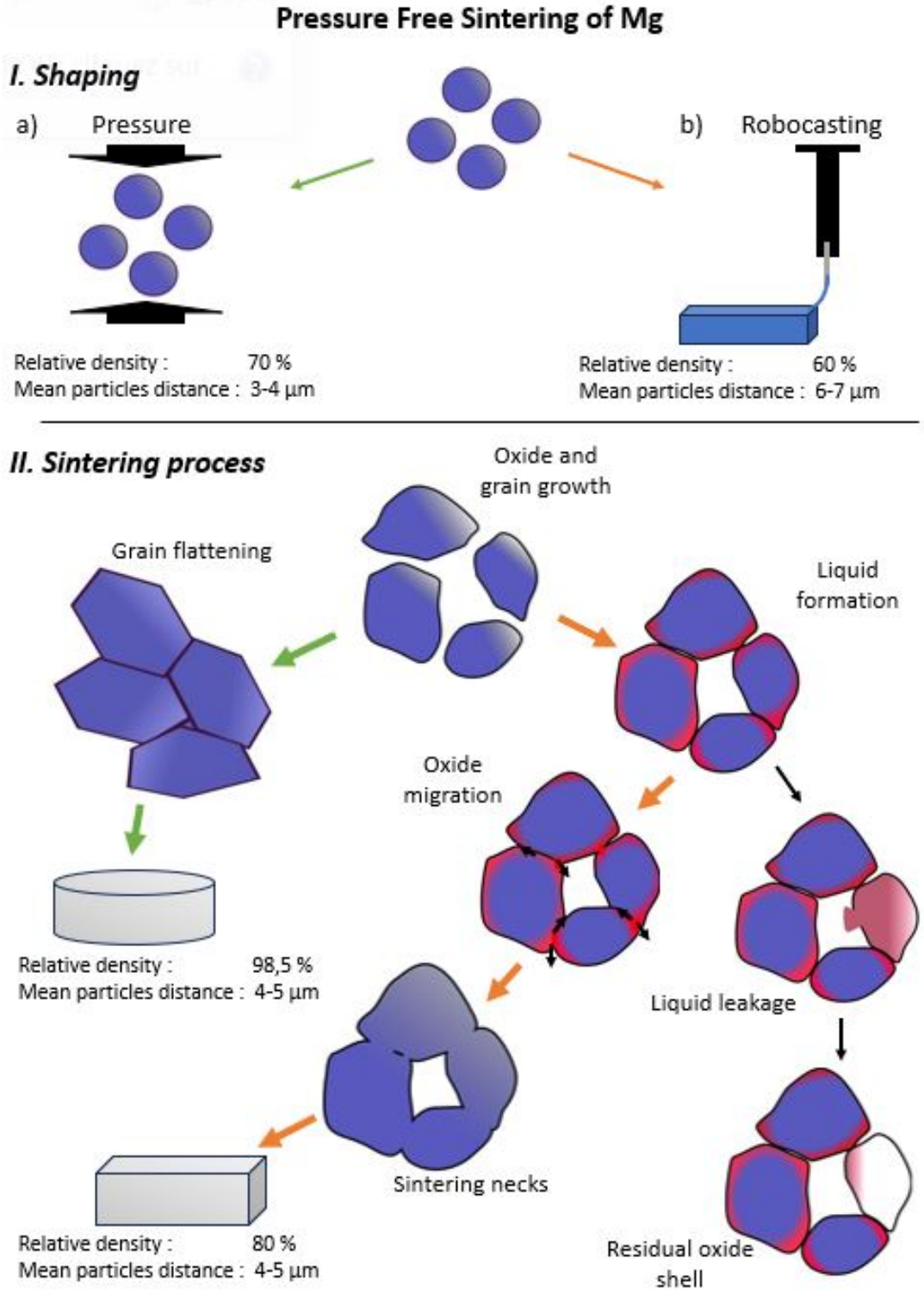


Figure 4.36: Schematic representation of the shaping and sintering steps of a) The die-pressed pellet and b) the printed scaffold, highlighting the differences in mechanism observed and the influence of the particle fraction and oxygen content

Thèse accessible à l'adresse : https://theses.insa-lyon.fr/publication/2025ISAL0008/these.pdf © [J. Moreau], [2025], INSA Lyon, tous droits réservés

Conclusion and perspectives

In this manuscript, we evaluated the potential of ZK30 alloy as a 3D-printed biodegradable orthopedic implant. This study was conducted using two approaches. The first involved manufacturing ZK30 using SPS to obtain dense parts and study their mechanical and corrosion properties. Due to the challenges associated with magnesium's reactivity, the second part of the study focused on assessing the feasibility of applying the DIW process to magnesium-based alloys. The problem was therefore, to find solutions compatible with this material for each stage of the process.

Powder metallurgy process of Magnesium

Manufacturing challenge

The SPS process is based on quick cycle with a loading pressure use to compact the powder. The first parts obtained highlighted high relative densities (>98%) with hardnesses similar to the casting process. Nevertheless, the main difficulty of sintering magnesium is the native oxide layer at the surface of the powder particles which either inhibits the sintering or still remain at the powder particle boundaries, which is the case in the SPS process. This remaining layer was observed to be detrimental to the mechanical properties (elongation at fracture and ultimate tensile strength). Indeed, the presence of the oxide was observed to induce a brittle behavior with an intergranular fracture at the powder particles boundaries

Overcoming of the oxide layer

The most used technique to overcome the oxide layer is the increase of the loading to mechanically destroy the oxide layer. However, this approach was initially used to evaluate the potential of free-pressure sintering for Mg alloys, and therefore aimed to maintain a low loading level. Therefore the study was directed toward the formation of the liquid phase during the sintering. This liquid fraction was believed to be able to break the layer in some areas due to the increase of pressure inside the powder particles. The use of SPS prevents reaching a high liquid fraction, as it could cause the liquid to escape from the matrix. Following thermal analysis on the powder, various temperatures were tested to successfully achieve dense parts (>99%).

Mechanical properties

The presence of the liquid phase was observed to improve the mechanical properties in a three points bending test. The best samples demonstrated an elongation at break of up to 18% and an ultimate tensile strength of 400 MPa. These mechanical properties are promising for the use of the ZK30 alloy as an orthopedic implant. These improvement of the mechanical properties are attributed to the breaking of the oxide layer at the powder particles boundaries in some areas observed in the samples.

Optimizing of the corrosion properties

Precipitation in the ZK30 alloy

Thèse accessible à l'adresse : https://theses.insa-lyon.fr/publication/2025ISAL0008/these.pdf © [J. Moreau], [2025], INSA Lyon, tous droits réservés

The precipitation sequence in ZK30 is similar to that observed in Mg-Zn alloys. Based on previous studies of binary alloys, the precipitation in ZK30 alloys was monitored through TEP and hardness measurements. The growth of two different precipitates was observed during aging, which could potentially slow down the rapid corrosion of Mg alloys.

Corrosion properties

The influence of microstructure on the corrosion rate was evaluated through the aging study. Initially, simple mass loss measurements were conducted to evaluate the degradation rate across different media and microstructures. Then, EIS measurements were performed allowing to better monitor the corrosion behavior. The equivalent circuit model determined for the corrosion of ZK30 fitted the data well, with minor discrepancies at low frequencies, and was used to determine the polarization resistance.

There was no clear evidence of a direct influence of precipitates on the corrosion rate; however, it was observed that aging at 200 °C resulted in a microstructure that accelerated degradation compared to both the solutionized alloy and the alloy aged at 170 °C. Additionally, during immersion, even when the mass remained stable, the material was primarily composed of corrosion products, and the polarization resistance reached low values before complete degradation occurred. This suggests that the mechanical properties of the alloy degrade significantly before noticeable mass loss, complicating the assessment of its suitability for orthopedic applications. It is challenging to directly compare the corrosion properties observed in this study with actual *in vivo* studies. The degradation rate of the alloy may be too high to design real implant but further investigations in physiological media are necessary. However, given these observations, an optimal treatment for the alloy in terms of hardness and corrosion resistance would be a sample aged at a peak of hardness, either 4 h or 20 h at 170 °C.

Free-pressure sintering of Mg alloys

Finally, the development and challenges of an AM process for magnesium, involving pressureless sintering after DIW were explored.

- **Confinement and Efficiency:**
- Using a labyrinth-like crucible effectively improves the sintering of magnesium by containing the vapor and enhancing wetting between the alloy's liquid and solid phases. This approach benefits from pre-applied pressure, contributing to the overall process efficiency.
- **Density Challenges and Solutions:**
- DIW is feasible for magnesium, the current relative densities levels may be adequate for implant applications but are still not well controlled during sintering. The insufficient particle cohesion also negatively affects mechanical properties, as shown by lower hardness.
- **Sintering Mechanisms:** The study identified two sintering mechanisms based on initial grain arrangements:
  - *Solid-State Sintering:* Characterized by grain coarsening and oxide growth, bringing powder particles closer. Grain boundaries flatten, forming dense parts, although the oxide layer persists.
  - *Liquid Phase Formation:* For samples with higher oxygen content, a liquid phase forms at the Mg-MgO boundary, potentially leading to oxygen-free sinter necks or, if conditions are not optimal, to high porosity and structural weaknesses due to liquid escape and oxide shell formation.

These findings highlight the need to optimize oxygen content and particle fraction while un-

Thèse accessible à l'adresse : https://theses.insa-lyon.fr/publication/2025ISAL0008/these.pdf © [J. Moreau], [2025], INSA Lyon, tous droits réservés

derstanding the role of liquid phases in sintering. Adjustments in the process could significantly impact the mechanical robustness and applicability of AM magnesium components.

Perspectives

Returning to the broader context of this thesis, some insights from this work warrant further exploration.

Potential of ZK30 alloy as a material for orthopedic implants Regarding the potential of ZK30 alloy for orthopedic implants, an aspect that remains unexplored is the modeling of precipitates. This modeling could give crucial information to better understand the effect of the precipitates on the degradation rate by comparing the radius and number density of the precipitates depending of the aging temperature. The corrosion resistance study was a first approach using simple media but extensive *in vitro* study could provide more information on the viability of the material as an orthopedic implants.

Furthermore, the impact of the precipitates on the mechanical properties has been measured using hardness but a deeper study of the other properties such as tensile testing, compression and fatigue would really validate or not the potential of ZK30 alloy.

Toward direct ink-writing of bio-degradable structures ? Pressure-free sintering of Mg alloys remains challenging. The obtained sample and microstructure for printed ZK30 could be acceptable, but the final density is not well controlled. To better improve the sintering and control the final density a few leads exist:

- Using a more homogeneous ink could prevent the discrepancies in the pore size in the sintered part. Small and well-distributed particles have proven to be particularly effective in the sintering of pressed pellets. A straightforward method to achieve this would be to optimize the mixing process of the powder with the binder. This can be done by increasing the mixing time or using alternative equipment, such as a paddle mixer or a tri-cylinder mixer.
- Decreasing the amount of oxygen on the binder could improve the sintering quality. Ethanol was chosen to prevent the use of water but a solvent without oxygen such as alkane compound (dodecane, hexadecane, ..) would allow to perform the whole preparation oxygen free.
- Another approach could be to compact the printed parts using Cold Isostatic Pressing (CIP). This technique allows pressure to be applied in an oil bath, increasing the relative density of the green parts without causing them to break. Tests were performed and the green parts went from 60% relative density to 68% relative density. Sintering post-CIP was not tested.

Based on the first successful sintering of the printed part the same study performed on the dense sample would be interesting. Testing the mechanical properties and the corrosion resistance of the printed scaffold would give more insight of the possibilities for DIW to produce architectured implants. Furthermore, the printed part design remained basic as the focus was to study the sintering. However, the repeating units of the geometry plays a huge role in the fatigue resistance, tensile and compressive strength, degradation rate and cytotoxicity [224] [225].

Thèse accessible à l'adresse : https://theses.insa-lyon.fr/publication/2025ISAL0008/these.pdf © [J. Moreau], [2025], INSA Lyon, tous droits réservés

In addition, an upscale of the sintering process may permit to sinter bigger parts as the sintered printed parts were only around a cm long. The upscale could be a challenge due to the precise conditions of the sintering but printing parts with dimensions close to the commercially available screws could bring DIW a step closer to the fabrication of orthopedic implants.

Exploring the Potential of Zn Alloys Zn alloys are less popular than Mg alloys but they are promising for orthopedic implants. Contrarily to Mg alloys they possess good corrosion resistance but exhibit a brittle behavior. Considering these properties a combination of Mg alloys and Zn alloys look very promising to compensate the weaknesses of each other. DIW of multi-materials has until now mainly been considered for soft (non-sintered) materials because it eliminates the problem of co-sintering [226]. However, a gradient from one Mg-Zn alloy grade to another Zn-Mg might be considered.

In this perspective a range of Zn-Mg alloys powders with concentration from 0.1 wt% to 3wt% were prepared by mixing pure Mg and Mg-22Zn. The powders were then densified using SPS. They exhibited relative density superior at 99% and were submitted to the same mass loss test in NaCl solution and three-point bending test. Zn-1Mg exhibited the better elongation at rupture and the mechanical testing and mass loss test of this alloy are presented in Fig.4.37

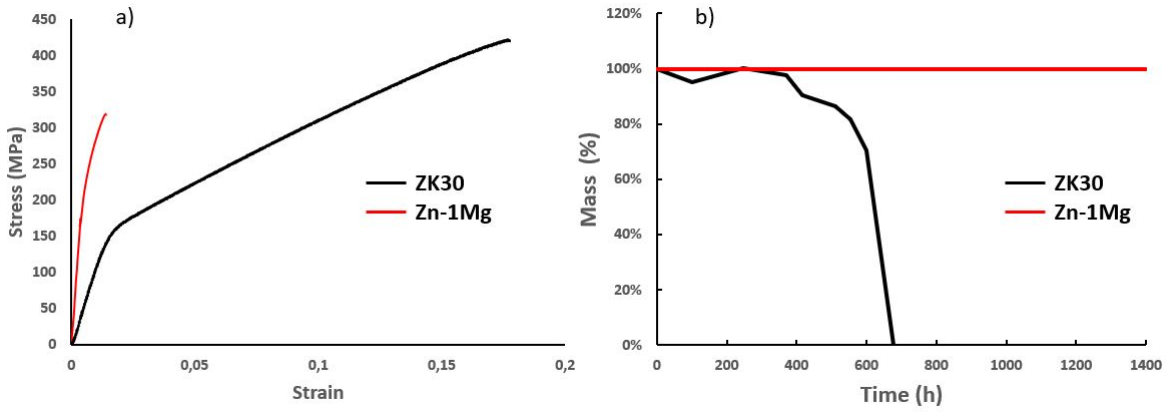


Figure 4.37: a) Three points bending test of Zn-1Mg alloy compared with ZK30, b) Mass loss test of the Mg-1Zn alloy compared with ZK30 alloy

These results demonstrate how these materials can complement each other by using a gradient: Zn on the surface to enhance corrosion resistance and Mg at the core to strengthen mechanical properties. An ink of Zn-Mg alloys was prepared using the same formulation of EC and ethanol and parts were printed. However, due to the size and morphology of the Zn powder the solid loading had to be decrease to 50%. Lastly, sintering tests were performed at temperature around 360 °C but no parts were successfully sintered. In addition, to improve the sintering, the densification of two materials with different sinterability temperature ranges can even be considered by adjusting the size of the powders.

The use of a Zn gradient appears promising for structured orthopedic implants.

Thèse accessible à l'adresse : https://theses.insa-lyon.fr/publication/2025ISAL0008/these.pdf © [J. Moreau], [2025], INSA Lyon, tous droits réservés

Robocaster used in the study

Thèse accessible à l'adresse : https://theses.insa-lyon.fr/publication/2025ISAL0008/these.pdf © [J. Moreau], [2025], INSA Lyon, tous droits réservés

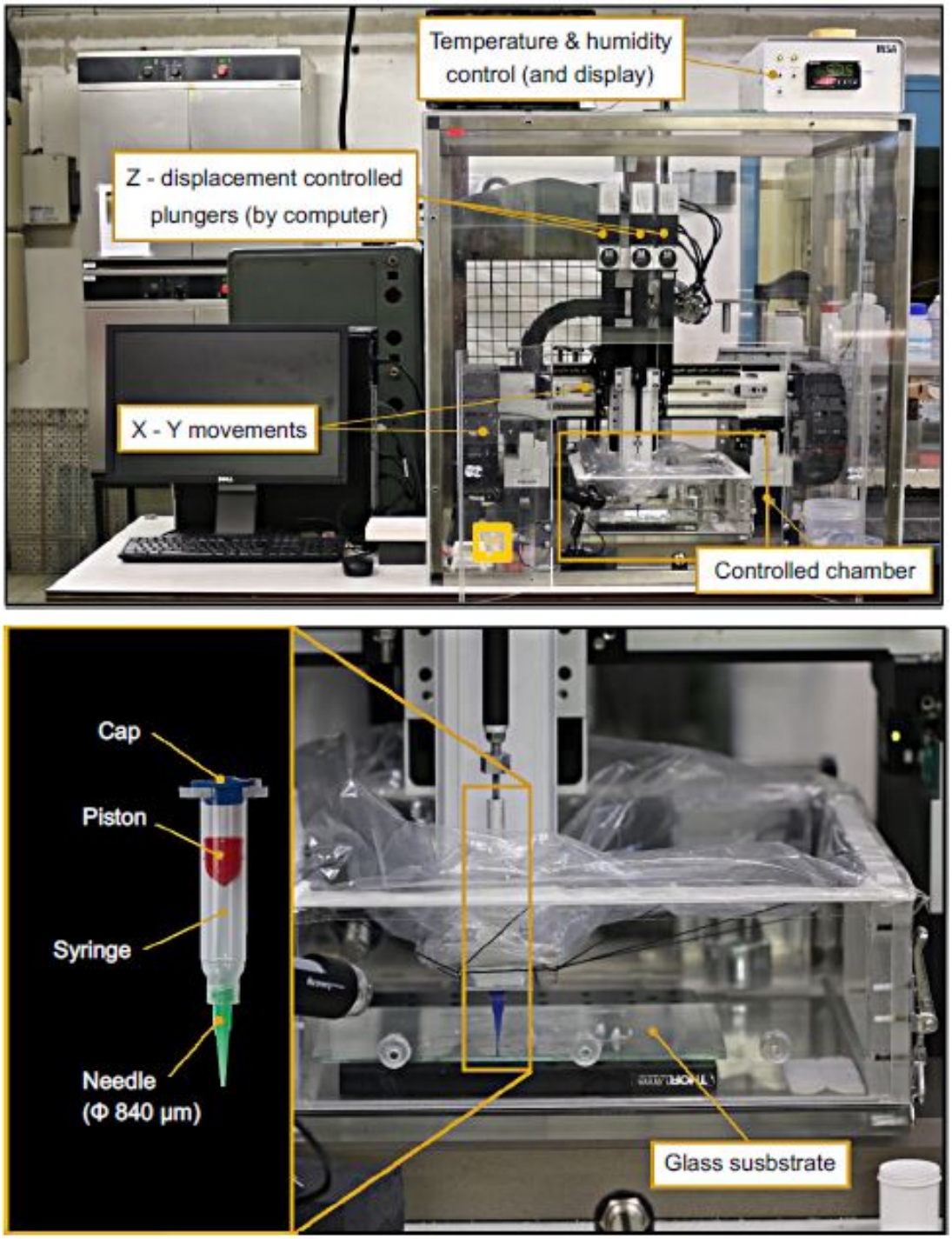


Figure 38:
Images o the different components of the robocaster used in this study

Thèse accessible à l'adresse : https://theses.insa-lyon.fr/publication/2025ISAL0008/these.pdf © [J. Moreau], [2025], INSA Lyon, tous droits réservés

Setup used for tubular furnace sintering

Thèse accessible à l'adresse : https://theses.insa-lyon.fr/publication/2025ISAL0008/these.pdf © [J. Moreau], [2025], INSA Lyon, tous droits réservés

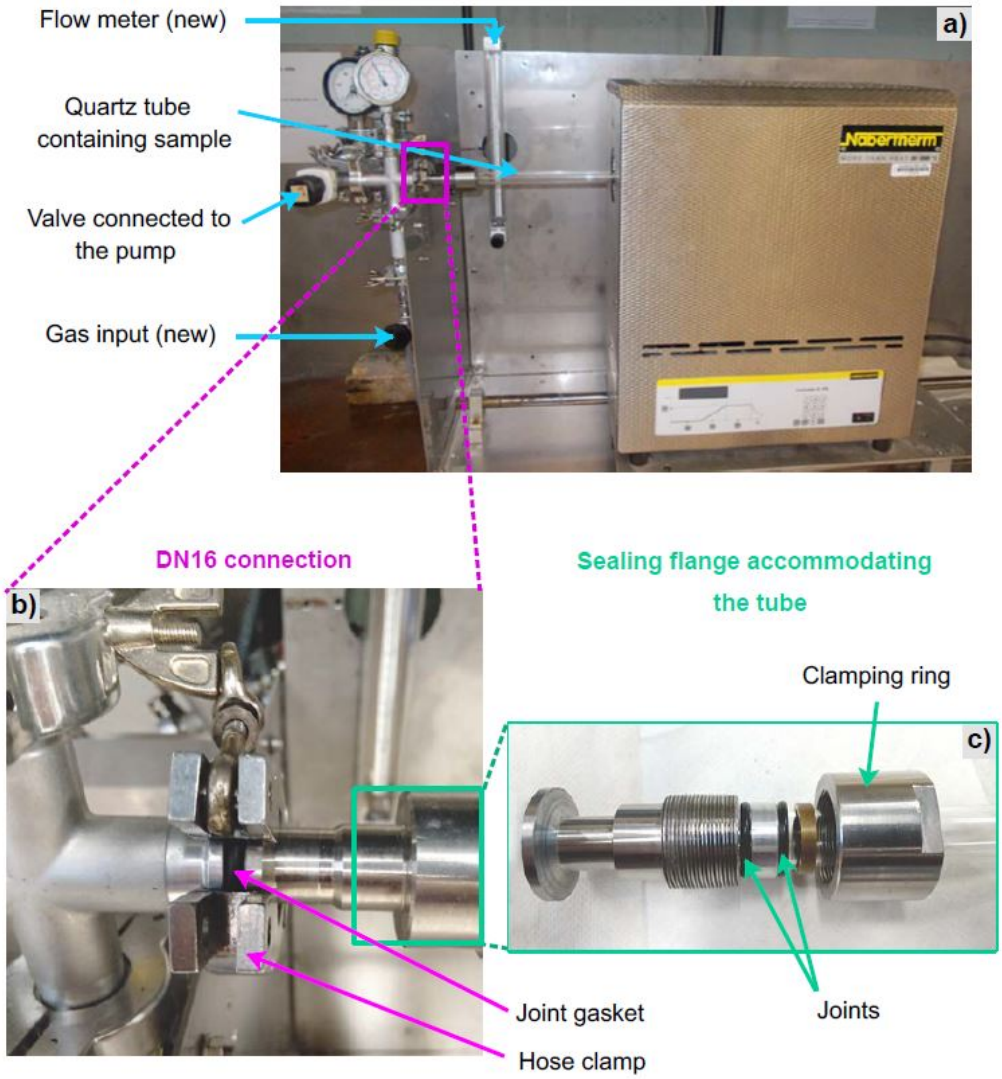


Figure 39: Illustration of the assembly used to carry out heat treatments in a controlled atmosphere: (a) Whole system; (b) Focus on the DN16 connection; (c) Focus on the system that enables sealing with the tube.

Thèse accessible à l'adresse : https://theses.insa-lyon.fr/publication/2025ISAL0008/these.pdf © [J. Moreau], [2025], INSA Lyon, tous droits réservés

Bibliography

[1] M. Navarro, A. Michiardi, O. Castaño, and J. Planell, "Biomaterials in orthopaedics," *Journal of the Royal Society Interface*, vol. 5, pp. 1137–1158, Oct. 2008.

[2] M. T. Lam and J. C. Wu, "Biomaterial applications in cardiovascular tissue repair and regeneration," *Expert review of cardiovascular therapy*, vol. 10, pp. 1039–1049, Aug. 2012.

[3] Y. Zhong and R. V. Bellamkonda, "Biomaterials for the central nervous system," *Journal of the Royal Society Interface*, vol. 5, pp. 957–975, Sept. 2008.

[4] M. Hawkins, "Orthopedic Surgery: Supply, Demand and Recruiting Trends," *Meriit Hawkins white paper serie*, p. 10, 2019.

[5] N. Fuggle, C. Cooper, and K. Javaid, "Groupe politique IOF-CTF :," *International osteoporosis foundation*, 2022.

[6] V. S. d. Viteri and E. Fuentes, *Titanium and Titanium Alloys as Biomaterials*. IntechOpen, May 2013.

[7] A. Aherwar, A. Singh, and A. Patniak, "Cobalt based alloy: A better choice biomaterial for hip implants," *Trends in Biomaterials and Artificial Organs*, vol. 30, pp. 50–55, Jan. 2016.

[8] M. Peron, J. Torgersen, and F. Berto, "Mg and Its Alloys for Biomedical Applications: Exploring Corrosion and Its Interplay with Mechanical Failure," *Metals*, vol. 7, p. 252, July 2017.

[9] B. G. Pound, "Corrosion behavior of metallic materials in biomedical applications. II. Stainless steels and Co-Cr alloys," *Corrosion reviews*, 2014.

[10] J. Toledano[U+2010]Serrabona, O. Camps[U+2010]Font, D. P. de Moraes, M. Corte[U+2010]Rodríguez, M. Montes[U+2010]Bayón, E. Valmaseda[U+2010]Castellón, C. Gay[U+2010]Escoda, and M. [U+FFFD]Sánchez[U+2010]Garcés, "Ion release and local effects of titanium metal particles from dental implants: An experimental study in rats," *Journal of Periodontology*, vol. 94, pp. 119–129, Jan. 2023.

[11] M. Haseeb, M. F. Butt, T. Altaf, K. Muzaffar, A. Gupta, and A. Jallu, "Indications of implant removal: A study of 83 cases," *International Journal of Health Sciences*, vol. 11, no. 1, pp. 1–7, 2017.

[12] I. I. Onche, O. E. Osagie, and S. INuhu, "Removal of orthopaedic implants: indications, outcome and economic implications," *Journal of the West African College of Surgeons*, vol. 1, no. 1, pp. 101–112, 2011.

Thèse accessible à l'adresse : https://theses.insa-lyon.fr/publication/2025ISAL0008/these.pdf © [J. Moreau], [2025], INSA Lyon, tous droits réservés

[13] H. Hermawan, "Biodegradable Metals: State of the Art," in *Biodegradable Metals: From Concept to Applications* (H. Hermawan, ed.), SpringerBriefs in Materials, pp. 13–22, Berlin, Heidelberg: Springer, 2012.

[14] R. K. Singh Raman, S. Jafari, and S. E. Harandi, "Corrosion fatigue fracture of magnesium alloys in bioimplant applications: A review," *Engineering Fracture Mechanics*, vol. 137, pp. 97–108, Mar. 2015.

[15] J. Singh, A. Wahab Hashmi, S. Ahmad, and Y. Tian, "Critical review on biodegradable and biocompatibility magnesium alloys: Progress and prospects in bio-implant applications," *Inorganic Chemistry Communications*, vol. 169, p. 113111, Nov. 2024.

[16] P. Wan, L. Tan, and K. Yang, "Surface Modification on Biodegradable Magnesium Alloys as Orthopedic Implant Materials to Improve the Bio-adaptability: A Review," *Journal of Materials Science & Technology*, vol. 32, pp. 827–834, Sept. 2016.

[17] D. Chen, Y. He, H. Tao, Y. Zhang, Y. Jiang, X. Zhang, and S. Zhang, "Biocompatibility of magnesium-zinc alloy in biodegradable orthopedic implants," *International Journal of Molecular Medicine*, vol. 28, pp. 343–348, Sept. 2011.

[18] P. Kumar Rout, S. Roy, and D. Rathore, "Recent advances in the development of Mg-Ca-Zn alloys as biodegradable orthopedic implants," *Materials Today: Proceedings*, July 2023.

[19] "Magnezix \textbackslashtextbackslashtextbar Sovereign Medical."

[20] A. Lafont and Y. Yang, "Magnesium stent scaffolds: DREAMS become reality," *Lancet (London, England)*, vol. 387, pp. 3–4, Jan. 2016.

[21] S. Luenam, A. Kosiyatrakul, C. Hansudewechakul, K. Phakdeewisetkul, B. Lohwongwatana, and C. Puncreobutr, "The Patient-Specific Implant Created with 3D Printing Technology in Treatment of the Irreparable Radial Head in Chronic Persistent Elbow Instability," *Case Reports in Orthopedics*, vol. 2018, no. 1, p. 9272075, 2018.

[22] Y. Wu, W. Liu, S. Ruan, and G. S. Chirikjian, "Primitive-Based Shape Abstraction via Nonparametric Bayesian Inference," in *Computer Vision – ECCV 2022* (S. Avidan, G. Brostow, M. Cissé, G. M. Farinella, and T. Hassner, eds.), (Cham), pp. 479–495, Springer Nature Switzerland, 2022.

[23] G. Strand, C. Juels, and J. Nowak, "Custom total talus replacement as a salvage option for failed total ankle arthroplasty: A prospective report of two cases," *Foot & Ankle Surgery: Techniques, Reports & Cases*, vol. 2, p. 100113, Mar. 2022.

[24] L. C. Silva, G. F. Batalha, F. Miranda, and R. S. Coelho, "Validation of lumbar fusion device TILIF (Ti-6Al-4 V) manufactured by EBM additive manufacturing through fem modeling high cycle fatigue tests," *Materials Today: Proceedings*, May 2023.

[25] X. Geng, Y. Li, F. Li, X. Wang, K. Zhang, Z. Liu, and H. Tian, "A new 3D printing porous trabecular titanium metal acetabular cup for primary total hip arthroplasty: a minimum 2-year follow-up of 92 consecutive patients," *Journal of Orthopaedic Surgery and Research*, vol. 15, p. 383, Sept. 2020.

[26] Y. Ao, L. Guo, H. Chen, R. He, P. Yang, D. Fu, L. Gu, Y. Peng, R. Xiong, L. Yang, and F. Wang, "Application of three-dimensional-printed porous tantalum cones in total knee arthroplasty revision to reconstruct bone defects," *Frontiers in Bioengineering and Biotechnology*, vol. 10, p. 925339, Sept. 2022.

Thèse accessible à l'adresse : https://theses.insa-lyon.fr/publication/2025ISAL0008/these.pdf © [J. Moreau], [2025], INSA Lyon, tous droits réservés

[27] M. Meng, J. Wang, H. Huang, X. Liu, J. Zhang, and Z. Li, "3D printing metal implants in orthopedic surgery: Methods, applications and future prospects," *Journal of Orthopaedic Translation*, vol. 42, pp. 94–112, Sept. 2023.

[28] M. A. Skylar-Scott, J. Mueller, C. W. Visser, and J. A. Lewis, "Voxelated soft matter via multimaterial multinozzle 3D printing," *Nature*, vol. 575, pp. 330–335, Nov. 2019.

[29] B. G. Compton and J. A. Lewis, "3D-Printing of Lightweight Cellular Composites," *Advanced Materials*, vol. 26, no. 34, pp. 5930–5935, 2014.

[30] S. K. Lan Levengood, S. J. Polak, M. B. Wheeler, A. J. Maki, S. G. Clark, R. D. Jamison, and A. J. Wagoner Johnson, "Multiscale osteointegration as a new paradigm for the design of calcium phosphate scaffolds for bone regeneration," *Biomaterials*, vol. 31, pp. 3552–3563, May 2010.

[31] S. J. Polak, L. E. Rustom, G. M. Genin, M. Talcott, and A. J. Wagoner Johnson, "A mechanism for effective cell-seeding in rigid, microporous substrates," *Acta Biomaterialia*, vol. 9, pp. 7977–7986, Aug. 2013.

[32] M. Z. Naser, "Space-native construction materials for earth-independent and sustainable infrastructure," *Acta Astronautica*, vol. 155, pp. 264–273, Feb. 2019.

[33] J. Wang, Y. Zou, C. Dang, Z. Wan, J. Wang, and F. Pan, "Research Progress and the Prospect of Damping Magnesium Alloys," *Materials*, vol. 17, p. 1285, Mar. 2024.

[34] n. khademian and Y. Peimaei, *Magnesium alloys and applications in automotive industry.* 5th International Conference on Science and Development of Nanotechnology, Aug. 2021.

[35] J. Tan and S. Ramakrishna, "Applications of Magnesium and Its Alloys: A Review," *Applied Sciences*, vol. 11, p. 6861, Jan. 2021.

[36] G. Lagrené, "Mise en forme des métaux et fonderie," 2000.

[37] F. Witte, V. Kaese, H. Haferkamp, E. Switzer, A. Meyer-Lindenberg, C. J. Wirth, and H. Windhagen, "In vivo corrosion of four magnesium alloys and the associated bone response," *Biomaterials*, vol. 26, pp. 3557–3563, June 2005.

[38] A. A. Luo, "Magnesium casting technology for structural applications," *Journal of Magnesium and Alloys*, vol. 1, pp. 2–22, Mar. 2013.

[39] J. Song, F. Pan, B. Jiang, A. Atrens, M.-X. Zhang, and Y. Lu, "A review on hot tearing of magnesium alloys," *Journal of Magnesium and Alloys*, vol. 4, pp. 151–172, Sept. 2016.

[40] X. Tong, G. You, F. Yao, M. Ebrahimi, X. Deng, and S. Attarilar, "Segregation behavior and its regulating process in as-cast magnesium alloy containing heavy rare earth," *Journal of Rare Earths*, vol. 40, pp. 1291–1304, Aug. 2022.

[41] F. Pan, M. Yang, and X. Chen, "A Review on Casting Magnesium Alloys: Modification of Commercial Alloys and Development of New Alloys," *Journal of Materials Science & Technology*, vol. 32, pp. 1211–1221, Dec. 2016.

[42] Z. Zeng, N. Stanford, C. H. J. Davies, J.-F. Nie, and N. Birbilis, "Magnesium extrusion alloys: a review of developments and prospects," *International Materials Reviews*, vol. 64, pp. 27–62, Jan. 2019.

[43] W. Sillekens, M. Hout, and F. Pravdic, "Extrusion technology for magnesium: Avenues for improving performance," in *2nd International Light Metals Technology Conference*, June 2005.

Thèse accessible à l'adresse : https://theses.insa-lyon.fr/publication/2025ISAL0008/these.pdf © [J. Moreau], [2025], INSA Lyon, tous droits réservés

[44] L. Gao, H. Yan, J. Luo, A. Luo, and R. Chen, "Microstructure and mechanical properties of a high ductility Mg–Zn–Mn–Ce magnesium alloy," *Journal of Magnesium and Alloys*, vol. 1, Dec. 2013.

[45] R. Radha and D. Sreekanth, "Insight of magnesium alloys and composites for orthopedic implant applications – a review," *Journal of Magnesium and Alloys*, vol. 5, pp. 286–312, Sept. 2017.

[46] Z. F. Al-Sherify, N. M. Dawood, and Z. T. Khulief, "Corrosion behavior of AZ31 magnesium alloys coated with PMMA/HA as biodegradable implants," *Materials Today: Proceedings*, vol. 61, pp. 1100–1108, Jan. 2022.

[47] Y. Yang, X. Xiong, J. Chen, X. Peng, D. Chen, and F. Pan, "Research advances of magnesium and magnesium alloys worldwide in 2022," *Journal of Magnesium and Alloys*, vol. 11, pp. 2611–2654, Aug. 2023.

[48] A. K. Dahle, Y. C. Lee, M. D. Nave, P. L. Schaffer, and D. H. StJohn, "Development of the as-cast microstructure in magnesium–aluminium alloys," *Journal of Light Metals*, vol. 1, pp. 61–72, Feb. 2001.

[49] S. Cai, T. Lei, N. Li, and F. Feng, "Effects of Zn on microstructure, mechanical properties and corrosion behavior of Mg–Zn alloys," *Materials Science and Engineering: C*, vol. 32, pp. 2570–2577, Dec. 2012.

[50] S. V. S. Prasad, S. B. Prasad, K. Verma, R. K. Mishra, V. Kumar, and S. Singh, "The role and significance of Magnesium in modern day research-A review," *Journal of Magnesium and Alloys*, vol. 10, pp. 1–61, Jan. 2022.

[51] Z. Munir, U. Anselmi-tamburini, and M. Ohyanagi, "The Effect of Electric Field and Pressure on the Synthesis and Consolidation of Materials: A Review of the Spark Plasma Sintering Method," *Journal of Materials Science*, vol. 41, pp. 763–777, Feb. 2006.

[52] P. Minárik, M. Zemková, M. Knapek, S. Šašek, J. Dittrich, F. Lukáč, J. Kozlík, and R. Král, "Effect of Short Attritor-Milling of Magnesium Alloy Powder Prior to Spark Plasma Sintering," *Materials*, vol. 13, p. 3973, Jan. 2020.

[53] G. Straffelini, A. P. Nogueira, P. Muterlle, and C. Menapace, "Spark plasma sintering and hot compression behaviour of AZ91 Mg alloy," *Materials Science and Technology*, vol. 27, pp. 1582–1587, Oct. 2011.

[54] Y. Chen, Z. Feng, and W. Zhang, "Effect of MgO Content on Mechanical Properties of Directionally Solidified Pure Magnesium," *Materials Research*, vol. 24, p. e20200469, Mar. 2021.

[55] K. Kim, H. Kim, S. Kwon, and D.-Y. Hwang, "The effect of sintering pressure on the microstructure and properties of a nanocrystalline magnesium alloy in spark plasma sintering," *Journal of the Korean Physical Society*, vol. 65, pp. 1669–1674, Dec. 2014.

[56] J. Soderlind, M. Cihova, R. Schäublin, S. Risbud, and J. F. Löffler, "Towards refining microstructures of biodegradable magnesium alloy WE43 by spark plasma sintering," *Acta Biomaterialia*, vol. 98, pp. 67–80, Oct. 2019.

[57] W. N. A. W. Muhammad, Z. Sajuri, Y. Mutoh, and Y. Miyashita, "Microstructure and mechanical properties of magnesium composites prepared by spark plasma sintering technology," *Journal of Alloys and Compounds*, vol. 509, pp. 6021–6029, May 2011.

Thèse accessible à l'adresse : https://theses.insa-lyon.fr/publication/2025ISAL0008/these.pdf © [J. Moreau], [2025], INSA Lyon, tous droits réservés

[58] A. M. Ralls, M. Daroonparvar, and P. L. Menezes, "Spark Plasma Sintering of Mg-based Alloys: Microstructure, Mechanical Properties, Corrosion Behavior, and Tribological Performance," *Journal of Magnesium and Alloys*, vol. 12, pp. 405–442, Feb. 2024.

[59] P. Minárik, J. Stráský, J. Veselý, F. Lukáč, B. Hadzima, and R. Král, "AE42 magnesium alloy prepared by spark plasma sintering," *Journal of Alloys and Compounds*, vol. 742, pp. 172–179, Apr. 2018.

[60] L. Ma, L. Ma, P. Jin, X. Feng, and L. Jia, "Effect of sintering temperature on microstructures and mechanical properties of ZK60 magnesium alloys," *Materials Research Express*, vol. 9, p. 016514, Jan. 2022.

[61] Y. Zhu, J. Qin, J. Wang, and P. Jin, "Effect of Sintering Temperature on Microstructure and Mechanical Properties of AZ91 Magnesium Alloy via Spark Plasma Sintering," *Advanced Engineering Materials*, vol. 24, no. 3, p. 2100905, 2022.

[62] S.-J. L. Kang, "6 - NORMAL GRAIN GROWTH AND SECOND-PHASE PARTICLES," in *Sintering* (S.-J. L. Kang, ed.), pp. 91–96, Oxford: Butterworth-Heinemann, Jan. 2005.

[63] M. Mondet, E. Barraud, S. Lemonnier, J. Guyon, N. Allain, and T. Grosdidier, "Microstructure and mechanical properties of AZ91 magnesium alloy developed by Spark Plasma Sintering," *Acta Materialia*, vol. 119, pp. 55–67, Oct. 2016.

[64] S. Eswarappa Prameela, P. Yi, Y. Hollenweger, B. Liu, J. Chen, L. Kecskes, D. Kochmann, M. Falk, and T. Weihs, *Strengthening magnesium by design: integrating alloying and dynamic processing*. Mechanic of Materials, May 2021.

[65] P. J. Burke, Z. Bayindir, and G. J. Kipouros, "X-ray photoelectron spectroscopy (XPS) investigation of the surface film on magnesium powders," *Applied Spectroscopy*, vol. 66, pp. 510–518, May 2012.

[66] A. Unal, "Rapid solidification of magnesium by gas atomization," *MATERIAL AND MANUFACTURING PROCESS*, vol. 7, pp. 441–461, Jan. 1992.

[67] C. Y. Xü, S. S. Jia, and Z. Y. Cao, "Synthesis of Al–Mn–Ce alloy by the spark plasma sintering," *Materials Characterization*, vol. 54, pp. 394–398, May 2005.

[68] R. Von mises, "Advances in Applied Mechanics, Volume 1 by Richard von Mises," 1948.

[69] C. Cáceres, G. Mann, and J. Griffiths, "Grain Size Hardening in Mg and Mg-Zn Solid Solutions," *Metallurgical and Materials Transactions A*, vol. 42, pp. 1950–1959, July 2011.

[70] H. Somekawa, Y. Osawa, and T. Mukai, "Effect of solid-solution strengthening on fracture toughness in extruded Mg–Zn alloys," *Scripta Materialia*, vol. 55, pp. 593–596, Oct. 2006.

[71] R. Zheng, J.-P. Du, S. Gao, H. Somekawa, S. Ogata, and N. Tsuji, "Transition of dominant deformation mode in bulk polycrystalline pure Mg by ultra-grain refinement down to submicrometer," *Acta Materialia*, vol. 198, pp. 35–46, Oct. 2020.

[72] M. R. Barnett, "Twinning and the ductility of magnesium alloys: Part I: "Tension" twins," *Materials Science and Engineering: A*, vol. 464, pp. 1–7, Aug. 2007.

[73] J. Nie, "Precipitation and Hardening in Magnesium Alloys," *Metallurgical and Materials Transactions A*, vol. 43, Nov. 2012.

[74] A. Akhtar and E. Teghtsoonian, "Solid solution strengthening of magnesium single crystals—I alloying behaviour in basal slip," *Acta Metallurgica*, vol. 17, pp. 1339–1349, Nov. 1969.

[75] F. Hauser, "Deformation and fracture of alpha solid solutions of lithium in magnesium," *Technical report N1 for US department of energy*, 1958.

Thèse accessible à l'adresse : https://theses.insa-lyon.fr/publication/2025ISAL0008/these.pdf © [J. Moreau], [2025], INSA Lyon, tous droits réservés

[76] J. D. Robson, N. Stanford, and M. R. Barnett, "Effect of precipitate shape on slip and twinning in magnesium alloys," *Acta Materialia*, vol. 59, pp. 1945–1956, Mar. 2011.

[77] S. Kandalam, P. Agrawal, G. S. Avadhani, S. Kumar, and S. Suwas, "Precipitation response of the magnesium alloy WE43 in strained and unstrained conditions," *Journal of Alloys and Compounds*, vol. 623, pp. 317–323, Feb. 2015.

[78] A. Barylski, M. Kupka, K. Aniołek, and J. Rak, "The effect of precipitation hardening on the structure and mechanical and tribological properties of magnesium alloy WE54," *Vacuum*, vol. 139, pp. 77–86, May 2017.

[79] Y. Yang, V. Massardier, M. R. G. Ferdowsi, L. Jiang, J. Wang, T. Dorin, S. R. Kada, M. R. Barnett, and M. Perez, "Revisiting Precipitation kinetics in Mg-Zn alloy – a multi-characterization and modeling study," *Acta Materialia*, vol. 260, p. 119276, Nov. 2023.

[80] M. L. Raffa, V.-H. Nguyen, P. Hernigou, C.-H. Flouzat-Lachaniette, and G. Haiat, "Stress shielding at the bone-implant interface: Influence of surface roughness and of the bone-implant contact ratio," *Journal of Orthopaedic Research: Official Publication of the Orthopaedic Research Society*, vol. 39, pp. 1174–1183, June 2021.

[81] D. R. Sumner, "Long-term implant fixation and stress-shielding in total hip replacement," *Journal of Biomechanics*, vol. 48, pp. 797–800, Mar. 2015.

[82] S. M. Kayhan, A. Tahmasebifar, M. Koç, Y. Usta, A. Tezcaner, and Z. Evis, "Experimental and numerical investigations for mechanical and microstructural characterization of micro-manufactured AZ91D magnesium alloy disks for biomedical applications," *Materials & Design*, vol. 93, pp. 397–408, Mar. 2016.

[83] D. Bairagi and S. Mandal, "A comprehensive review on biocompatible Mg-based alloys as temporary orthopaedic implants: Current status, challenges, and future prospects," *Journal of Magnesium and Alloys*, vol. 10, pp. 627–669, Mar. 2022.

[84] J. Cordero, L. Munuera, and M. D. Folgueira, "Influence of metal implants on infection. An experimental study in rabbits," *The Journal of Bone and Joint Surgery. British Volume*, vol. 76, pp. 717–720, Sept. 1994.

[85] M. Yazdimamaghani, M. Razavi, D. Vashaee, K. Moharamzadeh, A. R. Boccaccini, and L. Tayebi, "Porous magnesium-based scaffolds for tissue engineering," *Materials Science and Engineering: C*, vol. 71, pp. 1253–1266, Feb. 2017.

[86] H. Alves, U. Koster, and D. Eliezer, "Environmental Behavior of Mg-Alloys," Jan. 2000.

[87] G. L. Song and A. Atrens, "Corrosion Mechanisms of Magnesium Alloys," *Advanced Engineering Materials*, vol. 1, no. 1, pp. 11–33, 1999.

[88] G. G. Perrault, "The potential-pH diagram of the magnesium-water system," *Journal of Electroanalytical Chemistry and Interfacial Electrochemistry*, vol. 51, pp. 107–119, Mar. 1974.

[89] M. Peron, F. Berto, and J. Torgersen, *Magnesium and Its Alloys as Implant Materials: Corrosion, Mechanical and Biological Performances*. Boca Raton: CRC Press, Apr. 2020.

[90] Y. Zheng, *Magensium alloys as degradable biomaterials*. Material Science, 2016.

[91] R. Willumeit, J. Fischer, F. Feyerabend, N. Hort, U. Bismayer, S. Heidrich, and B. Mihailova, "Chemical surface alteration of biodegradable magnesium exposed to corrosion media," *Acta Biomaterialia*, vol. 7, pp. 2704–2715, June 2011.

[92] R. Lindström, L. Johansson, G. Thompson, P. Skeldon, and J. Svensson, "Corrosion of magnesium in humid air," *Corrosion Science*, 2004.

Thèse accessible à l'adresse : https://theses.insa-lyon.fr/publication/2025ISAL0008/these.pdf © [J. Moreau], [2025], INSA Lyon, tous droits réservés

[93] X.-l. He, Y.-h. Wei, L.-f. Hou, Z.-f. Yan, C.-l. Guo, and P.-j. Han, "Corrosion fatigue behavior of epoxy-coated Mg–3Al–1Zn alloy in gear oil," *Transactions of Nonferrous Metals Society of China*, vol. 24, pp. 3429–3440, Nov. 2014.

[94] G. Song and A. Atrens, "Understanding Magnesium Corrosion—A Framework for Improved Alloy Performance," *Advanced Engineering Materials*, vol. 5, no. 12, pp. 837–858, 2003.

[95] D. Mei, S. V. Lamaka, X. Lu, and M. L. Zheludkevich, "Selecting medium for corrosion testing of bioabsorbable magnesium and other metals – A critical review," *Corrosion Science*, vol. 171, p. 108722, July 2020.

[96] Y. Ding, C. Wen, P. Hodgson, and Y. Li, "Effects of alloying elements on the corrosion behavior and biocompatibility of biodegradable magnesium alloys: a review," *Journal of Materials Chemistry B*, vol. 2, pp. 1912–1933, Mar. 2014.

[97] E. Mcbride, "ABSORBABLE METAL IN BONE SURGERY: A FURTHER REPORT ON THE USE OF MAGNESIUM ALLOYS," *Medecine, engineering*, 1938.

[98] C. P. Mccord, J. J. Prendergast, S. F. Meek, and G. C. Harrold, "Chemical gas gangrene from metallic magnesium," *Indust Medicine beloit*, vol. 11, pp. 71–76, Mar. 1942.

[99] R. Zan, H. Wang, W. Cai, J. Ni, B. J. Luthringer-Feyerabend, W. Wang, H. Peng, W. Ji, J. Yan, J. Xia, Y. Song, and X. Zhang, "Controlled release of hydrogen by implantation of magnesium induces P53-mediated tumor cells apoptosis," *Bioactive Materials*, vol. 9, pp. 385–396, Aug. 2021.

[100] R.-C. Zeng, Z.-Z. Yin, X.-B. Chen, and D.-K. Xu, *Corrosion Types of Magnesium Alloys*. IntechOpen, Nov. 2018.

[101] P.-W. Chu and E. A. Marquis, "Linking the microstructure of a heat-treated WE43 Mg alloy with its corrosion behavior," *Corrosion Science*, vol. 101, pp. 94–104, Dec. 2015.

[102] L. J. Liu and M. Schlesinger, "Corrosion of magnesium and its alloys," *Corrosion Science*, vol. 51, pp. 1733–1737, Aug. 2009.

[103] R. Zeng, W. Dietzel, F. Witte, N. Hort, and C. Blawert, "Progress and Challenge for Magnesium Alloys as Biomaterials," *Advanced Engineering Materials*, vol. 10, no. 8, pp. B3–B14, 2008.

[104] P. Hou, P. Han, C. Zhao, H. Wu, J. Ni, S. Zhang, J. Liu, Y. Zhang, H. Xu, P. Cheng, S. Liu, Y. Zheng, X. Zhang, and Y. Chai, "Accelerating Corrosion of Pure Magnesium Co-implanted with Titanium in Vivo," *Scientific Reports*, vol. 7, p. 41924, Feb. 2017.

[105] R. Zeng, K. U. Kainer, C. Blawert, and W. Dietzel, "Corrosion of an extruded magnesium alloy ZK60 component—The role of microstructural features," *Journal of Alloys and Compounds*, vol. 509, pp. 4462–4469, Mar. 2011.

[106] R. Zeng, W. Qi, F. Zhang, H. Cui, and Y. Zheng, "In vitro corrosion of Mg–1.21Li–1.12Ca–1Y alloy," *Progress in Natural Science: Materials International*, vol. 24, pp. 492–499, Oct. 2014.

[107] Z. Li, Z. Peng, K. Qi, H. Li, Y. Qiu, and X. Guo, "Microstructure and Corrosion of Cast Magnesium Alloy ZK60 in NaCl Solution," *Materials (Basel, Switzerland)*, vol. 13, p. 3833, Aug. 2020.

[108] R. Ambat, N. Aung, and W. Zhou, "Evaluation of microstructural effects on corrosion behaviour of AZ91D magnesium alloy," *Corrosion Science*, vol. 42, pp. 1433–1455, Aug. 2000.

Thèse accessible à l'adresse : https://theses.insa-lyon.fr/publication/2025ISAL0008/these.pdf © [J. Moreau], [2025], INSA Lyon, tous droits réservés

[109] G. Frankel, S. Papavinasam, N. Berke, S. Brossia, and S. Dean, "Electrochemical Techniques in Corrosion: Status, Limitations, and Needs," *Journal of ASTM International*, vol. 5, p. 101241, Feb. 2008.

[110] S. Fajardo, F. García-Galván, V. Barranco, J. C. Galvan, and S. Jr, "A Critical Review of the Application of Electrochemical Techniques for Studying Corrosion of Mg and Mg Alloys: Opportunities and Challenges," in *Magnesium alloys -Selected issues*, Magnesium alloys -Selected issues, Dec. 2018.

[111] M. Stern and A. L. Geary, "Electrochemical Polarization: I . A Theoretical Analysis of the Shape of Polarization Curves," *Journal of The Electrochemical Society*, vol. 104, p. 56, Jan. 1957.

[112] L. Bland, A. King, N. Birbilis, and J. Scully, "Assessing the Corrosion of Commercially Pure Magnesium and Commercial AZ31B by Electrochemical Impedance, Mass-Loss, Hydrogen Collection, and Inductively Coupled Plasma Optical Emission Spectrometry Solution Analysis," *Corrosion*, vol. 71, pp. 128–145, Feb. 2015.

[113] S. Bender, J. Goellner, A. Heyn, and S. Schmigalla, "A new theory for the negative difference effect in magnesium corrosion," *Materials and Corrosion*, vol. 63, no. 8, pp. 707–712, 2012.

[114] J. Scully, "Polarization Resistance Method for Determination of Instantaneous Corrosion Rates," *Corrosion*, vol. 56, pp. 199–204, Feb. 2000.

[115] S. Jr, "Electrochemical Impedance Spectroscopy for the Measurement of the Corrosion Rate of Magnesium Alloys: Brief Review and Challenges," *Metals*, vol. 10, p. 775, June 2020.

[116] C. M. A. Brett, L. Dias, B. Trindade, R. Fischer, and S. Mies, "Characterisation by EIS of ternary Mg alloys synthesised by mechanical alloying," *Electrochimica Acta*, vol. 51, pp. 1752–1760, Jan. 2006.

[117] A. D. King, N. Birbilis, and J. R. Scully, "Accurate Electrochemical Measurement of Magnesium Corrosion Rates; a Combined Impedance, Mass-Loss and Hydrogen Collection Study," *Electrochimica Acta*, vol. 121, pp. 394–406, Mar. 2014.

[118] F. Mansfeld, "Electrochemical impedance spectroscopy (EIS) as a new tool for investigating methods of corrosion protection," *Electrochimica Acta*, vol. 35, pp. 1533–1544, Oct. 1990.

[119] I. J. Polmear, *Light alloys: metallurgy of the light metals*. Metallurgy and Materials Science, London [etc]: Edward Arnold, 2nd ed ed., 1989.

[120] G. L. Makar and J. Kruger, "Corrosion of magnesium," *International Materials Reviews*, vol. 38, pp. 138–153, Jan. 1993.

[121] J. E. Hillis, "The Effects of Heavy Metal Contamination on Magnesium Corrosion Performance," *SAE Transactions*, vol. 92, pp. 553–559, 1983.

[122] H. G. Paris, W. H. Hunt, T.-A. N. M. Committee, I. M. Association, and M. Society (U.S.), eds., *Advances in magnesium alloys and composites: proceedings of a symposium sponsored by the International Magnesium Association and the Non-Ferrous Metals Committee, held at the Annual Meeting of the Minerals, Metals, and Materials Society in Phoenix, Arizona, January 26, 1988*. Warrendale, Pa: The Society, 1988.

Thèse accessible à l'adresse : https://theses.insa-lyon.fr/publication/2025ISAL0008/these.pdf © [J. Moreau], [2025], INSA Lyon, tous droits réservés

[123] M. Esmaily, J. E. Svensson, S. Fajardo, N. Birbilis, G. S. Frankel, S. Virtanen, R. Arrabal, S. Thomas, and L. G. Johansson, "Fundamentals and advances in magnesium alloy corrosion," *Progress in Materials Science*, vol. 89, pp. 92–193, Aug. 2017.

[124] E. Zhang, D. Yin, L. Xu, L. Yang, and K. Yang, "Microstructure, mechanical and corrosion properties and biocompatibility of Mg–Zn–Mn alloys for biomedical application," *Materials Science and Engineering: C*, vol. 29, pp. 987–993, Apr. 2009.

[125] A. Atrens, M. Liu, N. I. Zainal Abidin, and G.-L. Song, "Corrosion of magnesium (Mg) alloys and metallurgical influence," *Corrosion of Magnesium Alloys*, pp. 117–165, Dec. 2011.

[126] Y. Lu, A. R. Bradshaw, Y. L. Chiu, and I. P. Jones, "Effects of secondary phase and grain size on the corrosion of biodegradable Mg-Zn-Ca alloys," *Materials Science & Engineering. C, Materials for Biological Applications*, vol. 48, pp. 480–486, Mar. 2015.

[127] Y. Hu, X. Guo, Y. Qiao, X. Wang, and Q. Lin, "Preparation of medical Mg–Zn alloys and the effect of different zinc contents on the alloy," *Journal of Materials Science: Materials in Medicine*, vol. 33, p. 9, Jan. 2022.

[128] S. Zhang, X. Zhang, C. Zhao, J. Li, Y. Song, C. Xie, H. Tao, Y. Zhang, Y. He, Y. Jiang, and Y. Bian, "Research on an Mg–Zn alloy as a degradable biomaterial," *Acta Biomaterialia*, vol. 6, pp. 626–640, Feb. 2010.

[129] F. Xing, S. Li, D. Yin, J. Xie, P. M. Rommens, Z. Xiang, M. Liu, and U. Ritz, "Recent progress in Mg-based alloys as a novel bioabsorbable biomaterials for orthopedic applications," *Journal of Magnesium and Alloys*, vol. 10, pp. 1428–1456, June 2022.

[130] M. Bornapour, N. Muja, D. Shum-Tim, M. Cerruti, and M. Pekguleryuz, "Biocompatibility and biodegradability of Mg–Sr alloys: The formation of Sr-substituted hydroxyapatite," *Acta biomaterialia*, vol. 9, Aug. 2012.

[131] D. Tie, F. Feyerabend, W.-D. Mueller, R. Schade, K. Liefeith, K. Kainer, and R. Willumeit, "Antibacterial biodegradable Mg-Ag alloys," *European cells & materials*, vol. 25, pp. 284–98, June 2013.

[132] Y. Zheng, "Mg-Ag-Based Alloy Systems for Biomedical Applications," in *Magnesium alloys as degradable biomaterials*, Material Science, pp. 269–284, Oct. 2015.

[133] L.-Y. Li, L.-Y. Cui, R.-C. Zeng, S.-Q. Li, X.-B. Chen, Y. Zheng, and M. B. Kannan, "Advances in functionalized polymer coatings on biodegradable magnesium alloys – A review," *Acta Biomaterialia*, vol. 79, pp. 23–36, Oct. 2018.

[134] P. Makkar, S. K. Sarkar, A. R. Padalhin, B.-G. Moon, Y. S. Lee, and B. T. Lee, "In vitro and in vivo assessment of biomedical Mg-Ca alloys for bone implant applications," *Journal of Applied Biomaterials & Functional Materials*, vol. 16, pp. 126–136, July 2018.

[135] Q. Peng, Y. Huang, L. Zhou, N. Hort, and K. Kainer, "Preparation and properties of high purity Mg-Y biomaterials," *Biomaterials*, vol. 31, pp. 398–403, Sept. 2009.

[136] C. Liu, Z. Ren, Y. Xu, S. Pang, X. Zhao, and Y. Zhao, "Biodegradable Magnesium Alloys Developed as Bone Repair Materials: A Review," *Scanning*, vol. 2018, p. e9216314, Mar. 2018.

[137] Y. Wan, G. Xiong, H. Luo, F. He, Y. Huang, and X. Zhou, "Preparation and characterization of a new biomedical magnesium–calcium alloy," *Materials & Design*, vol. 29, pp. 2034–2037, Dec. 2008.

Thèse accessible à l'adresse : https://theses.insa-lyon.fr/publication/2025ISAL0008/these.pdf © [J. Moreau], [2025], INSA Lyon, tous droits réservés

[138] S. E. Harandi, M. Mirshahi, S. Koleini, M. H. Idris, H. Jafari, and M. R. A. Kadir, "Effect of calcium content on the microstructure, hardness and in-vitro corrosion behavior of biodegradable Mg-Ca binary alloy," *Materials Research*, vol. 16, pp. 11–18, Nov. 2012.

[139] Z. Li, X. Gu, S. Lou, and Y. Zheng, "The development of binary Mg–Ca alloys for use as biodegradable materials within bone," *Biomaterials*, vol. 29, pp. 1329–1344, Apr. 2008.

[140] H. S. Brar, J. Wong, and M. V. Manuel, "Investigation of the mechanical and degradation properties of Mg–Sr and Mg–Zn–Sr alloys for use as potential biodegradable implant materials," *Journal of the Mechanical Behavior of Biomedical Materials*, vol. 7, pp. 87–95, Mar. 2012.

[141] W. Jiang, A. F. Cipriano, Q. Tian, C. Zhang, M. Lopez, A. Sallee, A. Lin, M. C. Cortez Alcaraz, Y. Wu, Y. Zheng, and H. Liu, "In vitro evaluation of MgSr and MgCaSr alloys via direct culture with bone marrow derived mesenchymal stem cells," *Acta Biomaterialia*, vol. 72, pp. 407–423, May 2018.

[142] M. Bosetti, A. Massè, E. Tobin, and M. Cannas, "Silver coated materials for external fixation devices: in vitro biocompatibility and genotoxicity," *Biomaterials*, vol. 23, pp. 887–892, Feb. 2002.

[143] M. Bian, X. Huang, and Y. Chino, "A room temperature formable magnesium–silver–calcium sheet alloy with high ductility," *Materials Science and Engineering: A*, vol. 774, p. 138923, Feb. 2020.

[144] G. Ben-Hamu, D. Eliezer, A. Kaya, Y. G. Na, and K. S. Shin, "Microstructure and corrosion behavior of Mg–Zn–Ag alloys," *Materials Science and Engineering: A*, vol. 435-436, pp. 579–587, Nov. 2006.

[145] L. Rokhlin, N. Bochvar, E. Lysova, and N. Leonova, "Study of the solubility of cerium and yttrium in solid magnesium," *Metal Science and Heat Treatment*, vol. 2005, pp. 263–268, May 2005.

[146] Q. Peng, N. MA, and H. LI, "Gadolinium solubility and precipitate identification in Mg-Gd binary alloy," *Journal of Rare Earths*, vol. 30, pp. 1064–1068, Oct. 2012.

[147] L. L. Rokhlin and N. I. Nikitina, "Mechanical properties of magnesium alloys with dysprosium," *Metal Science and Heat Treatment*, vol. 41, pp. 271–273, June 1999.

[148] T. Takenaka, T. Ono, Y. Narazaki, Y. Naka, and M. Kawakami, "Improvement of corrosion resistance of magnesium metal by rare earth elements," *Electrochimica Acta*, vol. 53, pp. 117–121, Nov. 2007.

[149] F. Rosalbino, E. Angelini, S. De Negri, A. Saccone, and S. Delfino, "Electrochemical behaviour assessment of novel Mg-rich Mg–Al–RE alloys (RE=Ce, Er)," *Intermetallics*, vol. 14, pp. 1487–1492, Dec. 2006.

[150] P. Jiang, C. Blawert, and M. L. Zheludkevich, "The Corrosion Performance and Mechanical Properties of Mg-Zn Based Alloys—A Review," *Corrosion and Materials Degradation*, vol. 1, pp. 92–158, June 2020.

[151] T. Ying, M. Y. Zheng, Z. T. Li, X. G. Qiao, and S. W. Xu, "Thermal conductivity of as-cast and as-extruded binary Mg–Zn alloys," *Journal of Alloys and Compounds*, vol. 621, pp. 250–255, Feb. 2015.

[152] Y. Jingyuan, W. Jianzhong, L. Qiang, S. Jian, C. Jianming, and S. Xudong, "Effect of Zn on Microstructures and Properties of Mg-Zn Alloys Prepared by Powder Metallurgy Method," *Rare Metal Materials and Engineering*, vol. 45, pp. 2757–2762, Nov. 2016.

Thèse accessible à l'adresse : https://theses.insa-lyon.fr/publication/2025ISAL0008/these.pdf © [J. Moreau], [2025], INSA Lyon, tous droits réservés

[153] Y. Song, M. Wang, Y. Zong, R. He, and J. Jin, "Grain Refinement by Second Phase Particles under Applied Stress in ZK60 Mg Alloy with Y through Phase Field Simulation," *Materials (Basel, Switzerland)*, vol. 11, p. 1903, Oct. 2018.

[154] Y. C. Lee, A. K. Dahle, and D. H. StJohn, "The role of solute in grain refinement of magnesium," *Metallurgical and Materials Transactions A*, vol. 31, pp. 2895–2906, Nov. 2000.

[155] L. Saldaña, A. Méndez-Vilas, L. Jiang, M. Multigner, J. L. González-Carrasco, M. T. Pérez-Prado, M. L. González-Martín, L. Munuera, and N. Vilaboa, "In vitro biocompatibility of an ultrafine grained zirconium," *Biomaterials*, vol. 28, pp. 4343–4354, Oct. 2007.

[156] O. B. Kulakov, A. A. Doktorov, S. V. D'iakova, I. I. Denisov-Nikol'skiĭ, and K. A. Grötz, "[Experimental study of osseointegration of zirconium and titanium dental implants]," *Morfologiia (Saint Petersburg, Russia)*, vol. 127, no. 1, pp. 52–55, 2005.

[157] J. B. Clark, "Transmission electron microscopy study of age hardening in a Mg-5 wt.% Zn alloy," *Acta Metallurgica*, vol. 13, pp. 1281–1289, Dec. 1965.

[158] L. Y. Wei, G. L. Dunlop, and H. Westengen, "Precipitation Hardening of Mg-Zn and Mg-Zn-RE alloys," *Metallurgical and Materials Transactions A*, vol. 26, pp. 1705–1716, July 1995.

[159] A. Singh and A. Tsai, "Structural characteristics of 1 ′ precipitates in Mg–Zn-based alloys," *Scripta Materialia - SCRIPTA MATER*, vol. 57, pp. 941–944, Nov. 2007.

[160] J. Rosalie, H. Somekawa, A. Singh, and T. Mukai, "Orientation relationships between icosahedral clusters in hexagonal MgZn2 and monoclinic Mg4Zn7 phases in Mg-Zn(-Y) alloys," *Philosophical Magazine - PHILOS MAG*, vol. 91, Apr. 2012.

[161] A. Hadadzadeh, F. Mokdad, B. S. Amirkhiz, M. A. Wells, B. W. Williams, and D. L. Chen, "Bimodal grain microstructure development during hot compression of a cast-homogenized Mg-Zn-Zr alloy," *Materials Science and Engineering: A*, vol. 724, pp. 421–430, May 2018.

[162] S. Bolte and F. P. Cordelières, "A guided tour into subcellular colocalization analysis in light microscopy," *Journal of Microscopy*, vol. 224, pp. 213–232, Dec. 2006.

[163] R. Dougherty and K.-H. Kunzelmann, "Computing Local Thickness of 3D Structures with ImageJ," *Microscopy and Microanalysis*, vol. 13, pp. 1678–1679, Aug. 2007.

[164] D. Mirković and R. Schmid-Fetzer, "Solidification Curves for Commercial Mg Alloys Determined from Differential Scanning Calorimetry with Improved Heat-Transfer Modeling," *Metallurgical and Materials Transactions A*, vol. 38, pp. 2575–2592, Oct. 2007.

[165] R. Arróyave, D. Shin, and Z. Liu, "Modification of the thermodynamic model for the Mg–Zr system," *Calphad-computer Coupling of Phase Diagrams and Thermochemistry - CALPHAD-COMPUT COUP PHASE DIA*, vol. 29, pp. 230–238, Sept. 2005.

[166] J.-O. Andersson, "Thermo-Calc & DICTRA, computational tools for materials science," *CALPHAD*, vol. 26, 2002.

[167] M. Perez, F. Perrard, V. Massardier, X. Kleber, A. Deschamps, H. Monestrol, P. Pareige, and G. Covarel, "Low Temperature Solubility of Copper in Iron : Experimental Study Using Thermoelectric Power, Small Angle X-ray Scattering and Tomographic Atom Probe," *Philosophical Magazine*, vol. 85, pp. 2197–2210, July 2005.

[168] X. KLEBER, "La mesure du pouvoir thermoélectrique : une technique originale de contrôle des alliages métalliques," in *Technique de l'ingénieur Matériaux Métallique*, Techniques de l'ingénieur, 2005.

Thèse accessible à l'adresse : https://theses.insa-lyon.fr/publication/2025ISAL0008/these.pdf © [J. Moreau], [2025], INSA Lyon, tous droits réservés

[169] I. INTERNATIONAL, "ISO 10271:2020 - Dentistry — Corrosion test methods for metallic materials," 2020.

[170] v. L. Nordheim and C. J. Gorter, "Bemerkungen über thermokraft und widerstand," *Physica*, vol. 2, pp. 383–390, Jan. 1935.

[171] J. M. Pelletier, G. Vigier, J. Merlin, P. Merle, F. Fouquet, and R. Borrelly, "Precipitation effects on thermopower in Al-Cu alloys," *Acta Metallurgica*, vol. 32, pp. 1069–1078, July 1984.

[172] M. Perez, V. Massardier, and X. Kleber, "Thermoelectric power applied to metallurgy: Principle and recent applications," *International Journal of Materials Research - INT J MATER RES*, vol. 100, pp. 1461–1466, Oct. 2009.

[173] G. M. Raynaud and P. Guyot, "Coherent precipitation effect on thermo-power of Al[U+E5F8]Cu alloys," *Acta Metallurgica*, vol. 36, pp. 143–147, Jan. 1988.

[174] P. A, S. Jr, M. Merino, R. Arrabal, and E. Matykina, "Electrochemical Estimation of the Corrosion Rate of Magnesium/Aluminium Alloys," *International Journal of Corrosion*, vol. 2010, Jan. 2010.

[175] G. Galicia, N. Pébère, B. Tribollet, and V. Vivier, "Local and global electrochemical impedances applied to the corrosion behaviour of an AZ91 magnesium alloy," *Corrosion Science*, vol. 51, pp. 1789–1794, Aug. 2009.

[176] F. Cao, Z. Shi, J. Hofstetter, P. J. Uggowitzer, G. Song, M. Liu, and A. Atrens, "Corrosion of ultra-high-purity Mg in 3.5% NaCl solution saturated with Mg(OH)2," *Corrosion Science*, vol. 75, pp. 78–99, Oct. 2013.

[177] S. Jr, F. García-Galván, I. Llorente, L. Diaz, and J. Simancas, "Influence of hydrogen bubbles adhering to the exposed surface on the corrosion rate of magnesium alloys AZ31 and AZ61 in sodium chloride solution," *materials and corrosion*, vol. 68, Nov. 2016.

[178] M. Jamesh, S. Kumar, and T. S. N. Sankara Narayanan, "Corrosion behavior of commercially pure Mg and ZM21 Mg alloy in Ringer's solution – Long term evaluation by EIS," *Corrosion Science*, vol. 53, pp. 645–654, Feb. 2011.

[179] R. Karunakaran, S. Ortgies, A. Tamayol, F. Bobaru, and M. P. Sealy, "Additive manufacturing of magnesium alloys," *Bioactive Materials*, vol. 5, pp. 44–54, Mar. 2020.

[180] C. C. Ng, M. M. Savalani, H. C. Man, and I. Gibson, "Layer manufacturing of magnesium and its alloy structures for future applications," *Virtual and Physical Prototyping*, vol. 5, pp. 13–19, Mar. 2010.

[181] K. Wei, Z. Wang, and X. Zeng, "Influence of element vaporization on formability, composition, microstructure, and mechanical performance of the selective laser melted Mg–Zn–Zr components," *Materials Letters*, vol. Complete, no. 156, pp. 187–190, 2015.

[182] J. Dong, N. Tümer, M. A. Leeflang, P. Taheri, L. E. Fratila-Apachitei, J. M. C. Mol, A. A. Zadpoor, and J. Zhou, "Extrusion-based additive manufacturing of Mg-Zn alloy scaffolds," *Journal of Magnesium and Alloys*, Dec. 2021.

[183] S. K. Manjhi, P. Sekar, S. Bontha, and A. S. S. Balan, "Additive manufacturing of magnesium alloys: Characterization and post-processing," *International Journal of Lightweight Materials and Manufacture*, vol. 7, pp. 184–213, Jan. 2024.

[184] R. Motallebi, Z. Savaedi, and H. Mirzadeh, "Post-processing heat treatment of lightweight magnesium alloys fabricated by additive manufacturing: a review," *Journal of Materials Research and Technology*, vol. 20, pp. 1873–1892, Sept. 2022.

Thèse accessible à l'adresse : https://theses.insa-lyon.fr/publication/2025ISAL0008/these.pdf © [J. Moreau], [2025], INSA Lyon, tous droits réservés

[185] C. K. Chua and K. F. Leong, *3d Printing And Additive Manufacturing: Principles And Applications (With Companion Media Pack) - Fourth Edition Of Rapid Prototyping*. World Scientific Publishing Company, Aug. 2014.

[186] M. Liard, "Suspension concentrées: systèmes non newtoniens et thixotropie sous écoulement," vol. Ecole doctorale physique et chimie de strabourg, p. 163, 2015.

[187] S. Gangireddy, B. Gwalani, K. Liu, E. J. Faierson, and R. S. Mishra, "Microstructure and mechanical behavior of an additive manufactured (AM) WE43-Mg alloy," *Additive Manufacturing*, vol. 26, pp. 53–64, Mar. 2019.

[188] Y. Wang, H. Huang, G. Jia, H. Zeng, and G. Yuan, "Fatigue and dynamic biodegradation behavior of additively manufactured Mg scaffolds," *Acta Biomaterialia*, vol. 135, pp. 705–722, Nov. 2021.

[189] C. Shuai, Y. Yang, P. Wu, X. Lin, Y. Liu, Y. Zhou, P. Feng, X. Liu, and S. Peng, "Laser rapid solidification improves corrosion behavior of Mg-Zn-Zr alloy," *Journal of Alloys and Compounds*, vol. 691, pp. 961–969, Jan. 2017.

[190] M. Wolff, T. Ebel, and M. Dahms, "Sintering of Magnesium," *Advanced Engineering Materials*, vol. 12, no. 9, pp. 829–836, 2010.

[191] M. Wolff, M. Marvi-Mashhadi, E. Nidadavolu, H. Lüneburg, T. Ebel, and R. Willumeit-Römer, "Comparison between compression tested and simulated Mg-6.3Gd bone scaffolds produced by binder based additive manufacturing technique," *Journal of Magnesium and Alloys*, vol. 11, pp. 2750–2762, Aug. 2023.

[192] M. Salehi, S. Maleksaeedi, M. L. S. Nai, and M. Gupta, "Towards additive manufacturing of magnesium alloys through integration of binderless 3D printing and rapid microwave sintering," *Additive Manufacturing*, vol. 29, p. 100790, Oct. 2019.

[193] M. Kachit, A. Kopp, J. Adrien, E. Maire, and X. Boulnat, "Direct-ink writing and compression behavior by *in situ* micro-tomography of architectured 316L scaffolds with a two-scale porosity," *Journal of Materials Research and Technology*, vol. 20, pp. 1341–1351, Sept. 2022.

[194] H. Elsayed, P. Rebesan, G. Giacomello, M. Pasetto, C. Gardin, L. Ferroni, B. Zavan, and L. Biasetto, "Direct ink writing of porous titanium (Ti6Al4V) lattice structures," *Materials Science and Engineering: C*, vol. 103, p. 109794, Oct. 2019.

[195] H. Gong, D. Snelling, K. Kardel, and A. Carrano, "Comparison of Stainless Steel 316L Parts Made by FDM- and SLM-Based Additive Manufacturing Processes," *JOM*, vol. 71, pp. 880–885, Mar. 2019.

[196] A. Kottasamy, M. Samykano, K. Kadirgama, M. Rahman, and M. M. Noor, "Experimental investigation and prediction model for mechanical properties of copper-reinforced polylactic acid composites (Cu-PLA) using FDM-based 3D printing technique," *The International Journal of Advanced Manufacturing Technology*, vol. 119, pp. 5211–5232, Apr. 2022.

[197] M. Sevastaki, M. Suchea, and G. Kenanakis, "3D Printed Fully Recycled TiO2-Polystyrene Nanocomposite Photocatalysts for Use against Drug Residues," *Nanomaterials*, vol. 10, p. 2144, Oct. 2020.

[198] M. Mbow, P. Marin, and F. Pourroy, "Extruded diameter dependence on temperature and velocity in the fused deposition modeling process," *Progress in additive manufacturing*, vol. 5, pp. 139–152, June 2020.

Thèse accessible à l'adresse : https://theses.insa-lyon.fr/publication/2025ISAL0008/these.pdf © [J. Moreau], [2025], INSA Lyon, tous droits réservés

[199] F. Baino and E. Fiume, "3D Printing of Hierarchical Scaffolds Based on Mesoporous Bioactive Glasses (MBGs)—Fundamentals and Applications," *Materials*, vol. 13, p. 1688, Jan. 2020.

[200] J. Cesarano, "A Review of Robocasting Technology," *MRS Online Proceedings Library (OPL)*, vol. 542, p. 133, 1998.

[201] M. Coffigniez, *Additive manufacturing of 3D architectured metallic biomaterials by robocasting*. These de doctorat, Lyon, Jan. 2021.

[202] Z. A. Munir, "Analytical treatment of the role of surface oxide layers in the sintering of metals," *Journal of Materials Science*, vol. 14, pp. 2733–2740, Nov. 1979.

[203] P. Burke, G. Kipouros, D. Fancelli, and V. Laverdiere, "Sintering Fundamentals of Magnesium Powders," *Canadian Metallurgical Quarterly*, vol. 48, pp. 123–132, June 2009.

[204] R. German, *Particulate composites: Fundamentals and applications*. Particulate composites, Jan. 2016.

[205] R. M. German, P. Suri, and S. J. Park, "Review: liquid phase sintering," *Journal of Materials Science*, vol. 44, pp. 1–39, Jan. 2009.

[206] J. G. Schaper, N. Scharnagl, M. Wolff, T. Ebel, S. Neumann, and R. Willumeit-Römer, "Polyolefin-Magnesium Interactions Performing Powder Injection Molding Process," *Advanced Engineering Materials*, vol. 20, no. 11, p. 1800530, 2018. _eprint: https://onlinelibrary.wiley.com/doi/pdf/10.1002/adem.201800530.

[207] M. Wolff, J. G. Schaper, M. R. Suckert, M. Dahms, F. Feyerabend, T. Ebel, R. Willumeit-Römer, and T. Klassen, "Metal Injection Molding (MIM) of Magnesium and Its Alloys," *Metals*, vol. 6, p. 118, May 2016. Number: 5 Publisher: Multidisciplinary Digital Publishing Institute.

[208] J. G. Schaper, M. Wolff, B. Wiese, T. Ebel, and R. Willumeit-Römer, "Powder metal injection moulding and heat treatment of AZ81 Mg alloy," *Journal of Materials Processing Technology*, vol. 267, pp. 241–246, May 2019.

[209] M. Wolff, J. G. Schaper, M. R. Suckert, M. Dahms, T. Ebel, R. Willumeit-Römer, and T. Klassen, "Magnesium Powder Injection Molding (MIM) of Orthopedic Implants for Biomedical Applications," *JOM*, vol. 68, pp. 1191–1197, Apr. 2016.

[210] C. M. Kipphut, A. Bose, S. Farooq, and R. M. German, "Gravity and configurational energy induced microstructural changes in liquid phase sintering," *Metallurgical Transactions A*, vol. 19, pp. 1905–1913, Aug. 1988.

[211] M. Salehi, S. Maleksaeedi, M. A. B. Sapari, M. L. S. Nai, G. K. Meenashisundaram, and M. Gupta, "Additive manufacturing of magnesium–zinc–zirconium (ZK) alloys via capillary-mediated binderless three-dimensional printing," *Materials & Design*, vol. 169, p. 107683, May 2019.

[212] M. Salehi, K. X. Kuah, J. H. Ho, S. X. Zhang, H. L. Seet, and M. L. S. Nai, "Towards Binder Jetting and Sintering of AZ91 Magnesium Powder," *Crystals*, vol. 13, p. 286, Feb. 2023.

[213] R. M. German, "Supersolidus liquid-phase sintering of prealloyed powders," *Metallurgical and Materials Transactions A*, vol. 28, pp. 1553–1567, July 1997.

[214] M. Salehi, K. X. Kuah, Z. Huang, D. J. Blackwood, S. X. Zhang, H. L. Seet, and M. L. S. Nai, "Enhancing densification in binder jet additive manufacturing of magnesium via

Thèse accessible à l'adresse : https://theses.insa-lyon.fr/publication/2025ISAL0008/these.pdf © [J. Moreau], [2025], INSA Lyon, tous droits réservés

nanoparticles as sintering aids," *Journal of Manufacturing Processes*, vol. 99, pp. 705–717, Aug. 2023.

[215] A. I. o. Physics, *American Institute of Physics Handbook*. McGraw-Hill, 1972.

[216] G. Deffrennes, *Étude expérimentale et évaluation thermodynamique du système Al-C-Mg*. phdthesis, Université de Lyon, Dec. 2018.

[217] J. Svoboda, H. Riedel, and R. Gaebel, "A model for liquid phase sintering," *Acta Materialia*, vol. 44, pp. 3215–3226, Aug. 1996.

[218] M. P. Brada and D. R. Clarke, "A thermodynamic approach to the wetting and dewetting of grain boundaries," *Acta Materialia*, vol. 45, pp. 2501–2508, June 1997.

[219] W. Beere, "A unifying theory of the stability of penetrating liquid phases and sintering pores," *Acta Metallurgica*, vol. 23, pp. 131–138, Jan. 1975.

[220] G. Martínez-Criado, J. Villanova, R. Tucoulou, D. Salomon, J.-P. Suuronen, S. Labouré, C. Guilloud, V. Valls, R. Barrett, E. Gagliardini, Y. Dabin, R. Baker, S. Bohic, C. Cohen, and J. Morse, "ID16B: a hard X-ray nanoprobe beamline at the ESRF for nano-analysis," *Journal of Synchrotron Radiation*, vol. 23, pp. 344–352, Jan. 2016.

[221] X. Zhang, L. Hua, and Y. Liu, "FE simulation and experimental investigation of ZK60 magnesium alloy with different radial diameters processed by equal channel angular pressing," *Materials Science and Engineering: A*, vol. 535, pp. 153–163, Feb. 2012.

[222] E. Lidén, E. Carlstrom, L. Eklund, B. Nyberg, and R. Carlsson, "Homogeneous Distribution of Sintering Additives in Liquid-Phase Sintered Silicon Carbide," *Journal of the American Ceramic Society*, vol. 78, pp. 1761–1768, July 1995.

[223] M. Pontoreau, M. Coffigniez, V. Trillaud, C. L. Bourlot, J. Lachambre, L. Gremillard, M. Perez, E. Maire, J. Adrien, P. Steyer, T. Douillard, A. King, and X. Boulnat, "*In* situ synchrotron study of sintering of gas-atomized Ti-6Al-4 V powders using concomitant micro-tomography and X-ray diffraction: Effect of particle size and interstitials on densification and phase transformation kinetics," *Acta Materialia*, vol. 246, p. 118723, Mar. 2023.

[224] J.-A. Kim, J. Lim, R. Naren, H.-S. Yun, and E. K. Park, "Effect of the biodegradation rate controlled by pore structures in magnesium phosphate ceramic scaffolds on bone tissue regeneration in vivo," *Acta Biomaterialia*, vol. 44, pp. 155–167, Oct. 2016.

[225] Y. Wang, P. Fu, N. Wang, L. Peng, B. Kang, H. Zeng, G. Yuan, and W. Ding, "Challenges and Solutions for the Additive Manufacturing of Biodegradable Magnesium Implants," *Engineering*, vol. 6, pp. 1267–1275, Nov. 2020.

[226] V. G. Rocha, E. Saiz, I. S. Tirichenko, and E. García-Tuñón, "Direct ink writing advances in multi-material structures for a sustainable future," *Journal of Materials Chemistry A*, vol. 8, pp. 15646–15657, Aug. 2020.

Thèse accessible à l'adresse : https://theses.insa-lyon.fr/publication/2025ISAL0008/these.pdf © [J. Moreau], [2025], INSA Lyon, tous droits réservés

Thèse accessible à l'adresse : https://theses.insa-lyon.fr/publication/2025ISAL0008/these.pdf © [J. Moreau], [2025], INSA Lyon, tous droits réservés

FOLIO ADMINISTRATIF

THESE DE L'INSA LYON, MEMBRE DE L'UNIVERSITE DE LYON

NOM : MOREAU DATE de SOUTENANCE : 24/01/2025

Prénom : Julien

TITRE: Sinter-based Additive Manufacturing of Mg-Zn Bio-degradable Metallic Materials for Orthopedic Implants

NATURE : Doctorat Numéro d'ordre : **2025ISAL0008**

Ecole doctorale : ED 34 Matériaux de Lyon

Spécialité : Matériaux

RESUME:

Magnesium (Mg) alloys are emerging as promising materials for biomedical applications due to their biocompatibility, biodegradability, and favorable mechanical properties. However, their rapid degradation in aqueous environments and the associated impacts have hindered their widespread use. In this study, we explore the incorporation of Zinc (Zn) and Zirconium (Zr) as alloying elements to improve corrosion resistance.The main focus of this thesis is the design of alloys, employing powder metallurgy manufacturing processes and microstructural modifications through aging treatments. These modifications were monitored using hardness and thermoelectric power measurements, with the ultimate objective of achieving a controlled and predictable degradation rate in physiological environments. High-purity Mg-Zn-Zr alloys were fabricated using Spark Plasma Sintering (SPS), with particular attention to the effects of sintering parameters on the native oxide layer surrounding the Mg alloy powder particles. The mechanical properties of the resulting dense parts were evaluated to determine the optimal manufacturing temperatures.Material properties were characterized using various techniques, including Energy-Dispersive X-ray Spectroscopy (EDS), optical microscopy, Scanning Electron Microscopy (SEM), Electron Backscatter Diffraction (EBSD), micro-indentation, potentiodynamic polarization measurements, and in vitro degradation studies. Thermal treatments of the alloys promoted the formation of precipitates, which were found to enhance corrosion resistance when their size and distribution were appropriately controlled. Another critical aspect of this study involves the use of Additive Manufacturing (AM) for Mg alloys. Beyond enabling personalization in the medical field, AM facilitates the creation of cellular structures with controlled porosity. These structures allow for the modulation of mechanical properties while promoting cellular invasion, a key factor in tissue engineering. The scaffolds were produced via robocasting, a layer-by-layer extrusion process using a paste composed of powder and binder. These structures were then debinded and sintered to achieve their final properties.
Although sintering Mg alloys presents significant challenges, the use of liquid-phase sintering and a labyrinth-like crucible enabled successful sintering of pressed pellets and printed scaffolds.
In summary, this PhD thesis presents the development of a biodegradable Mg-Zn-Zr alloy designed for orthopedic applications. The mechanical and corrosion properties were optimized through the fabrication of dense parts via SPS, and a robocasting method for Mg alloys was developed, paving the way for 3D-printed biodegradable implants.

MOTS-CLÉS : Magnesium alloys, Sintering, Robocasting, Biodegradable, Orthopaedic implants

Laboratoire (s) de recherche : MATEIS – UMR CNRS
INSA LYON
7 Avenue Jean Capelle Ouest
69621 VILLEURBANNE CEDEX
France

Directeurs de thèse : Laurent GREMILLARD, Xavier BOULNAT, Benoît TER-OVANESSIAN, Michel PEREZ, Olivier DEZELLUS

Président de jury : Ghislaine BERTRAND

Composition du jury : Rajashekhara SHABADI(Rapporteur)
Frédéric BERNARD (Rapporteur)
Marion COFFIGNIEZ (Examinatrice)
Ghislaine BERTRAND (Examinatrice)

Thèse accessible à l'adresse : https://theses.insa-lyon.fr/publication/2025ISAL0008/these.pdf © [J. Moreau], [2025], INSA Lyon, tous droits réservés